Structure and Relaxation Studies of High Performance Thermoplastics

by

Xin Lu

M.S., University of Missouri-Kansas City
Kansas City, MO
(1992)

Submitted to the Department of Materials Science and Engineering in Partial Fulfillment of the Requirements for the Degree of

DOCTOR OF PHILOSOPHY

at the

Massachusetts Institute of Technology

June, 1995

Signature of Author _____
Department of Materials Science and Engineering
May 5, 1995

Certified by _____
Associate Professor Peggy Cebe
Thesis Supervisor

Accepted by _____
Carl V. Thompson II
Professor of Electronic Materials
Chair, Departmental Committee on Graduate Studies

Structure and Relaxation Studies of High Performance Thermoplastics

by
Xin Lu

Submitted to the Department of Materials Science and Engineering
on May 5, 1995, in partial fulfillment of the requirements for the degree of
Doctor of Philosophy

Abstract

The objective of this research is to explore the behavior of the amorphous phase and rigid amorphous phase (RAP) in two high performance semicrystalline thermoplastics: NEW-TPI and poly(phenylene sulphide) (PPS). Both polymers contain phenyl-rings in their monomer repeat units, and have wide application as composite matrices and cable insulation. Small angle X-ray scattering (SAXS) has been applied to obtain the crystal lamellar structure, while thermally stimulated depolarization current (TSDC) and modulated differential scanning calorimetry (MDSC) are used to study the relaxations of the amorphous phase and of RAP.

In our NEW-TPI study, SAXS indicates that while the crystal lamellae increase in thickness linearly with the crystallization temperature (T_c), relatively more amorphous phase resides in between the lamellar stacks when the sample is crystallized at higher temperatures. The relaxation of the amorphous phase in semicrystalline NEW-TPI is not much constrained by the crystal phase, as suggested by the small increment in the glass transition temperature (T_g) observed from TSDC experiments. The thermal expansion of the amorphous phase, however, is constrained laterally along the lamellar plane by the crystalline phase expansion. The coefficient of thermal expansion (CTE) of the amorphous phase derived from SAXS agrees well with that derived from thermomechanical analysis, and is about four times larger than the CTE of the crystal phase.

While only a small amount of RAP is observed in NEW-TPI, we find a large amount of RAP in PPS. Almost all the amorphous phase in as-received film processed PPS is RAP. When PPS film is annealed at a temperature higher than T_g, some RAP can relax and become liquid-like amorphous phase. MDSC study on the effect of thermal treatment of PPS suggests that annealing of the amorphous phase between the nominal T_g and T_c will increase the RAP content. Both T_c and molecular weight (M_w) will also affect the RAP content. Lower T_c results in higher RAP content in the temperature range between T_g and the melting temperature. Lower M_w material contains more RAP compared to its higher M_w counterpart when both are crystallized at the

same crystallization rate. It is found that the well crystallized PPS sample with lower M_w shows a higher modulus at higher temperature in dynamic mechanical analysis. This is considered to be due to the better reorganization ability of the lower M_w sample as suggested by MDSC.

Thesis Supervisor: Dr. Peggy Cebe
Title: Associate Professor of Polymer Physics

Table of Content

List of Figures

List of Tables

Acknowledgements

I would like to express my great gratitude to Professor Peggy Cebe, my thesis advisor, for her professional guidance, constant encouragement and generous support. It has been a wonderful and valuable experience working with her.

I would like to thank my committee members: Professor F. J. McGarry, Professor M. Rubner and Professor L.C. Kimerling for their time, interests and advice throughout my research at MIT.

The fruitful discussion with Professor C. Lacabanne for the TSDC cell is greatly acknowledged. Special thanks go to Dr. L. Thomas and Mr. D. Geller from TA Instruments for the use of Modulated DSC Instruments.

I also like to extend my thankfulness to all my colleagues for their help and friendship (in alphabetical order): Mark Brillhart, Dr. Bruce Carvalho, John Chen, Dr. Yao-Yi Cheng, Janelle Greer, Honglin Guo, Julie Holmes, Christian Honeker, Paul Kang, Preston Li, Ingchie Kwan, Kwanki, Dr. Yaping Liu, Yingchun Liu, Dr. Norene Lucas, Linda Molnar, Mary Jane O'Rourke, Dr. Pengtao Huo, Dave Rich, Wendy Russell, Ed Shaffer, Tom Schaub, Dr. Enid Sichel, Hua Shen, Stephanie Simmons, Bill Stockton, Jie Sun, Justyna Teverovsky, Dr. Michael Yoo, Shi Yuan, Rocky Zhu and Ken Zemack. Working with them has been an wonderful experience. Ms. Amy Sklivas is also gratefully acknowledged.

The research funding from Electric Power Research Institute (RP: 8007-13) and the U.S. Army Research Office (DAAH 04-94-G-0317) is gratefully acknowledged.

I own great debts to my parents and my brother for their unconditional love and constant encouragement throughout my study.

Last but not least, I want to thank my husband, Fanqi Gan, for his understanding, support, encouragement and love.

Chapter 1

Introduction and Background

1.1 SEMICRYSTALLINE POLYMERS

Generally speaking, there are two different forms in which polymers can display their properties as solids: one is in the crystal form, and one is in the glassy form [1-4]. The biggest distinction between them is that the crystal form has perfect molecular order relatively speaking and the glass does not. Not all polymers are able to crystallize. Those crystallizable polymers usually possess a certain level of microscopic regularity in their monomer repeat units. Even in the polymers that do crystallize, the degree of crystallinity is not 100%. Therefore, the crystallizable polymers are referred to as semicrystalline polymers. In this work, we will deal mainly with semicrystalline polymers.

1.1.1 Structure of Typical Semicrystalline Polymer

Upon crystallization, semicrystalline polymers will form spherulites, each of which will consist of alternating crystal/amorphous lamellar structure, as shown in Figure 1.1 [taken from Fig. 13 of Ref. 5]. As we can see, there are three phases in the system: crystalline phase, amorphous phase and crystal/amorphous interphase. Here, we are not using 'phase' in the thermodynamic sense, but merely to indicate regions having different properties but which are chemically indistinguishable. While the crystal structure and the crystal phase have been quite well understood, the understanding of the amorphous phase lags far behind. For example, molecular simulation can predict polymer crystal structure and scattering

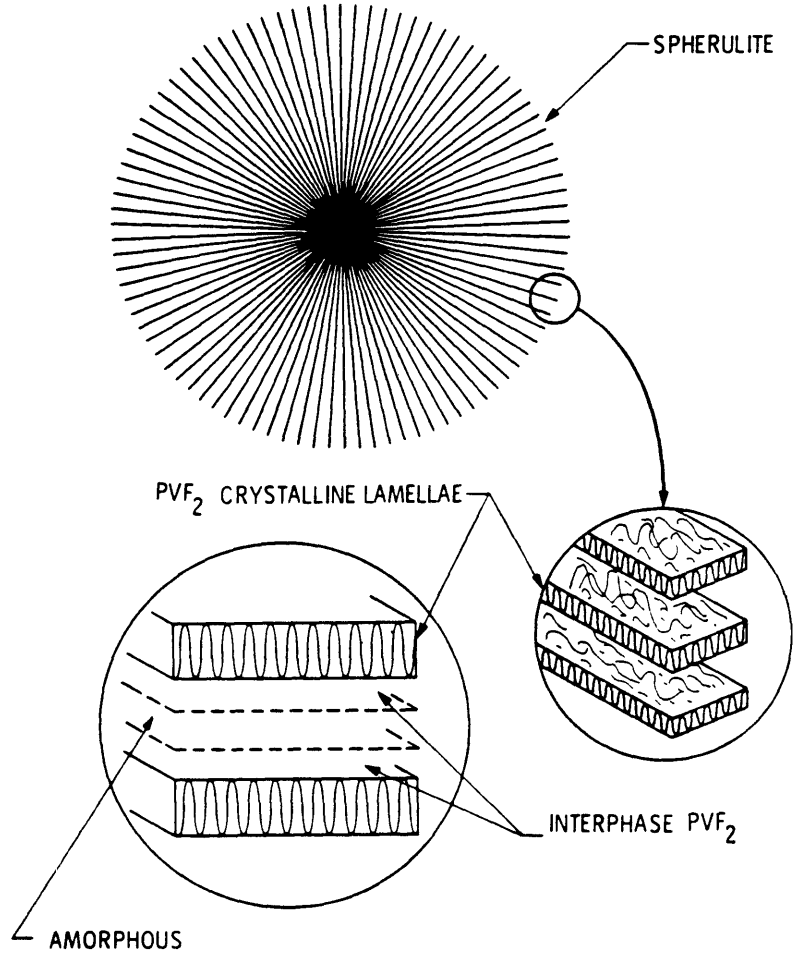

Figure 1.1 Schematic view of the spherulitic and crystal/amorphous lamellar structures.
(Figure taken from Ref. 5, Fig. 13)

patterns very well [6-11], yet up to now, nobody has ever predicted the glass transition temperature of an amorphous polymer. In a semicrystalline polymer, the amorphous phase is even more complicated. In addition to residing in between the lamellar stacks, amorphous phase can also reside in between the lamellar bundles or in between the spherulites. Amorphous phase location depends upon the material's characteristics and crystallization conditions. Amorphous phase residing at different places experiences different levels of constraints, thus resulting in different relaxation times. The role of the amorphous phase in semicrystalline polymers has long been one of the greatest interests in the polymer field [12].

Another important yet even more complicated phase in a semicrystalline polymer is the crystal/amorphous interphase [13-22]. Unlike some small molecular systems where the interphase can be treated as a sharp boundary and no connections exist between the two phases [23], the crystal/amorphous interphase in a polymer system is usually a transition regime where the molecular chains are changing from an ordered state to a disordered state. Two reasons may be considered to explain this. First, the entanglements of polymer long chains induce lots of connections between the crystal phase and the amorphous phase. These connections are usually strong covalent bonds. Second, rising again from the connectivity of the polymer, a distinct interphase is usually present. Its dimension may actually have the same order of magnitude as that of the other two phases as a result of the gradual change from ordered crystal phase to disordered amorphous phase. Considering these two effects, it is not difficult to realize that an understanding of the interphase has profound scientific importance and

engineering value. However, up to the moment, there is still a lack of direct evidence for the morphology, property and function of these interphases.

1.1.2 Relaxation of Semicrystalline Polymer

The properties of a polymer depend not only on its structure, but also on the equilibrium state of the chain movement [1-4,24-25]. When the outside conditions such as temperature, pressure, or electric fields etc., are changed, polymer chains may respond and change to a new equilibrium state. This process is strongly time-dependent for polymers, and often referred to as relaxation. For example, the transition of an amorphous polymer changing from the glassy state to the rubbery state is called the glass transition relaxation. At the glass transition temperature (T_g), polymer long chains start to move in a long range cooperative fashion, as opposed to the frozen state where the chains can only move locally. For the polymer having side chains, there may also exist sub-T_g relaxations. Whenever a polymer experiences a relaxation, it usually results in property changes and energy absorption.

For a semicrystalline polymer, the relaxation behavior can be quite complicated. From low temperature to high temperature, we may observe several sub-T_g relaxations, glass transition relaxation, relaxation in the crystal fold surface, and relaxation in crystal stems. Polymer relaxations can be observed from different aspects, for example, by using thermal, mechanical, electrical or dielectric measurements [26-28]. In semicrystalline polymers, we can observe the above relaxations if we measure dielectric properties at a fixed temperature while varying frequency from high frequency to low frequency [24-27].

As we have just discussed in the previous section, the amorphous phase may reside in different places in a semicrystalline polymer. Different constraints on the amorphous phase bring differences in the amorphous phase relaxation times. It has been found [29-39] that there exists a third phase, the so called 'rigid amorphous phase' (RAP), that does not contribute to the heat capacity step at T_g. The amount of RAP, χ_{rap}, can be calculated using a three-phase assumption:

$$\chi_{rap} = 1 - \chi_a - \chi_c \tag{1.1}$$

where χ_a and χ_c are the amounts of liquid-like amorphous phase and crystalline phase, respectively. RAP has only been found in semicrystalline polymers, and χ_{rap} is a strong function of the polymer thermal history [29-39]. Some researchers [38,39] have suggested that RAP is located in the crystal/amorphous interphase. However, we still lack direct and strong evidence for the nature of RAP.

Polymer relaxations relate closely to its properties, and directly to the micromolecular motion which bridges the polymer's structure and properties. Through this research, we hope to understand the correlation between the polymer's structure and relaxation behavior. Ultimately, we want to predict a polymer's property and tailor the polymer's structure according to our needs.

1.2 ANALYTICAL METHODS TO STUDY SEMICRYSTALLINE POLYMERS

Over the years, researchers have developed many analytical instruments to study polymer structure and properties [1-4,26-28]. Analytical methods to study relaxation are also those that study properties, ranging from thermal, mechanical, dielectric and electrical analysis. Mastering these analytical techniques is very important in polymer research. However, knowing how to operate the instrumentation is only a small part of it. The most important thing is to know the capability of each technique and be able to choose those techniques that can provide us with the most valuable information about the systems of interest, and help us understand the unknown world quicker and better. In this section, some background information on both structure and relaxation characterization are introduced with some detailed theory of some important techniques used in this study.

1.2.1 Structure Analysis

The obvious way to know polymer structure is to 'see' it. Microscopy is therefore the ideal candidate [1-4,26-27,40]. From optical microscopy and scanning electron microscopy, to more advanced scanning tunneling microscopy and atomic force microscopy, microscopy involves the most sophisticated equipment and sometimes somewhat tedious sample preparation. It is an excellent tool to study polymer morphology, polymer surfaces, liquid crystalline polymers and block copolymers.

Another excellent means to study polymer structure is through scattering techniques, which includes light scattering [1,2,4,26,27], neutron scattering [26,41] and X-ray scattering [1,2,4,26,41-45]. The scattered wave is

obtained from the interaction between the incident beam and matter. Different beam sources have different de Broglie wavelengths and are used in different types of polymeric systems. For example, light scattering with a wavelength λ_{light} ~ 4000-7000Å is typically used in studying particle sizes in solution [1,2,4,26,27], while X-ray scattering with a wavelength $\lambda_{X\text{-}ray}$ ~ 1-2Å is widely used in exploring solid state crystalline phase structure [1,2,4,26,27,41-45]. In this work, small angle X-ray scattering (SAXS) will be used to study different polymeric systems. Details about this technique will be discussed in the following. One of the extensions of X-ray scattering is synchrotron X-ray radiation [26,27,41,42]. The power of the synchrotron is its ability to reduce the data collection time from 4-6hrs to 20-30sec due to the high intensity of the X-ray source and the rapid data collection instrumentation. Therefore, real time testing can be performed to study in-situ polymer structure changes under a simulated processing condition. For example, crystallization, melting, stretching induced crystallization, etc., can all be studied while the sample's structure is changing.

The investigation of semicrystalline polymers structure using SAXS has been developed greatly on top of the fundamental work of Porod [46] and Debye [47]. The basic theory and data analysis are summarized here, while the details can be found in some excellent books and articles [1,2,4,26,41-45].

When the incident X-ray beam interacts with matter, it generates the coherent scattered waves. Although incoherent scattering will occur, its effect can be ignored as we are studying the extremely small angle scattering. The wavelength of coherent waves can be added and the intensity is then given by the absolute square of the resulting amplitude. A single secondary wave can

be represented by the complex $e^{i\varphi}$, where $\varphi = 2\pi/\lambda$ and λ is the wavelength of the incident beam. The electron density of the matter is expressed as $\rho(\mathbf{r})$, therefore, the amplitude of diffracted electric field from the matter with volume V can be expressed as:

$$F(\mathbf{h}) = \iiint dV\, \rho(\mathbf{r})\, e^{-ihr} \tag{1.2}$$

where $h = (4\pi/\lambda)\sin\theta$, and θ is the diffraction angle. Thus the intensity $I(\mathbf{h})$, which is the absolute square of the electric field vector, is found to be:

$$I(h) = FF^* = \iiint\iiint dV_1\, dV_2\, \rho(r_1)\, \rho(r_2)\, e^{-ih(r_1-r_2)} \tag{1.3}$$

This is the Fourier integral, involving only the relative distance. The above I(h) can be transformed into another form:

$$I(h) = \int dV\, \tilde{\rho}^2(r)\, e^{-ihr} \tag{1.4}$$

where $\tilde{\rho}^2(r)$ is the auto-correlation function and is defined as:

$$\tilde{\rho}^2(\mathbf{r}) = \int dV_1\, \rho(\mathbf{r_1})\, \rho(\mathbf{r_2}) \tag{1.5}$$

It represents the degree of correlation between the electron density at $\mathbf{r_1}$ to that at $\mathbf{r_2}$, and $\mathbf{r} = \mathbf{r_1} - \mathbf{r_2}$ is constant.

In many cases of semicrystalline polymers, we can assume that the systems under study are statistically isotropic and no long range order exists. The intensity can then be simplified to the following equation:

$$I(h) = \int 4\pi r^2 dr \, \tilde{\rho}^2(r) \frac{\sin hr}{hr} \tag{1.6}$$

Here:

$$\langle e^{-ihr} \rangle = \frac{\sin hr}{hr} \tag{1.7}$$

is the fundamental formula of Debye [47].

If we define electron density fluctuation η, as $\eta = \rho(\mathbf{r_1}) - \rho_{ave}$, where ρ_{ave} is the average density, the auto-correlation is then redefined as:

$$\tilde{\eta}^2(\mathbf{r}) = \overline{(\rho - \rho_{ave})^2} = \tilde{\rho}^2 - V\rho_{ave}^2 = V\gamma(r) \tag{1.8}$$

where $\gamma(r)$ is the correlation function which represents the electron density correlation between two points at $\mathbf{r_1}$ and $\mathbf{r_2}$ and is defined as:

$$\gamma(r) = \langle \eta(\mathbf{r_1}) \, \eta(\mathbf{r_2}) \rangle \tag{1.9}$$

Notice that the integral of ρ_{ave} is zero and $r = |\mathbf{r_1} - \mathbf{r_2}|$ is constant, Eqn. 1.6 then becomes:

$$I(h) = V \int_0^\infty 4\pi r^2 dr \, \gamma(r) \frac{\sin hr}{hr} \tag{1.10}$$

For systems with flat plate-like structure, such as semicrystalline polymer lamellar structure, the problem can be simplified by applying the following equation:

$$\rho(x, y, z) = \rho(z)\, \rho(x, y, L_x, L_y) \tag{1.11}$$

Here $\rho(x, y, L_x, L_y)$ is a very weak function of x,y, provided that the length scales in x and y directions are smaller than L_x and L_y. Therefore, a three-dimensional problem can be reduced to a one-dimensional problem where the correlation function is solely a function of z. The most common form to express the relationship between the electron density difference and the scattering intensity is:

$$I(h) = \int_0^T \gamma(r) \cos(hz)\, dz \tag{1.12}$$

or

$$\gamma(z) = \frac{1}{\pi} \int_0^\infty I(h) \cos(hz)\, dh \tag{1.13}$$

where T is the long period of each lamellar structure. From these Eqn. 1.12 or Eqn. 1.13, the long period L, lamellar thickness l_c and volume crystallinity χ_c can all be determined as shown below.

We present in Figure 1.2 (taken from Ref. 45, Fig. 1) the plots of both the electron density and the one-dimensional correlation function as a

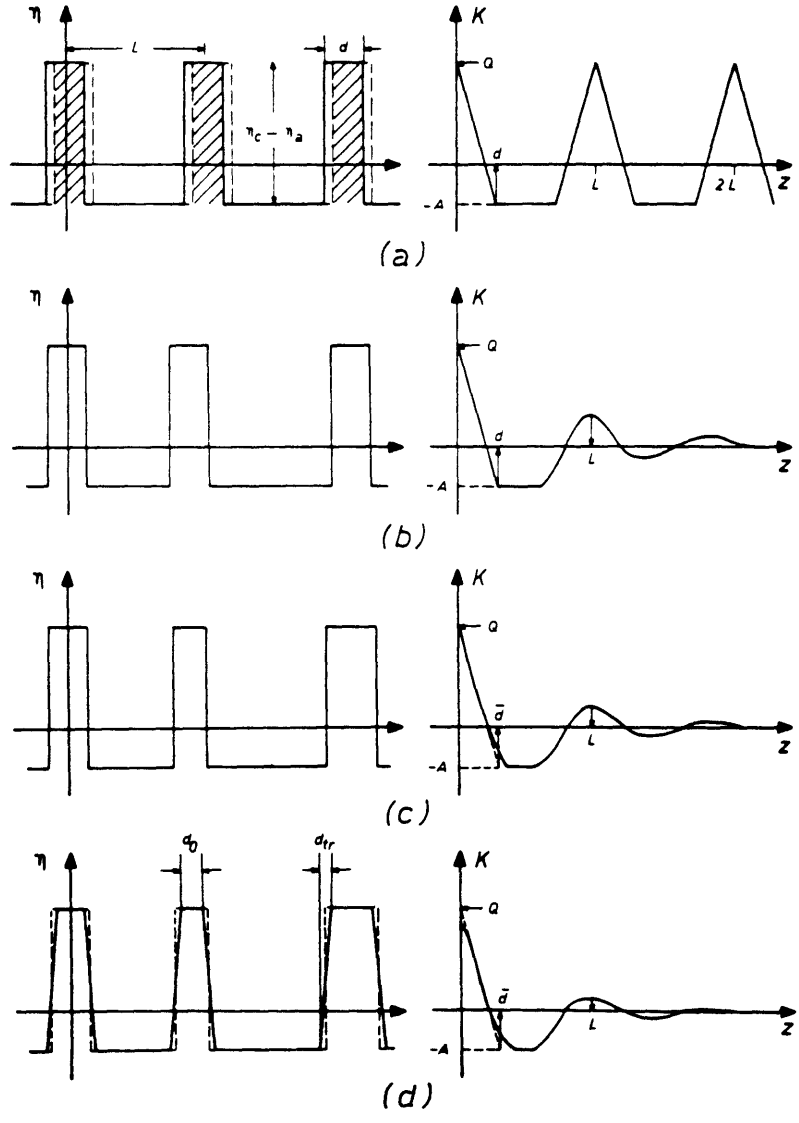

Figure 1.2 The one dimensional electron density correlation function. (Figure taken from Ref. 45, Figure 1)

function of z according to Strobl and Schneider [45]. Figure 1.2a represents the most ideal case where L and l_c are fixed values. Figure 1.2b shows the changes induced when L varies. Figure 1.2c further relaxes the restriction on l_c. Figure 1.2d introduces the effect of diffuse phase boundaries. L and l_c can be obtained as shown in the figure, and χ_c is calculated according to the following equation:

$$\chi_c = \frac{A}{A + Q} \tag{1.14}$$

Here A and Q are values shown in Figure 1.2.

To summarize this section, the microscopy technique and the scattering technique each has its own advantages and limitations. Microscopy can let us see the exact polymer morphology, but it often takes a long time to prepare the sample, and sometimes, it is not always possible to see the structure. For scattering techniques, the sample preparation is usually quite simple. However, a mathematical model usually has to be assumed before data analysis. Therefore, for a particular system, we need to choose carefully which technique can give us the information we are looking for.

1.2.2 Relaxation Analysis

As we have discussed earlier, relaxation analysis is often coupled with property analysis, since a change in polymer property is usually the result of polymer relaxations. Typical polymer property characterization techniques [1-4,26-28] include differential scanning calorimetry (DSC), which studies how heat capacity changes with temperature, and dynamic mechanical analysis

(DMA), which investigates how polymer modulus and loss change with temperature as well as frequency. Others include thermomechanical analysis (TMA), thermogravimetric analysis (TGA) and tensile testing, etc. From the changes in the physical parameters, as well as the structural information from structure analysis, we are able to understand how the molecules relax. There also exist some experimental methods that allow us to measure the polymer chain relaxations directly, such as dielectric analysis (DEA) [26,27,38,39,48-52]. In DEA measurement, the motion of existing dipoles on the polymer backbone and side chains is probed. When an oscillating electric field is applied, these dipoles will respond to the change in temperature as well as frequency. In the following, some detailed information is presented on two powerful characterization techniques: thermally stimulated depolarization current and Modulated DSC.

1.2.2.1 Thermally Stimulated Depolarization Current

Thermally stimulated depolarization current (TSDC) measurement is an important branch from the family of thermally stimulated relaxation (TSR) methods [53,54]. Two basic conditions have to be fulfilled for the occurrence of the TSR process. First, the system must be removed from thermal equilibrium and exist in a state that requires the reactants to overcome a free energy barrier in order to move toward the reestablishment of equilibrium. Second, the system must be in contact with a temperature reservoir that provides the thermal energy necessary to activate the relaxation process. Other major techniques included under TSR are thermally stimulated conductivity, thermally stimulated luminescence and exoemission.

The distinct advantage [53-56] of TSDC over DMA and dielectric relaxation is its increased resolution. According to Hedvig [48], the low frequency range is best for studying polymer transitions by dynamic spectroscopy because of the increased resolution at low frequency. Figure 1.3 (taken from Fig. 4 of Ref. 55) shows how resolution of TSDC compares with the other two techniques.

TSDC was first proposed in 1964 by Bucci and Fieschi [57] as ionic thermocurrent (ITC) to study point defects in alkali halides. Since then, scientists have been using this method to study a wide variety of materials such as crystals [58-60], semiconductors [61], inorganic glasses [62,63] and polymers [24,25,64-81]. It was first utilized to characterize polymer by J. Vanderschueren [64] in his Ph.D. thesis in 1970. Almost at the same time, C. Lacabanne [65] and D. Chatain [66] initiated thermal sampling (t.s.) techniques to study the fine structure of polymers in their Ph.D. work. In later years, scientists started to study the correlation between TSDC and other experimental techniques [42,54]. Several books [24,25,67,68] have been published regarding this issue and related problems. A lot of research has been done on all kinds of polymers, such as: amorphous polymers [69-71], semicrystalline polymers [72], copolymers [73], polymer blends [74,75], liquid crystalline polymers [76] and polymer composites [77]. The influence of additives [78], dopants [79], plasticisers [80] and water [81] has also been followed.

The basic principle of TSDC [53-56] is to orient polar molecules or permanent polar groups of macromolecules, by applying a high voltage field at high temperature, then quench the material to a much lower temperature

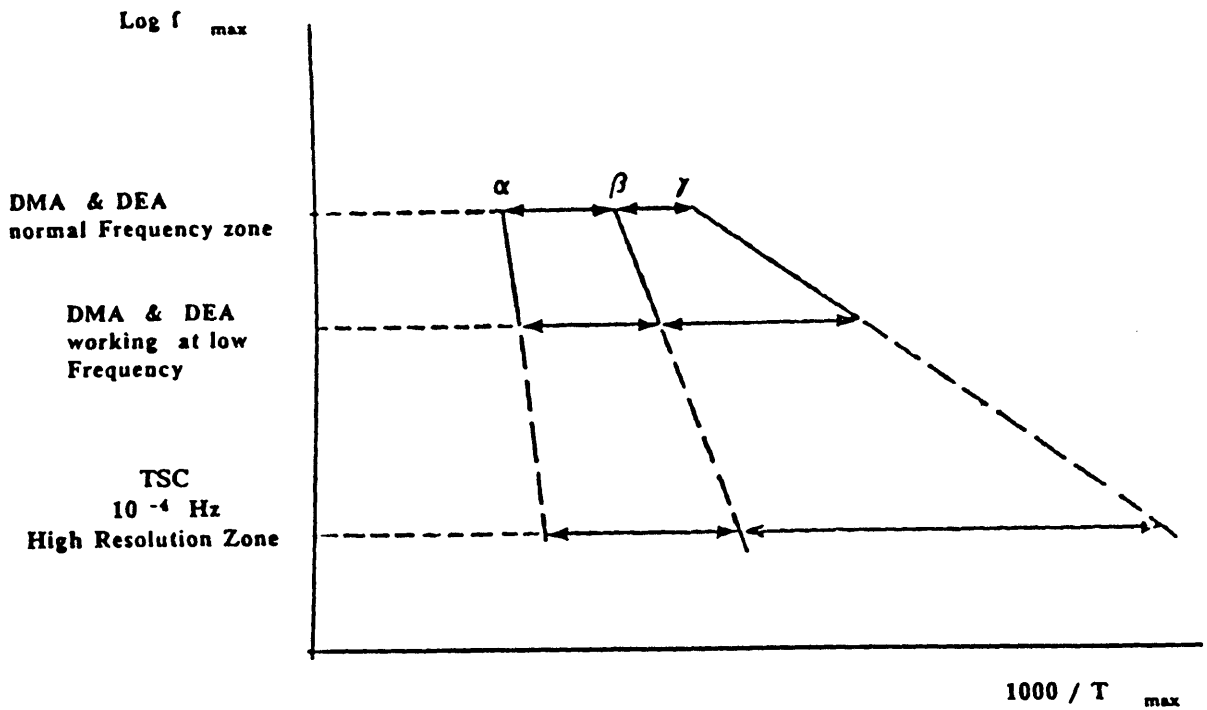

Figure 1.3 Resolution of TSDC vs. DMA and dielectric measurement. (Figure taken from Ref. 55, Fig. 4)

where the molecular motion ceases. After the electrodes have been shorted, the material is heated at a controlled rate and the depolarization current vs. temperature is recorded. This process is illustrated in Figure 1.4.

There are two techniques commonly used in TSDC measurements and these are presented and compared in Figure 1.5. For a global TSDC spectrum, a polymer sample is first heated to a temperature T_p, at which the poling voltage V_p is applied. After a certain time t_p, the sample is quickly quenched with cooling rate v_c to a temperature T_0, at which the poling voltage is withdrawn and the two electrodes are short-circuited. The sample is then heated up slowly with heating rate v_h. The current vs. temperature is recorded. For a thermal sampling spectrum, the voltage is on only from T_p to T_p-ΔT°C. The sample is held at T_p-ΔT°C for a certain time t_d ($t_p = t_d$), then quenched to more than 80°C below T_p. The thermally stimulated current vs. temperature is then recorded. In order to obtain precise measurement, TSDC samples are usually evaporated with metal such as Gold, Aluminum, etc., to ensure the best contact between the sample and the electrodes.

The origin of the current one observes in the TSDC measurement relates directly to the mechanism of molecular polarization [24,25,53-56,68]. The 'frozen in' aligned dipoles will randomized themselves as the temperature increases to give them the mobility to move, producing a displacement current. In addition, if there are different phases existing in the polymer bulk, charges can accumulate at the interphase due to the difference in conductivity between the two phases. While these charges can not move at low temperature, they can give current at high temperature. In addition, no polymer is absolutely impurity free. Those ionizable species can move

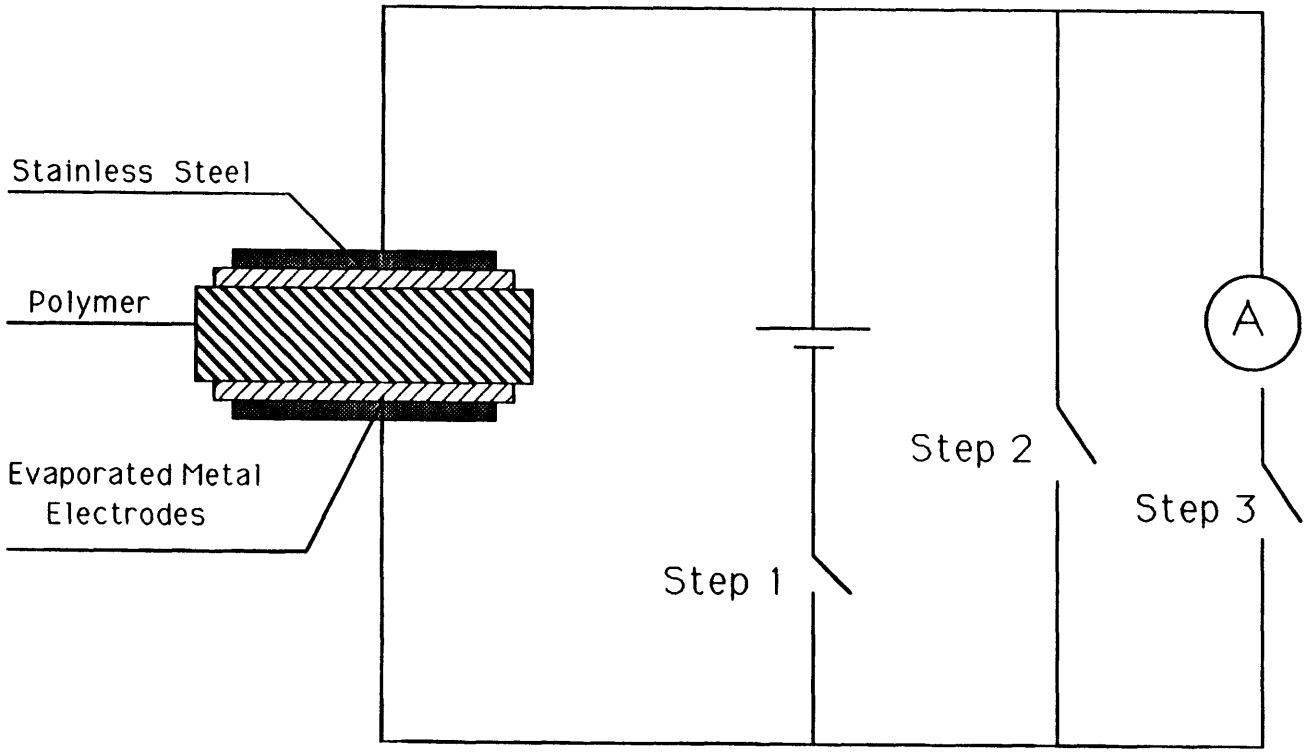

Figure 1.4 TSDC experiment procedure

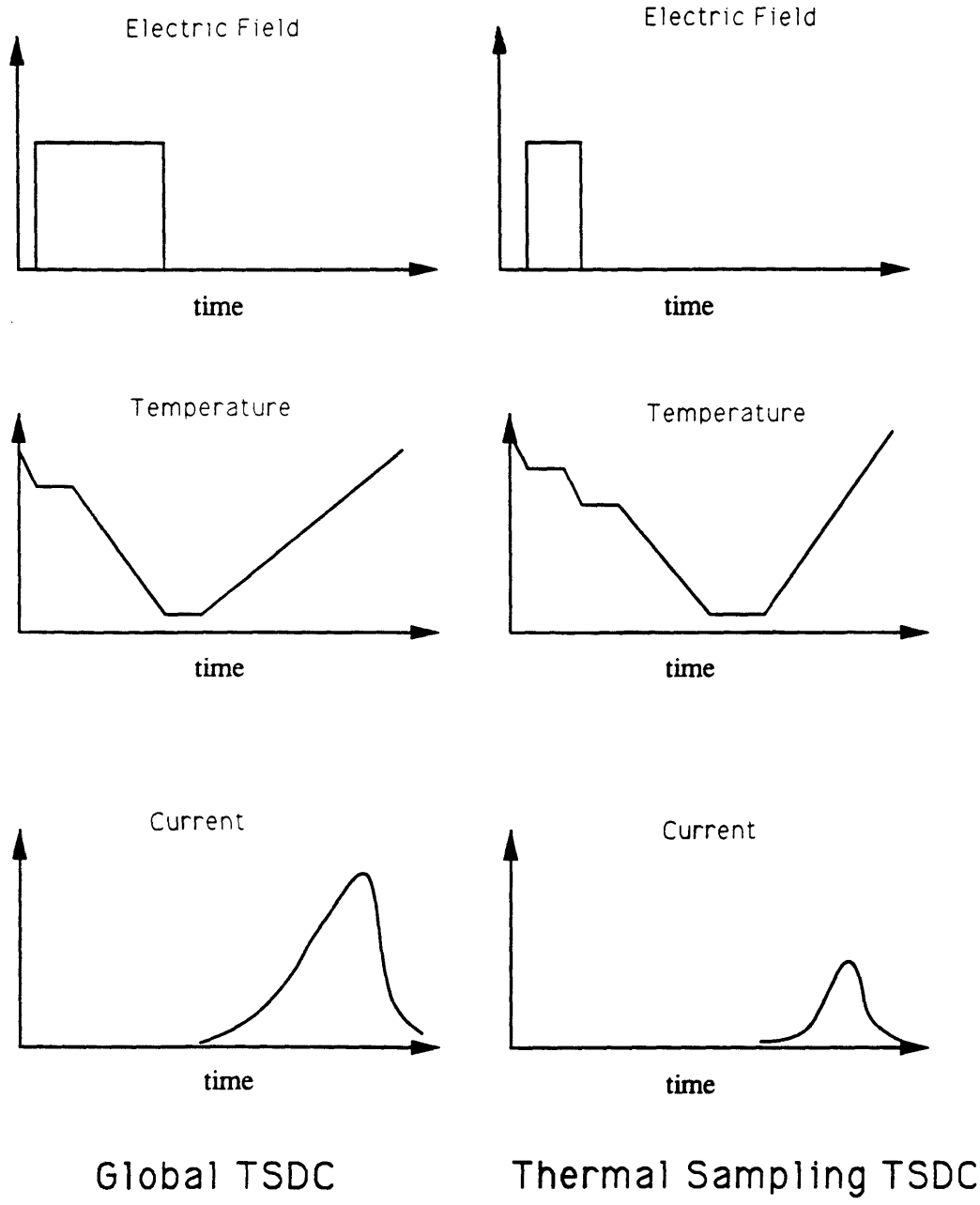

Figure 1.5 Comparison of two TSDC methods

under the influence of the electric field and produce a current when the polymer sample is heated up. Besides these intrinsic origins of current, extrinsic sources of current still exist because of either Schottky emission or Townsend breakdown at the polymer/metal interface.

Theoretical aspects of TSDC have been discussed in some excellent reviews [25,53-56,82]. As we have discussed previously, thermally stimulated current can be generated by dipole reorientation or by motion of real charges. In some cases, the current may be caused by both processes simultaneously. We will only consider the theories of TSDC resulting from a homogeneous polarization occurring in dielectrics free of charge.

Bucci and Fieschi [57] assumed an ideal rotational friction model, i.e., simple Debye model, to establish the polarization. The build up of polarization per unit volume of the material during time t after the application of an electric field E_p at a temperature T_p can be described by the following equation:

$$P(t) = P_e [1- \exp(-t/\tau)] \tag{1.15}$$

where τ is dipolar relaxation time and P_e is the equilibrium or steady state polarization at infinite t. Provided that the relaxation times for polarization and depolarization are the same, the decay of polarization after removal of the field at infinite time is given by:

$$P(t) = P_e \exp(-t/\tau) \tag{1.16}$$

The corresponding depolarization current density, J, can be written as:

$$J(t) = -dP/dt = P(t)/t \tag{1.17}$$

In a TSDC experiment, temperature and time vary simultaneously. Assume $T = T_o + qt$, where $q = dT/dt$, i.e., q is the heating rate, we arrive at:

$$P(t) = P_e [\exp(-\int_0^t dt/\tau)] \tag{1.18}$$

Several conditions have to be satisfied to use Eqn. 1.18. First, this relation also holds for varying temperature. Second, the initially frozen-in polarization $P(T_o)$ is equal to the equilibrium polarization reached at the poling temperature $P_e(T_p)$. Third, the temperature variation of τ has to be given by an Arrhenius-type equation:

$$\tau = \tau_o \exp(E/RT) \tag{1.19}$$

where τ_o is the relaxation time at infinite temperature and E is the activation energy of dipole disorientation. A general description of the current density for a TSDC experiment is given by the following equation:

$$J_D(T) = (P_e(T_p)/\tau_0) \exp(-E/kT) \exp[-(1/q\tau_0) \int_{T_o}^{T} \exp(-E/kT')dT'] \tag{1.20}$$

It has been shown from dielectric measurements that most polymers have distributed relaxation times, rather than a single relaxation time. To

modify the above theory, we rewrite the total polarization per unit volume as:

$$P(t) = \int_0^{\infty} P_i(t, \tau_0)\, d\tau_0 \tag{1.21}$$

Taking into account the formation and storage conditions and neglecting the temperature dependence of the equilibrium polarization, we can then write at each temperature during the TSDC experiment:

$$P(t) = P_e(T_p) \int_0^{\infty} H(\tau_0) f(\tau_0) \exp\left[-\frac{1}{q\tau_0}\int_{T_0}^{T} \exp(-E/kT')dT'\right] d\tau_0 \tag{1.22}$$

and:

$$J_D(T) = P_e(T_p)\exp(-E/kT) \int_0^{\infty} \tau_0^{-1} f(\tau_0) H(\tau_0) \exp\left[-\frac{1}{q\tau_0}\int_{T_0}^{T} \exp(-E/kT')dT'\right] d\tau_0 \tag{1.23}$$

Theoretical treatment for the global TSDC spectrum is a rather complicated issue as both orientational dipoles, with all the different relaxation times, and free charges may come into play at a certain temperature. Thus, most peak analysis is given to the thermal sampling spectrum. The above equations give the relationship in current and temperature space and can be used to fit experimental data directly.

Despite the power of TSDC, it has not yet become a conventional analytical tool used by many polymer scientists. Some of it comes from the

complexity of polymer systems. It is very easy to induce spurious charges that may come from moisture, poor contact between polymer and electrodes, thermal cycling, etc., which lead to irreproducible data. And more, theoretical development is far from perfect to account for the complex experimental difficulties. Nevertheless, a lot of experimental and theoretical work has been done and is currently being done in this area to improve our understanding.

1.2.2.2 Modulated DSC

MDSC is the recent advancement of DSC originated by Dr. M. Reading [83,84] and now is commercially available from TA Instruments. It provides the same information as normal DSC plus the additional benefit that enables us to know material properties in more detail [85-88]. Following the treatment of Ref. 85, in a normal DSC scan, the programmed temperature change can be described as:

$$T(t) = T_0 + \beta t \tag{1.24}$$

where T_0 is the starting temperature, t is time and β is the linear heating rate. The resulting heat flow dQ/dt is then the sum of the heat capacity component, $C_p\beta$, and a kinetic component, $f(t, T)$:

$$dQ/dt = C_p \beta + f(t, T) \tag{1.25}$$

In a typical MDSC heating scan, however, a sine wave is added to the temperature profile so that the temperature is written as:

$$T(t) = T_0 + \beta t + A_T (\sin\omega t) \tag{1.26}$$

where A_T is the amplitude of the temperature modulation and ω is the modulation frequency, $\omega = 2\pi/\text{Period}$. By substituting Eqn. 1.26 into Eqn. 1.24, we obtain a modulated heat flow:

$$dQ/dt = C_p(\beta + A_T\omega\cos\omega t)) + f'(t, T) + A_k(\sin\omega t) \quad (1.27)$$

Here, $(\beta + A_T\omega\cos\omega t))$ is the measured heating rate (dT/dt), $f'(t, T)$ is the kinetic response without temperature modulation, and A_k is the amplitude of kinetic response to the temperature modulation. The raw data directly obtained from MDSC are modulated heat flow and modulated temperature. The first work is to extract the effect of modulation from the recorded signals. It is accomplished by a Fourier transformation or deconvolution of the signals. Since the oscillating part of the signal averages to zero when integrated over an entire oscillation, the deconvolution is done by continued integration, averaging and smoothing over several cycles. The output obtained is:

$$C_p = K_{cp}\frac{A_{HF}}{A_{HR}} \quad (1.28)$$

where C_p is the heat capacity of the material, K_{cp} is the calibration constant, A_{HF} is the amplitude of the modulated heat flow, and A_{HR} is the amplitude of the heating rate. From Eqn. 1.28, we can obtain the two heating flow curves:

$$\text{Reversing heat flow} = -C_p\psi \quad (1.29)$$

$$\text{Non-reversing heat flow} = \text{Total heat flow} - \text{Reversing heat flow} \quad (1.30)$$

Here ψ is the average heating rate. Therefore, besides the total heat flow as obtained from normal DSC, MDSC gives two additional heat flows curves: reversing heat flow and non-reversing heat flow. Reversing heat flow is defined as the **heat capacity component** of the total heat flow. Transitions seen is this signal are usually thermodynamically reversible at the time and temperature at which they are detected. Typical transitions include the glass transition and most crystalline melts. In contrast, the non-reversing component is defined as the **kinetic component (non-heat capacity component)** of the total heat flow. Transitions seen in this signal are usually thermodynamically non-reversible at the time and temperature at which they are detected. Typical non-reversing transitions include enthalpic relaxation, cold crystallization, evaporation, thermal cure and decomposition [58].

There are many significant benefits by using MDSC. It can separate the complex transitions into more easily interpreted components. The initial crystallinity of a material can be obtained. The precision of a heat capacity measurement can be increased about ten times compared to using normal DSC, and the value can be obtained in single measurement [88]. Both sensitivity and resolution are increased at the same time. Thermal conductivity can also be measured using MDSC [85,87].

Special attention is required in order to get meaningful results from MDSC. For sample preparation, always use thin film sample. Special effort should be put to make sure of the best contact between the sample and the pan. A lid is always required to cover the sample. In choosing the experimental parameters, a minimum four cycles is required during a transition. The temperature modulation amplitude and modulation period

should be matched so that no cooling is applied during the heating scan. Generally, long periods are required for thick samples, low thermal conductivity samples, and thicker and heavier sample pans. Carefully matching the weights of the sample pan and reference pan is required in order to get accurate heat capacity measurement.

To summarize, structure studies and relaxation studies are two different approaches for the investigation of a polymer. They are complimentary to each other. Sometimes, structure studies give us more direct feeling about the polymer; sometimes, relaxation studies provide more insights about what happens to the polymer. For either an old puzzle in polymer science or a new member in the polymer family, we always want to look from different angles, and try to combine all the information we have to get a whole a picture of the subject.

1.3 HIGH PERFORMANCE THERMOPLASTICS

With the fast developments in the polymer industry and increasing demand for wide applications of polymers, many research groups have concentrated on exploring polymers other than commodity polymers that have been used mostly as packaging materials. One of these areas is the development of high performance thermoplastics. These polymers usually possess excellent thermal stability, toughness, solvent resistance, radiation resistance, dimensional stability, dielectric properties, and/or optical properties. Thus they can be applied in some harsh environments and for particular applications. It is also of particular interest to study thermoplastics as opposed to thermoset polymers because of processing advantages and

environmental recycling considerations. Some typical thermoplastics include polycarbonate (PC), poly(butylene terephthalate) (PBT), poly(etheretherketone) (PEEK) and poly(arylate) (PAr). The current work will mainly focus on two of the most promising higher performance semicrystalline thermoplastics, NEW-TPI and poly(p-phenylene sulphide) (PPS). A brief description of these two polymers is introduced here. More detailed discussions pertaining to our specific research can be found in the introduction section of the following chapters.

1.3.1 NEW-TPI

NEW-TPI, a product from Mitsui Toatsu Chemical Company, is the first commercially available crystallizable thermoplastic in the polyimide family. It has excellent high temperature stability, outstanding mechanical toughness, low dielectric constant and loss, and good solvent resistance [89-106]. Its monomer repeat unit contains rigid phenyl and imide linkages in the dianhydride and the more flexible ether-phenyl linkages in the diamine. Its chemical structure is shown below:

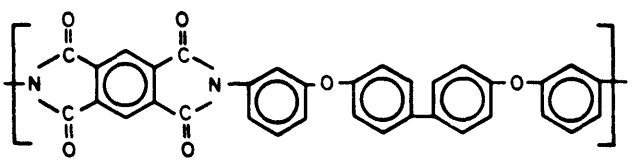

NEW-TPI is a crystallizable material and has a T_g around 250°C, and a melting temperature of 385°C from DSC. The induced crystallinity increases its solvent resistance and reduces its moisture uptake. It is fully imidized in the solid state, therefore, it can be melt processed by the standard thermoforming

methods. Details about this material can be found in an excellent review article [107].

1.3.2 Poly(phenylene sulfide)

PPS is one of the most important engineering thermoplastics having a wide range of applications as composite matrices and molding resins. It has excellent thermal and mechanical properties [37,38,108-120]. After doping, PPS also becomes a conductive polymer and has some electrical applications. It's monomer repeat unit is:

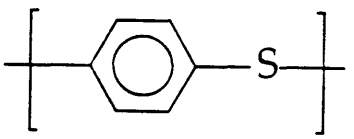

Extensive research has been carried out on this polymer. Several excellent review articles have covered all the research topics about this material from synthesis and processing to characterization and modeling [121-124].

One of the most interesting properties observed in PPS is that it can have a large amount of RAP when crystallized either from the melt or from the glassy state [37,38]. Research in our group has found that all the amorphous phase is rigid amorphous phase in the film processed PPS [119]. Therefore, it opens a wide thermal processing window for us to investigate the origin of this RAP.

1.4 OVERVIEW AND OBJECTIVE OF CURRENT RESEARCH

The ultimate goal of this research is to understand the structure, property and processing relationship of high performance thermoplastics in

order to expand their ultimate use. In the mean time, we want to explore the nature of crystal/amorphous interphase and/or rigid amorphous phase. We will be looking into these issues through the study of both structure and relaxation, and will try to connect them if possible to obtain a better understanding of these materials.

In Chapter 2, SAXS and TSDC are employed to investigate the structure and relaxation behavior of semicrystalline thermoplastic NEW-TPI [97]. Both room temperature and real-time SAXS show that long period, lamellar thickness and amorphous layer thickness change as functions of crystallization temperature and crystallization time. From our TSDC study, we observe strong relaxations for amorphous and semicrystalline NEW-TPI. The amorphous phase in the semicrystalline sample is slightly restricted by the crystals. Complex TSDC behavior is observed in both samples.

The high temperature thermal stability and thermal expansion behavior of NEW-TPI are studied in Chapter 3, along with three other high performance thermoplastics containing carbonyl and/or ether linking groups: PEEK, LARC-CPI and LARC-IA [106]. Chemical structures for these polymers are shown later on in Figure 3.1. TGA studies show NEW-TPI has excellent thermal stability compared to the other three polymers. Both TMA and SAXS are used to determine linear coefficients of thermal expansion (CTE) of NEW-TPI. By applying appropriate thermal expansion models to the data, the amorphous phase CTE can be obtained for the first time from both experiments.

Chapter 4 discusses the unique relaxation behavior of film processed PPS Ryton^{TM}. When PPS is annealed at a temperature higher than T_g, the film shows a higher relaxation temperature from the loss factor in DMA data. DSC thermograms indicate that a large amount of RAP exists inside the as-received film. Detailed analysis suggests the relaxation of RAP and the formation of small crystals when the sample was annealed at a temperature higher than T_g. These conclusions are further confirmed by TSDC experiments. A relationship between the interfacial relaxation peak, ρ-peak, and interphase roughness is also suggested.

In Chapter 5, the effects of molecular weight (M_w) on crystallization, structure and properties of Fortron^{TM} PPS cold crystallized under large degree of undercooling (at temperatures close to T_g) are investigated. Structure development during isothermal cold crystallization is studied using SAXS for the different M_w samples crystallized at the same crystallization rate. Systematic variation in long period, lamellar thickness and linear crystallinity are observed with both crystallization temperature and M_w. Large amounts of RAP are found in these materials. DMA shows that lower M_w PPS has a higher modulus when the sample is heated to a higher temperature. Using modulated DSC, this effect is considered to be due to the better reorganization ability of the lower M_w PPS.

Explicit exploration necessary to the understanding of RAP is carried out using the modulated DSC in Chapter 6. Two sections are devoted to two different systems. The first section explores the effect of thermal history on cold crystallized PPS Ryton^{TM}. It is observed that the amorphous phase in the semicrystalline material can be annealed at a temperature higher than T_g.

The data also suggest the correlation between annealing and RAP. The second section studies both single stage and multiple stage melt crystallized PEEK. A transition temperature is found for two different melting mechanisms. It also suggests the existence of crystal lamellae with different sizes.

The thesis concludes with a chapter summarizing the main results and providing suggestions for future research.

Finally, I include some detailed information about our home-built TSDC apparatus in the Appendix. It covers TSDC background, theory, apparatus set-up, and operation procedures.

Chapter 2

NEW-TPI Thermoplastic Polyimide: Structure and Relaxation Using SAXS and TSDC

2.1 INTRODUCTION

Aromatic polyimides have unique structure and broad engineering applications. The imide and aromatic moieties in the monomer unit impart rigidity to the polymer chain resulting in high thermal transition temperatures. Polyimides exhibit outstanding thermal stability and excellent mechanical properties, especially toughness. These materials also generally have low dielectric constant and dielectric loss, resulting in applications in electronic packaging and cable and wire insulation.

NEW-TPI, one of the important new members of the aromatic polyimide family, has been the recent subject of many research groups [89-106]. This novel polymer, a product of Mitsui Toatsu Chemical Company, is also a semicrystalline melt-processible material. Its monomer unit contains flexible ether and meta-phenyl linkages which lower its glass transition temperature (T_g) to 250°C [89]. The crystalline material has a melting temperature (T_m) of 385°C (DSC) [89,91] which enables NEW-TPI to be processed by standard thermoforming methods. Crystallinity is also likely to result in property enhancement, such as improving solvent resistance. According to our previous studies, NEW-TPI has a dielectric constant at 1kHz of 3.2 and modulus of elasticity at room temperature of 3-4 GPa [93,95].

Characterization of the structure and properties of NEW-TPI have been reported by our group and others. Using X-ray diffraction, NEW-TPI crystal structure has been studied by Okuyama, et al.[90]. Its thermal and rheological properties have been studied by Hou and Reddy [91]. Brillhart, et al.[96] determined the crystal lattice thermal expansion coefficient while Lu, et al. [106] reported lamellar stack and bulk thermal expansion properties. Morphology of spherulites has been studied by Takahashi, et al. [100] using transmission electron microscopy and by Hsiao, et al.[98] using optical microscopy. Friler and Cebe [94] described the non-isothermal crystallization kinetics, while Huo, et al. [92,93] first studied the isothermal cold crystallization kinetics. We showed [93] that NEW-TPI crystallizes relatively slowly from the rubbery amorphous state. At a given crystallization temperature, the kinetics can be described by a single Avrami parameter over the entire crystallization process. As a function of crystallization temperature, a regime transition, from Regime II to Regime III, was observed in the growth kinetics at a temperature near 327°C, which was the temperature at which the fastest cold crystallization occurred [93].

These results were later confirmed by Hsiao, et al. [98] who reported on the isothermal melt crystallization kinetics. These workers also determined spherulite growth rates, and spherulite birefringence, and suggested that radial growth occurs along the crystallographic b-axis. In the melt crystallization study of Hsiao, et al. [98] discontinuities were observed in some of the parameters determined from small angle X-ray scattering (SAXS) as a function of the melt crystallization temperature, T_c. The long period, L, and lamellar thickness, l_c, both exhibited a jump, showing lower (and approximately constant) values for $T_c \leq 330°C$, and higher values for $T_c \geq$

340°C. The temperature at which the break occurs is very close to the crystallization temperature at which fastest crystal growth occurs both for melt [98] and for cold crystallization [93].

In this report, we continue our investigation of NEW-TPI using real time small angle X-ray scattering (SAXS) to study structure, and thermally stimulated depolarization current (TSDC) to study relaxation behavior. SAXS is used to study structure of NEW-TPI crystallized either isothermally or non-isothermally from the rubbery amorphous state. Long period, lamellar thickness and crystallinity are obtained using the one-dimensional electron density correlation function for NEW-TPI samples cold crystallized at different temperatures. Relaxation behavior of NEW-TPI from -80°C to 270°C has been studied using TSDC. No sub-T_g relaxation is found within this temperature range which may explain the relatively brittle mechanical behavior of the semicrystalline NEW-TPI.

2.2 EXPERIMENTAL SECTION

2.2.1 Characterization Techniques

A differential scanning calorimeter, DSC, Perkin Elmer DSC-4, has been used to study crystallization and melting behavior of Regulus^{TM} NEW-TPI. Indium was used to calibrate temperature and heat flow throughout our DSC study. Sample weight was around 8mg and a scan rate of 10°C/min was used. Crystallinity was calculated from endotherm area using the manufacturer's published value of 139J/g as the heat of fusion of perfect crystalline NEW-TPI [99].

WAXS experiments were carried out at room temperature in reflection mode using a Rigaku RU-300 X-ray diffractometer with a diffracted beam graphite monochromator. The normal operating condition was 50keV and 200mA with Cu-K_α radiation (λ = 1.54Å). The scattering angle 2θ ranged from 5° to 55° with a step scan interval of 0.02 degree and a scan rate of 1°/min. Silicon powder (from National Institute of Standards and Technology) was rubbed on the sample surface to serve as a calibration standard for peak position.

SAXS experiments were done at Brookhaven National Synchrotron Light Source using a high intensity X-radiation source in transmission mode. The wavelength was 1.54Å and sample-to-detector distance was about 1.80m calibrated using cholesteral meristate. The beam profile at the detector is 300μm x 300μm, and therefore can be treated according to a pinhole geometry. The isotropic SAXS intensity was circularly integrated and normalized for changes in incident beam intensity and sample absorption. The background and thermal density fluctuations were subtracted from the normalized Lorentz-corrected scattered intensity. The one-dimensional electron density correlation function was then calculated to obtain long period, lamellar thickness and linear crystallinity of NEW-TPI, according to the method of Strobl and Schneider [45] for flat, parallel lamellae.

TSDC measurements were carried out on our self-designed and self-assembled apparatus. The major part is the sample cell which contains two layers. The first layer is for liquid nitrogen cooling. The second layer is for heating and Faraday shielding. The triaxially shielded electrical conduction path is concentric with the two layers of the cell. A polymer film sample is

placed between a spring loaded pair of disc-shaped electrodes. Helium gas is used as a heat transfer agent inside the cell, but the experiments were conducted at a base pressure of approximate 1 torr. To obtain a global TSDC spectrum, Regulus^{TM} was first heated to a temperature T_p where the poling field is applied (E_p=1x10^6 V/m). After holding at T_p for 10 min, the cell was quickly quenched with liquid nitrogen at a cooling rate of about -15°C/min to a temperature T_o where the poling field was reduced to zero and the two high voltage electrodes were short-circuited to ground voltage. The current vs. temperature was recorded continuously during heating at a rate of 2°C/min. Unless otherwise mentioned, gold was evaporated on the samples to avoid the spurious charges that might come from the poor contact between the sample and the electrodes. Details about TSDC techniques have been discussed in some excellent reviews [45,48,53,56,82].

2.2.2 Sample Preparation

Regulus^{TM} NEW-TPI film, 100μm thick, was supplied by Mr. Yasunori Sugita of Mitsui Toatsu Chemical Co. Figure 2.1 shows DSC scans of NEW-TPI as-received (AR), curve 1, and crystalline, curve 2. No crystallinity was detected in the AR sample, either from thermal analysis, optical birefringence, or wide angle X-ray scattering (WAXS). The film was dried in a vacuum oven at 100°C for 20 hrs prior to any further treatment and it will be referred to as amorphous sample. Some of the amorphous samples were cold crystallized from 300°C to 360°C until the completion of crystallization, as determined from our prior experiment [93]. For our TSDC experiment, two kinds of samples were prepared. One set was annealed at 260°C for 1hr. After annealing, the samples were either cooled to room temperature by air-quenching, or cooled slowly to room temperature at 2°C/min. Another set of

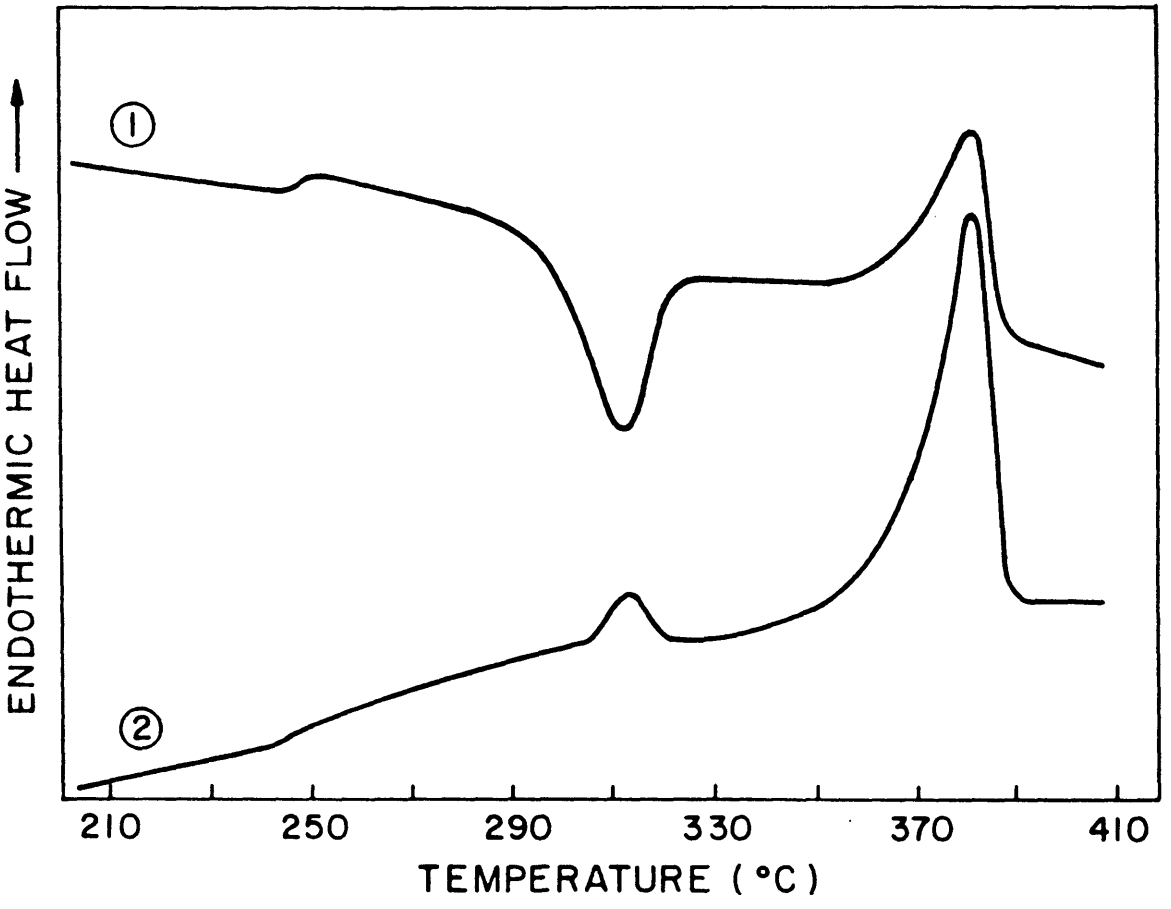

Figure 2.1 DSC scans at 10°C/min. for Regulus™ NEW-TPI amorphous film (curve 1) and semicrystalline film cold crystallized at 300°C for 1hr (curve 2).

samples was cold crystallized at 300°C for 1hr and quenched quickly to room temperature.

2.3 RESULTS AND DISCUSSION

2.3.1 Room Temperature SAXS of Isothermally Cold-Crystallized Samples

We show in Figure 2.2 the room temperature, Lorentz corrected SAXS intensity, Is^2, vs. scattering vector, s ($s=2\sin\theta/\lambda$) for NEW-TPI samples cold crystallized from 300°C to 360°C. Systematic variation of peak position with cold crystallization temperature T_c is observed. As T_c increases, the peak maximum shifts to smaller s. We assume that the structure consists of stacks of lamellae alternating with amorphous material. This assumption is justified since spherulites have been observed from Takahashi's TEM study of NEW-TPI [100]. Spherulitic structure and lamellar detail have also been observed in other polyimides which were either crystallized from the melt and etched [125,126] or grown from solution [127-129].

A discrete Fourier transform [130] has been applied to the Lorentz corrected intensity to obtain K(z), the one-dimensional electron density correlation function, as shown in the following equation:

$$K(z) = \sum_{j=1}^{N} 4\pi I_{corr} s^2 \omega_N^{(j-1)(z-1)} \tag{2.1}$$

where

$$\omega_N = e^{-2\pi i/N} \tag{2.2}$$

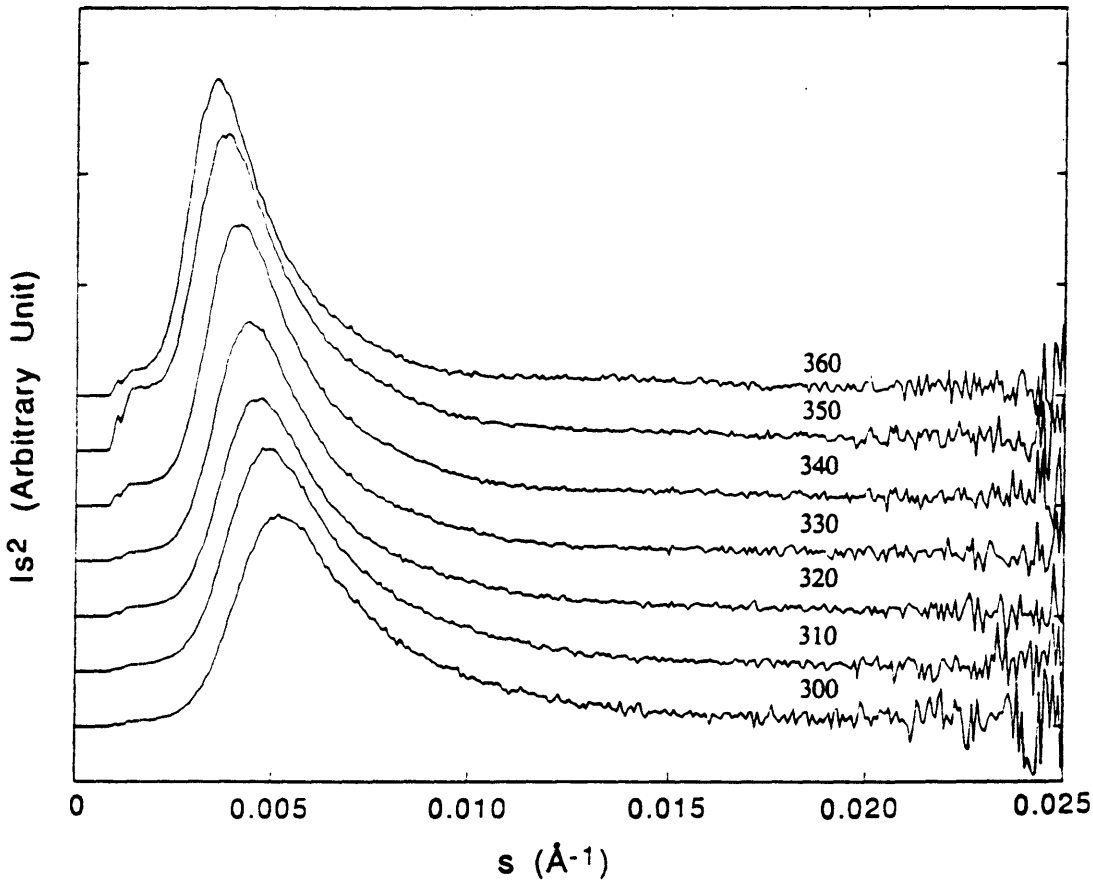

Figure 2.2 Lorentz-corrected SAXS intensity vs. scattering vector, s, for NEW-TPI cold crystallized at the indicated temperatures (in °C).

In Eqn. (2.1), z is the direction normal to lamellar stacks, N is the number of actual data points and I_{corr} is the intensity corrected for background and thermal density fluctuations. Linear extrapolation of intensity from the beam stop region to s=0 was used in the summation. The resulting correlation function starts off with a z spacing of $1/s_{max}$, but a spline interpolation routine fills in the missing values in the region of interest. The treatment of Strobl and Schneider [45] was used for data analysis, but any effects of curvature of the lamellae have been ignored.

From K(z) we obtain long period (squares) and lamellar thickness (triangles), and the results are plotted in Figure 2.3. Both long period and lamellar crystal thickness show an increase with cold crystallization temperature. The long period increases from 182Å for T_c=300°C to 264Å for T_c=360°C, while lamellar thickness increases from 52Å to 76Å over the same temperature range. (The low value of l_c at T_c=350°C is attributed to measurement error. This error at T_c=350°C appears in all quantities determined from K(z)). Using a two-phase assumption,

$$L = l_c + l_a \tag{2.3}$$

where l_a is the amorphous layer thickness, also shown in Figure 2.3 (circles). Relatively more amorphous phase is included in between the lamellar stacks as cold crystallization temperature increases. We see a change in the slope of L vs. T_c at 330°C. Below T_c = 330°C, L increases linearly with T_c. At 330°C, there is a slope change, and above T_c=330°C, L once again increases linearly with T_c. We see no corresponding change in the lamellar thickness. Lamellar thickness generally changes linearly with T_c, increasing as the

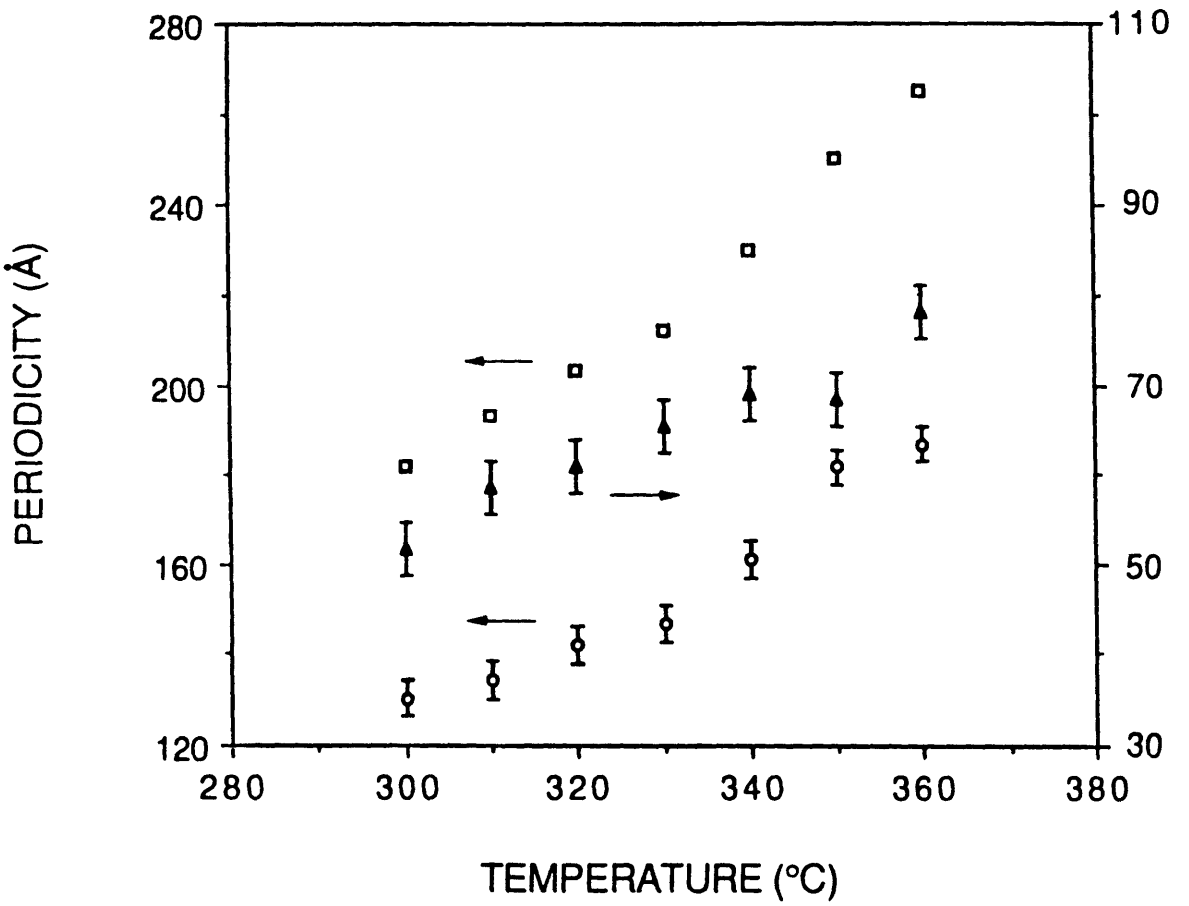

Figure 2.3 SAXS parameters as a function of cold crystallization temperature for NEW-TPI: (□) long period, and (O) amorphous layer thickness, both using left hand vertical axis; and (▲) lamellar thickness, using right hand vertical axis.

degree of undercooling (defined as T_m^0-T_c) decreases. This, together with the slope change in L vs. T_c, results in an increase in the amount of the amorphous phase that is contained between the lamellae ("interlamellar") at the higher crystallization temperatures (i.e., at lower degrees of undercooling). The increases in L and l_c with crystallization temperature have also been observed in other polymers and blends [131-136].

We have previously studied cold crystallization kinetics of NEW-TPI using isothermal DSC [93]. A slow crystallization rate is observed and the maximum crystallization rate occurs at around 327°C. We showed that the temperature at which fastest cold crystallization occurred served to divide the crystal growth into Regime II ($T_c \geq 327°C$) and Regime III ($T_c \leq 327°C$) [137]. The temperature of the minimum was estimated from a single polynomial fit to the growth curve. Hsiao, et al.[98] subsequently found the same Regime transition in melt crystallization studies, but the temperature at which the Regime transition occurred was 340°C. Also, these workers reported a discontinuous change in both L and l_c for temperatures below or above the transition. The average long period changed from 170Å ($T_c < 335°C$) to 194Å ($T_c > 335°C$), while the average lamellar thickness changed from 120Å to 135Å.

In Figure 2.4, we present the crystallinity of NEW-TPI samples vs. cold crystallization temperature. The linear crystallinity (circles) was obtained directly from the one-dimensional electron density correlation function evaluated at room temperature. These values range from 0.33 to 0.30 (The extreme low value at T_c=350°C is believed due to error in measurement). The volume crystallinity (squares) calculated from DSC data [53] ranges from 0.21

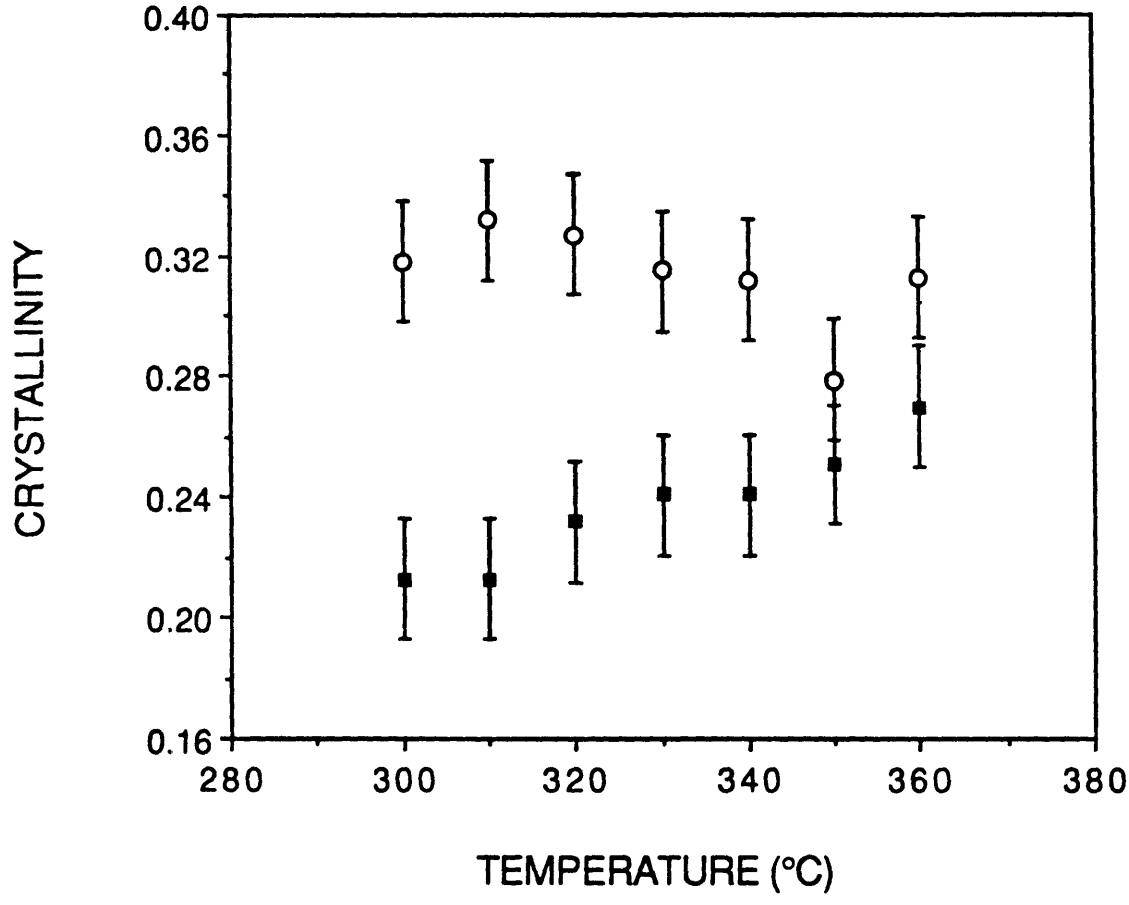

Figure 2.4 (O) Linear crystallinity from K(z), and (■) volume crystallinity from DSC, vs. cold crystallization temperature for NEW-TPI.

to 0.28. Volume fraction crystallinity, χ_c^v, was obtained from weight average crystallinity, χ_c^w, using the following equation:

$$\chi_c^v = \frac{\chi_c^w(\rho_a/\rho_c)}{1-\chi_c^w+\chi_c^w(\rho_a/\rho_c)} \qquad (2.4)$$

where ρ_a and ρ_c are the amorphous phase and crystal phase densities, respectively. A linear relationship between density and volume fraction crystallinity has been assumed. We have used ρ_a = 1.33g/cm^3 [99] and ρ_c = 1.47g/cm^3 calculated from the unit cell structure [90]. In Figure 2.4, a slight decrease is observed for linear crystallinity obtained from the correlation function. However, within experimental error, the change can be considered minimal. At the same time, the volume fraction crystallinity calculated from DSC increases gradually. The difference between the two gets smaller as the cold-crystallization temperature increases.

The one-dimensional electron density correlation function calculation is based on a model of very strict one dimensional alternating lamellar stacks. The model assumes densely packed, isotropically distributed stacks of parallel lamellae. All stacks should obey the same internal statistics, and the system is a strict periodic two-phase system with low crystallinity. However, for cold crystallized NEW-TPI, the arrangement of lamellar stacks may not follow the model's assumptions. For example, as we have discussed above, when the cold-crystallization temperature increases, more amorphous phase is included inside the lamellar stacks. However, any amorphous phase left outside the lamellar stacks during crystallization is undetectable. Therefore,

current calculation of linear crystallinity from K(z) gives an over-estimation of crystalline phase fraction compared to the crystallinity determined from DSC. The deviation becomes smaller as the cold crystallization temperature increases as seen in Figure 2.4, since more and more amorphous phase is included between the crystal lamellae.

Hsiao, et al. [98] have also determined the degree of crystallinity of NEW-TPI using both DSC and wide angle X-ray scattering. They assume a linear relationship between mass fraction crystallinity (heat of fusion measurement) and density to determine a crystal heat of fusion of 116J/g. However, when mass fraction is used, the linear relationship is with the *specific volume* (inverse of density). This may be the reason that their heat of fusion value is considerably smaller that the value of 139J/g suggested by Mitsui Toatsu [99]. These researchers also found that the WAXS crystallinities ranged from 0.34 to 0.46, and linear crystallinities from K(z) ranged from 0.71 to 0.67. The WAXS crystallinities were around 0.34-0.36 for T_c<350°C, then jumped to 0.46 (350°C) and 0.42(360°C). No trend with T_c was observed in linear crystallinity from K(z) .

The lamellar thickness derived from K(z) is used to determine the thermodynamic melting temperature (T_m^0) and the polymer fold surface free energy (σ_e) using following equation [137]:

$$T_m = T_m^0 \left(1 - \frac{2\sigma_e}{\Delta H_f l_c}\right) \tag{2.5}$$

where T_m is the DSC melting temperature and ΔH_f is the heat of fusion for 100% crystalline material. The results are shown in Figure 2.5. T_m^0 is found to be 424±20 °C, which is higher than previous published data of 400°C [93] and 405°C [98]. The error bar on T_m^0 reflects the scatter in the data set. This scatter results in a correlation coefficient, $r^2 = 0.87$. Using T_m^0 of 424°C, ΔH_f of 139 J/g [99] and crystal density of 1.47 g/cm^3 [99], we obtain fold surface free energy, σ_e = 41±3erg/cm^2. From spherulite growth rate studies, Hsiao, et al. [98] obtained the product, $\sigma\sigma_e$, which was 1176 erg^2/cm^4. This results in a side surface free energy, σ, of 29±3erg/cm^2. The close values of the side and fold surface free energies of NEW-TPI bear great similarity to another phenyl ring containing polymer, PEEK, whose side and fold surface free energies were found to be 38 and 49 erg/cm^2, respectively [138].

We expect in rigid chain polymers that the fold surface will be very irregular, consisting of very loose folds. This would tend to reduce the work of chain folding, and cause the fold surface and side surface free energies to be similar. Error bars on these surface free energies were determined by considering possible errors that may be introduced in our calculation of T_m^0 and σ_e. First, the lamellar thickness we have obtained is the room temperature measurement. At the cold crystallization temperature, thermal expansion would give a slightly higher l_c. Second, it has been found that crystal lamellae can thicken quite significantly at high temperature [132]. Compared to thermal expansion, this effect could be more pronounced. Nevertheless, using this l_c obtained from SAXS from Eqn. (2.5) does allow us to calculate the side and fold surface free energies of NEW-TPI for the first time. Third, although T_m^0 is a constant for this material, σ_e may change slightly as a function of cold crystallization temperature.

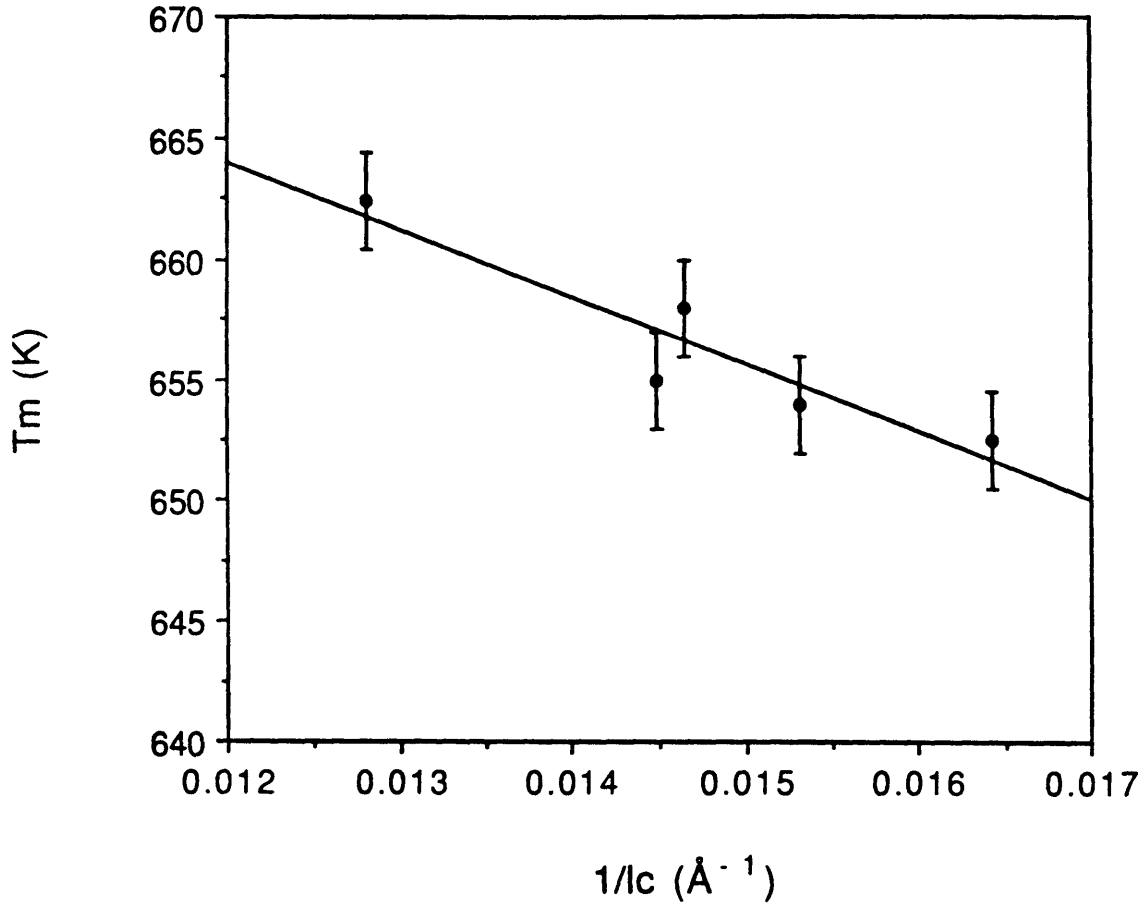

Figure 2.5 Melting temperature vs. 1/(lamellar thickness) for cold crystallized NEW-TPI.

In a prior study of NEW-TPI [93], interphase thickness, d, was determined as a function of crystallization time at 300°C. Here, using the same formalism of Koberstein, et al. [43] we calculate interphase thickness as a function of cold crystallization temperature, T_c, from:

$$I_{corr}(s) = C\exp(-\pi^2 d^2 s^2)/s^4 \tag{2.6}$$

where C is a constant. Eqn. (2.6) holds only at large scattering vector. After transforming, we find:

$$\ln(I_{corr}(s)s^4) = \pi^2 d^2 s^2 + C \tag{2.7}$$

Interphase thickness is obtained at room temperature from the slope of $\ln(Is^4)$ vs. s^2 and is shown in Figure 2.6 as a function of cold crystallization temperature. A slight increase can be observed, although within experimental error, the change is small. The average interphase thickness is around 23Å, as compared to the monomer repeat unit, previously determined to be ~25Å [90,96]. The interphase is the region over which the electron density decreases from that of the crystal to that of the isotropic amorphous phase. Whether or not this region corresponds to a fold surface is unknown in this polymer. Interphase thicknesses determined here as a function of crystallization temperature agree well with previous d values determined as a function of crystallization time [93]. The interphase thickness is smaller than the average value of lamellar thickness: l_c ranges from two to three times the monomer repeat unit length.

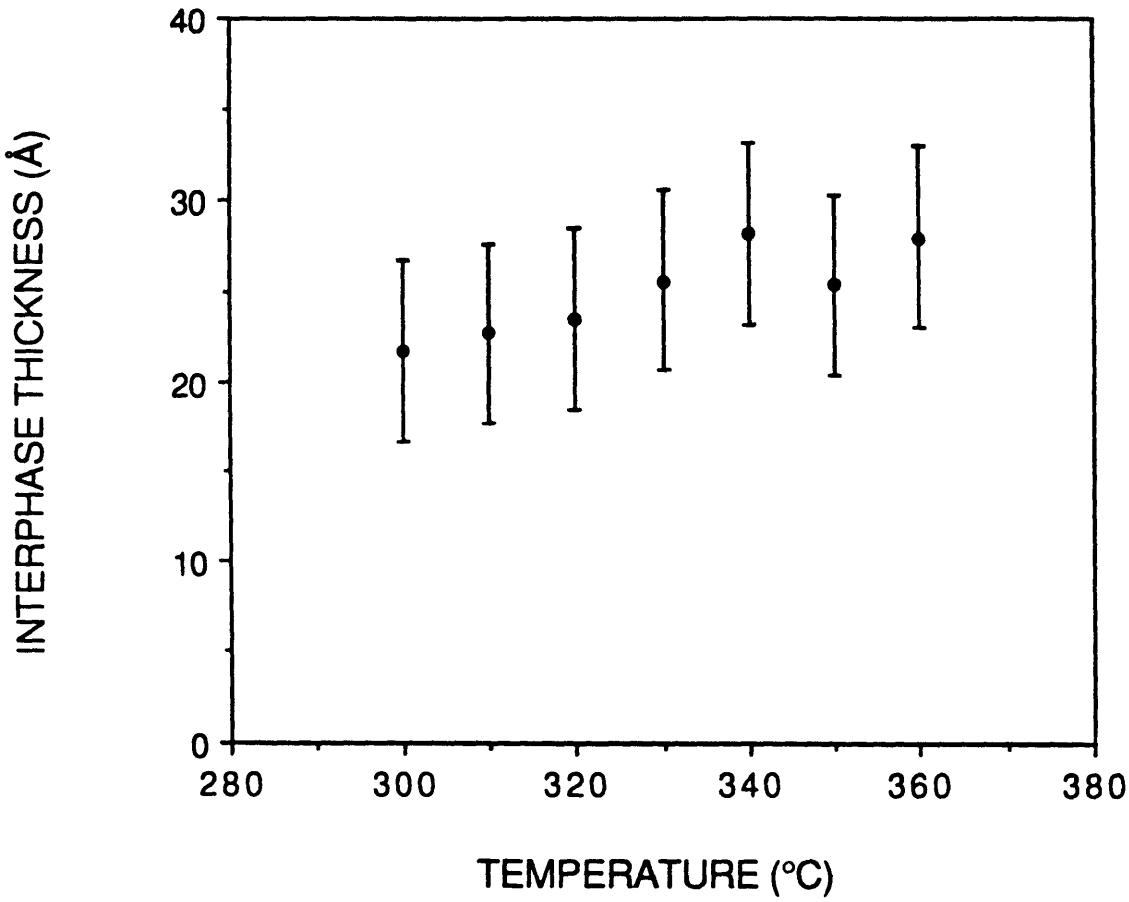

Figure 2.6 Interphase thickness of NEW-TPI as a function of cold crystallization temperature.

2.3.2 Real-Time SAXS Study of Nonisothermal Cold Crystallization

We have carried a real-time SAXS experiment during non-isothermal cold crystallization of NEW-TPI. The amorphous sample was heated from 250°C to 350°C at a rate of 5°C/min and the data collection period was 30 sec. The Lorentz corrected SAXS intensity vs. s is shown in Figure 2.7. Two temperatures are marked in Figure 2.7 representing scans taken one minute apart. No scattering peak develops until the temperature reaches 300°C. After that, a strong scattering peak starts to grow quite rapidly and shifts to a lower s indicating the beginning of the crystallization and crystal growth. As the temperature increases, the peak becomes sharper and the intensity gets stronger. No significant shift in peak position is observed over the temperature range from 330°C to 350°C.

The same data analysis method has been used as discussed in the previous section, and the results are shown in Figure 2.8. Figure 2.8a shows the long period as a function of measured temperature. Each data point represents an average over 2.5 degrees. A significant drop in long period starts around 305°C. L decreases from 245Å, and levels off at ~203Å when temperature reaches 322.5°C. This temperature is quite close to 327°C, the temperature at which NEW-TPI has its fastest crystallization rate [93]. The long period then increases only slightly until melting begins at a temperature of 350°C. In Figure 2.8b, we present the lamellar thickness as a function of temperature. A lamellar thickness of 42Å increases gradually to 60Å, as temperature increases from 305°C to 315°C, then levels off showing only a very slight decrease until the temperature reaches 350°C. In Figure 2.8c, we present the linear fraction crystallinity as a function of measurement

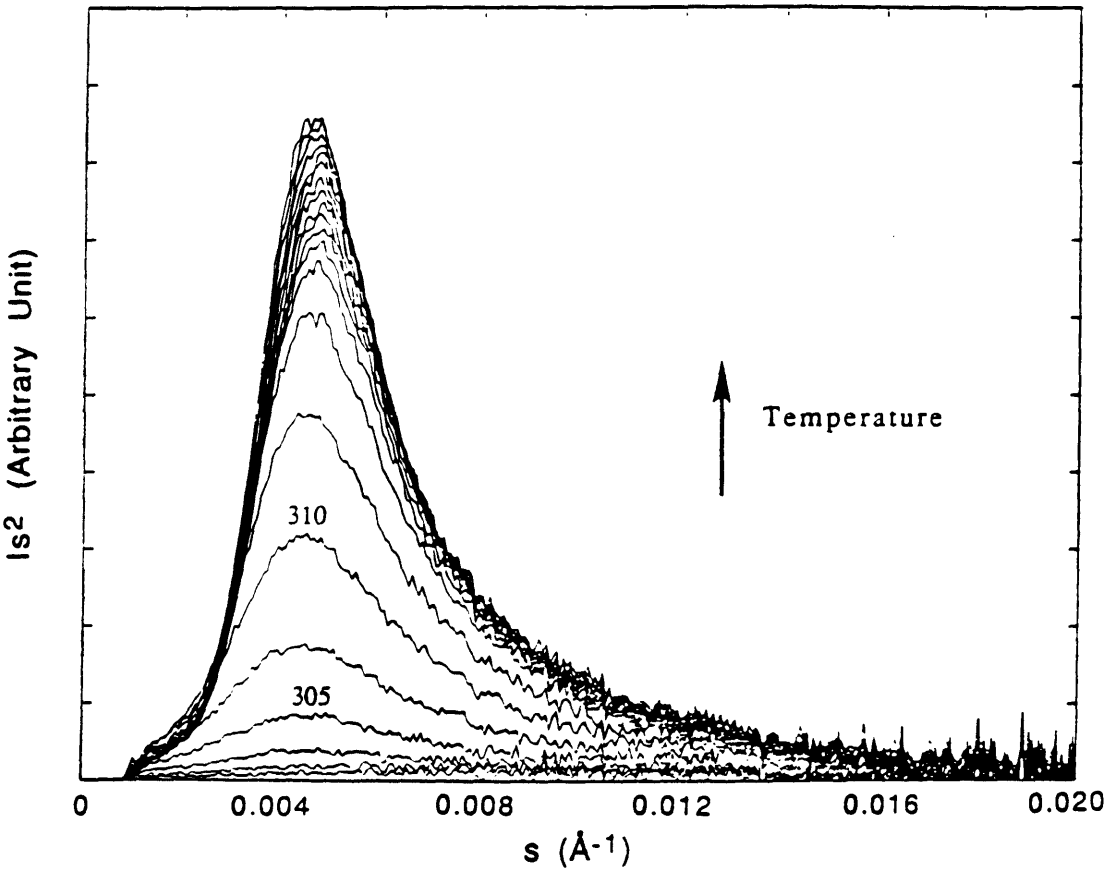

Figure 2.7 Lorentz-corrected SAXS intensity, Is^2, vs. scattering vector, s, during non-isothermal cold crystallization of NEW-TPI at 5°C/min heating rate. Temperature is marked for two traces taken one minute apart.

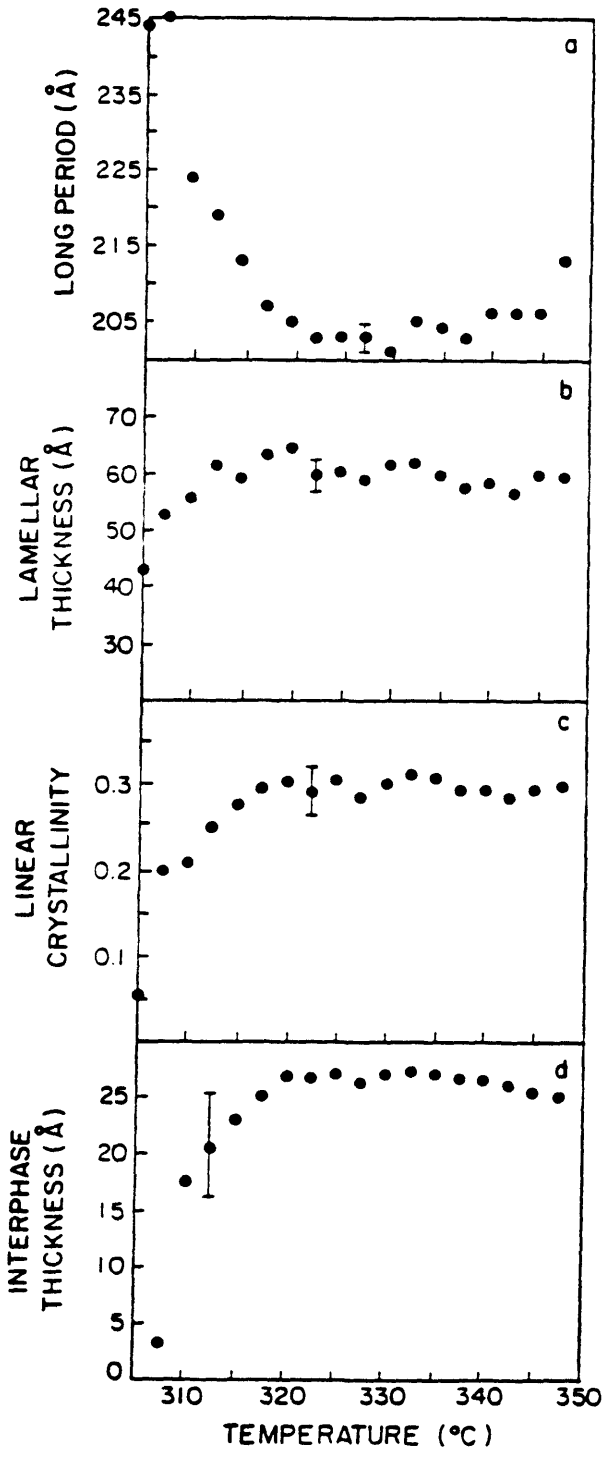

Figure 2.8 SAXS parameters as a function of temperature during non-isothermal crystallization of NEW-TPI at 5°C/min.
a) long period, b) lamellar thickness, c) linear crystallinity, d) interphase thickness.

temperature. Crystallinity increases from 0.05 to 0.30 as temperature increases to 320°C, and then remains constant until 350°C.

Similar changes in long period and lamellar thickness have been observed in our previous isothermal SAXS study [93], indicating the same crystallization mechanism is followed in both isothermal and non-isothermal crystallization. These observations could be explained by a lamellar insertion mechanism, which was first proposed by Keller [139], and later was used by Hsiao et al.[131,132] in their isothermal crystallization study of PEEK. In this model, it has been suggested that some thinner lamellae form between existing crystal lamellae as crystallization proceeds. This mechanism can explain why the average long period and the average lamellar thickness both decrease as crystallization time increases during isothermal crystallization.

This model may be used to explain our current data. At the beginning of the non-isothermal crystallization process, the crystals are very small and therefore, the distance between lamellae is large. As the temperature increases, more and more lamellae are formed causing a decrease in the average long period. At the same time, the already formed crystals are also growing in thickness and newly formed lamellae are crystallizing at higher temperature. Both effects will tend to increase the average lamellar thickness. When the temperature approaches the temperature of the fastest crystallization (327°C), a relatively stable lamellar structure consisting of firmly packed alternating lamellar and amorphous phase is formed. Now we observe that L, l_c and linear crystallinity all approach stable values. The crystal structure formed during non-isothermal crystallization is initially not

well-organized and can change to a more stable state with either crystallization time or temperature. In our case, as temperature increases, we observe a slight increase in L, caused by the removal of the thinner crystals.

We have calculated the interphase thickness as a function of temperature using Eqn. (2.6) and (2.7). The results are shown in Figure 2.8d. Interphase thickness increases with temperature during non-isothermal crystallization and reaches a steady value of about 25Å when temperature reaches 320°C. The temperature at which the interphase thickness becomes constant agrees well with previous changes seen in the lamellar thickness and crystallinity. This suggests that the interphase formation is related to crystal formation in such a way that they reach steady values at the same time, when the polymer structure is formed and relatively stabilized.

2.3.3 TSDC Study of NEW-TPI

SAXS is an excellent analytical method to study the development of crystal structure of NEW-TPI after sufficient long range order has been established to provide electron density contrast. However, the method is difficult to apply prior to the appearance of periodic structure. Therefore, we adopted another analytical method, TSDC, to study the amorphous phase relaxation behavior for both amorphous and semicrystalline NEW-TPI. Relaxation of dipoles is directly related to the microscopic environment (structure) in the amorphous phase. The temperatures chosen for TSDC studies are well below those at which crystalline dipoles are active [94]. TSDC results are shown in Figure 2.9 for amorphous NEW-TPI, and Figure 2.10 for semicrystalline NEW-TPI.

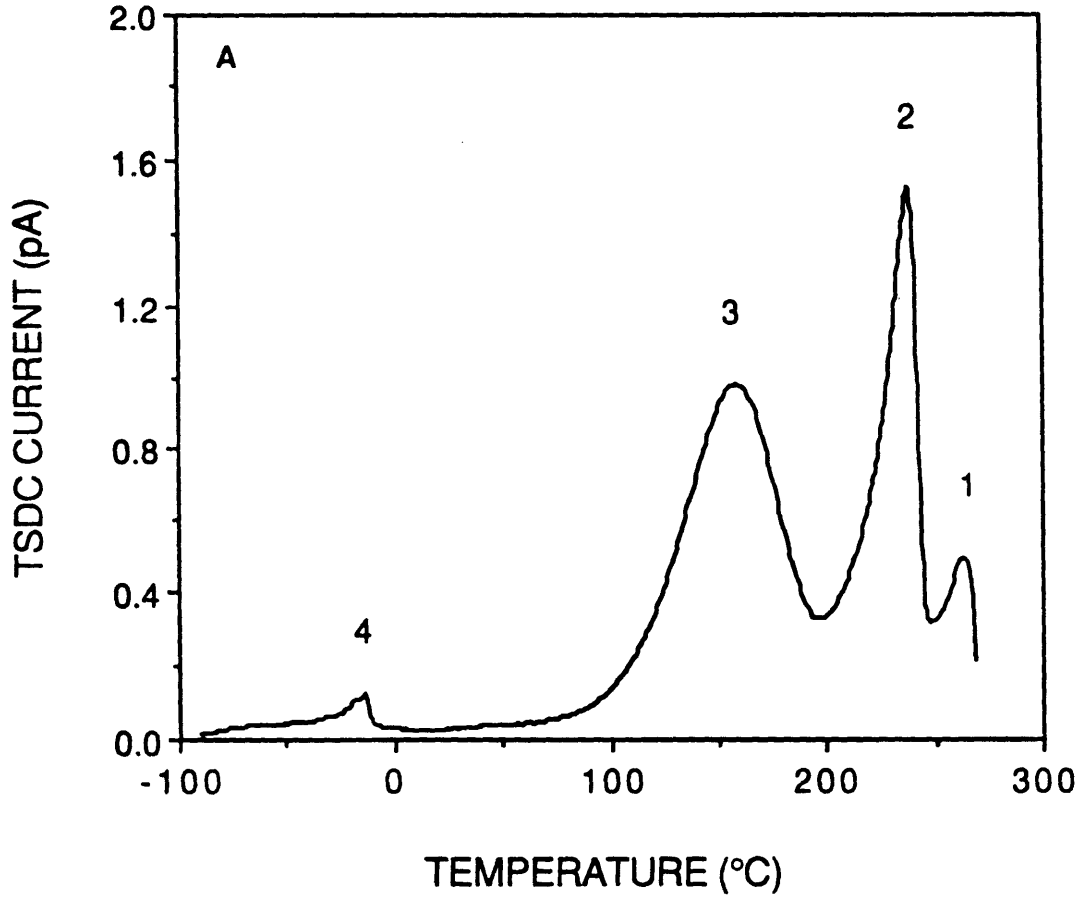

Figure 2.9 TSDC current vs. temperature for amorphous NEW-TPI poled at 250°C under different experimental conditions. a) Au-coated, fast quenched, b) Au-coated, slow cooled, c) Al-coated, fast quenched. Refer to text for description of numbered peaks.

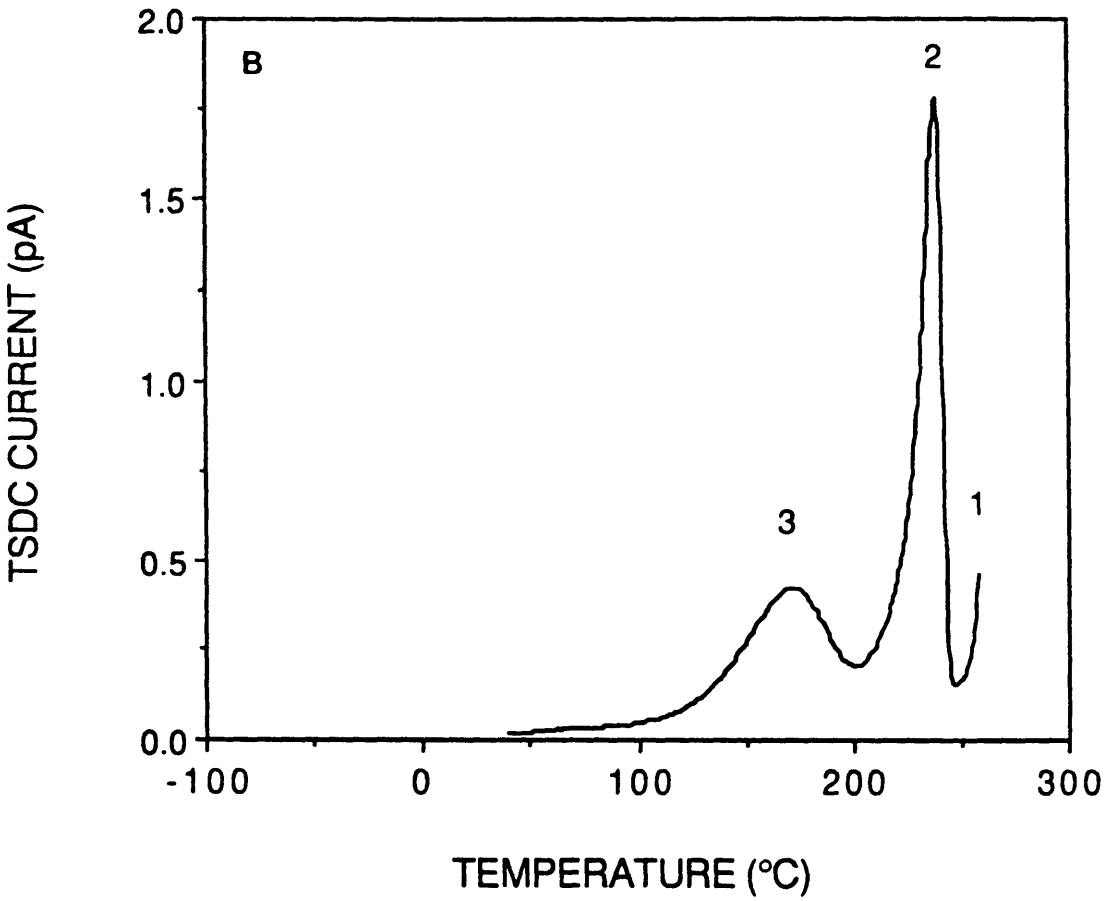

Figure 2.9, Continued

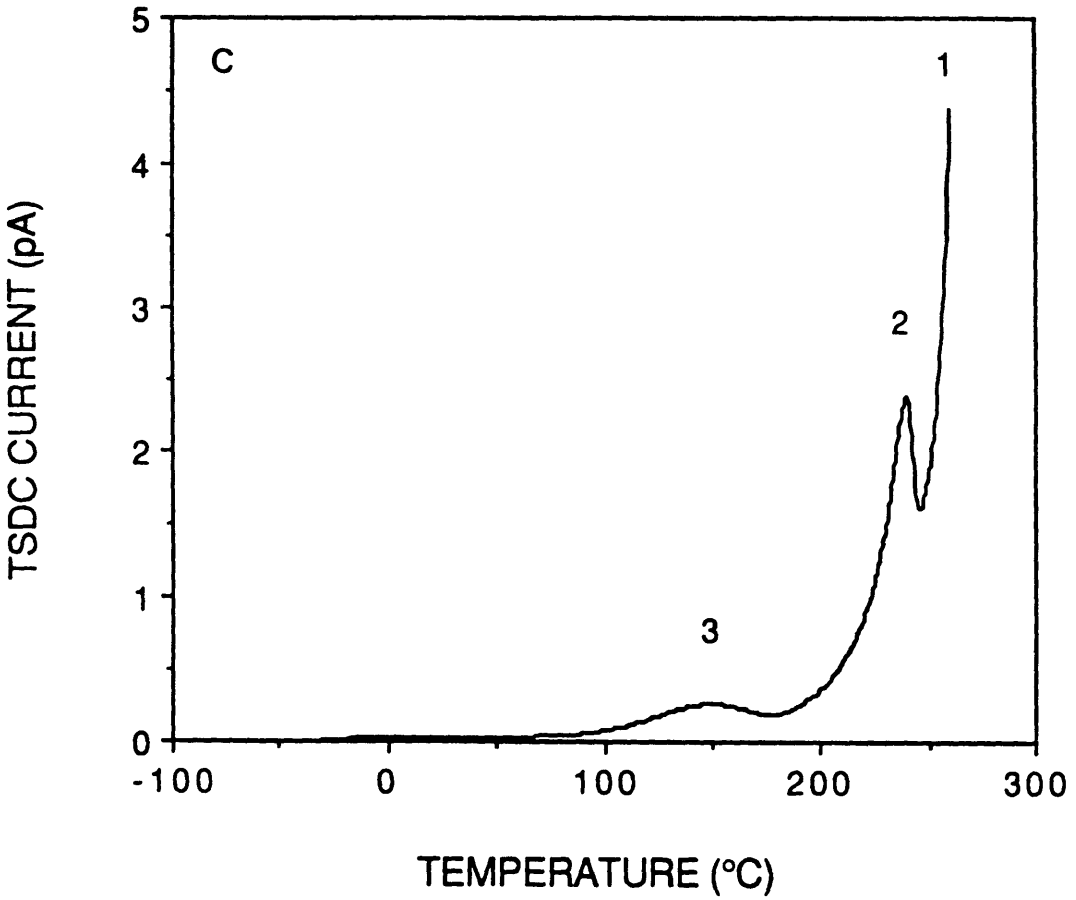

Figure 2.9, Continued

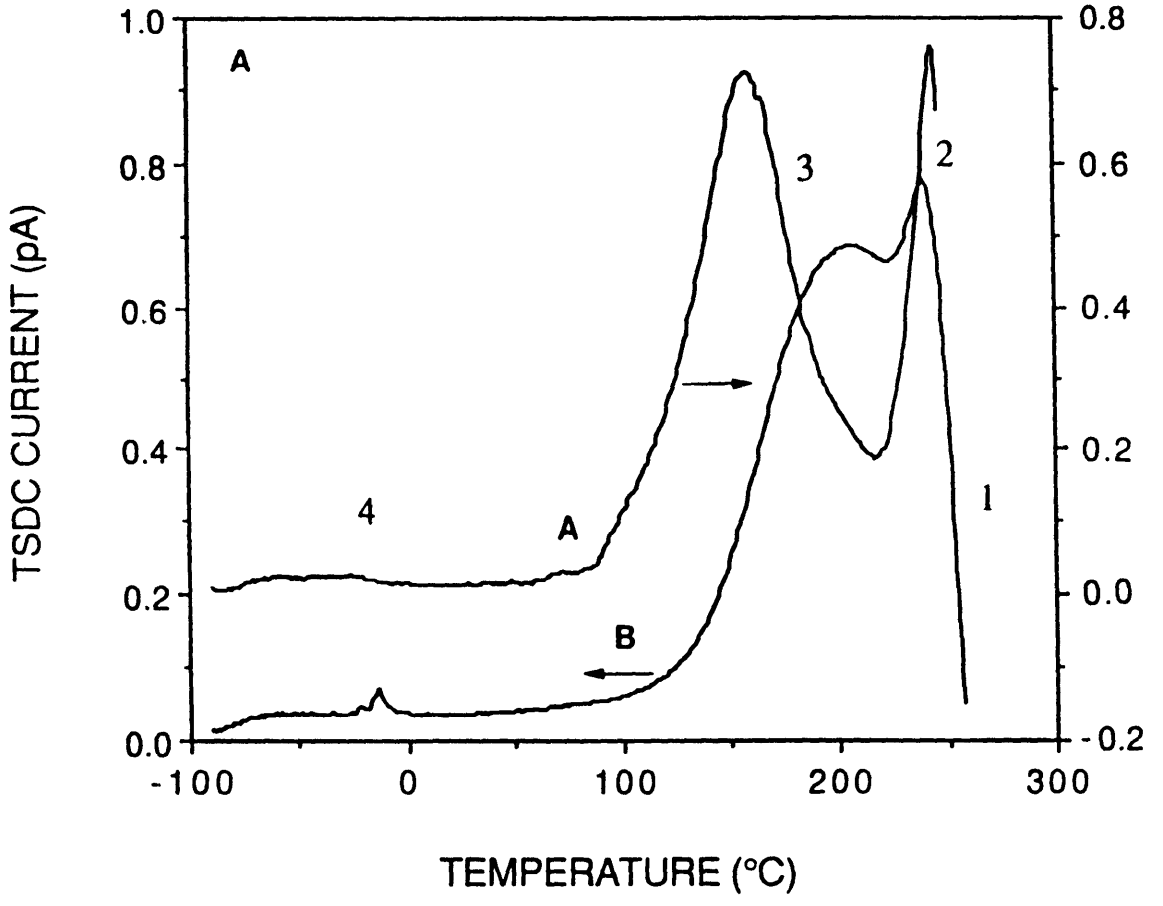

Figure 2.10 TSDC current vs. temperature for semicrystalline NEW-TPI poled at 250°C under different experimental conditions. a) Au-coated, fast quenched, b) Au-coated, slow cooled, c) Al-coated, fast quenched. Refer to text for description of numbered peaks.

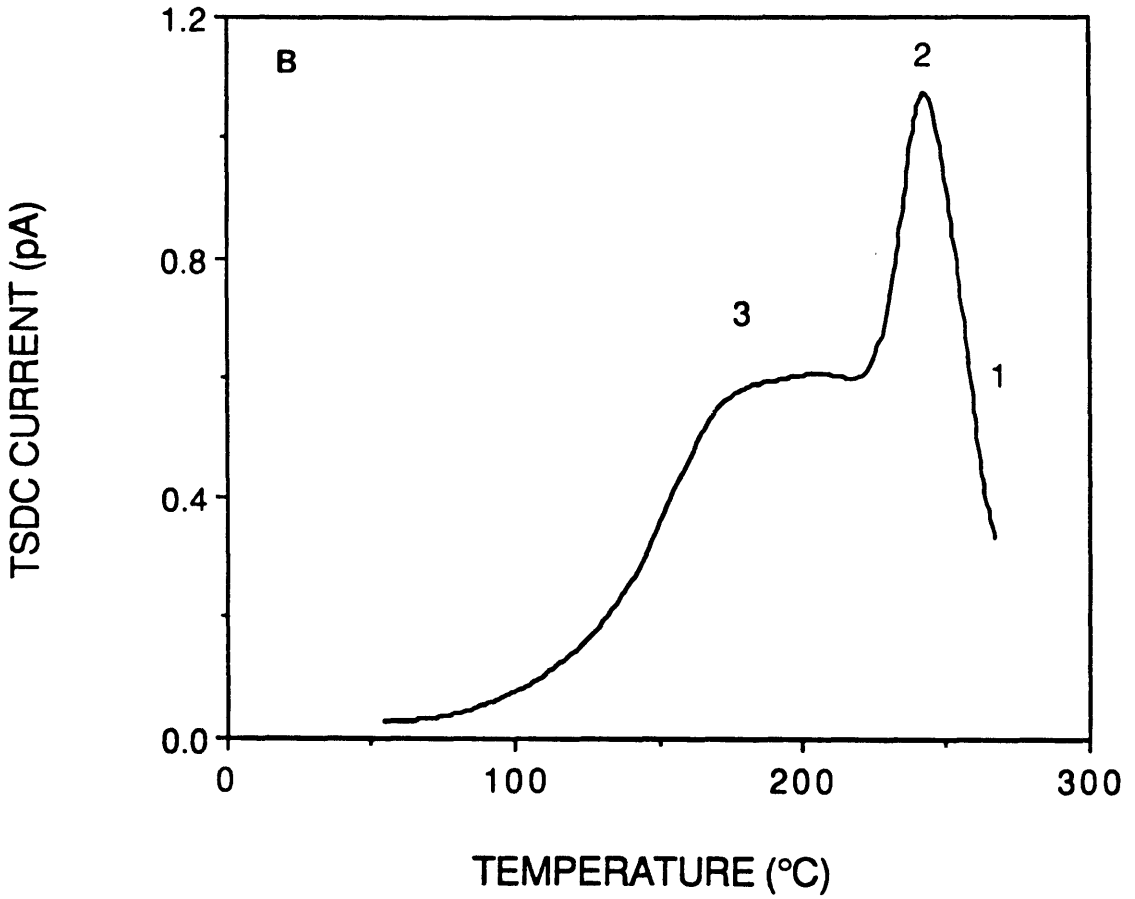

Figure 2.10, Continued

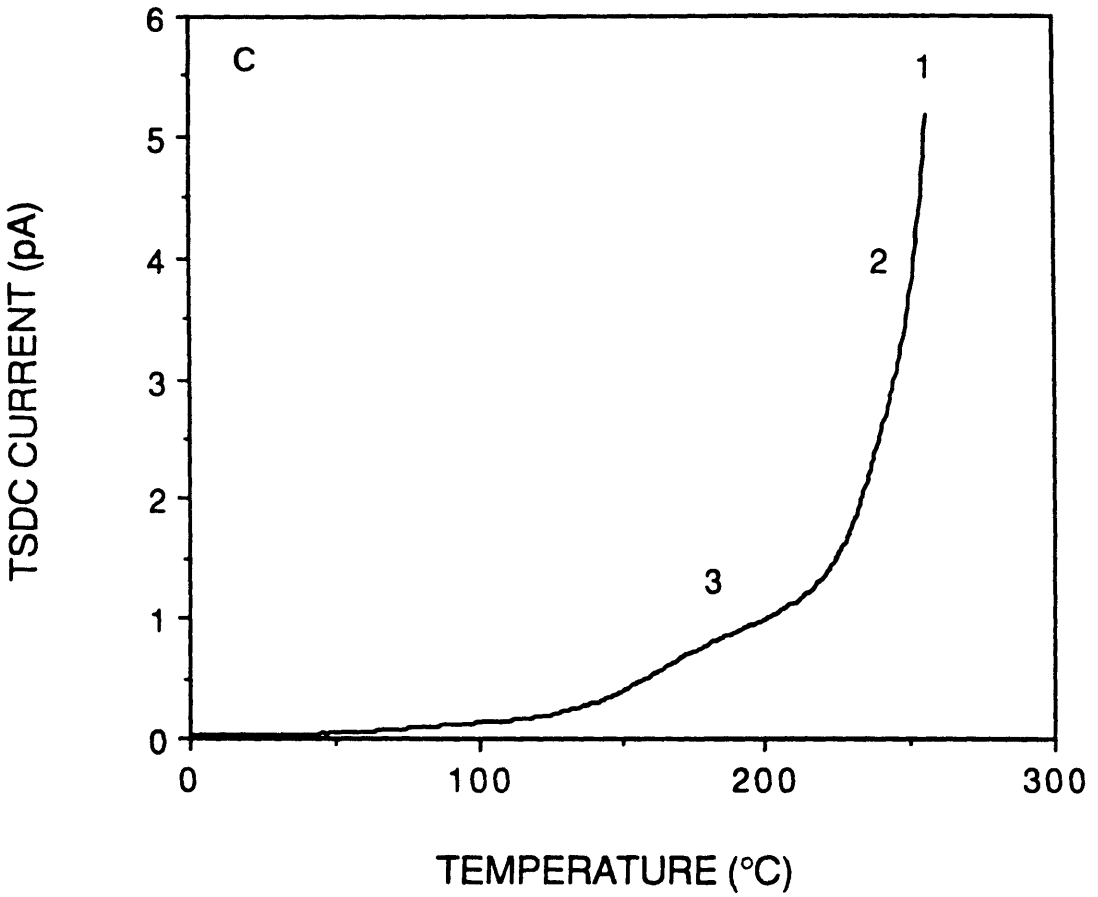

Figure 2.10, Continued

2.3.3.1 TSDC Study of Amorphous NEW-TPI

We first performed a global TSDC study of amorphous NEW-TPI relaxed at 260°C for 1 hr. The sample was coated with thermally evaporated Au and then poled at 250°C and fast quenched. Results are shown in Figure 2.9a for temperatures ranging from -80°C to 270°C. Four TSDC peaks are labeled from high to low temperature. A small peak, Peak 1, is observed at 265°C which is above the glass transition temperature. Since no crystal peaks from Bragg scattering were seen [140,141] when WAXS was used to examine this sample after the TSDC tests, we conclude that the sample had not been crystallized.

However, we want to compare in Figure 2.11 the WAXS scans for this TSDC sample (curve 2) with a semicrystalline sample (curve 1) which had been cold crystallized at 300°C for 1 hr, and with an amorphous film (curve 3) which had been relaxed at 260°C for 1 hr. The shape of the TSDC amorphous halo was very similar to the shape underneath the semicrystalline sample, and dissimilar to the halo of the relaxed amorphous sample. These results indicate a change in the state of order of the amorphous phase when the TSDC sample is heated to 270°C. We conclude Peak 1 is due to the formation of short range order in the amorphous phase prior to crystallization of NEW-TPI. This observation agrees well with our previous dielectric experiment data where we observed a high temperature shoulder just above T_g on the amorphous sample [92]. It is also consistent with our previous non-isothermal crystallization study [94] which showed no crystals form below 270°C for the heating rate used here.

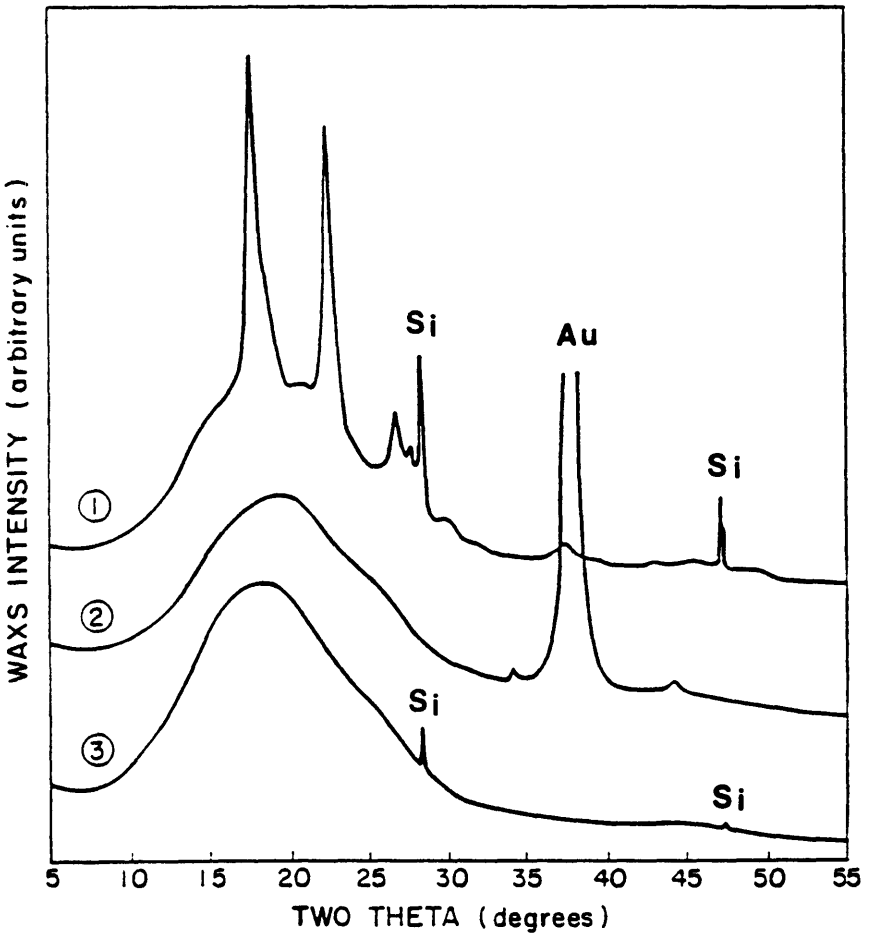

Figure 2.11 WAXS intensity vs. scattering angle, 2θ, for NEW-TPI semicrystalline film (curve 1) cold crystallized at 300°C for 1 hr, amorphous sample used in TSDC test heated to 270°C (curve 2), and amorphous sample (curve 3) relaxed at 260°C for 1 hr. Silicon reference standard powder and gold coating on the TSDC sample contribute several peaks as marked.

Three more peaks are observed in Figure 2.9(a). Peak 2 at 239°C has the largest current, with a peak height of 1.5 pA. Peak 3, observed at 159°C, is much broader and has a peak current around 1 pA. Peak 4, at -13°C, is quite small and sharp, covering only a ten degree spread and was not reproducible. It shifted in position, and sometimes disappeared entirely. This suggests that it must come from spurious charges, and we will not consider this peak further.

Peak 2 in Figure 2.9a comes from the glass transition relaxation of the sample. It occurs at the temperature at which long range cooperative motion of the polymer chains becomes possible, and the dipoles, frozen by the poling/quenching process, are liberated. The glass transition temperature found from TSDC is about 10°C lower than that from DSC and the peak is spread over about 50°. Our observation is also in good agreement with Hsiao et al. who found T_g=244°C at a heating rate of 7°C/min [98]. If we use van Turnhout's frequency equation [54,142] to obtain an equivalent TSDC frequency, the present data are consistent with the WLF plot from our previous dielectric and mechanical relaxation study [92]. The observation of a lower T_g under the comparatively lower frequency of the TSDC test is consistent with the manufacturer's quoted heat distortion temperature, which is 238°C for amorphous NEW-TPI [99].

Peak 3 is the peak with second highest current. The peak transition is not as sharp as Peak 2, and is spread out over about 100°C. Although our previous dielectric and mechanical relaxation measurements did not show any transition at this temperature range, Hsiao, et al.[98] previously reported a TSDC peak in this temperature region attributed to electrode surface effects.

In order to establish whether this peak can be dipole relaxation, we carried out a lower temperature 160°C poling TSDC experiment [141]. This poling temperature was chosen because it is the location of the current maximum of Peak 3. No depolarization current peak was observed in the temperature range from 0°C to 180°C. This is strong evidence that no dipolar relaxation is involved in Peak 3 [98,140,141].

A possible origin of this sub-T_g peak is considered to relate to space charge in the polymer. In most cases studied, space charge peaks, or ρ-peaks, occur above the glass transition temperature [53]. Free charge carriers may be created in the material at elevated temperature as a result of ionization of species left as residue of the initial processing, and/or as a result of injection of carriers from the electrodes. Upon application of the electric field during poling, charge separation/injection may occur, and the charge mobility is reduced during the cooling stage. During the TSDC measurement, these charges become mobile as a function of increasing temperature and contribute to Peak 3. To verify the origin of Peak 3, we have carried out two TSDC experiments and the results are shown in Figure 2.9 b,c for comparison.

The first experiment we did is the slow cooling experiment. It is well known that polymer free volume can be reduced by slow-cooling through the glass transition region, as the amorphous phase approaches a more dense state. This treatment is similar to physical aging, in which the glassy polymer is held for a period of time at or below its glass transition temperature. Thus a reduced free carrier mobility would be expected because of a reduction in free volume. In this experiment, a Au-coated amorphous sample was poled at 250°C and slowly cooled. The results are shown in Figure 2.9b. Peak 1 was

not observed because the test was stopped at too low a temperature. The glass transition, Peak 2, is at the same location and about the same peak current as the rapidly cooled sample of Figure 2.9b. Slow cooling results in a more homogeneous distribution of dipoles, and consequently, a narrower Peak 2. Peak 3 is found to have a greatly reduced height, while its peak position shifts about 10°C to higher temperature. These changes agrees with our previous expectation that reduced free volume leads to the impeded ability of the free carriers to move through the material.

The second TSDC experiment involves changing the electrode material to alter the work function of the electrodes relative to the polymer. Here we used Al instead of Au as the electrode material. The sample was poled at 250°C and cooled rapidly followed by a subsequent heating. The TSDC results are shown in Figure 2.9c. We see that Peak 1 (previously occurring at 265°C) is hidden under a steeply increasing current after T_g. Peak 2 at 239°C is also superimposed upon this current. This phenomenon is never observed on samples with gold electrodes, which suggests a different contacting mechanism for Au and Al with respect to NEW-TPI. The sharp current we observed is therefore a result of contact charging that causes conduction in the polymer above T_g. Peak 3 is observed with a much smaller peak maximum and about 100°C spread. Compared to Peak 3 in Figure 2.9a, its position shifts to a temperature 10°C lower and the relative ratio between Peak 3 and Peak 2 reduces from 0.64 (Au electrodes) to 0.22 (Al electrodes). This is additional strong evidence that Peak 3 originates from space charge effects.

There are two possible reasons why there is no space charge peak observed in the TSDC experiment where the sample is poled at 160°C [141].

First, although contact charging does exist at all temperatures, charge mobility through the sample depends not only on temperature but also on the physical state of the polymer. At 160°C, NEW-TPI is still in its glassy state, thus the penetration of the charges created at the electrode-polymer surface is inhibited. Second, the ionizable species inside the polymer can not move appreciably if the material is still in its glassy state. Therefore no significant space charge peak is observed when NEW-TPI was poled at 160°C.

To summarize the results from Figure 2.9b and 2.9c, we conclude that Peak 3 observed in TSDC scans does not relate to secondary dipole relaxation. No sub-T_g relaxation is found in NEW-TPI for the temperature range of our study. This is not surprising if we consider its molecular structure. There are no side groups in the rigid monomer unit to give secondary relaxation. From the mechanical property point of view, the rigid main chain and no secondary relaxation would give NEW-TPI fewer energy absorbing mechanisms during deformations.

2.3.3.2 TSDC Study of Semicrystalline NEW-TPI

Semicrystalline NEW-TPI films were cold crystallized at 300°C for 1hr prior to gold coating. We adopted the same experimental conditions and same method of peak assignment for semicrystalline samples as for the amorphous sample described in Section 3.3.1. The resulting two global TSDC spectra are shown in Figure 2.10a, sample A and sample B for two independent trials of similarly treated films. Fresh samples were used in each case and the sample treatment and experimental conditions were identical. No peak is observed in region 1 in sample B(testing for sample A was halted at too low a temperature due to experimental difficulties). Since the crystal

structure has already formed in the semicrystalline samples, the amorphous phase is locked either in between the lamellar stacks or within the lamellar bundles. The amorphous phase mobility is constrained by the crystals. No additional short range order can form when the temperature is below the treatment temperature. Therefore no peak is observed for the semicrystalline samples in the temperature region where Peak 1 was seen in amorphous sample. This observation provides additional confirmation of our previous assignment of Peak 1 in the amorphous polymer as due to the formation of short range order prior to the crystallization. The glass transition, Peak 2, is seen in both samples at the same location and will be discussed in the following paragraph. Peak 3 appears in both samples A and B, however it shifts its position. While Peak 3 occurred in all the semicrystalline and amorphous samples we tested, its peak height and location were widely variable. We have not yet determined which stage of our sample treatment affects its location. As in the amorphous sample, Peak 4 comes from spurious charges and will not be considered further.

After carefully examining the glass transition relaxation peak, Peak 2 in Figure 2.10a, we report the following observations which are very consistent with previous results. First, T_g of the semicrystalline polymer occurs at 244°C, which is 5°C above that of the amorphous sample. The crystals act as thermo-reversible crosslinks and constrain amorphous phase mobility. This leads to slightly higher T_g in semicrystalline films. Second, this peak has a greater full width at half maximum than the amorphous NEW-TPI indicating a broader distribution of relaxation times in semicrystalline film. Third, the height of Peak 2 is also reduced in semicrystalline film. The relative peak height ratio of semicrystalline Peak 2 to amorphous Peak 2 is calculated to be 0.65. This

may be related to the relative quantity of amorphous phase dipoles in the semicrystalline sample compared to the amorphous sample. Using DSC, our previous calculation of amorphous moieties from the step height of the heat capacity change at T_g gave an amorphous fraction of 0.63 by weight [93].

The origin of Peak 3, which in the amorphous sample we attributed to space charge and/or ionizable species inside the polymer bulk, appears to be even more complex in the semicrystalline sample [72,143]. Peak 3 for semicrystalline NEW-TPI sample A (Figure 2.10a) has a maximum at 159°C while Peak 3 in sample B has a maximum at 207°C. Generally speaking, there exist at least two phases inside the semicrystalline polymer bulk, i.e., amorphous phase and crystalline phase, which provide current pathways of different conductivities. For semicrystalline NEW-TPI, in addition to the crystal phase, both mobile and rigid amorphous phases are observed [92,93], and different conductivity between them can be safely assumed. When the electric field is applied, homocharges will build up at the phase boundaries due to the differences in conductivity in addition to space charges and/or ionizable species inside the semicrystalline bulk. These factors come into play to give Peak 3.

Experiments have been carried out on semicrystalline NEW-TPI to further investigate the space charge effect of Peak 3. Figure 2.10b shows the result of TSDC measurement on semicrystalline sample slowly cooled after being poled at 250°C for 10 min. Again, Peak 1 was not observed because the polymer has already crystallized completely. The glass transition, Peak 2, is at the same location and about the same peak current as the rapidly cooled sample of Figure 2.10a. No significant narrowing is observed, which suggests

that amorphous phase is constrained in between the crystalline phase and does not relax as it does in the pure amorphous polymer. Peak 3 broadens significantly in the slowly cooled sample. This is probably due to the longer separating distance of the charges and the impeded ability of the free carriers to move through the crystalline and amorphous interphase region.

Figure 2.10c shows the TSDC result for semicrystalline sample coated with aluminum electrodes, poled at 250°C for 10 min and cooled rapidly. Similar to what we have observed for the amorphous sample, the sample coated with Al shows ionic conduction [140,141] at high temperature, which suggests a different contact mechanism for Au and Al. This strong current starts to occur just below T_g and masks Peak 2. Peak 3 can be observed around 163°C but it is difficult to determine the peak shape. Combining these observations, it is clear that Peak 3 is not due to dipolar relaxation. Its origin is quite complicated, and space charge, electrode type, ionizable species and interfacial charges can all contribute to its shape and position.

2.4 CONCLUSIONS

Regulus™ NEW-TPI has been studied by SAXS and TSDC. Both static and real time SAXS have been employed to study the cold crystallization behavior of NEW-TPI and obtain crystallization parameters from the one-dimensional electron density correlation function. We observed that both long period and lamellar thickness increase significantly with isothermal cold crystallization temperature, but linear crystallinity changes very little. Samples crystallized at a higher temperature contain a larger fraction of amorphous phase between the crystal lamellae because of slower

crystallization kinetics. In non-isothermal crystallization of NEW-TPI, lamellar thickness, crystallinity and interphase thickness all increase with crystallization temperature and reach steady values at the same time. Long period drops at the beginning of the crystallization, then levels off as the temperature passes the region of fastest crystal growth.

TSDC has been used to study the relaxation behavior of NEW-TPI. The glass transition temperature of the semicrystalline polymer is only slightly higher than that of the amorphous sample. Thus, the crystals appear to have only a minor effect on the relaxation time distribution of the amorphous chains. These results are consistent with our prior studies using DSC and dynamic mechanical relaxation [92]. Space charge, electrode type, ionizable species and interfacial charges may all affect the TSDC spectrum.

Chapter 3

High Temperature Thermal Properties of Polymers Containing Carbonyl and Ether Linking Groups

3.1 INTRODUCTION

One of the key properties that distinguishes high performance polymers from their low performance counterparts is their outstanding high temperature stability. To achieve high thermal transition temperatures and thermoplasticity, recent synthetic approaches have focused on incorporation of phenyl-ether and phenyl-ketone linkages in the monomer repeat unit. This strategy resulted in the development of the class of poly(aryl ether ketones) or PAEKs [144]. Polymers in this category which have been studied extensively include poly(etheretherketone), PEEK [39,131,132,144-157], and similar chemical relatives such as PEK [144,152,154,156,158] and PEKK [72,159-161]. These types of high performance polymers are technologically very important, with applications as composite matrices, high temperature films and adhesives, and wire and cable insulation.

In the mid-1980's development of semicrystalline, thermoplastic polyimides (TPIs) was undertaken in which the diamine portion of the chain contained phenyl-ether and phenyl-ketone linkages [89,99,162-168]. As a result, the molecular mobility of the polyimides was increased sufficiently to allow crystallization to occur from the melt [89,99,162-166] while still retaining the excellent high temperature properties of the polyimides. The dianhydride portion of the polyimide chain, which contains the imide ring, could be made

either rigid or somewhat more flexible. Included in the category of semicrystalline TPIs are Regulus^{TM} NEW-TPI (from Mitsui Toatsu Chemical Co.) [89,99] and LARC-CPI [162-166] and LARC-IA [167,168] (from NASA Langley Research Center). The NEW-TPI monomer contains the pyromellitic dianhydride (PMDA), while LARC-CPI contains the benzophenone tetracarboxylic dianhydride (BTDA) and LARC-IA contains the oxydiphthalic dianhydride (ODPA). The chemical repeat units for these novel polyimides, and for PEEK polymer, are shown in Figure 3.1.

Our group [92-94,96,97,169-172] and others [89,90,98,99,126,162-168,173] have been studying the structure and properties of this class of high performance polyimides (PIs). NEW-TPI, LARC-CPI and LARC-IA can be processed by standard thermoforming techniques such as injection molding and extrusion of pellets or film and can be drawn into oriented films. These polyimides all have relatively high glass transition temperatures (above 200°C) and melting points (above 300°C). Therefore, like PEEK, their processing temperatures are correspondingly high. One of the factors determining the ultimate use of these polymers is the coefficient of thermal expansion (CTE). In composites, the difference in CTE between polymer matrix and fiber reinforcement would produce high residual stresses during cooling and/or thermal cycling. Therefore, determination of CTE has both scientific value and engineering application.

We have previously studied crystal lattice expansion of NEW-TPI and LARC-CPI using wide angle X-ray scattering (WAXS) [96]. There is a very close similarity in crystal lattice CTE among NEW-TPI, LARC-CPI, and PEEK, whose thermal expansion has been studied by Blundell and D'Mello [155] and

PEEK

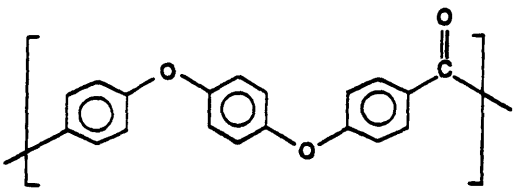

NEW-TPI

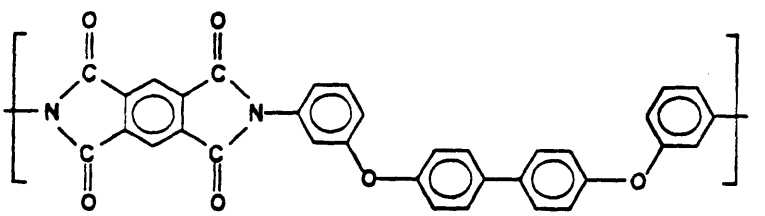

LARC-CPI

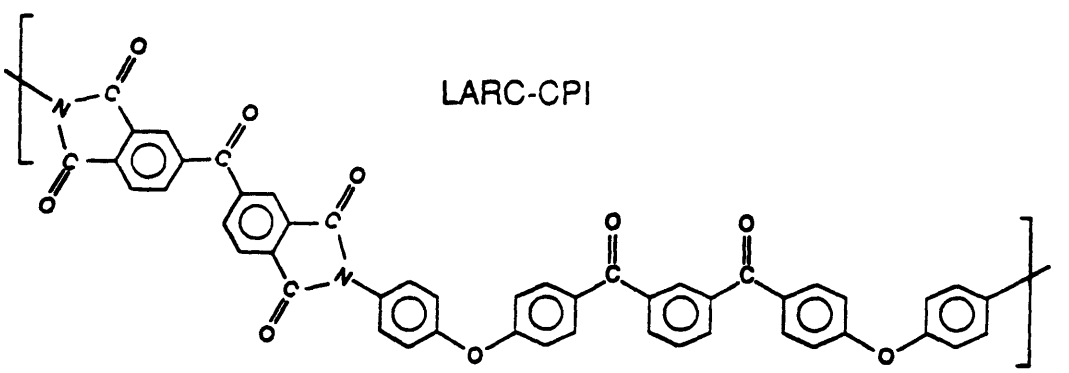

LARC-IA

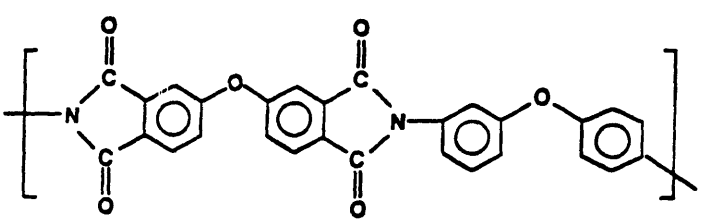

Figure 3.1 Chemical repeat units for PEEK, NEW-TPI, LARC-CPI, and LARC-IA.

Choy, et al. [153]. In these three polymers, the crystal lattice CTE is highly anisotropic. Along the c-axis (molecular chain direction) the thermal expansion is either too small to be measured [155], or possibly even negative, as in the case of PEEK studied by Choy, et al. [153]. The lateral expansions of the unit cell in the a and b directions are predominant, with magnitudes of the order of 50-100 $x10^{-6}/°C$.

TMA has long been used as the standard method to measure one-dimensional bulk expansion. Other non-thermoplastic polyimides have been studied by TMA [99,153,174-177] and their CTE's reported to span a wide range depending upon the chemical structure of the repeat unit, and whether the films were imidized as free-standing or on a substrate. Numata and co-workers [174-177] examined various low CTE aromatic polyimides. They observed no correlation between the polyimide CTEs and their packing coefficients or crystallinity. It was proposed that the appearance of low CTE (10-20 $x10^{-6}/K$) might relate to the linearity of the polymer molecular skeletons. These researchers also studied CTE of uniaxially stretched polyimides and found that low or even negative CTE tends to be correlated with higher elastic modulus in the chain direction.

In this work, we compare the thermal stability of PEEK, NEW-TPI, LARC-CPI and LARC-IA studied using thermogravimetric analysis (TGA). We also report our investigation of the thermal expansion behavior of these four polymers using thermal mechanical analysis (TMA) and/or small angle X-ray scattering (SAXS). Recently, we showed that above the glass transition temperature, SAXS could be used to study the thermal expansion behavior of poly(butylene terephthalate), PBT [178]. In particular, we used SAXS to derive

the expansion properties of the *amorphous* phase above T_g [178]. Here we apply this approach to PEEK and NEW-TPI. For the first time, we derive the amorphous phase CTE from SAXS measurement of the long period expansion. We suggest a model in which crystals serve to constrain the mobility of the amorphous phase. Amorphous phase CTEs deduced using this model show very good agreement with amorphous phase CTEs obtained from TMA.

3.2 EXPERIMENTAL SECTION

3.2.1 Sample Preparation and Characterization

Semicrystalline PEEK 450G plaques were obtained from ICI Americas, Inc. with a thickness of 1mm. The plaque was annealed at 300°C for 1 hr before the experiments.

Regulus™ NEW-TPI amorphous film was supplied by Mitsui Toatsu Chemical Company with a thickness of 100μm. Twelve pieces of the NEW-TPI were stacked and cold crystallized for 1 hr in a hot press which had been preset at 300°C. The sample was then cooled slowly to room temperature. The films were easily consolidated into a 1mm thick plaque which was subsequently annealed at 350°C for one hour.

LARC-CPI and LARC-IA were received from NASA Langley and Imitec, respectively. As received LARC-CPI was fully imidized semicrystalline film processed by Foster Miller, Inc. The sample was annealed at 300°C for 1hr to obtain a stable crystal structure. LARC-IA powder was

compression molded at 310°C between ferro-type plates covered with Kapton^{TM} film, then quenched into ice water.

A Perkin Elmer DSC-4 was used to study the crystallization behavior of PEEK, NEW-TPI and LARC-CPI. Indium was used to calibrate the temperature and heat of fusion. Sample weights around 8mg were used with a scan rate of 20°C/min. Crystallinity was calculated from endotherm area using 130J/g as the heat of fusion of perfect crystalline for PEEK [138], 139J/g for NEW-TPI [99] and 92J/g for LARC-CPI [170].

Thermomechanical analysis (TMA) was performed using a TA Instruments 2100 TMA at a scan rate of 20°C/min and a quartz probe weighted with 0.2 Nt. Thermogravimetric analysis (TGA) experiments were conducted using a TA Instruments 2100 TGA with automated sample changer, scan rate of 20°C/min, in nitrogen purge.

3.2.2 Small Angle X-ray Scattering

Real-time SAXS experiments were done in transmission mode at the Brookhaven National Synchrotron Light Source using high intensity X-radiation with a wavelength of 1.48Å. Distance from the sample to the two-dimensional histogramming gas-filled wire detector was about 1.46m, calibrated using cholesterol meristate and collagen fiber. The beam profile was treated according to pinhole geometry. A Mettler FP-80 Hot Stage was used to heat (or cool) the sample with a ramp and hold temperature profile (10°C/min. ramp and 2 min. isothermal hold).

3.3 RESULTS

3.3.1 Thermogravimetric Analysis

Figure 3.2a-d shows the results of thermogravimetric analysis on semicrystalline PEEK, NEW-TPI, LARC-CPI, and amorphous LARC-IA, respectively. Each plot shows the percent of original weight remaining on the left vertical axis, and the derivative curve on the right vertical axis, as a function of temperature over the range from 25°C to 750°C. The derivative curves are most illustrative of the degradation behavior. When major weight loss begins, there is a sharp increase in the derivative, which then reaches a maximum rate of weight loss. After the maximum, the derivative curves tend to level off somewhat, except for the case of LARC-CPI which exhibits very complex degradation kinetics. PEEK (Figure 3.2a), NEW-TPI (Figure 3.2b), and LARC-IA(Figure 3.2d) all showed almost no weight loss up to about 525°C, while LARC-CPI (Figure 3.2c) started to undergo major weight loss by about 425°C. PEEK (Figure 3.2a) and LARC-CPI (Figure 3.2c) both had greater ultimate weight loss at 750°C compared to the other two materials. The percent of weight remaining at 750°C is listed in the first column of Table 3.1. By this criterion, NEW-TPI and LARC-IA appear to be the least subject to degradation weight loss at very high temperature.

Figure 3.3 is a composite plot showing percent of original weight for all four materials over an expanded region at lower temperatures. In the region near 100°C, where water loss is expected, both PEEK (solid line) and NEW-TPI (dotted line) have negligible weight loss. LARC-CPI (dot-dashed line) and LARC-IA (dashed line) both lose about 0.5% in this temperature range. LARC-CPI begins major weight loss at lower temperature than the other materials. The intersection of the curves on the temperature axis occurs at

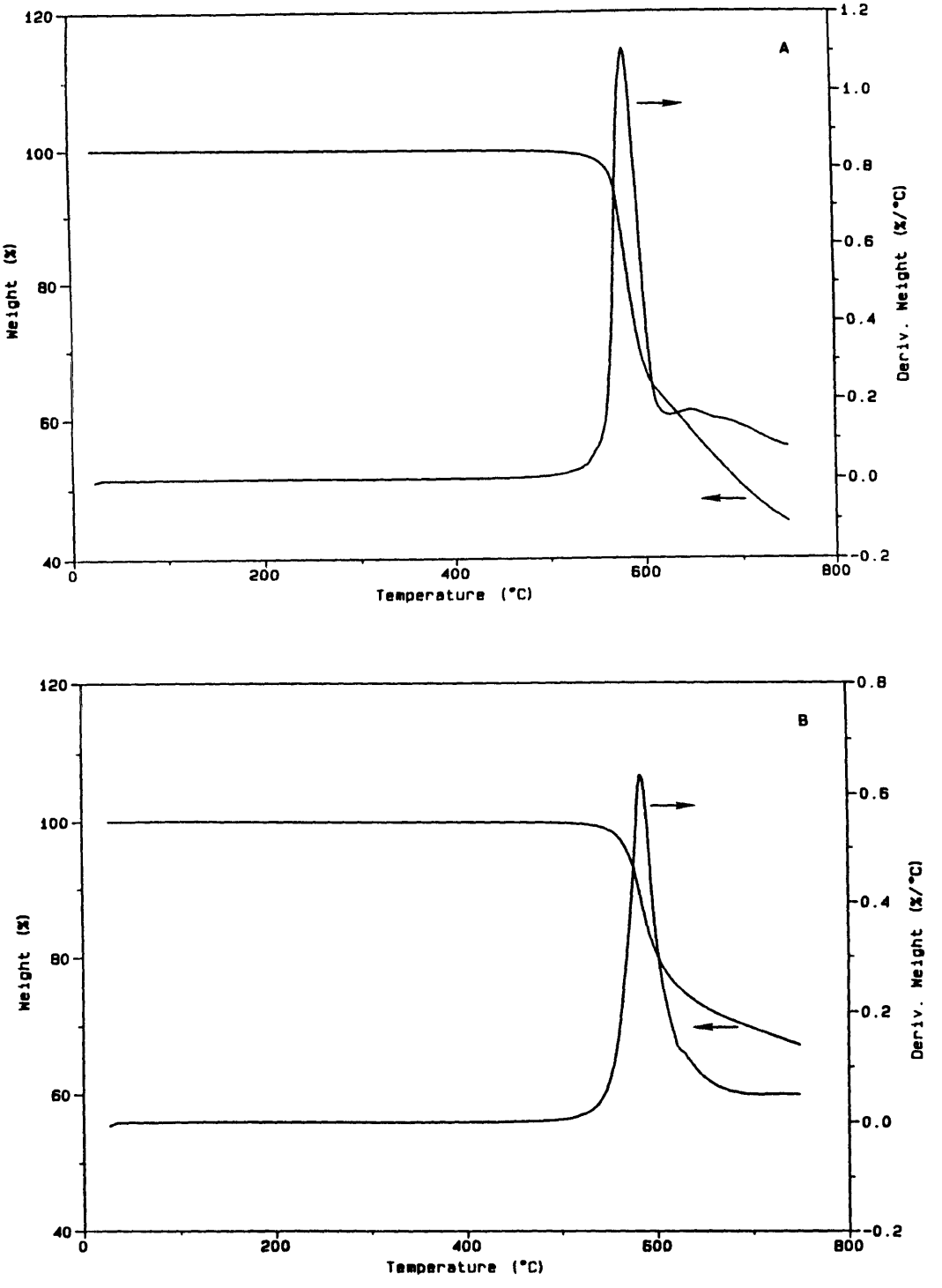

Figure 3.2 Thermogravimetric analysis showing percent of original weight remaining and its derivative, vs. temperature.
a) PEEK, b) NEW-TPI, c) LARC-CPI, and d) LARC-IA.

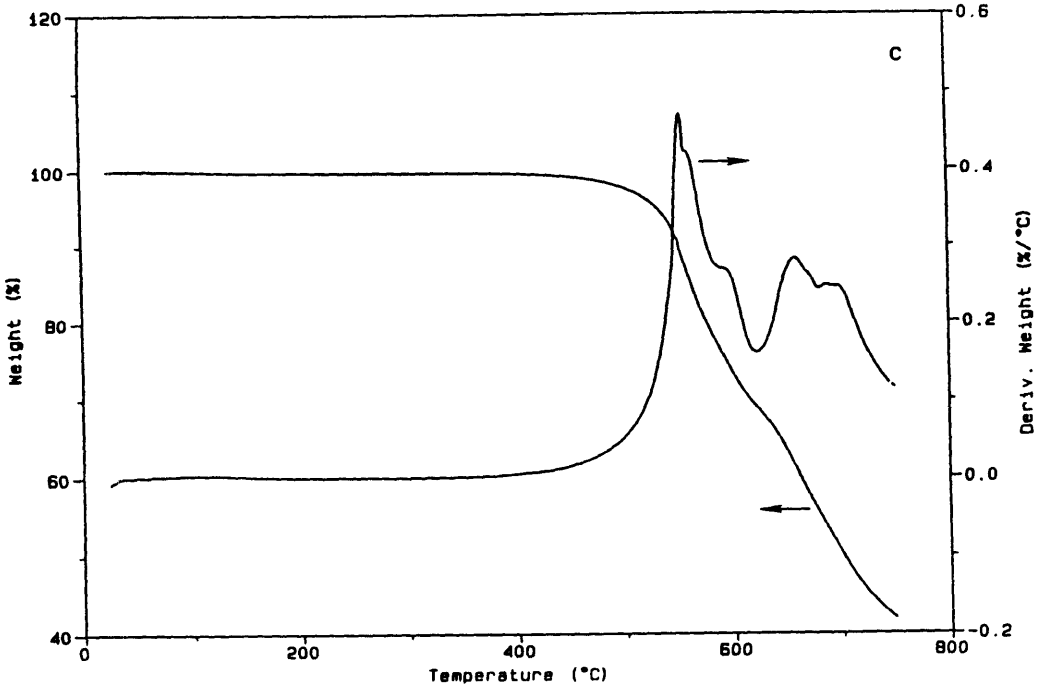

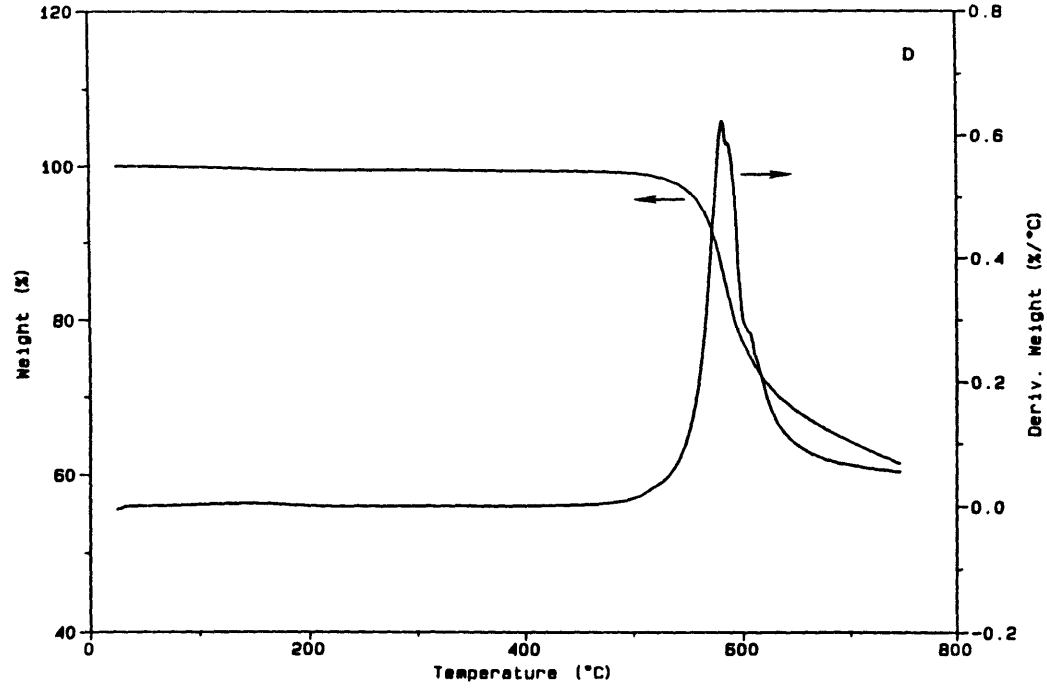

Figure 3.2, Continued

Table 3.1 Weight remaining at 750°C, five percent weight loss temperature, glass transition temperature and volume fraction crystallinity for polymers used in this study.

Polymer	% of Weight Remaining at 750°C (± 1)	5% Weight Loss Temp., °C (± 2)	T_g, °C * (± 2)	χ_c § (± 0.01)
PEEK	46	568	170	0.35
NEW-TPI	68	570	265	0.30
LARC-CPI	42	530	225	0.31
LARC-IA#	62	562	225	0

* Estimated from TMA

§ Determined from equation Eqn. 2.4.

\# 3% Offset

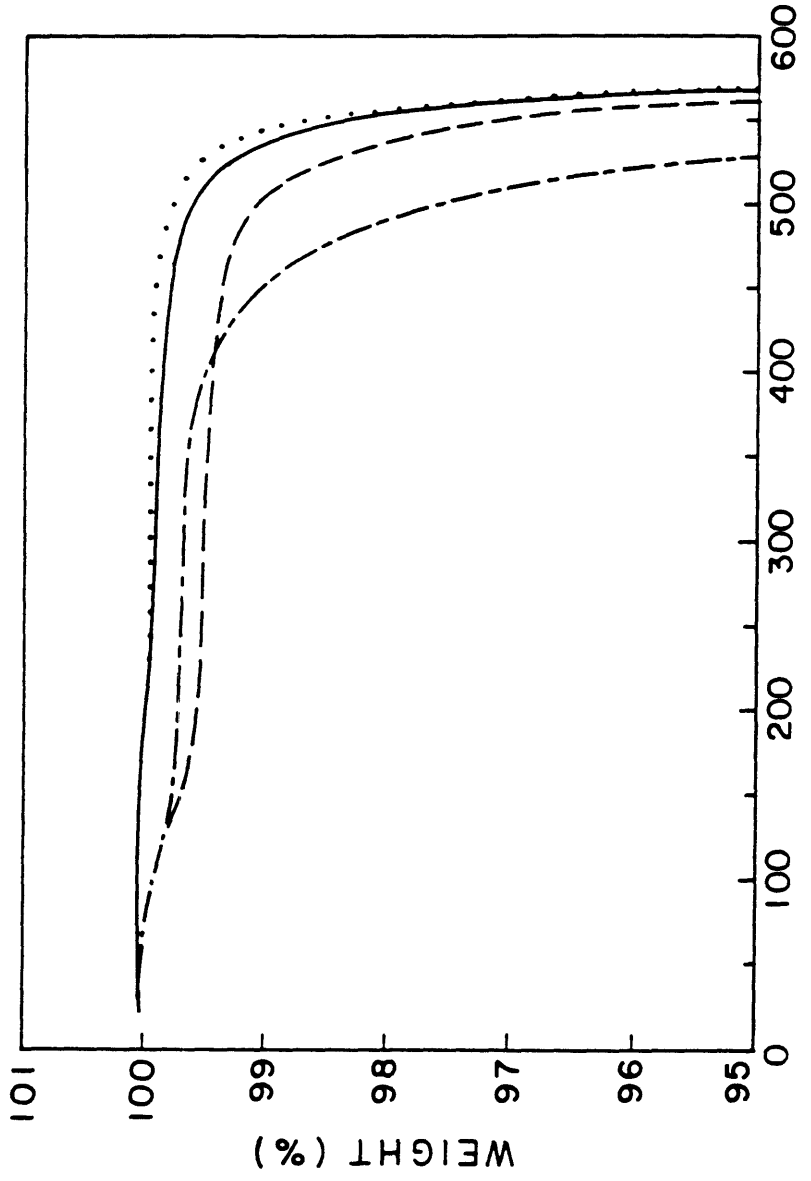

Figure 3.3 Expanded temperature scale thermogravimetric analysis showing percent of original weight remaining vs. temperature for PEEK (solid line), NEW-TPI (dotted line), LARC-CPI (dot-dashed line), and LARC-IA (dashed line).

the point where the samples have lost 5% of their original weight. The temperatures for 5% weight loss are listed in the second column of Table 3.1. Once again, according to this measure, LARC-CPI is the least stable of the four polymers.

3.3.2 Thermomechanical Analysis

Results of thermomechanical studies are shown in Figure 3.4a-d for PEEK, NEW-TPI, LARC-CPI and LARC-IA, respectively. Dimension change relative to original sample thickness is plotted as a function of temperature. All four polymers show a clear change in slope at their glass transition temperatures indicating an increase in thermal expansion coefficient above T_g. The intersection of the tangents to the lower temperature (below T_g) and higher temperature (above T_g) portions of the curve were used to identify the glass transition temperatures. These are listed in the third column of Table 3.1, and correlate well with T_g determined by other methods, such as thermal analysis [39,92,94,149,171,172].

Three materials, PEEK, NEW-TPI, and LARC-CPI are semicrystalline. Volume fraction crystallinity, χ_c, was determined for each polymer from DSC endotherm area and the known crystal and amorphous phase densities. The volume fraction crystallinity is obtained directly from the weight fraction crystallinity, χ_c^w, using Eqn. 2.4. For PEEK, ρ_a=1.263g/cm^3 and ρ_c=1.400g/cm^3 [138], for NEW-TPI, ρ_a=1.33g/cm^3 and ρ_c=1.47g/cm^3 [98,99], and for LARC-CPI, ρ_a=1.335g/cm^3 and ρ_c=1.507g/cm^3 [172]. Volume crystallinities are listed in the last column of Table 3.1.

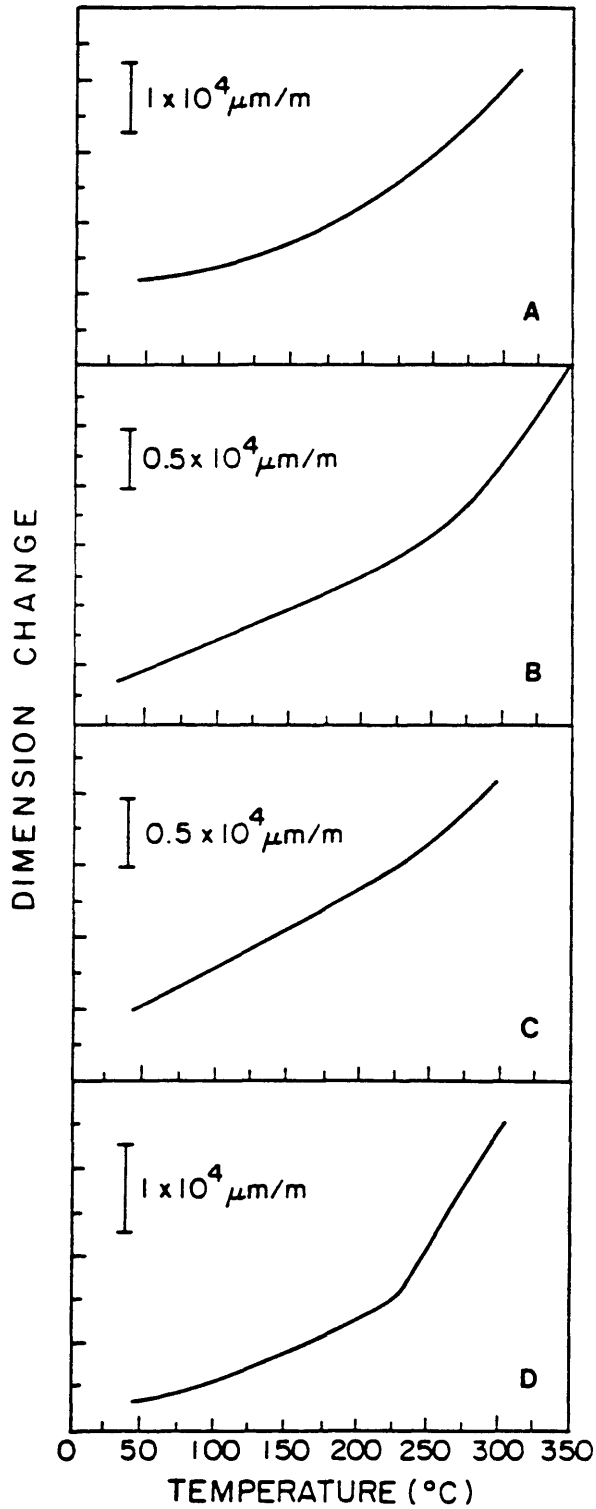

Figure 3.4 Thermomechanical analysis showing dimension change relative to original sample thickness, vs. temperature for PEEK (curve a), NEW-TPI (curve b), LARC-CPI (curve c), and LARC-IA (curve d).

Semicrystalline samples were selected for the TMA studies so that expansion properties above the glass transition could be evaluated. When purely amorphous samples are heated above T_g all three semicrystalline polymers tend to undergo rapid crystallization. This change in physical state, and the attendant density change, prevented accurate measurement of sample dimension above T_g. The TMA curves shown in Figure 3.4a-c represent the behavior of the semicrystalline materials, which are treated as isotropic composites comprising the crystal regions and amorphous regions. Below the glass transition of the amorphous phase, we expect that the expansion behavior of the glassy amorphous chains and the crystal chains might be very similar. On the other hand, above T_g, amorphous chains experience large scale segmental motions. Thus, we expect the expansion behavior above T_g to be largely dominated by the expansion within the amorphous phase.

The linear coefficient of thermal expansion of the material, α^l, is the slope of the relative dimension change vs. temperature curve. α^l is shown in Figure 3.5a-d for PEEK, NEW-TPI, LARC-CPI, and LARC-IA, respectively. All four materials show the same general trends in thermal expansion coefficient. Below T_g, α^l is low (50-70 $x10^{-6}/°C$) and relatively flat. α^l increases steeply at T_g reaching a maximum. At high temperature, all materials show an apparent decrease in CTE. For the semicrystalline samples, the apparent decrease in α^l occurs just before crystal melting/reorganization begins. LARC-IA also has a similar decrease in α^l which we attribute to penetration and sticking of the probe. (LARC-IA proved to have such good adhesive properties to quartz that the probe and support platform became irretrievably bonded to the polymer.)

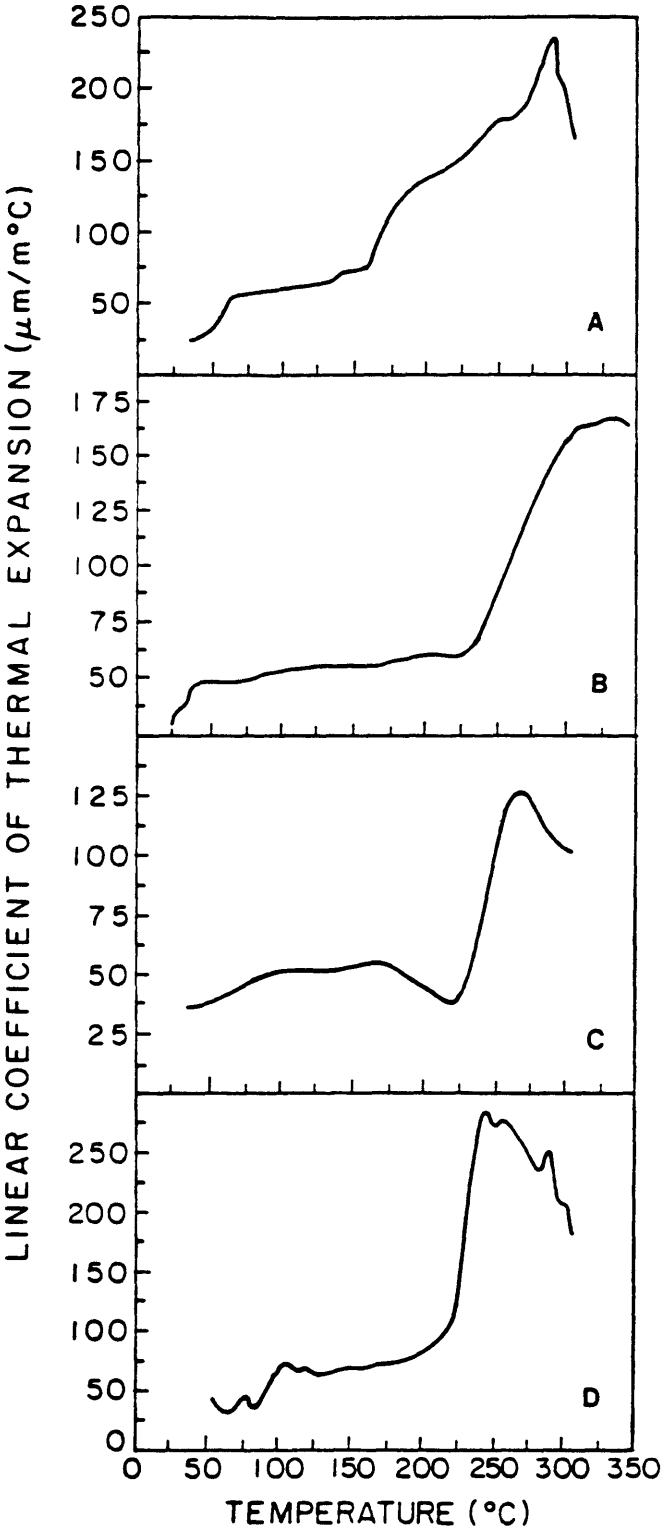

Figure 3.5 Linear coefficient of thermal expansion vs. temperature for PEEK (curve a), NEW-TPI (curve b), LARC-CPI (curve c), and LARC-IA (curve d).

All materials showed temperature dependence in their CTEs, especially above T_g. Therefore, a single reported number for CTE will not accurately reflect the expansion behavior, except below T_g where α^1 changes little. Nonetheless, it is customary to select a representative value of CTE for comparison purposes. Since these four polymers have different glass transition temperatures, we report the bulk linear CTE of these materials at temperatures 75°C below and above T_g. These values are shown in Table 3.2 as $\alpha^1(T_g - 75°C)$ and $\alpha^1(T_g + 75°C)$. For PEEK, NEW-TPI and LARC-IA the higher temperature CTE is about three times larger than the lower temperature CTE. In LARC-CPI it is roughly two times larger at the higher temperature. The error estimates were made using the standard method described in ASTM test E831-86.

3.3.3 Small Angle X-ray Scattering

In Figure 3.6a,b, we present a sequence of Lorentz corrected intensities $I_{corr}s^2$ vs. s, for PEEK measured from 40°C to 300°C, and NEW-TPI measured from 60°C to 340°C, respectively. A temperature interval of 20°C separates adjacent curves. Distinct maxima are observed which reflect the Bragg scattering from the periodic lamellar structures. As the temperature increases, the intensity increases and the peak maximum shifts to lower s. The upper limit of temperature was chosen to be just below the prior crystallization treatment temperature, in order to avoid major melting of the sample.

Long period L was obtained from K(z) according to the method of Strobl and Schneider [45]. The procedure has also been described in our other SAXS studies [93,97]. Results for PEEK (Figure 3.7a) and NEW-TPI (Figure

Table 3.2 Coefficients of thermal expansion (10^{-6}/°C) of bulk and amorphous material, at temperatures below and above the glass transition, evaluated from thermomechanical analysis.

Polymer*	Bulk CTE, α^l		Amorphous phase CTE, $\langle\alpha_a^l\rangle$	
	(T_g - 75°C)	(T_g + 75°C)	(T_g - 75°C)	(T_g + 75°C)
PEEK	60±3	180±4	63±8	246±25
NEW-TPI	54±2	162±7	55±10	210±39
LARC-CPI	55±4	105±8	51±10	123±26
LARC-IA#	70±7	200±15	70±7	200±15

* PEEK, NEW-TPI, and LARC-CPI bulk materials are semicrystalline

\# 3% Offset

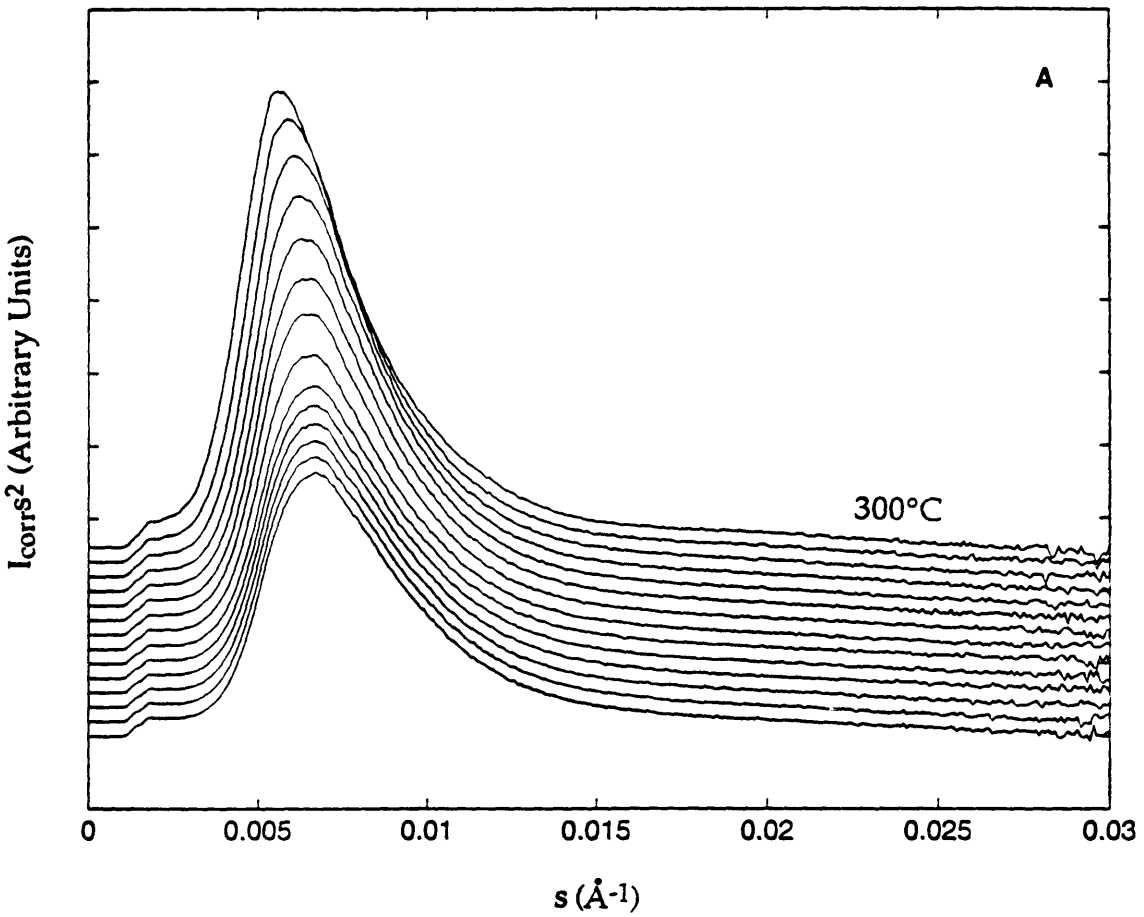

Figure 3.6 Lorentz corrected scattering intensity, $I_{corr}s^2$, vs. scattering vector, s, at different temperatures for a) PEEK, from 40°C to 300°C, and b) NEW-TPI, from 60°C to 340°C. A temperature interval of 20°C separates adjacent curves.

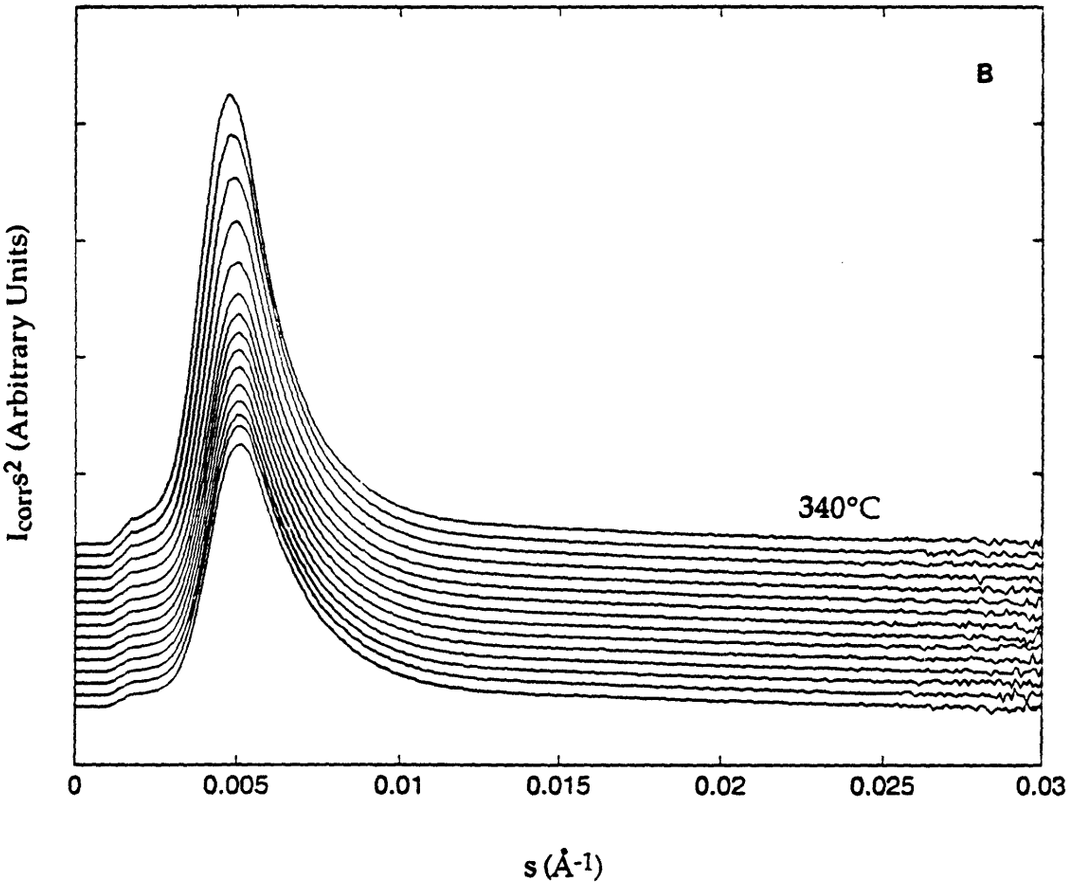

Figure 3.6, Continued

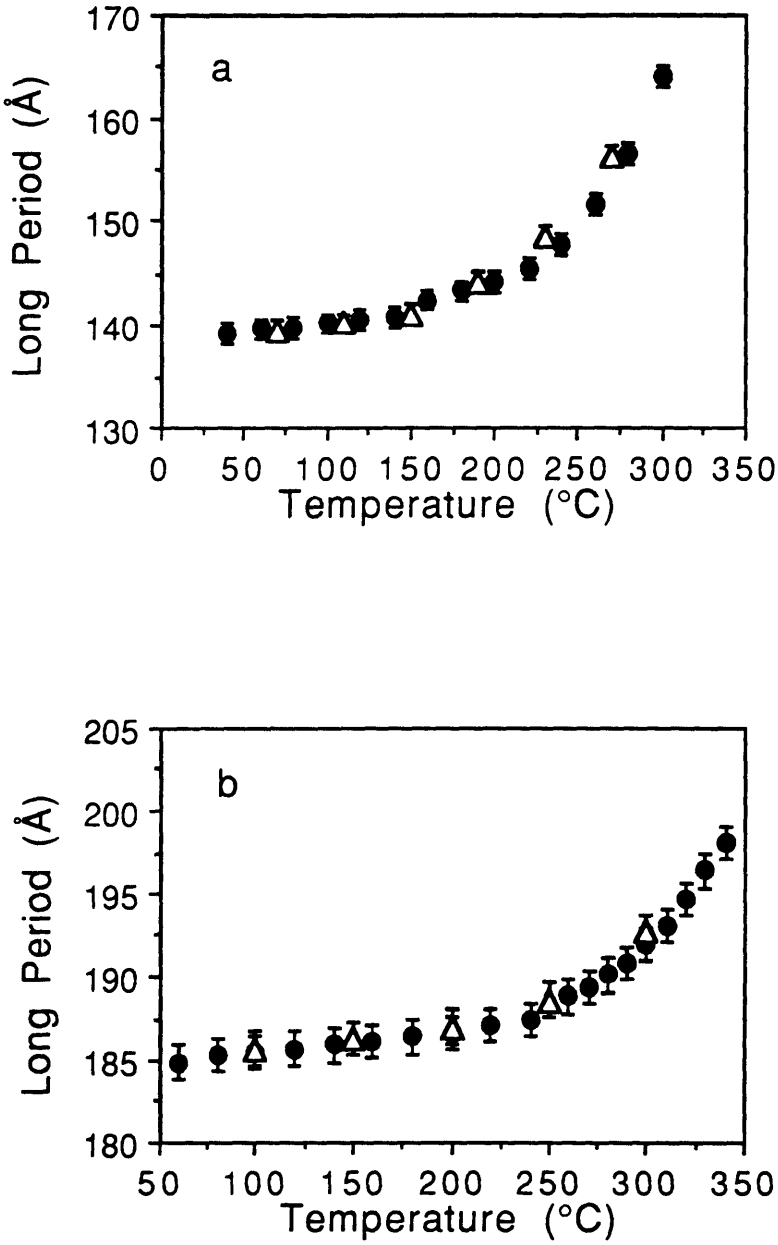

Figure 3.7 Long period, L, vs. temperature for a) PEEK, and b) NEW-TPI. Solid circles represent data collected during heating, while empty triangles represent data collected during cooling.

3.7b) obtained from both heating (circles) and cooling (triangles) are plotted together. The cooling data fall closely on the heating curves in both plots. This indicates that our heating process did not significantly affect the crystal stacks, and the changes in L obtained are reversible.

For PEEK polymer, in Figure 3.7a, the long period has a value of 140Å at 60°C and increases steadily to 165Å at 300°C. Above T_g, from 170°C up to 300°C, L increases about 20 Å from ~143 Å to ~165 Å. This observation agrees well with published data [131,132]. Similar trends in L are observed for NEW-TPI, as shown in Figure 3.7b. As temperature increases above T_g, there is a noticeable change in the slope of L vs. T. For NEW-TPI, from 250°C up to 335°C, L increases about 10Å, from ~188Å to ~198Å.

3.4 DISCUSSION

The linear coefficient of thermal expansion, α_p^l describes the temperature dependent change of a characteristic dimension of the material, p, measured along the l direction, according to:

$$p(T) = p(0)\ (1 + \alpha_p^l\ T) \tag{3.1}$$

where p(T) is the value of the characteristic dimension at temperature T. In the case of TMA measurement, the characteristic dimension is the sample thickness; in the SAXS measurement, it is the long period, L. Both the sample thickness and the long period may be treated according to a simple two-phase model. In this model, the crystals and amorphous phase are

assumed to act in series along the direction in which the linear expansion is measured. Thus, we write:

$$p(T) = p_a(T) + p_c(T) \tag{3.2}$$

where the subscripts a and c refer to the amorphous phase and crystalline phase, respectively. The crystal and amorphous phase CTEs we will write as α_a^l and α_c^l. Then combining Eqn. 3.1 and 3.2 we arrive at the following expression which relates the expansion of the characteristic dimension to that of the component phases:

$$\alpha_p^l = \alpha_a^l (\chi_a) + \alpha_c^l (\chi_c) \tag{3.3}$$

In Eqn. 3.3, χ_a and χ_c are the volume fractions of the amorphous and crystalline phases, respectively, and $\chi_a + \chi_c = 1$ according to the two phase model. We now apply this model to deduce the CTE of the amorphous phase from the TMA and SAXS experiments.

3.4.1 TMA

The linear CTE values listed in Table 3.2 allow us to calculate the thermal expansion of the amorphous phase using Eqn. 3.3, provided we have knowledge of the thermal expansion coefficient of the crystals. This may be estimated from the known CTEs of the crystal unit cell lattice parameters which have been determined from prior wide angle X-ray scattering studies of PEEK [155], NEW-TPI [96] and LARC-CPI [96]. In Table 3.3 we list the CTEs of the a, b, and c lattice parameters for these polymers. All three polymers have highly anisotropic crystal lattice expansions. The expansion along the

Table 3.3 Coefficients of thermal expansion ($10^{-6}/°C$) for the a, b, and c lattice parameters, and the isotropic crystal phase determined from wide angle X-ray scattering studies.

Polymer	a-axis	b-axis	c-axis	Isotropic crystal# $<\alpha_c l>$
PEEK [13]	133±7	39±6	0	57±4
NEW-TPI [37]	93±6	60±19	0	51±7
LARC-CPI [37]	117±7	75±23	0	64±8

Determined from equation Eqn. 3.4.

molecular chain (c-axis) is unmeasurable in most experiments, though Choy, et al [153] reported a negative CTE for the c-axis expansion in PEEK. In all investigations, the c-axis expansion is considered to be much smaller than the expansions observed along the other two directions of the unit cell.

The average *linear* CTE of the crystal phase, $<\alpha_c^l>$, assuming an isotropic distribution of crystals within the bulk semicrystalline polymer, is derived from:

$$<\alpha_c^l> = (1/3) \sum_i (\alpha_{ci}^l) \qquad (3.4)$$

where the summation is over the i^{th} crystal unit cell lattice parameter (i=1,2,3). The average linear crystal CTE is listed in the last column of Table 3.3. The amorphous phase CTEs $<\alpha_a^l>$, derived using Eqn. 3.3 and the isotropic estimate for the linear crystal CTE, are shown in the last two columns of Table 3.2 for the regimes below and above the glass transition temperature. For all three semicrystalline polymers, the amorphous phase expansion is greater than the expansion of the bulk semicrystalline material which accords with our intuition.

The flexibility of the polymer backbone containing carbonyl and/or ether linking groups results in relatively larger CTEs in the polymers we studied, compared to those in Numata's study [174-177]. Smaller bulk linear CTE values were measured in the more rigid chain aromatic polyimides studied by Numata [174-177]. The polyimides used in their study were prepared by reacting different diamine groups with three common dianhydride groups, PMDA, BTDA and s-BPDA, and generally have T_g's

higher than the TMA test temperatures. The PI films were cured either on or off a substrate, and relationship of bulk linear CTE to chemical structure was investigated. Bent structures generally had higher CTEs. For PIs containing BTDA, bulk linear CTE ranged from 30-50 $x10^{-6}/K$, while PIs containing PMDA, which is a more rigid group, had lower CTE ranging from 10-20 $x10^{-6}/K$ [174-177]. All the phenyl-ether/phenyl-ketone containing polymers we studied had larger CTEs in the glassy state, and much larger CTEs once T_g was exceeded.

3.4.2 SAXS

Eqn. 3.1 may be used to deduce the linear coefficient of thermal expansion of the long period in the z direction from the data shown in Figures 3.7a and 3.7b. Below T_g, the changes in long period are slight, and although a trend is observed in which L increases with temperature, the error bars on the measurement of L are large. Only above T_g does the increase in L exceed the error range. Therefore, we will only apply Eqn. 3.1 to analysis of the data in the temperature range above the glass transition. To compare with the TMA data, we consider the variation of L at temperatures about 50-75°C above T_g. We find in PEEK and NEW-TPI, there is a similar expansion coefficient of the long period, $\alpha_L{}^z$, above T_g. In PEEK, $\alpha_L{}^z$ is 428 x 10^{-6} /°C while In NEW-TPI, it is $423x10^{-6}$/°C. These values are listed in Table 3.4.

The two phase model may also be applied to the lamellar stack, to deduce the amorphous phase CTE in the z direction from the SAXS data. In Eqn. 3.3, the volume fraction crystallinity refers to the crystallinity of the lamellar stack. However, the crystal expansion coefficient now refers to the expansion of the crystal lattice in the z direction which is normal to the

Table 3.4 Coefficients of thermal expansion (10^{-6}/°C) above the glass transition for long period and amorphous phase in the z-direction, and average amorphous phase expansion, determined from small angle X-ray scattering studies.

Polymer	Long period CTE, α_L^z	Amorphous CTE, α_a^z	Avg. amorphous CTE *, $<\alpha_a^l>$
PEEK	428±13	658±26	273±22
NEW-TPI	423±17	604±30	252±36

* Determined from Eqn. 3.5.

lamellar stack. In PEEK, the c-axis is normal to the lamellar surfaces [150]. We will make the same assumption about NEW-TPI, although the direction of the c-axis relative to the lamellar surfaces is not yet known in this material. From Table 3.3, we see that the c-axis expansion is negligible for both PEEK and NEW-TPI. Thus, Eqn. 3.3 reduces simply to $\alpha_L^z = \alpha_a^z (1- \chi_c)$. The degree of crystallinity used here must be the crystallinity within the lamellar stack. We found this crystallinity, which can also be deduced from the correlation function, to be the same as the volume crystallinity deduced from DSC. In PEEK and NEW-TPI the amorphous phase resides within the lamellar stacks.

The expansion of the long period in the z direction comes solely from the expansion of the amorphous phase between the lamellae. The amorphous phase CTE, α_a^z, deduced from SAXS (listed in Table 3.4) is much greater than the linear amorphous phase CTE deduced from thermomechanical analysis (Table 3.2). Whereas the SAXS results relate to amorphous phase expansion in one direction relative to the crystal surfaces, the TMA data refer to the average linear expansion of the amorphous phase in an isotropic sample. In the next section, we present a model of the amorphous phase expansion in which crystals act to constrain the amorphous phase within the lamellar stacks.

3.4.3 Model of Lamellar Constraint

We suggest a model of lamellar constraint, which accounts for the large amorphous phase CTE observed to occur in the z-direction, as deduced from SAXS data. The lamellar crystals serve to constrain the amorphous phase so that it expands laterally (i.e., in the x and y directions parallel to the lamellar surfaces) with an expansion coefficient no greater than that of the crystal

phase. To avoid the build up of stresses at the crystal/amorphous interfaces, all the remaining volume expansion of the amorphous phase is forced to occur along the z direction, normal to the lamellar stacks. The constrained expansion is depicted in Figure 3.8. Similar constraints have been used to explain large thermal expansion observed in amorphous diblock copolymers in which one block exhibits much larger expansion in the direction normal to the layer structure [179].

Using the model of Figure 3.8, the average linear expansion of the bulk amorphous phase, $<\alpha_a^l>$, in a sample in which the lamellae are arranged isotropically, would be written in a manner analogous to Eqn. 3.4 as:

$$<\alpha_a^l> = (1/3)\,[\alpha_c^x + \alpha_c^y + \alpha_a^z] \qquad (3.5)$$

This calculation results in amorphous expansions for PEEK of 273 $x10^{-6}/°C$ and for NEW-TPI of 252 $x10^{-6}/°C$. These values are in very reasonable agreement with the average linear amorphous phase expansion deduced from TMA measurements.

3.5 CONCLUSIONS

High temperature thermal properties of novel thermoplastic polyimides containing ether and carbonyl linking groups were studied and compared to PEEK polymer. NEW-TPI has the highest glass transition temperature and greatest stability against weight loss in nitrogen. The increased flexibility of the polymer backbone results in larger CTE in these polymers compared to more rigid, non-thermoplastic polyimides. All

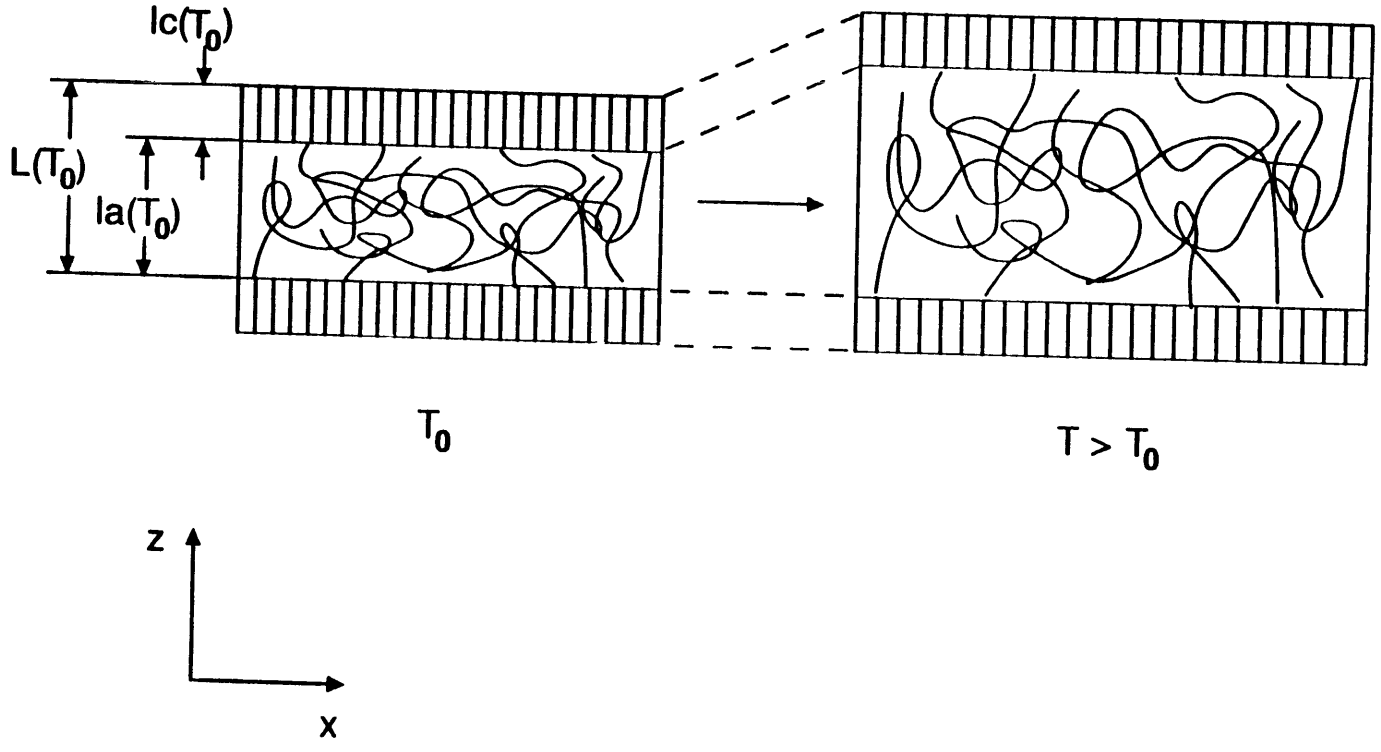

Figure 3.8 Model of lamellar stack expansion showing no expansion of the crystals in the z direction. Crystals expand primarily in the x direction (and also in the y direction which is not shown) and constrain the amorphous phase to the same x,y expansion. The remaining volume expansion of the amorphous phase occurs in the z direction.

materials showed about a factor of three increase in CTE above the glass transition temperature. Using a two phase model, the amorphous phase CTE was deduced from TMA measurements and the known crystallinity.

We applied SAXS to study PEEK and NEW-TPI to determine the expansion properties of the long period in a direction perpendicular to the lamellar stacks. The resultant amorphous phase expansion in this direction is very large. We propose that crystals constrain the amorphous phase mobility so that the amorphous phase expands laterally with the same CTE as the crystals. The average amorphous phase CTE deduced using this model is in very good agreement with amorphous phase CTE obtained from TMA measurement.

Chapter 4

Relaxation Behavior in Film Processed Poly(phenylene sulfide) (PPS)

4.1 INTRODUCTION

Poly(p-phenylene sulfide) (PPS) is a semicrystalline engineering thermoplastic with excellent properties for use as a matrix in high temperature composites. Brady [108] first studied the effect of crystallinity on its properties using wide angle X-ray scattering (WAXS) and differential scanning calorimetry (DSC). Its crystal unit cell structure was reported by Tabor et al. [109] using X-ray scattering of drawn fibers. Later on, extensive research was performed to study its crystallization kinetics, crystal structure and crystal morphology [34,110-120]. Several earlier reviews [121-123] and one most recent review [124] have covered these researches completely.

One of the interesting properties of PPS discovered by Wunderlich and co-workers is the existence of the rigid amorphous phase (RAP) [34]. It is the portion of the amorphous phase which does not relax when the temperature is above the glass transition temperature (T_g) of the mobile amorphous phase. Huo and Cebe later investigated the behavior of RAP using dielectric measurement [38]. They observed that the RAP formed in PPS relaxes little by little as temperature increases. It is examined in the later chapters the molecular weight effect and the thermal history effect of PPS. It is suggested that the existence of RAP is the result of annealing at the treatment temperature.

PPS can be processed by many methods such as compression molding, injection molding, etc., and in the form of films, fibers or composites reinforced with glass fibers. As molecular structure and relaxation behavior have direct effect on its properties, it is most desirable that the initial processing method would have provided the desired structure when it is processed into a final product. We have previously studied the effects of film processing on PPS [119]. The results show a unique orientation of lamellae with respect to the film surface. In this study we will continue our study on this film processed PPS to investigate its relaxation behavior. DSC, WAXS, dynamic mechanical analysis (DMA), and thermally stimulated depolarization current (TSDC) will all be used in the characterization.

4.2 EXPERIMENTAL SECTION

The PPS polymer used in this study is Ryton V-1 film, a product from Phillips Petroleum Company. The as-received (AR) polymer is semicrystalline film with a thickness of 75 μm and molecular weight of 60,000. Some of the AR films were used directly in our study, while the others were annealed in a Mettler FP80 hot stage for 15 min at a certain annealing temperature (T_a) before the experiments. For comparison, amorphous Ryton films were also prepared by heating the AR film to 320°C, holding for 2 min to destroy the nucleation seeds, then quenching the sample into an ice water bath. Some of these amorphous samples were later cold crystallized at T_a for further study.

The relaxation and melting behavior of AR films were studied using a Perkin-Elmer DSC-4 differential scanning calorimeter. Inside the DSC cell,

the AR film was heated from 60°C at 20°C/min to T_a and held for 15 min. The sample was then cooled at 20°C/min to 30°C. After the temperature was equilibrated, a subsequent rescan was performed at 20°C/min up to the melting temperature. An average sample weight of 8mg was used in the study and the temperature and heat flow were calibrated using Indium.

Dynamic mechanical relaxation experiments were carried out on a Seiko DMS 200 system. Both AR and treated AR films were cut into a 5mm x 10mm rectangular shape with a cross-sectional area of 0.375mm^2. The samples were scanned from 30°C to 220°C at a heating rate of 2°C/min and measured at frequencies of 0.5, 1, 5 and 10 Hz. All the experiments were carried out under nitrogen gas flow of 300ml/min.

The crystallinity and crystal orientation of the samples were examined using WAXS. A Rigaku RU300 X-ray generator and a diffracted beam graphite monochromator were used to carry out the experiments. Copper K_α radiation (λ=1.54Å) was used with a step scan interval of 0.02 degree and a scanning rate of 2°/min.

The relaxation behavior of PPS films at T_g was studied using the TSDC method. The experiments were performed on our self-designed and self-assembled apparatus. All the samples studied were coated with thermally evaporated gold to ensure better contact between the sample and the electrodes. The film was first poled at temperature T_p for 15min with a poling voltage of 100V. Then the sample was quenched to 0°C to freeze in the dipole orientation. After the two electrodes were shorted, the sample was

heated at 2°C/min and the current vs. temperature data were recorded. Details about our TSDC apparatus are described in the Appendix.

4.3 RESULTS

4.3.1 Dynamic Mechanical Relaxation Study

We have studied the dynamical mechanical relaxation behavior of AR PPS annealed at temperatures of 30°C, 60°C, 100°C, 120°C and 138°C. Figure 4.1 shows DMA results from 40°C to 220°C of AR PPS. Curve (a) represents the dynamic modulus E'. In the glassy region from 40°C to 100°C, it is quite flat with an E' of 1.8GPa. A drop occurs between 105°C to 160°C indicating a softening of the material at T_g. After that, E' drops steadily as temperature increases up to 220°C at which temperature the experiment was stopped. Dissipation factor tanδ (tanδ=E'/E") is shown in curve (b). A relaxation peak is observed with a peak maximum temperature (PMT) at 120°C and a peak height (PH) of 0.15 for frequency of 1Hz. The peak has an asymmetric shape and starts an upturn after 180°C. Similar upturn in the high temperature region is also observed dielectrically from our previous study [119]. The reason may be due to the pre-melting of the imperfect crystals formed during fast processing from the melt.

PMT and PH of tanδ represent characteristics of the molecular dipole relaxation. In Figure 4.2 a,b, tanδ's PMT and PH are plotted as a function of treatment temperature for different frequencies. Both PMT and PH show flat curves until 100°C, then PMT increases with T_a, while PH decreases. The observation suggests that annealing above T_g pushes the relaxation to a higher temperature and reduces the amount of chain movement, which

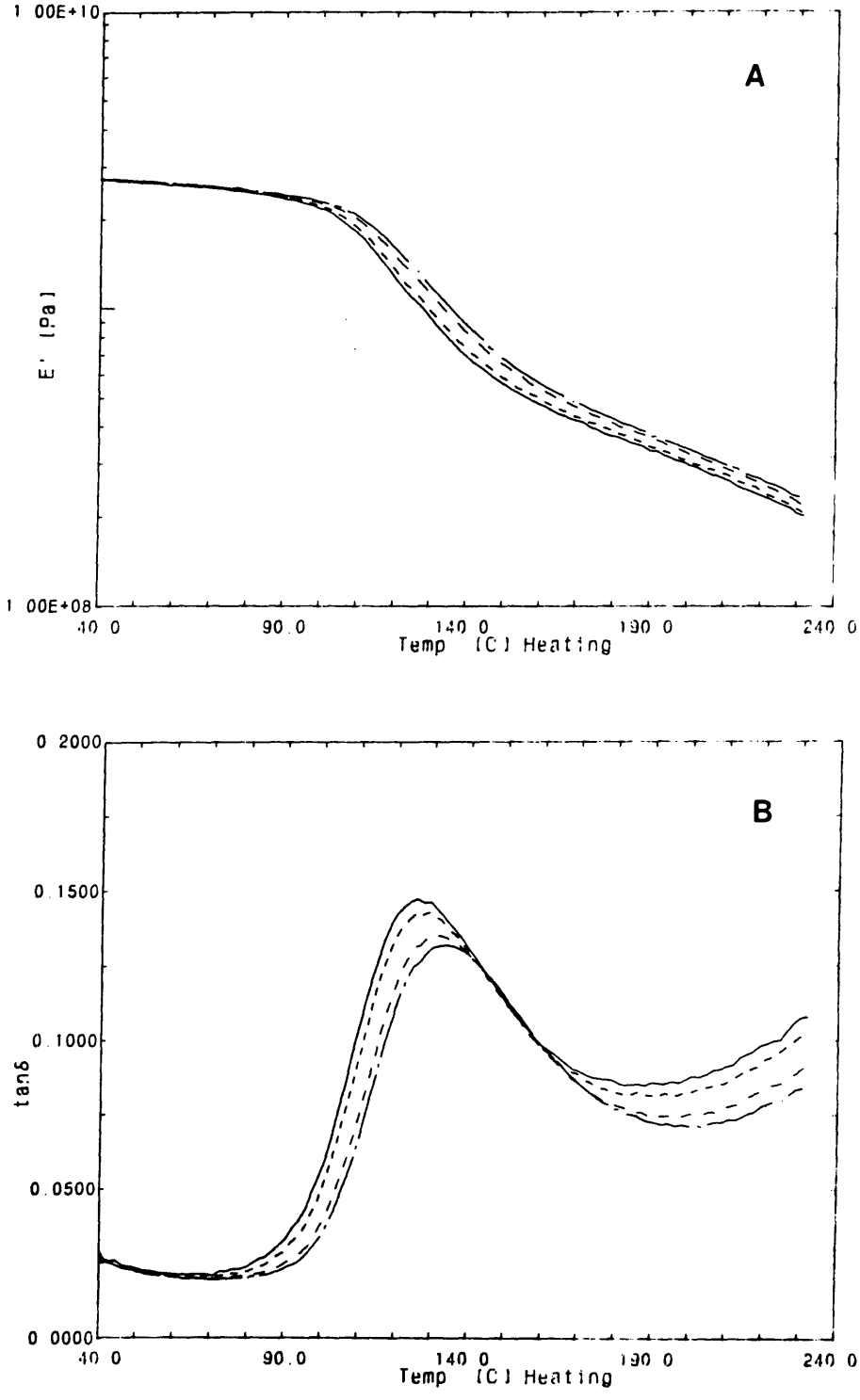

Figure 4.1 DMA results for AR PPS measured at 0.5Hz(solid line), 1Hz(dense dash line), 5Hz(loose dash line) and 10Hz(dash-dot line). a) Modulus E′, and b) Loss factor tanδ.

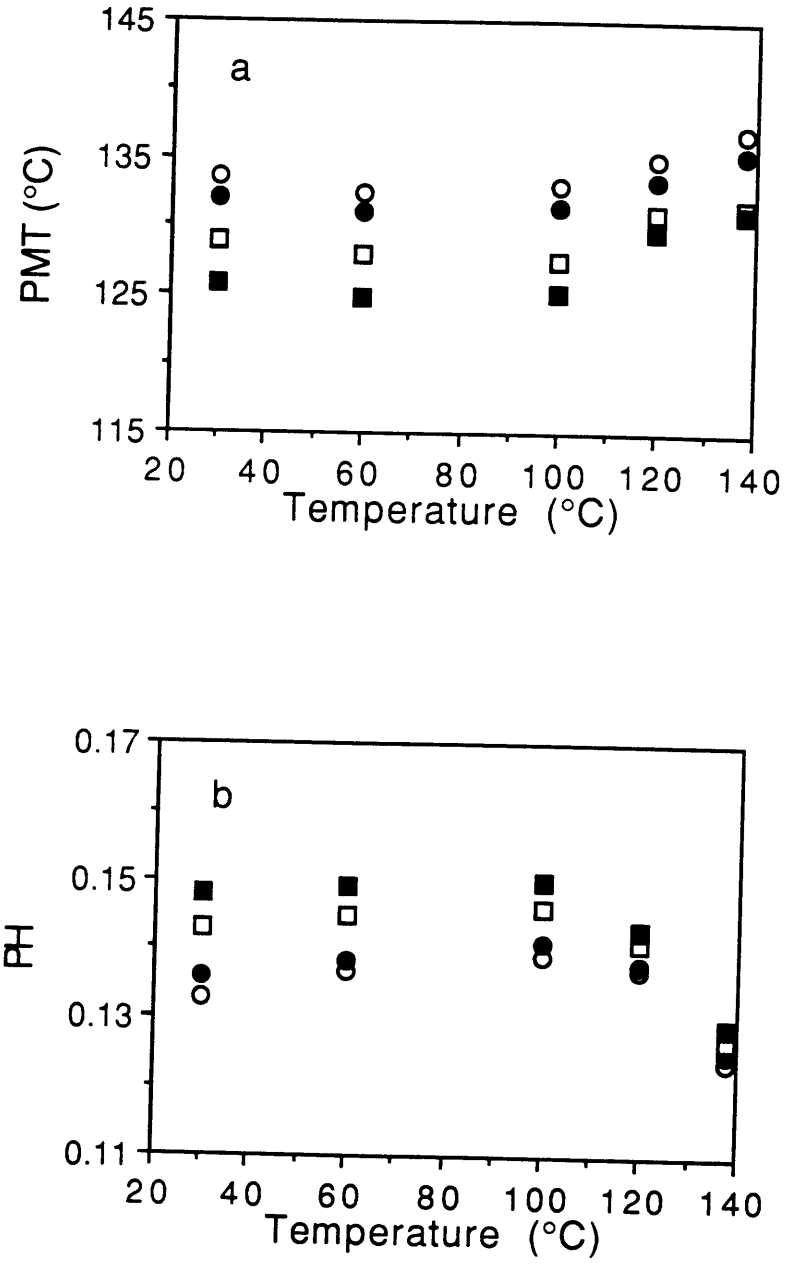

Figure 4.2 DMA results from tan(δ) for PPS films annealed at different temperatures: a) PMT vs. T_a, and b) PH vs. T_a. The samples were measured at different frequencies: 0.5Hz(solid square), 1Hz(empty square), 5Hz(solid circle), and 10Hz(empty circle).

indicates an overall increase in the chain rigidity. For the same material, PMT increases while PH decreases with increasing frequency. This is consistent with our intuition that an alternating force at a high frequency activates less polymer chain movement and requires a higher temperature for chains to respond. Studies both from melt and cold crystallized polymers have shown that annealing at a higher temperature relaxes polymer chains and shifts the relaxation peak to a lower temperature [37,38,112-114,120]. This somewhat unusual behavior of the film processed PPS must relate to the polymer's thermal history which plays an important part in determining how the relaxation is affected by later treatment.

4.3.2 Differential Scanning Calorimetric Study

As we have shown in our previous DSC study [119], the AR PPS film has unique relaxation properties. It shows no discernible glass transition in DSC scanning, i.e., no apparent heat capacity increment, leaving almost 40% rigid amorphous phase. DSC experiments were performed on both AR PPS and AR PPS annealed at different T_as to study relaxation and melting behavior. We show in Figure 4.3 a DSC scan of the AR films (curve 1), AR film treated at 120°C (curve 2), and quenched amorphous PPS for comparison (curve 3). Very large difference is observed at T_g between curves 1, 2 and curve 3, which reflects the fact that AR samples contain a large amount of RAP. Little change is observed between curves 1 and 2 from (T_a+10°C) up to the melting temperature. Thus we will plot the low temperature part in an expanded scale.

A composite plot of the low temperature range DSC thermographs of annealed AR films is presented in Figure 4.4. The treatment temperatures are

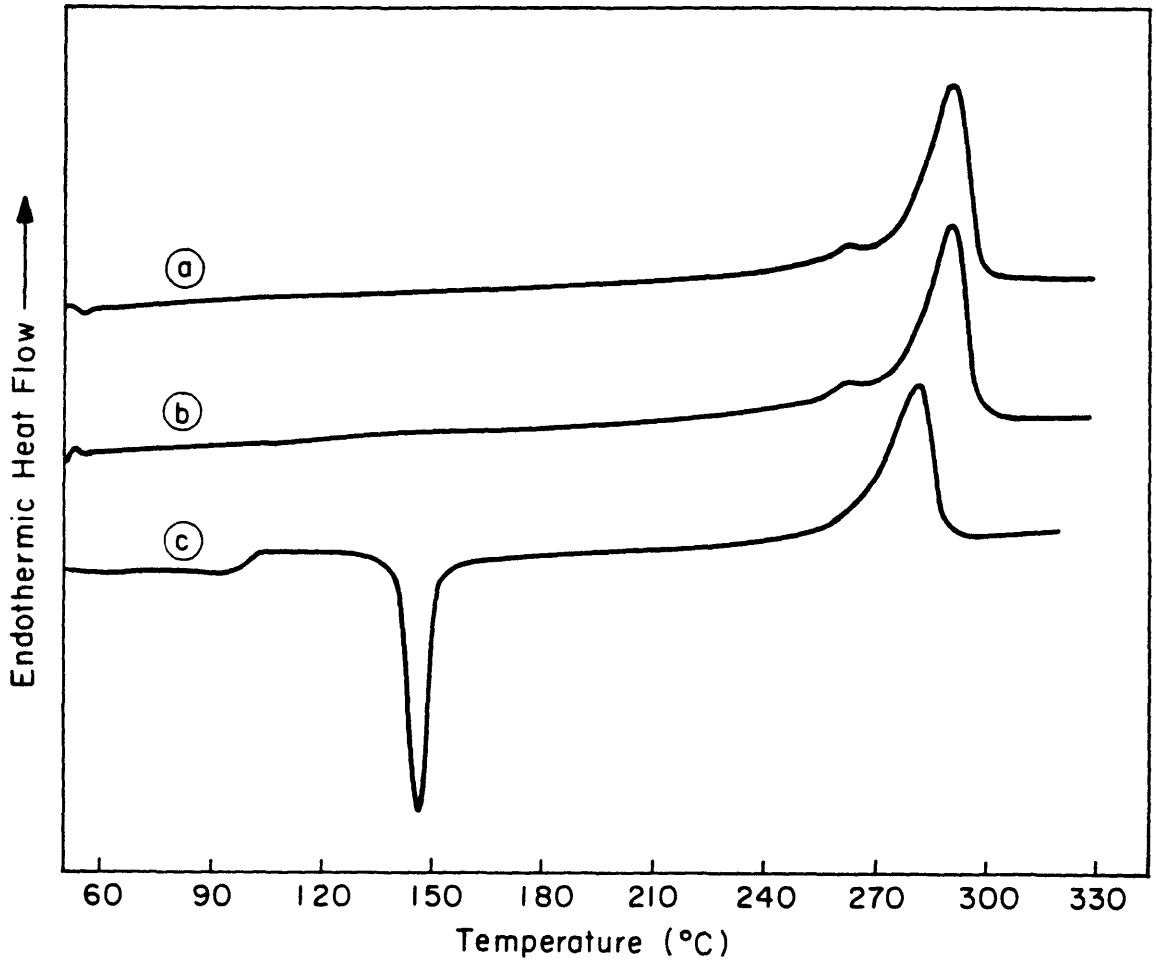

Figure 4.3 DSC results of PPS films, a) AR film, b) AR film annealed at 120°C, and c) quenched amorphous PPS.

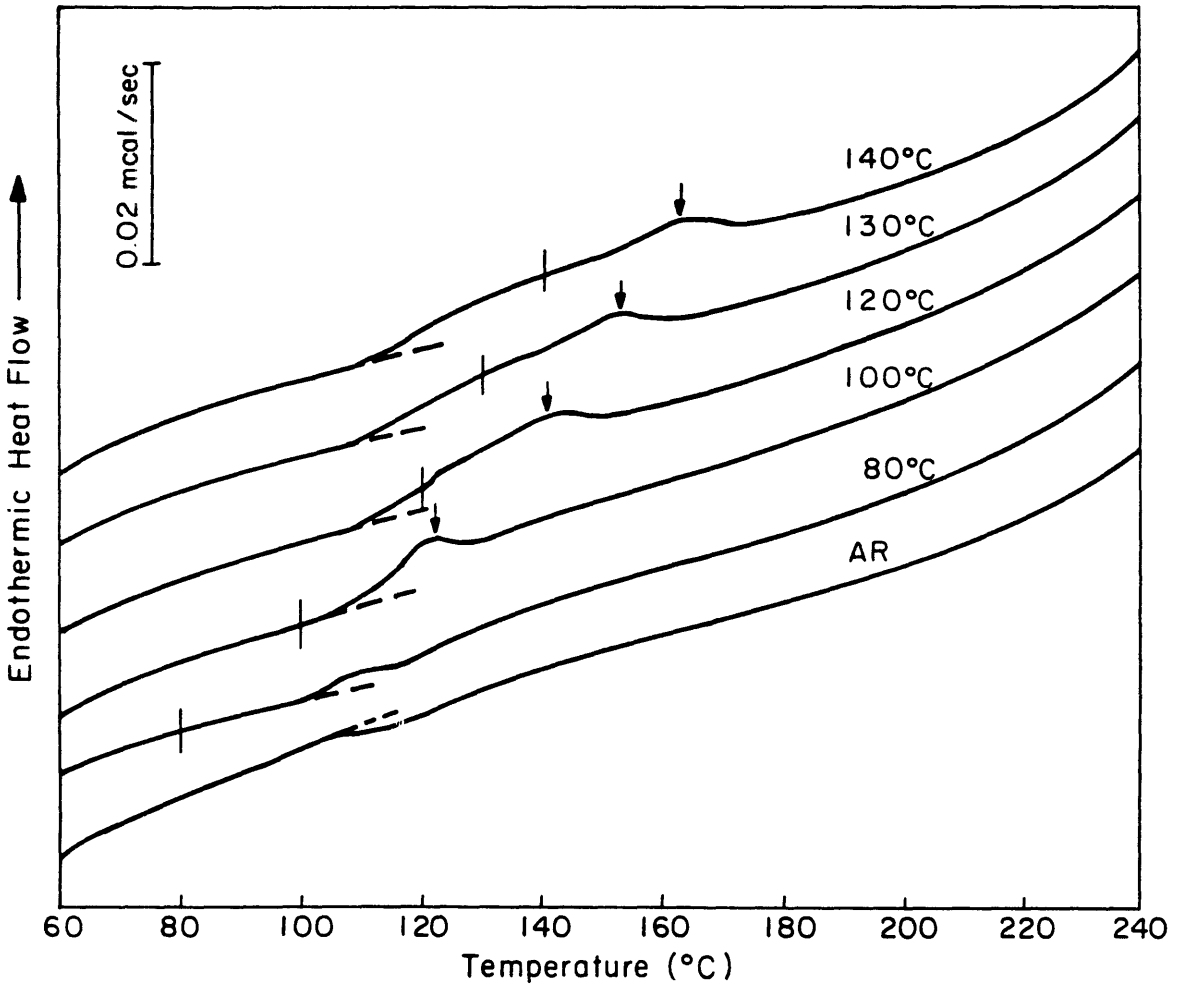

Figure 4.4 Composite plot of lower temperature regime of DSC scans for PPS AR films annealed at the temperatures represented by both the labeled temperatures and the bars on the curves. The intersection between the dashed line and the curve represents the glass transition temperatures. The arrow shows the observed small melting peak.

indicated by the bars on the curves, as well as the labeled temperatures. The intersections between the dashed lines and the curves show the starting temperatures of the glass transition relaxation. The observed small melting peaks are indicated by the arrows. For the AR sample, we only observe a very shallow exothermic peak just above 100°C. No T_g is found for this material. For the sample annealed at 80°C, which is below the T_g of amorphous PPS, we observe a very small step starting at around 95°C, followed by a very shallow exothermic peak around 110°C. This indicates that annealing at 80°C can somewhat relax the material as a physical aging, however, no crystals can form at this low temperature. As T_a increases, a small step and a small peak develop, as indicated by the arrows in Figure 4.4. As represented by the intersections between the dashed lines and the curves, the small step stays at almost a constant temperature. It comes from the glass transition relaxation and does not change significantly with T_a. It is interesting to note that this small step does not appear in AR film, which suggests that it may come from some relaxation of the amorphous phase that was originally rigid. In contrast, the small peak shifts its PMT to about (T_a+10°C) as T_a increases. In many polymers either cold crystallized from the glassy state or melt crystallized from the melt state, there exists an endothermic melting peak several degrees above T_a in addition to the dominant melting peak appearing at higher temperature [112-114]. The origin of the low temperature peak has been studied extensively [113,114] and is generally considered due to the melting of the crystal lamellae formed at T_a. Thus the results indicate that AR PPS has the ability to crystallize when the temperature is above T_g. To summarize, the DSC study shows that AR PPS film is able to relax some of its RAP fraction and recrystallize when annealed at a temperature above T_g. To

confirm this idea, we performed a TSDC study on PPS since this technique is very sensitive to amorphous phase relaxation.

4.3.3 Thermally Stimulated Depolarization Current Study

TSDC has been used quite widely in studying relaxation behavior of amorphous and semicrystalline polymers and their blends [69-81,97]. This technique probes the depolarization current of the oriented dipoles aligned under the electric field and frozen by the quenching process. It provides detailed information about relaxation of the amorphous phase. In the TSDC experiments, the films first need to be poled at T_p. We observe that poling the sample at T_p also anneals the sample. Since no difference was found in our DSC and WAXS study on samples annealed with or without the electric field, we assume that the electric field has no effect on the crystal structure of the samples except that it orients the dipoles of the amorphous phase. Therefore, the AR films were used directly in our TSDC study and the samples were annealed as well as poled at T_p.

We present in Figure 4.5 a composite plot of the TSDC spectra of AR PPS films poled at different temperatures (82°C, 94°C, 105°C, 116°C and 128°C). The arrows indicate the temperatures where the samples are annealed as well as poled. When the sample is annealed and poled at 82°C, a PMT at 95°C is observed. The peak is quite broad with a PH of 0.6pA. As T_p increases to 94°C, a much stronger depolarization current shows up with a PH of 2.2pA and PMT of 98°C. In both cases, the poling temperatures are lower than the PMTs. When the sample is poled at 105°C, PH reduces to 1.6pA and the PMT increases to 102°C. This peak also shows less symmetry compared with the previous two peaks and the peak full width at half maximum (FWHM)

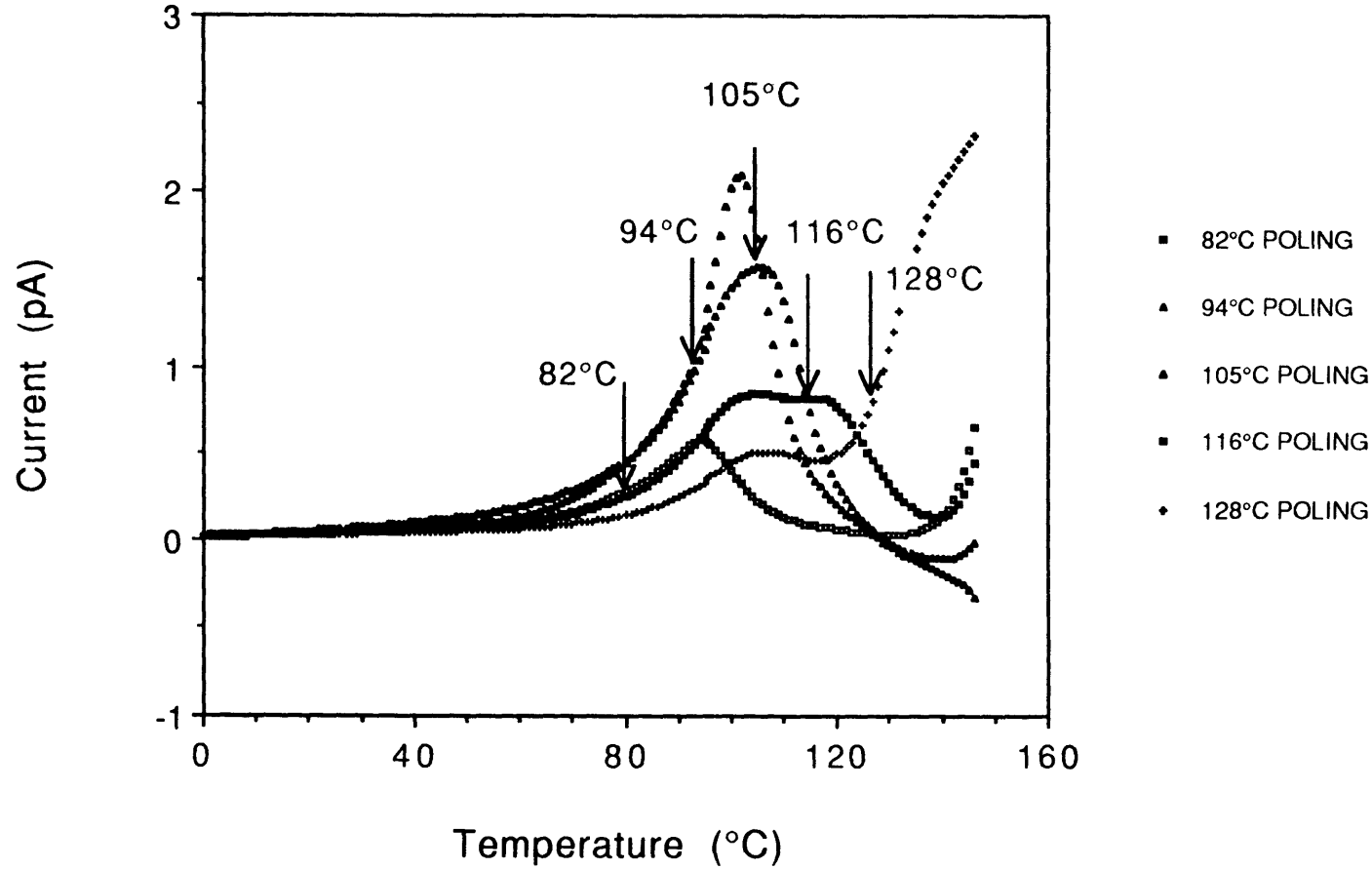

Figure 4.5 Composite plot of TSDC results of PPS AR films poled at the temperatures indicated.

covers a much broader temperature range. When the sample is poled at 116°C, we observe two peaks overlapping each other. One looks as though it has been reduced from the 105°C poled peak, with a PMT around 105°C and a PH around 0.85pA. The second is merged with the previous peak, and has an approximate PMT at about 120°C and PH of 0.8pA. Two current peaks appear again when the sample is poled at 128°C. This time the first peak current is further reduced to 0.4pA with the PMT about the same as the previous one. The second peak increases in both height and maximum position, and is hidden under a steeply-rising current. This steeply-rising current is observed for all the other samples. The origin of this peak is considered as a complex TSDC phenomenon and has been attributed to the increased conduction of the sample at high temperature [54,142].

When a polymer is poled at T_p, the electric field will orient those dipoles which are able to align themselves along the field. Therefore, as long as there exist amorphous dipoles that can be activated at a higher temperature, the higher the poling temperature, the more the dipoles will be activated, and the stronger the depolarization current will appear. At the same time, as we have mentioned earlier, the PPS sample is also annealed when it is poled inside the TSDC cell. Thus both the annealing effect and the poling temperature effect need to be considered when we interpret the data.

When the sample is poled at 82°C, which is about 10°C below the amorphous PPS T_g, not much amorphous phase is able to orient along the electric field direction. This sample shows a broad and small relaxation current peak with T_p quite far away from the PMT. As T_p increases to 94°C, more amorphous phase is able to be poled, and the TSDC spectrum shows

about four-times stronger relaxation peak height. However, T_p is still smaller than the PMT, which indicates not all the dipoles from the amorphous phase have been activated. When the poling temperature increases to 105°C, T_p is found to be slightly higher than the PMT. At the same time, the PH is reduced and the peak FWHM is broader. These observations suggest that the annealing increases the chain rigidity and the poling process is able to activate more dipoles. When T_p further increases to 116°C and 128°C, two peaks are observed. We consider the first peak to be due to the dipole relaxation as its PMT is around 105°C and does not change much with T_p. It is obvious that the PH, as well the area underneath the peak (PA), decreases with increasing T_p when the sample is poled above 105°C. As PA is directly proportional to the number of dipoles in the amorphous phase, the amount of amorphous phase may have decreased through the formation of crystals, as we have seen from DSC. At the same time, we have to keep in mind that the formation of the crystals also broadens the relaxation time distribution of the amorphous phase, which is suggested by the smaller, yet broader peak.

From the TSDC spectra, we observe the formation of a second peak when the sample is poled at 116°C and 128°C. The origin of this peak comes from the release of the charges formed at the crystal/amorphous interphase, the so called ρ-peak. This peak has been observed in many semicrystalline polymers [72,97]. The reason it was not observed during the low temperature poling may be due to the extremely rough and ambiguous interphase between the amorphous phase and crystalline phase. These rough interphases were formed during the fast cooling process when the PPS film was originally produced, and become less rough after annealing at higher temperature. To

confirm our idea, the following TSDC experiments have been performed on the quenched amorphous and cold-crystallized PPS films.

A TSDC experiment was performed on the quenched amorphous PPS film and the result is shown in Figure 4.6. The film sample is evaporated with Au and poled at 92°C, as indicated by the arrow shown in the Figure. A strong relaxation peak occurs at 82°C with a PH of 7pA. The shape of the peak is quite asymmetric showing common features which have been reported for amorphous polymers [53]. The peak is the result of dipole relaxation. The lower T_g observed here compared to that from DSC is due to the lower heating rate [72,97]. During the testing, the amorphous film begins to crystallize. As no crystals were originally in the polymer, no ρ-peak is observed at the higher temperature. The only feature seen at high temperature is the high-rising current.

We also studied PPS samples cold-crystallized at T_c = 120°C and 200°C. The same experimental conditions were adopted except that the samples were poled at 120°C since higher T_gs are expected for semicrystalline polymers. We present the results for T_c=200°C and 120°C in Figure 4.7a,b, respectively. Two peaks are observed for both samples besides the steeply-rising current. For T_c = 200°C, the first peak appears at 95°C, while for T_c = 120°C, the peak appears at 100°C. Our previous study [37,38,112,119] has shown that amorphous material is more constrained by crystals when the sample is crystallized at lower T_c because of the lower chain mobility. Thus, the relaxation peak shifts slightly to a higher temperature when T_c is lower. Both low temperature peaks have broad peak shape which is similar to those we observed in the AR samples. The difference in the peak shapes compared with that of the amorphous

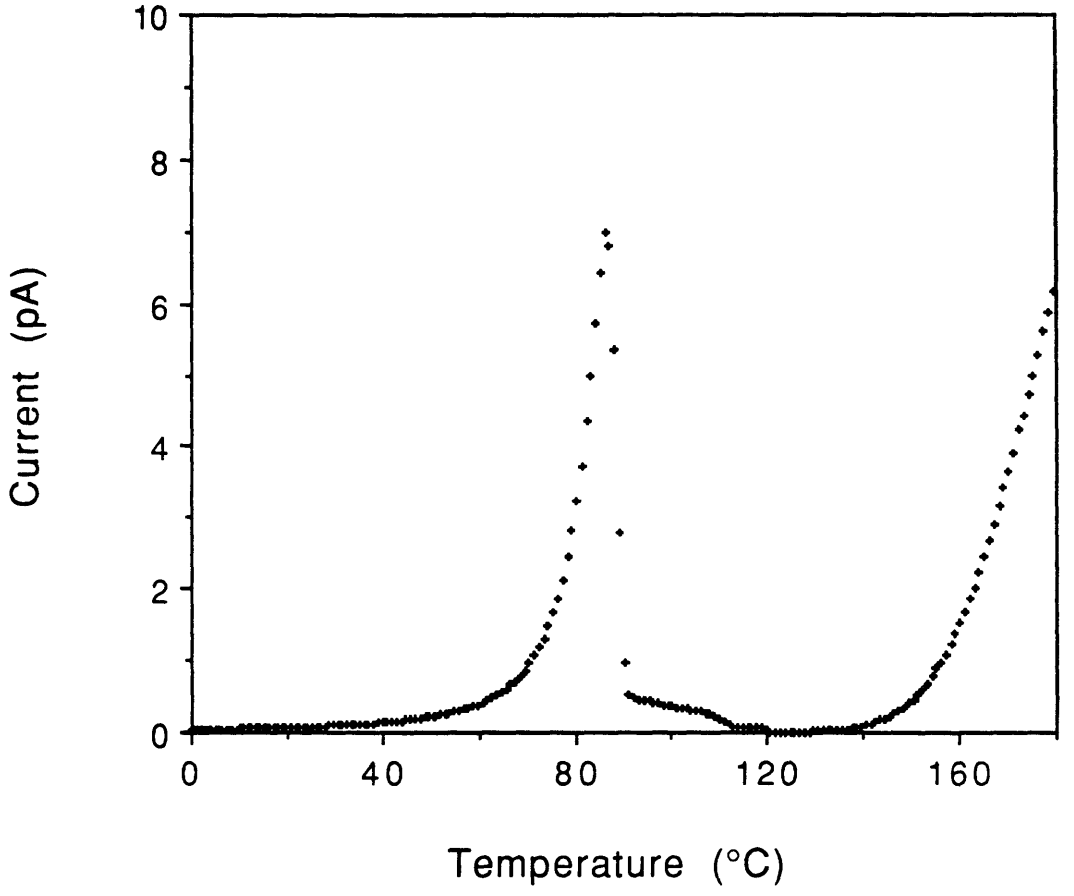

Figure 4.6 TSDC result of quenched amorphous PPS.

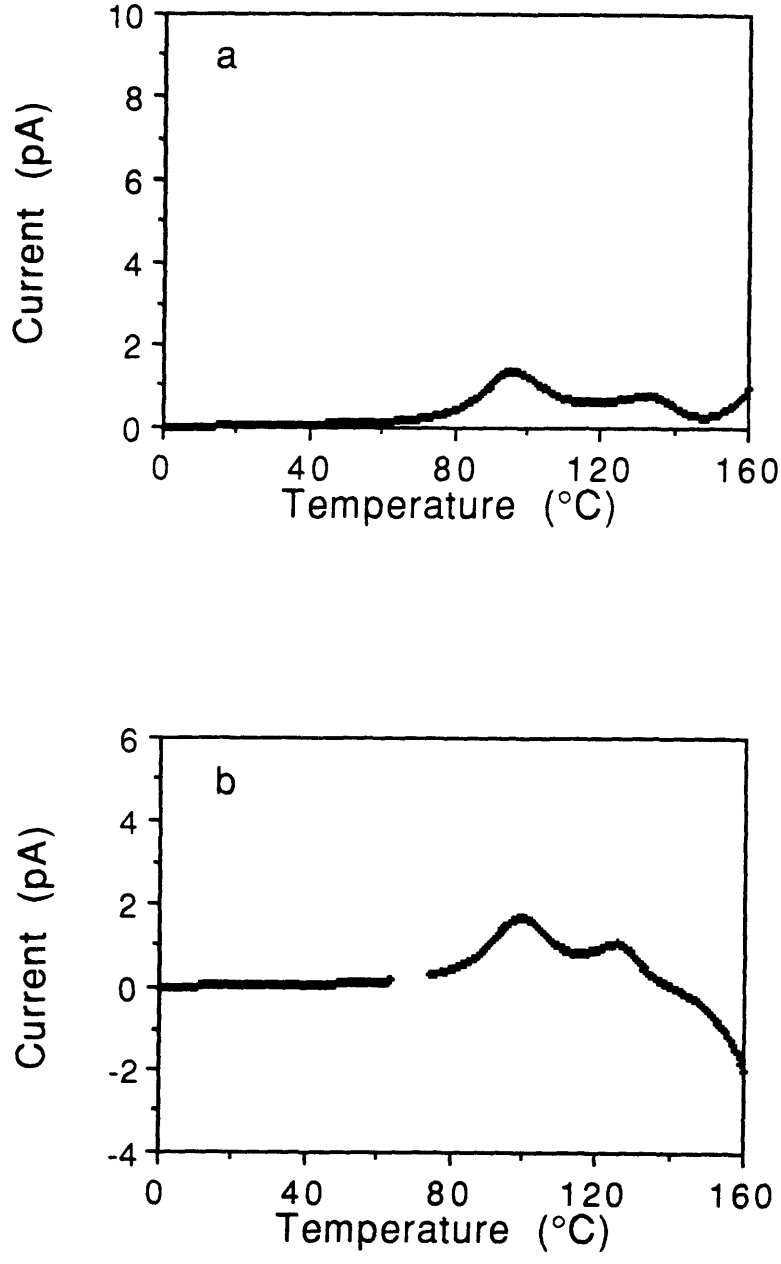

Figure 4.7 TSDC results of cold crystallized PPS: a) T_c = 200°C, and b) T_c = 120°C.

sample is due to the broad distribution of dipole relaxation times and the effects of the rigid amorphous phase. A distinct second peak, the ρ-peak, shows up in both samples with a PMT at about 134°C for T_c = 200°C, and 125°C for T_c = 120°C. The sample crystallized at lower T_c possesses a larger amount of RAP and a coarse interphase because of the higher chain rigidity [37,38,112,119]. The less perfect the interphase, the less strong will be the interfacial polarization. Therefore, charges will be released more easily at a higher temperature, resulting in a shift in the second peak to a lower temperature for lower T_c.

4.4 DISCUSSION

4.4.1 Special Relaxation Behavior of AR PPS Film

When PPS experiences isothermal melt crystallization, Chung and Cebe [113,114,120] have found that constraints on crystal growth gets severe after spherulitic crystal impingement, and only secondary crystals can form in the interlamellar region. The existence of the crystals previously formed almost makes it impossible to form new crystals at a temperature below the annealing temperature. In our case, AR PPS films are processed by general film processing method where the material is cooled quickly from the molten state. During this fast-cooling process, the films experience non-isothermal crystallization where the number density of nucleation sites increases and crystal growth rate decreases as temperature drops. This process puts quite severe constraints on the amorphous chains such that almost all the uncrystallizable material is rigid amorphous phase and can not relax when temperature reaches T_g. The crystals formed during this process show very small spherulites and poorly-defined interphases due to the short time given

for the crystals to grow [119]. Therefore, quite different relaxation behavior is observed in this material compared to that seen in the melt-crystallized PPS. Although the amorphous phase does not show any relaxation at T_g, it is able to crystallize at a higher temperature. The very shallow exothermic peaks we observed for AR film and the AR film annealed at T_a=80°C (Figure 4.4) come from the crystallization of these rigid amorphous materials. The quick crystallization process results in the formation of short range order in the amorphous phase. When the temperature is increased above T_g, the amorphous material gains mobility and crystallizes to form some small crystals. Since the crystal structure has already developed during the cooling process, the constraints on this amorphous phase are very high. Only a very small amount of amorphous material was able to form crystallites. Some rigid amorphous material is also able to relax as shown from DSC. In addition, previously formed imperfect crystals now have a chance to form better crystals and better crystal/amorphous interphases.

The study of mechanical properties of PPS was first reported as a function of crystallinity by Brady [108]. In his work, the author observed that an increase in polymer crystallinity was accompanied by a decrease in tensile strength. He suggested that this behavior came from the modest molecular weight effect and slightly crosslinked nature of the PPS. In this work, we have used DMA to investigate the effect of annealing on the mechanical properties of AR films. No significant difference is found in the modulus because of the small amount of crystallites formed. However, a clear increase in the relaxation PMT and a decrease in the PH are observed as a function of increasing treatment temperature, which suggest that less amorphous phase may experience more constraint. This implies that if somehow we can

anneal a fast-cooled polymer material above its T_g, a small amount of crystals will form which will both increase its relaxation temperature and improve its mechanical properties. As a matter of fact, commercial processing of PET bottles is carried out in a similar way [180]. In order to obtain the clarity of the amorphous material and the rigidity of the semicrystalline material, PET is first fast-cooled from the melt, and then re-annealed above its T_g. Therefore, small imperfect crystals will form which do not scatter too much light, yet provide excellent rigidity to handle the weight of the liquid.

4.4.2 TSDC ρ-peak and Interphase Roughness

TSDC has been used to study many semicrystalline polymers [72,97]. A common feature observed in TSDC spectra is the interphase relaxation peak right above the polymer glass transition peak. It has been proposed that this ρ-peak is due to the release of the injected space charges trapped at crystal/amorphous interphase during poling. It can be separated from the dipole relaxation by running the experiments at different electric fields. In this work, we hope to describe the unique feature of the ρ-peak and its possible correlation with the interphase roughness which has been suggested to be an important factor in determining the relaxation of liquid-like amorphous phase [119].

From the TSDC study, we have the following observations. First, no ρ-peak appears in the amorphous sample since no crystals exist during poling, therefore, there is no crystal/amorphous interphase. Sauer, et al. [72] observed a peak after the α-relaxation peak when they studied PEKK, and attributed it to the spontaneous reorientation of amorphous phase into crystallites. Second, a ρ-peak appears in the cold-crystallized PPS samples.

Third, it does not show up in AR sample and AR samples annealed at lower temperatures. However, when the AR samples were annealed at a higher temperature, it appears again. From these observations, we speculate that the ρ-peak is likely to appear in PPS samples that have been given sufficient time to stabilize their structure at a certain temperature, such as during isothermal annealing, and have formed better crystals and better interphases.

The correlation between the glass transition behavior and the interphase roughness of PPS has been reported by our group [119]. We suggest that the reason that the original AR film is unable to relax at T_g during DSC scanning may be because the crystal/amorphous interphase is irregular or rough. Since the ρ-peak has been considered to be the result of the released charge at the interphase, it is natural to think that this peak should provide us with detailed information about the interphase. For AR film and AR films annealed at the lower temperatures, little relaxation at T_g is observed. In the mean time, no ρ-peak is observed in these samples from TSDC indicating few charges, if any, build up at the interphase. On the other hand, for AR films annealed at the higher temperatures and cold crystallized PPS, DSC thermographs show observable heat capacity steps at T_g leaving the signature of the long range cooperative motion. At the same time, TSDC scans show strong ρ-peaks because of the release of the interphase charges. These observations support our idea that there exists a strong correlation between the interphase roughness and the ρ-peak.

Furthermore, the PMT of the ρ-peak also provides more information regarding the interphase roughness. PPS cold crystallized at a higher T_a contains less RAP and has better crystal/amorphous interphase. The better

interphase will hold charges at the interphase more strongly, and release them at a higher temperature. Therefore, we observed the PMT of the ρ-peak appears at a higher temperature when T_a is higher. For AR samples, no ρ-peak shows up because of the rough interphase formed during the cooling process. When AR samples are annealed at temperatures above T_g, the interphase gets more regular and the ρ-peak appears. As T_a increases, the ρ-peak shifts to a higher temperature.

4.5 CONCLUSIONS

Film processed Ryton^{TM} PPS films have been investigated using DSC, DMA, WAXS and TSDC. Unique relaxation properties are observed in this film. A small amount of crystals is able to form when the temperature is above T_g, while at the same time, some amorphous phase is able to relax. The annealing pushes the dynamic mechanical relaxation tanδ to a higher temperature, and reduces the amount of mobile chains.

Our TSDC results suggest the correlation between the interfacial relaxation peak, ρ-peak, and the interphase roughness. Crystallinity is a necessary, but not sufficient, condition for the observation of a ρ-peak. The ρ-peak shifts to a higher temperature when the sample is cold crystallized at a higher temperature with a better interphase. No ρ-peak is observed in the original AR film indicating very rough interphases form when the film is processed.

Chapter 5

Molecular Weight Effect on Crystallization, Structure and Properties of Cold Crystallized Poly(phenylene sulfide)

5.1 INTRODUCTION

Over the years, poly(phenylene sulfide) (PPS) has become an important engineering thermoplastic having wide range of applications for uses such as moulding resins, fibers and composites matrices. It is a semicrystalline polymer with a glass transition temperature (T_g) at 90°C, and a melting temperature (T_m) of 280°C from differential scanning calorimetry (DSC) [113,114]. Its structure and properties can vary quite significantly with previous thermal history [37,38,112-114,119] and molecular weight (M_w) [110,111]. Extensive research has been carried out on PPS and details about this polymer can be found in some excellent review articles [121-124].

Several research groups have studied the effect of molecular weight on the crystallization kinetics of PPS [110,111,116-118]. Generally, it is found that the crystallization rate of PPS decreases as M_w increases [110,116]. Asymmetric linear growth rate curves are observed for PPS in different groups [112,181]. Non-isothermal crystallization from the melt state has also been studied by Collins et al. [117,118].

While a lot of work has been concentrated on the melt state crystallization and crystallization with small undercooling, crystallization from the glassy state of amorphous polymers is also worth investigating

because certain engineering applications may require crystallization from the glassy amorphous state. It is also interesting to investigate the *real* cold crystallization of the material, as opposite to cold annealing. In the former, the sample is cold crystallized from the amorphous state at a temperature lower than the temperature of the maximum crystallization rate. In the latter case, the amorphous sample has already experienced crystallization during heating, and is then annealed at the treatment temperature.

In this work, we will explore the M_w effect on the crystallization and structure of cold crystallized PPS using small angle X-ray scattering (SAXS). DSC and wide angle X-ray scattering will also be used to study the constitutive phases in these materials. More importantly, we will investigate the M_w effect on the mechanical properties of PPS using a combination of DMA and Modulated DSC.

5.2 EXPERIMENTAL SECTION

Three kinds of PPS powder, Fortron^{TM}, from Hoechst Celanese have been used in this investigation and are referred to as F-200, F-214 and F-300. Their intrinsic viscosity, molecular weight (M_w) and chain linearity are summarized in Table 5.1. These PPS powders were first dried inside a desiccator for several days at room temperature. Amorphous films were prepared by first melting the powder in between two pieces of Kapton^{TM} film at 320°C for 2min to destroy the crystallization seeds, then quickly quenching into ice water. The amorphous samples obtained were transparent and showed no birefringence under crossed polarizers. Some of these amorphous samples were used directly in our study. Others were cold crystallized at

Table 5.1 Information† about different M_w Fortron™ PPS used in this study

Fortron™	Intrinsic Viscosity* [η] g/dl	Viscosity Average Molecular Weight# M_v	Chain Linearity
F-200	0.20	30,000	Linear
F-214	0.29	50,000	Linear
F-300	0.45	91,000	Linear

† Provided by Dr. George Collins, Hoechst Celanese.

* Intrinsic viscosities were measured in 1-chloronaphthalene at 208°C.

\# The viscosity average molecular weights M_v were calculated using:

$M_v = (1.122 \times 10^4 \times [\eta])^{1.339}$

different cold crystallization temperatures T_c until the completion of the crystallization.

A differential scanning calorimeter, DSC, Perkin Elmer DSC-7 has been utilized to study the isothermal crystallization kinetics of all the powders. The sample was first loaded into the DSC cell at 60°C, then heated at 20°C/min to T_c. The exothermic crystallization data were then recorded until the completion of the crystallization. The curves were digitized into a PC and analyzed to obtain the crystallization kinetic parameters. Another DSC-4, also from Perkin Elmer, has been used to study the crystallization and melting behavior of PPS. Indium was used to calibrate temperature and heat flow throughout the DSC study. Sample weight was around 8mg and a scan rate of 20°C/min was used.

WAXS experiments on both amorphous and semicrystalline samples were performed at room temperature in reflection mode using a Rigaku RU-300 X-ray diffractometer with a diffracted beam graphite monochromator. The normal operating condition was 50keV and 200mA with Cu-K_α radiation (λ = 1.54Å). The scattering angle 2θ ranged from 5° to 55° with a step scan interval of 0.02 degree and a scan rate of 1°/min.

SAXS experiments were performed at Brookhaven National Synchrotron Light Source using a high intensity X-radiation source in transmission mode. The wavelength was 1.487Å and sample-to-detector distance was about 1.46m calibrated using cholesteral meristate.

Dynamic mechanical analysis were carried out on a Seiko DMS 200 system. The samples were cut into a 5mm x 10mm rectangular shape with a thickness of 0.6 - 1.0 mm. The scans were performed from 30°C to ~ 240°C at a heating rate of 2°C/min and the data were measured at frequencies of 1, 2, 5, 10 and 20 Hz. All the experiments were carried out under nitrogen gas flow of 300ml/min.

In order to understand the changes in the different phases of the cold crystallized samples as the result of slow heating from DMA studies, we performed Modulated DSC experiments using the same heating rate of 2°C/min. A modulation amplitude of 0.318°C and a modulation frequency of 60sec were used to ensure that no cooling occurred during the experiments. Average sample weight was 8mg.

5.3 RESULTS AND DISCUSSION

5.3.1 Crystallization Kinetics of PPS

Cold crystallization kinetics of different M_w PPS samples have been characterized using isothermal DSC. The data obtained were first fit using the Avrami equation:

$$\chi_c(t)/\chi_{c\infty} = 1 - \exp(-kt^n) \qquad (5.1)$$

where $\chi_c(t)$ is the crystallinity at time t and $\chi_{c\infty}$ is the crystallinity when t reaches ∞. The left hand side of Eqn. 5.1 represents the relative crystallinity. The equation can also be transformed as:

$$\ln(-\ln(1-\chi_c(t)/\chi_{c\infty})) = \ln k + n\ln t \quad (5.2)$$

where the left hand side of the equation should be a linear function of lnt. After fitting the data using Eqn. 5.2, Avrami parameters k and n were obtained. We then used k and n to calculate the crystallization half time $t_{1/2}$:

$$t_{1/2} = \ln 2/(k)^{1/n} \quad (5.3)$$

Here $t_{1/2}$ reflects the time when half of the crystals have formed in the sample. We plot in Figure 5.1 $t_{1/2}$ vs. temperature of the three different M_w samples.

Similar to what many researchers have found in PPS [110,111,116-118], we observe an increase in $t_{1/2}$ with increasing M_w, which indicates a slower crystallization kinetics for the higher M_w sample. From the classical theory of crystallization from the melt [1-4], the crystal growth rate can be expressed as follows:

$$\ln(G) = \ln(G_0) - \{U^*/R(T_c-T_\infty)\} - \{K_g/T_c(\Delta T)f\} \quad (5.4)$$

where

$$K_g = nb_0\sigma\sigma_e T_m^0/(\Delta H_f)k \quad (5.5)$$

$$f = 2T_c/(T_m^0 + T_c) \quad (5.6)$$

Here G is the linear crystal growth rate, G_0 is the prefactor, U^* is the activation energy for chain motion, $T_\infty = T_g - 30$, n is a constant of either 4 (Regime I or

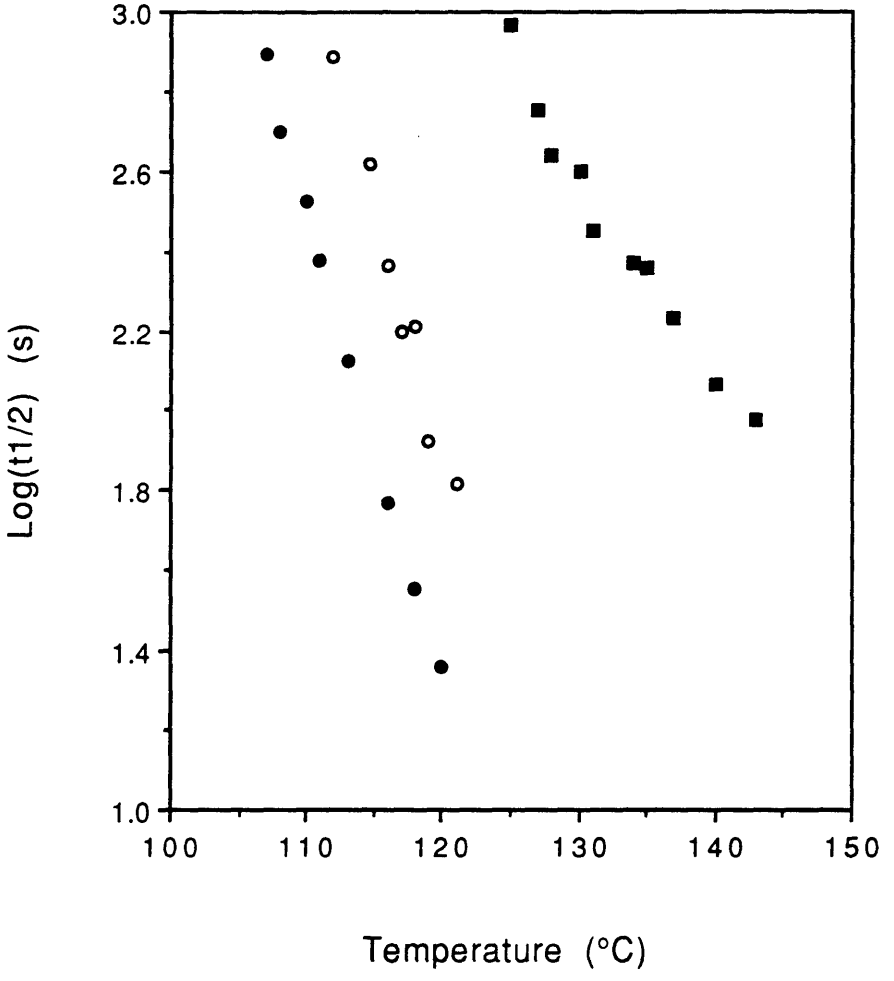

Figure 5.1 Crystallization kinetics of different M_w Fortron™ PPS from isothermal DSC: $t_{1/2}$ vs. temperature.
F-200 (●), F-214 (O), and F-300 (■).

III) or 2 (Regime II), b_0 is the molecular thickness in the growth direction, σ is the side surface free energy, σ_e is the fold surface free energy, T_m^0 is the infinite crystal melting temperature, ΔH_f is the heat of fusion of 100% crystals and k is Boltzmann's constant. When the polymer experiences small undercooling, i.e. ΔT is small, the term describing nucleation, $K_g/T_c(\Delta T)f$, is dominant. When the polymer experiences large undercooling, i.e. ΔT is large, the chain transport term, $U^*/R(T_c-T_\infty)$, will be the dominant part.

Several attempts have been made to introduce a molecular weight dependence into Eqn. 5.4 by either incorporating the M_w into the third term of Eqn. 5.4 [182,183], or by adding a new term into the right hand side of the equation [184,185]. Some empirical functions [186] have also been proposed to fit the M_w dependent growth rate data. A recent work by Lopez and Wilkes [110] on the M_w effect on the crystallization of PPS supported the logarithmic function suggested by Cheng and Wunderlich [187] when they fit their crystal growth rate data of poly(ethylene oxide) using:

$$\ln(G) = b \ln\langle M_n \rangle + a \tag{5.7}$$

Here a and b are constants and M_n is the number average molecular weight.

In this work, we want to explore the temperature region close to the polymer's T_g which represents a large degree of undercooling. Therefore, we expect no energy barrier for nucleation. The crystallization should be dominated totally by the ability of the chain transportation. Here, we choose the crystallization temperatures that give different M_w PPS the same ln(G). The cold crystallization temperatures obtained from Figure 5.1 for different

M_w samples with a $t_{1/2}$ = 200s and $t_{1/2}$ = 700s are summarized in Table 5.2. Later, we crystallize the amorphous PPS at these temperatures (T_c) to ensure that they all have the same crystallization kinetics.

5.3.2 Isothermal Crystallization Study Using SAXS

Real time SAXS has been utilized to study the isothermal cold crystallization of different M_w PPS. Amorphous sample was first loaded into a Mettler hot stage equilibrated at 60°C, then heated to T_c at 20°C/min. The computer started recording data as soon as the temperature got to T_c. The data collection time for one slice is 20 seconds for $t_{1/2}$ = 200s, and 60 seconds for $t_{1/2}$ = 700s. We plot the first ten slices of the data, the Lorentz corrected intensity $I_{corr}s^2$ vs. s, in Figure 5.2 for F-200 (a), F-214 (b) and F-300 (c) with a $t_{1/2}$ = 200s, and in Figure 5.3 for F-200 (a), F-214 (b) and F-300 (c) with a $t_{1/2}$ = 700s. Here I_{corr} is the intensity after background subtraction and thermal density fluctuation correction, and s is the scattering vector ($s = 2\sin\theta/\lambda$), and θ is the half scattering angle. The development of the scattering peak as a function of time is observed in all the cases.

In Figure 5.4 and Figure 5.5, we present the SAXS data obtained using the correlation function for $t_{1/2}$ = 200s and $t_{1/2}$ = 700s, respectively. Long period (curve a), lamellar thickness (curve b) and linear crystallinity (curve c) are plotted as a function of isothermal crystallization time. The arrows indicate the crystallization half time, $t_{1/2}$. The following observations are obtained after analyzing the data. First, from both Figures, we find that the structure develops very quickly for linear PPS. All the parameters reach steady values at a time about 1/3 of $t_{1/2}$. Second, we observe that L increases with M_w when the crystallization time is long enough. For the same material

Table 5.2 Cold crystallization temperatures (±0.5°C) for different M_w PPS with $t_{1/2}$=200s and $t_{1/2}$ = 700s

	F-200	F-214	F-300
$t_{1/2}$ = 200 s	110.6°C	116.0°C	135.0°C
$t_{1/2}$ = 700 s	107.0°C	112.0°C	125.0°C

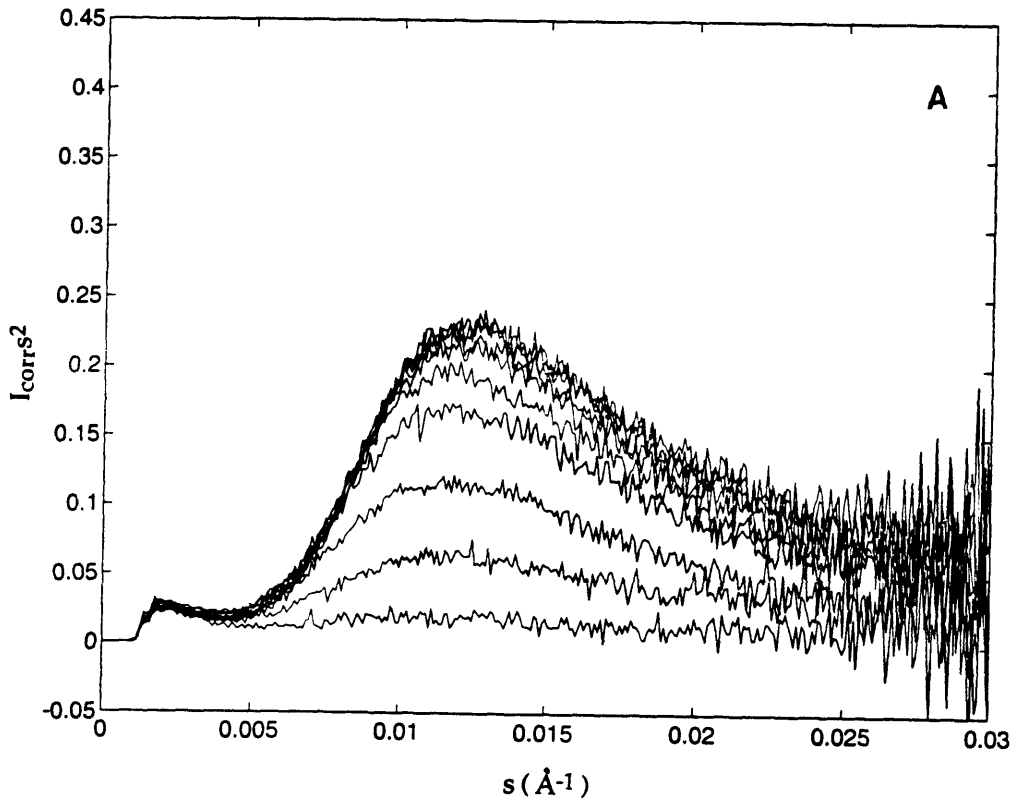

Figure 5.2 Lorentz-corrected SAXS intensity vs. scattering vector, s, for: a) F-200, b) F-214, and c) F-300 cold crystallized with $t_{1/2}$ = 200s. 20 seconds separate each adjacent curve.

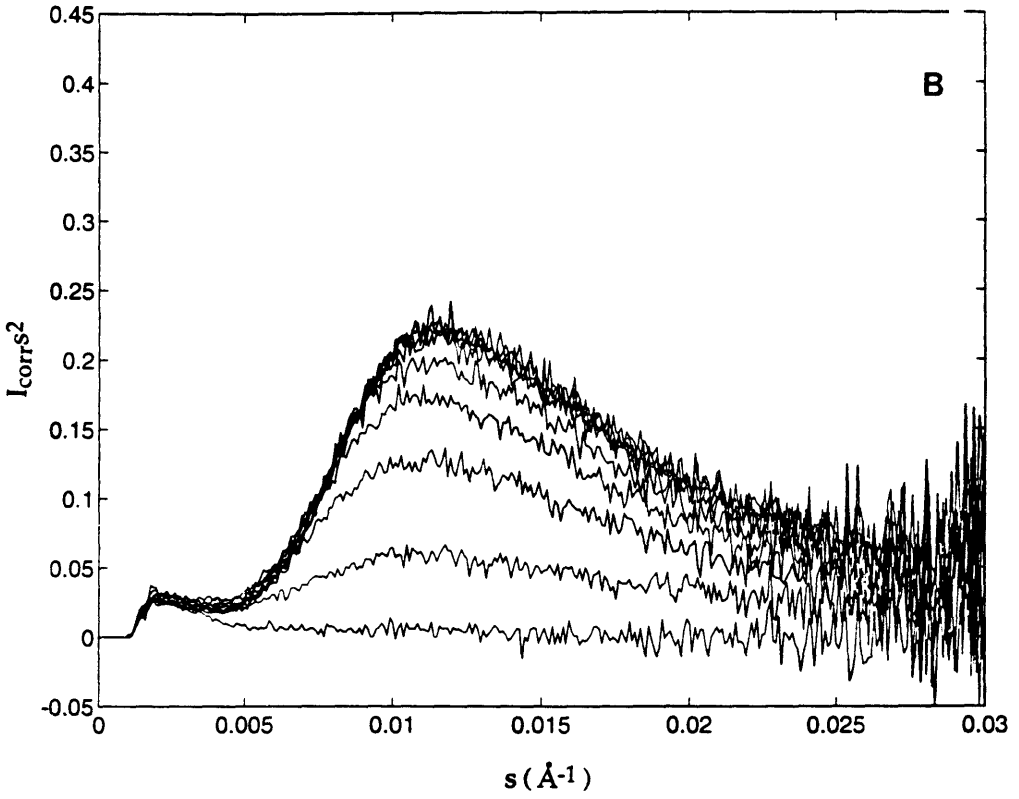

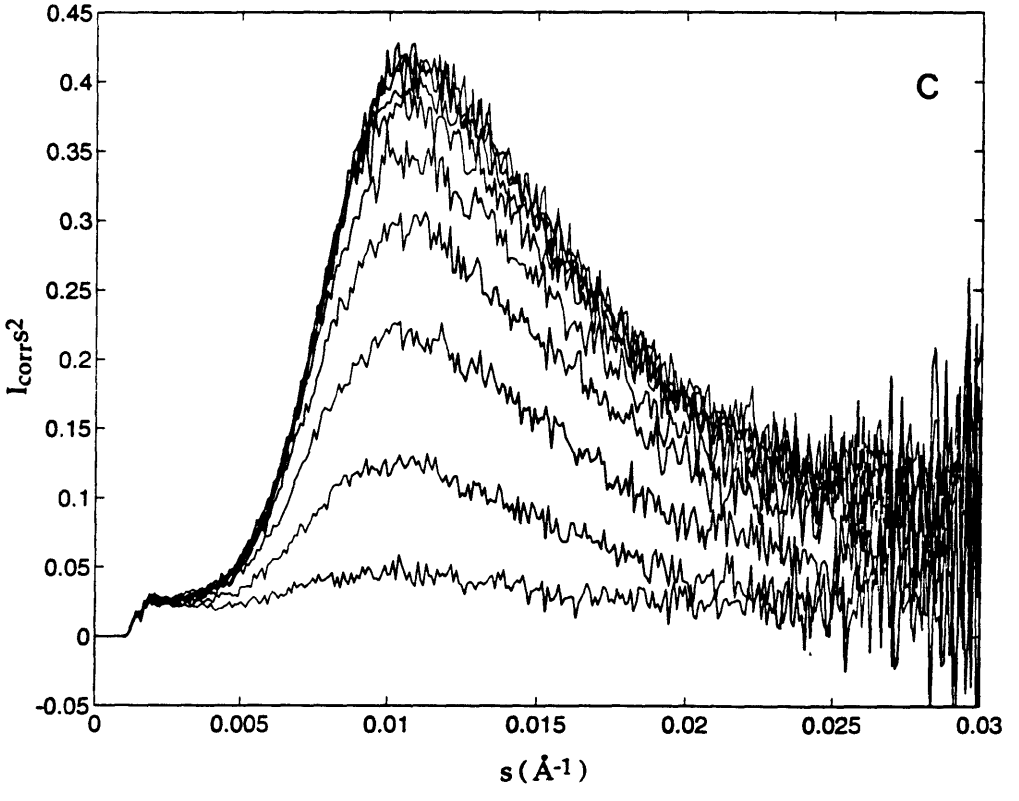

Figure 5.2, Continued

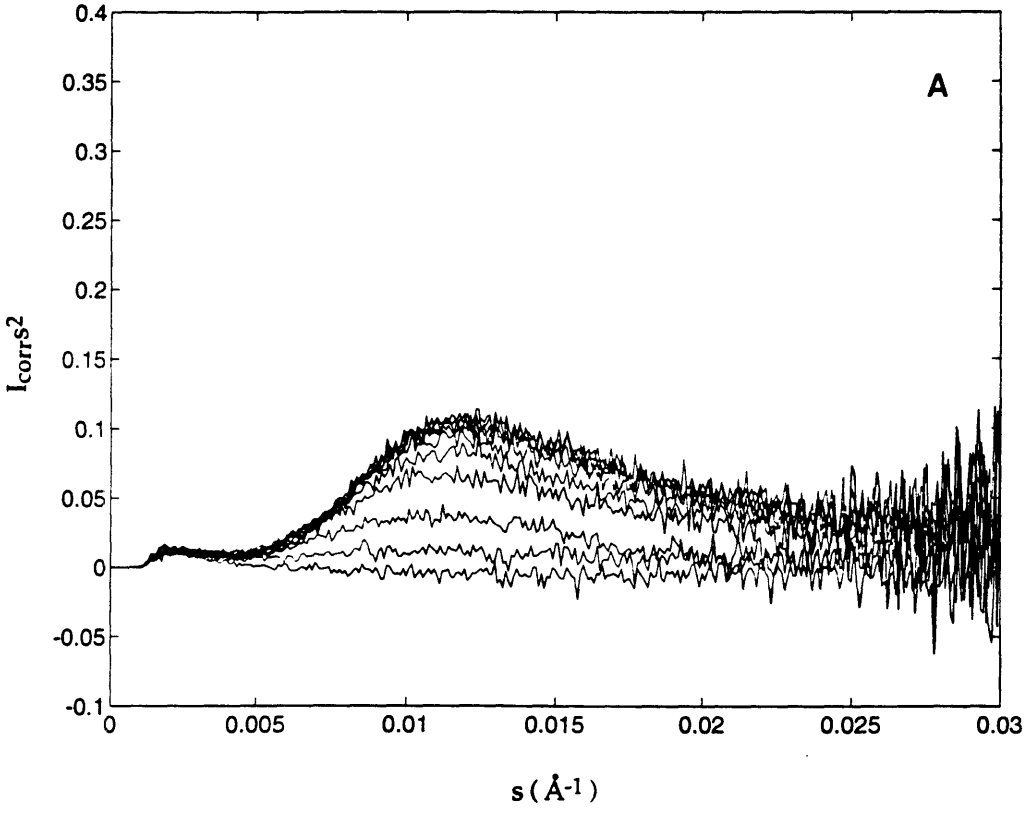

Figure 5.3 Lorentz-corrected SAXS intensity vs. scattering vector, s, for: a) F-200, b) F-214, and c) F-300 cold crystallized with $t_{1/2}$ = 700s. 60 seconds separate each adjacent curve.

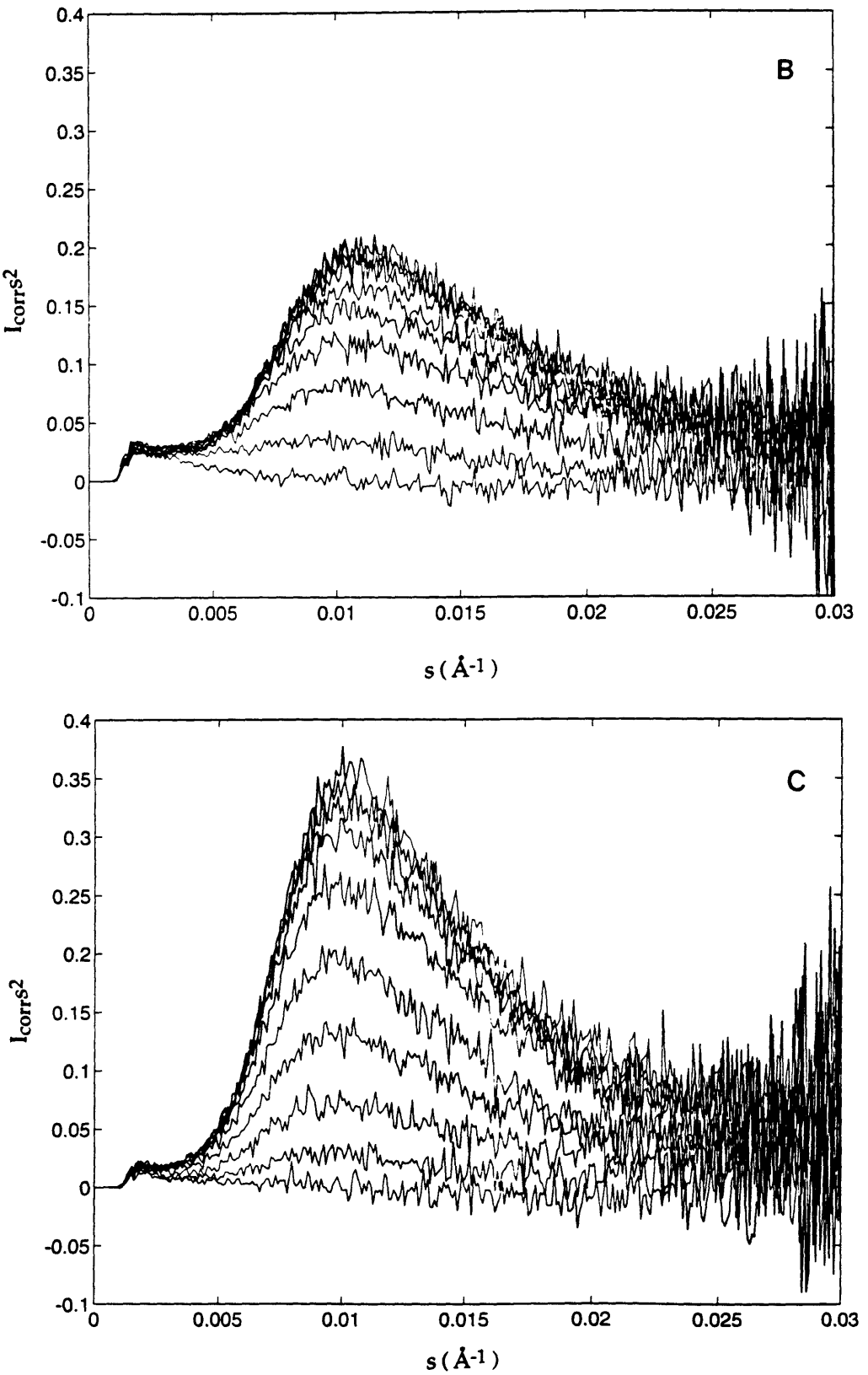

Figure 5.3, Continued

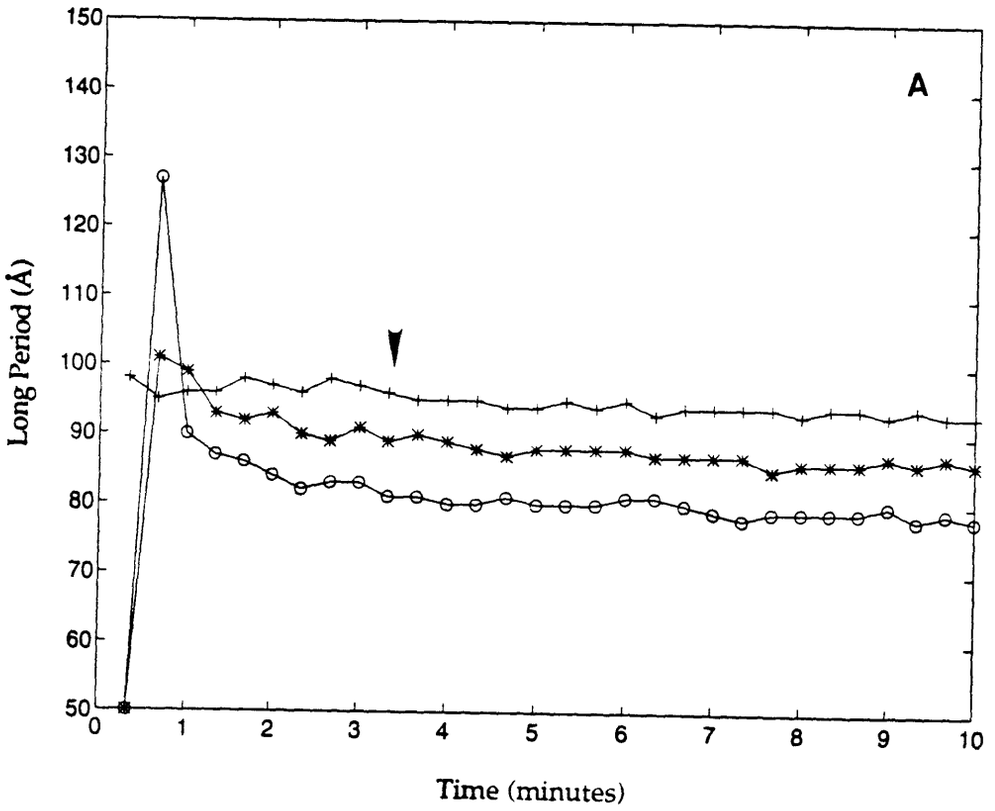

Figure 5.4 SAXS parameters as a function of crystallization time for: F-200 (o), F-214 (*) and F-300 (+) cold crystallized with $t_{1/2}$ = 200s. a) long period L, b) lamellar thickness l_c, c) linear crystallinity χ_c. The arrows indicate the time at $t_{1/2}$.

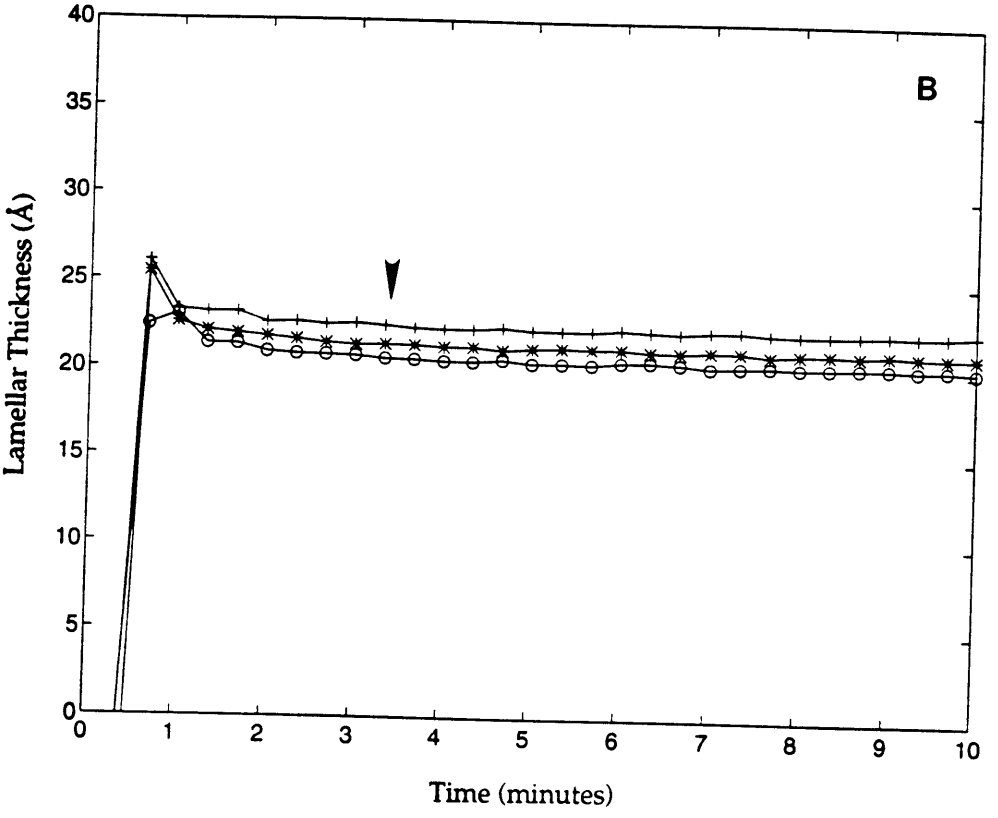

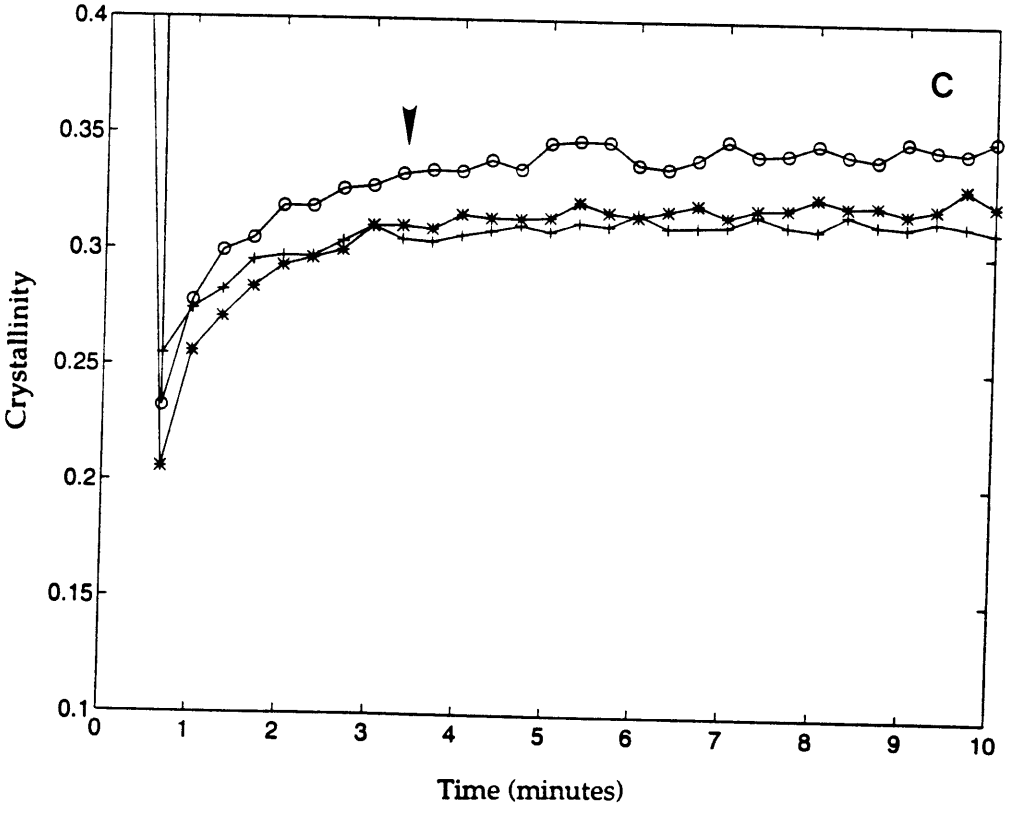

Figure 5.4, Continued

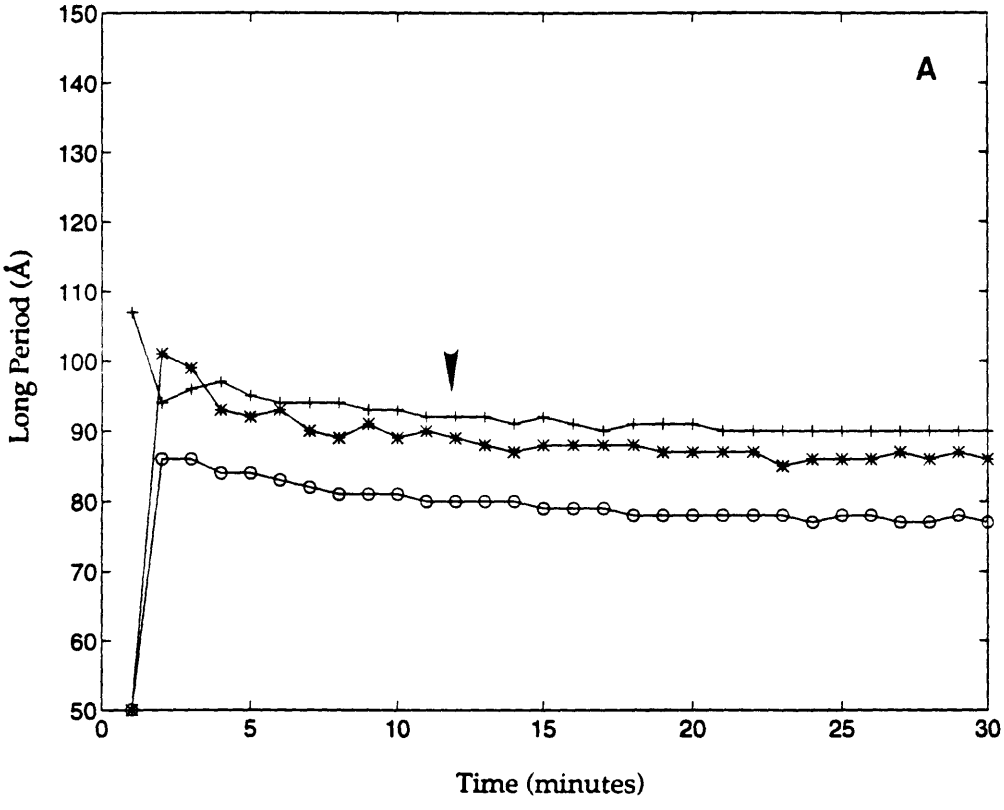

Figure 5.5 SAXS parameters as a function of crystallization time for: F-200 (o), F-214 (*) and F-300 (+) cold crystallized with $t_{1/2}$ = 700s. a) long period L, b) lamellar thickness l_c, c) linear crystallinity χ_c. The arrows indicate the time at $t_{1/2}$.

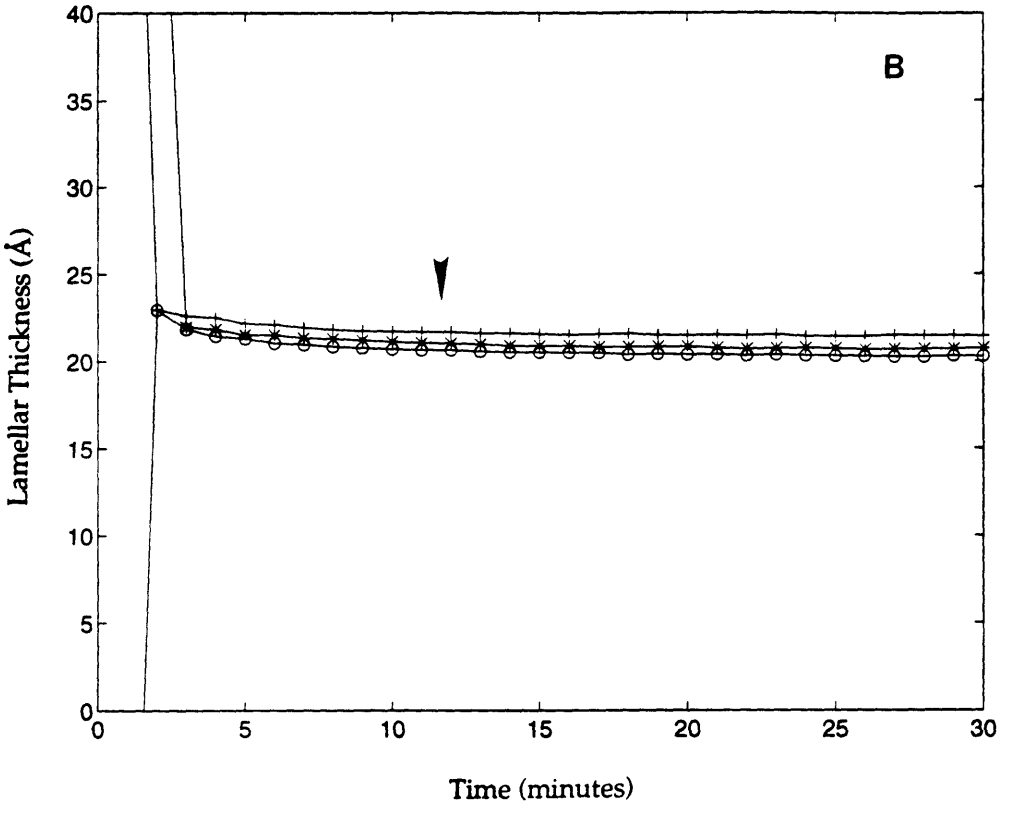

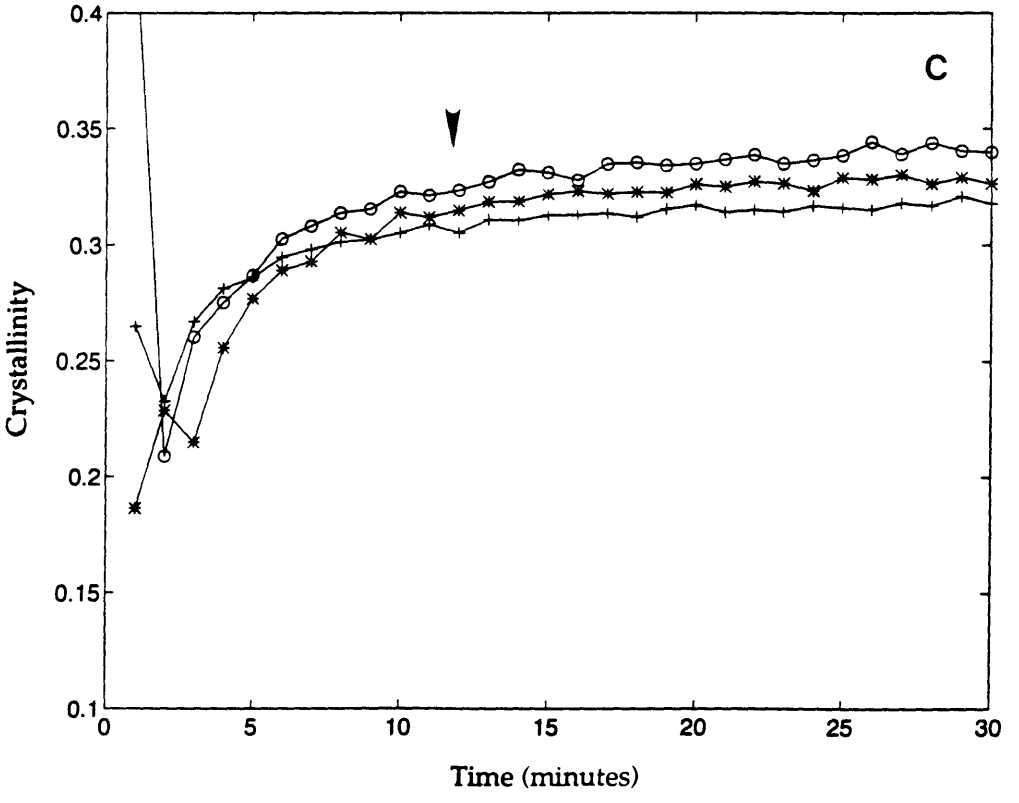

Figure 5.5, Continued

crystallized at different $t_{1/2}$, slightly larger L is observed for higher T_c. A similar trend is observed in l_c, except that within experimental errors, the difference in l_c is minimal. If we adopt a two phase model and consider that lamellar stacks contain alternating crystal phase (l_c) and amorphous phase (l_a), as Eqn. 2.3, we know that there is slightly more amorphous phase in the higher M_w sample within the lamellar stacks. This may be due to the difference in the linear crystallinity. As we have found in Figure 5.4c and Figure 5.5c, lower M_w material has a slightly higher χ_c compared with higher M_w material. However, the experimental errors are large enough to cover the systematic changes observed in crystallinity.

5.3.3 Thermal Properties of PPS

After the samples had been crystallized inside the hot stage for a time equal to six times $t_{1/2}$, they were air-quenched to room temperature for further analysis to determine the constituting components. DSC was used to determine the amount of liquid-like amorphous phase from the heat capacity step at T_g, and WAXS was used to determine the crystallinities of the samples by subtracting the amorphous halo from the WAXS pattern of purely amorphous samples. The results are listed in Table 5.3. For the same M_w material, higher χ_a is observed for the sample crystallized with a faster crystallization rate, i.e. at a higher T_c. For PPS crystallized with the same $t_{1/2}$, the higher M_w sample contains a larger amount of liquid-like amorphous phase.

We observe that all the PPS samples have a weight average crystallinity of 25-28% from DSC, which is 23-26% volume crystallinity after being transformed using the usual equation which was derived in Chapter 2, Eqn.

Table 5.3 Summary of χ_a, χ_c and χ_{rap} in semicrystalline PPS samples a) $t_{1/2}$ = 200s, b) $t_{1/2}$ = 700s

a) $t_{1/2}$ = 200s	χ_a (±1) (%)	χ_c (±2) (%)	χ_{rap} (±2) (%)
F-200	19	27	54
F-214	23	28	49
F-300	29	28	43

b) $t_{1/2}$ = 700s	χ_a (±1) (%)	χ_c (±2) (%)	χ_{rap} (±2) (%)
F-200	--	26	--
F-214	20	25	55
F-300	24	26	50

-- The value was unable to be determined from DSC.

2.4. The crystallinity is lower than what we obtained from the SAXS correlation function. This may because some portion of the amorphous phase resides outside the lamellar stacks resulting in a relatively higher crystallinity inside the lamellar stacks.

The sum of χ_c and χ_a is much smaller than 1. We therefore adopt a three phase model, and include the rigid amorphous phase, χ_{rap}, as expressed in Eqn. 1.1. χ_{rap} values are calculated and are listed in Table 5.3. The data indicate that there exists a large amount of RAP inside the cold crystallized PPS. For different M_w samples with the same crystallization rate, the lower M_w sample contains more RAP. For the same M_w material, there is more RAP when the sample is crystallized at a slower crystallization rate. In our previous cold crystallization study on Ryton^{TM} PPS [38], χ_{rap} decreased from 0.42 to 0.33 when T_c increased from 150°C to 210°C. Thus current results agree well with our previous study. It suggests that a large amount of RAP can form when T_c gets close to T_g. The results are also consistent with our later discovery about the correlation between RAP and the amorphous phase. RAP is just a part of the amorphous phase that is constrained by the crystals. The higher the crystallization temperature, the higher the amorphous chain mobility, and the less the fraction of RAP.

5.3.4 Mechanical Properties of Different M_w PPS

In order to explore the correlation between M_w and the mechanical properties of these cold crystallized samples, we have performed DMA experiments on both the highest M_w sample F-300 and the lowest M_w sample F-200. In Figure 5.6, we present the DMA data of F-300 with a crystallization rate of $t_{1/2}$=700s. Curves a and b represent the modulus E' and loss factor

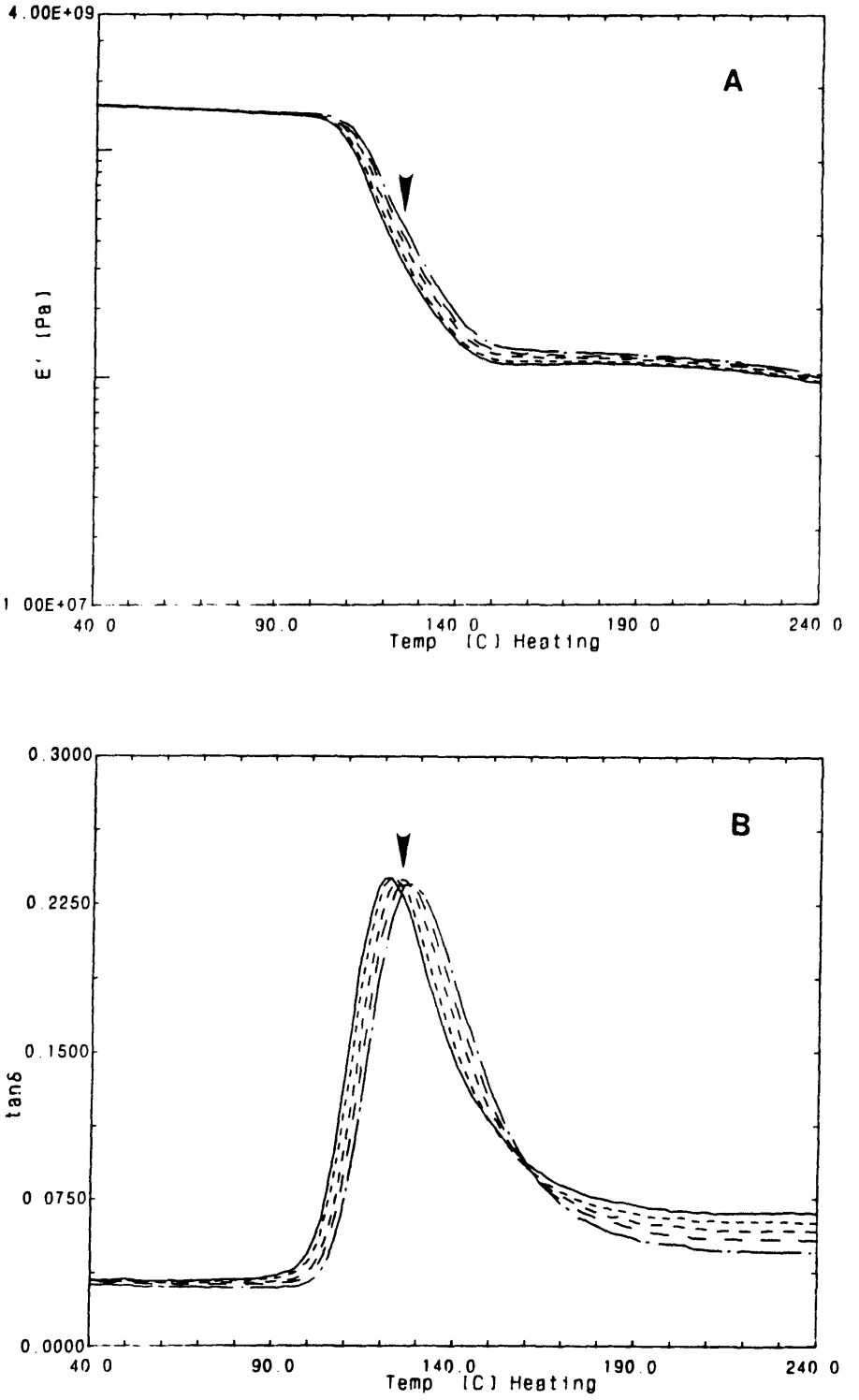

Figure 5.6 DMA results of F-300 cold crystallized with $t_{1/2}$ = 700s measured at 1Hz(——), 2Hz(- - - -), 5Hz(- - -), 10Hz(— —), and 20Hz(- · - · -). a) modulus E', b) loss factor tanδ. The arrows indicate T_c.

tanδ, respectively, changing as a function of temperature. The arrows indicate the crystallization temperature T_c. We observe in Figure 5.6a that the modulus shows quite a flat region with E' of 1.5GPa at the lower temperature (glassy region). As temperature reaches 100°C, the material starts to soften resulting in a drop in E'. E' continues to drop about one order of magnitude, then flattens at 140°C with E' around 0.13GPa. In Figure 5.6b, a strong asymmetric relaxation tanδ loss peak is observed. The peak maximum temperature for 1Hz is around 120°C, and the peak height is about 0.24. We observe no appreciable changes in either E' or tanδ for F-300 crystallized at other cold crystallization temperatures.

DMA experiments have also been performed on the F-200 samples. Similar to what has been observed for F-300, we found no discernable difference in E' or tanδ between $t_{1/2}$=200s and $t_{1/2}$=700s samples. Therefore, we only plot the DMA data in Figure 5.7 for F-200 with $t_{1/2}$=700s. The arrows indicate the temperature at which the sample was crystallized. In curve a, we find E' remains a constant value, 1.5GPa, before 100°C, then drops off as temperature increases, and reaches a rubbery plateau after the temperature is above 130°C. When the temperature is low, F-200 has the same E' as that of F-300. However, when the temperature is high, F-200 has a slightly higher E' of 0.23GPa. In curve b, we find the relaxation peak tanδ shows a similar shape as in F-300 sample with a peak maximum temperature of 120°C. The peak height is about 0.26, which is slightly higher than that from F-300.

It is generally considered that higher M_w material has better mechanical properties because of higher density of chain entanglements [1-4,188]. However, we were first surprised to find out that a lower E' was

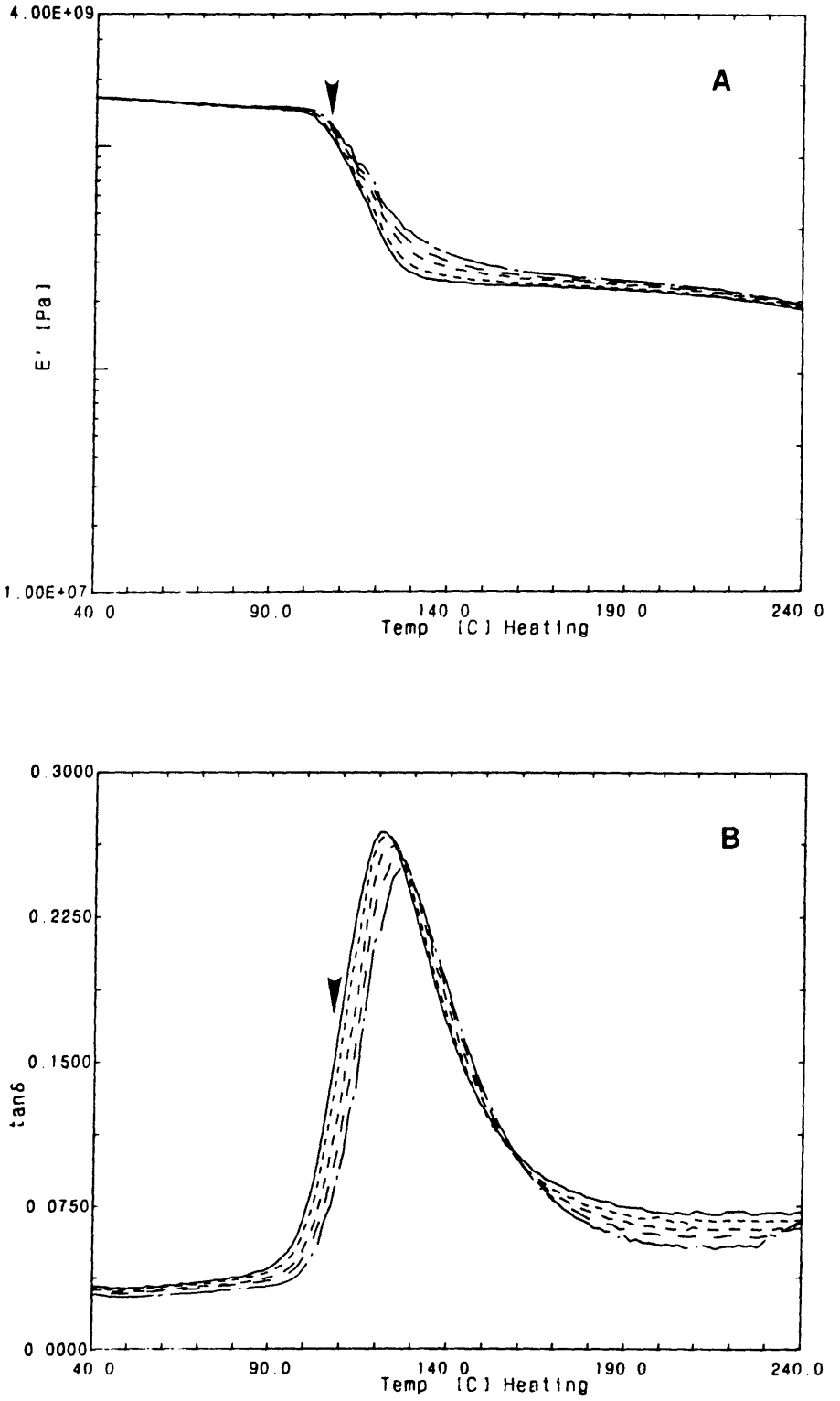

Figure 5.7 DMA results of F-200 cold crystallized with $t_{1/2}$ = 700s measured at 1Hz(——), 2Hz(- - - -), 5Hz(- - -), 10Hz(— —), and 20Hz(— · —). a) modulus E', b) loss factor tanδ. The arrows indicate T_c.

observed for F-300 at the higher temperature. Of course, we also noticed that the temperature has already increased above the cold crystallization temperature T_c (represented by the arrows shown in both Figures). When the temperature is above the crystallization temperature, we know that there must be a change in polymer structure. Therefore, we postulate that changes inside the samples when $T > T_c$ must result in the lower E' observed in the higher M_w F-300. To confirm our idea, we performed a Modulated DSC study on these two samples.

5.3.5 Modulated DSC Study

In order to understand the mechanical properties of F-200 and F-300 at temperatures above T_c, we have employed an advanced technique, Modulated DSC, to help us understand the structure change inside the samples. MDSC is able to separate the total heat flow (T) into two parts: one is the result of the heat capacity effect, such as glass transition and melting, often referred to as reversing heat flow (R); the other is the result of the non-heat capacity effect, such as cold crystallization, often referred to as non-reversing heat flow (NR) [85]. In this study, the same heating rate is used as in the DMA experiments for direct comparison. We plot in Figure 5.8 the raw MDSC data of F-300 cold crystallized with $t_{1/2}$=700s. The upper curve is the modulated heat flow, and the lower curve is the simultaneous heating rate obtained from the derivative of the temperature. The heating rate is above zero at all times, therefore no cooling was applied during the scan. The three heat flow curves can be obtained from the raw data, and the results are plotted in Figure 5.9a,b for F-300 and F-200, respectively. The arrows again indicate the temperatures at which the samples have been cold crystallized.

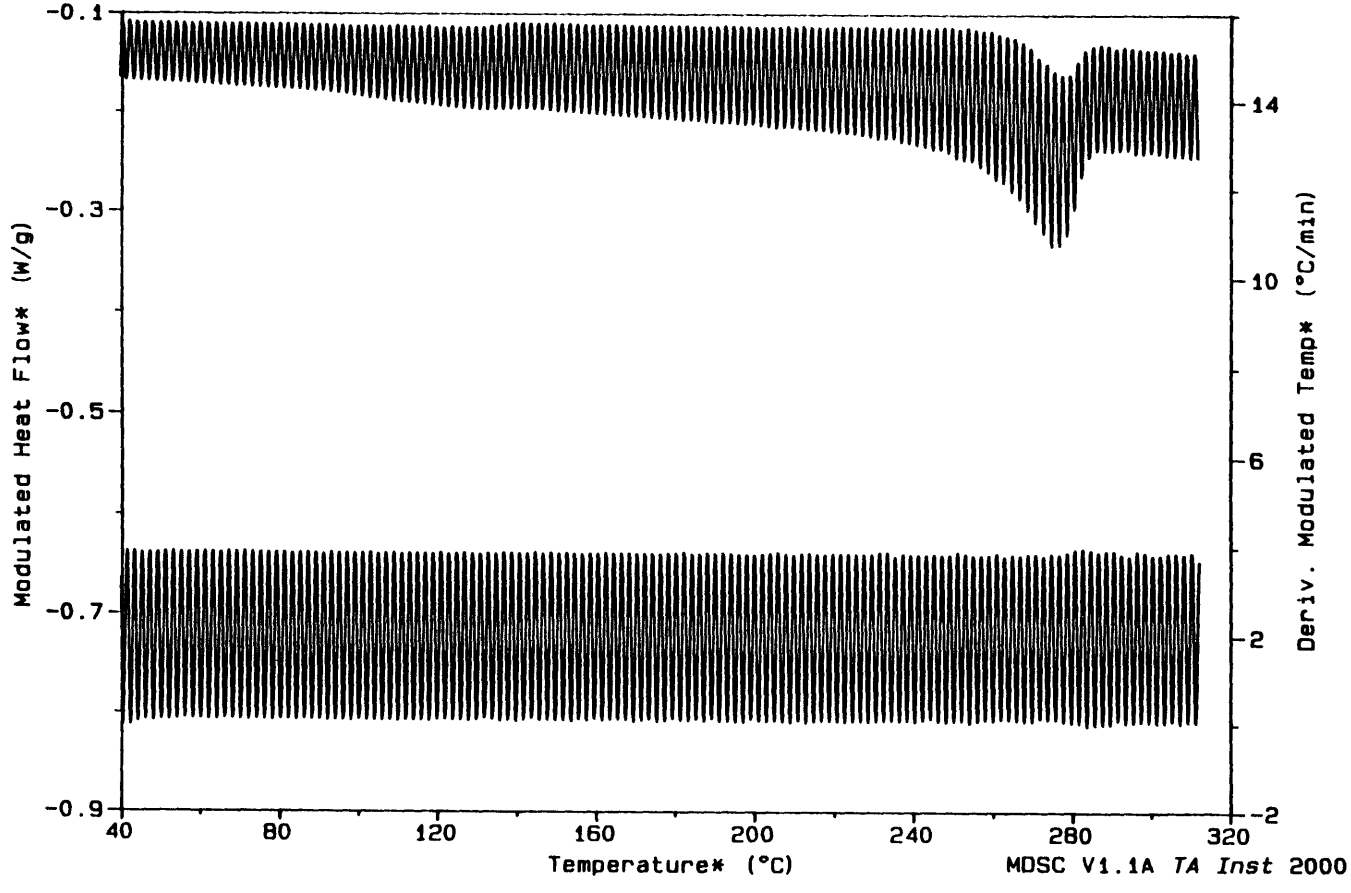

Figure 5.8 MDSC raw data for F-300 cold crystallized with $t_{1/2}$ = 700s. The upper curve is the modulated heat flow, and the lower curve is the simultaneous heating rate.

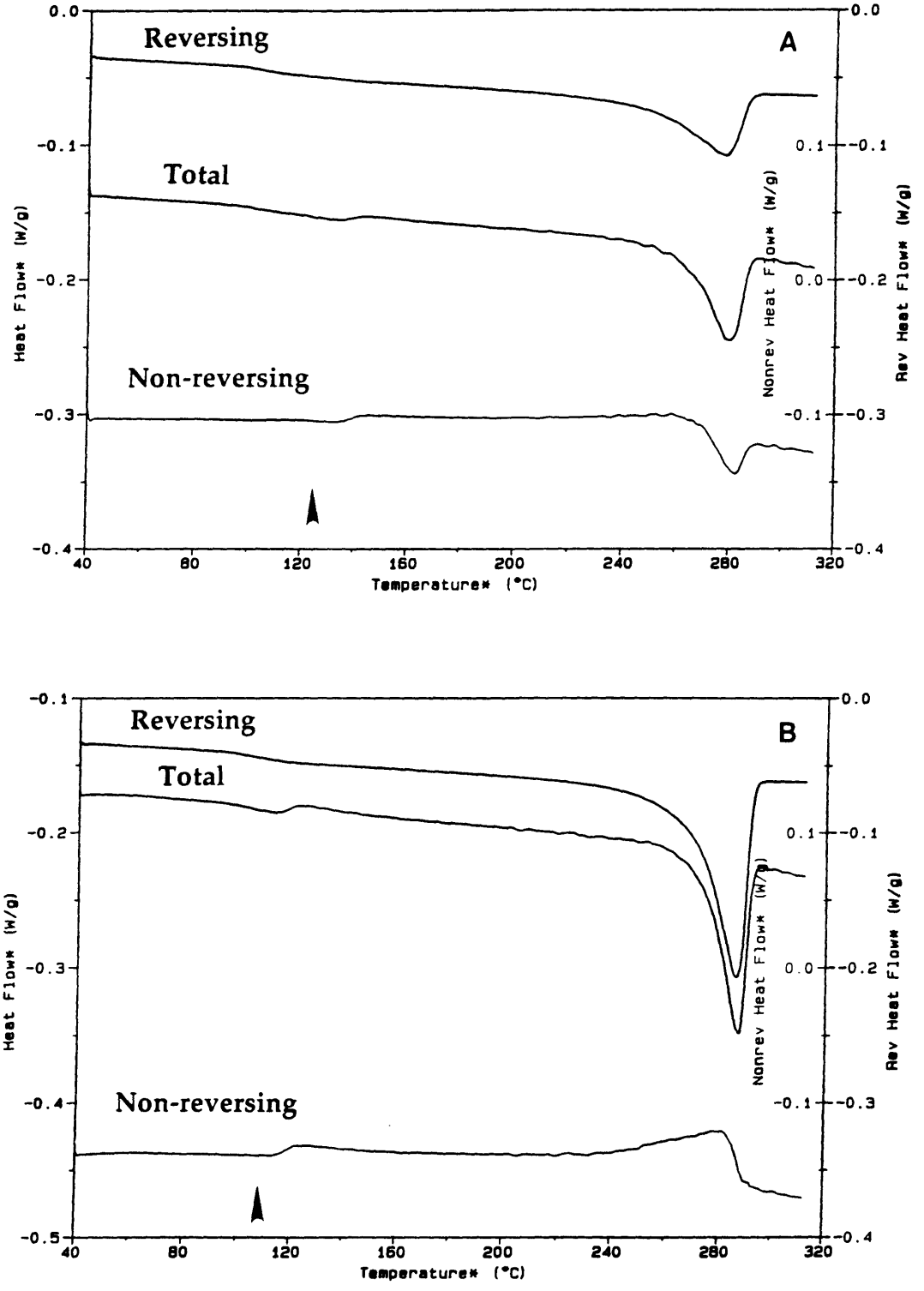

Figure 5.9 Total heat flow, reversing heat flow and non-reversing heat flow from MDSC for: a) F-300 cold crystallized with $t_{1/2}$ = 700s, b) F-200 cold crystallized with $t_{1/2}$ = 700s. The arrows indicate T_cs.

Figure 5.9a shows the MDSC results for F-300 sample. In the total heat flow curve (T), a small step shows up at about 105°C as the result of the glass transition, followed by a small melting peak just above T_c (T_c = 125°C), and an immediate upturn crystallization at about 10°C higher than T_c, then a major melting peak at about 278°C. In the reversing heat flow curve (R), a glass transition appears at 105°C, followed by a major melting peak at around 276°C. In the non-reversing heat flow curve (NR), the cold crystallization starts about 10°C higher than T_c. The material continues to crystallize until the temperature reaches 270°C, then a non-reversable melting occurs driving the curve downward. All three curves become flat when the temperature is above 285°C, indicating the melting of all the crystals.

MDSC results of F-200 sample with $t_{1/2}$ =700s are shown in Figure 5.9b. In the total heat flow curve (T), we observe that the glass transition and the small melting occur at the same time since T_c (T_c = 107°C) is very close to T_g. Following that, crystallization occurs as the curve shows an upturn. A melting peak finally appears at about 287°C. In the reversing heat flow curve (R), a glass transition appears at about 110°C followed by a major melting peak with the peak maximum at 285°C. In the non-reversing heat flow curve (NR), a cold crystallization exotherm appears at about 10°C higher than T_c. The material continues to crystallize as temperature increases. The major cold crystallization peak appears at about 282°C. No melting endotherm is observed in the NR curve.

If we compare Figure 5.9a and 5.9b, three significant differences in the thermal behavior between F-300 and F-200 can be obtained. First, the melting temperature of the major peaks in both the T and R curves of the F-200

sample are higher than those of the F-300 sample. Second, in the non-reversing heat flow curve (NR), F-300 shows both cold crystallization and non-reversing melting at the higher temperature, while F-200 gives only a cold crystallization exothermic peak. Third, we observe that even though the two materials have initially the same crystallinity, F-200 has the ability to form more crystals during the heating scan than F-300. The heats of fusion from the three heat flow curves are calculated, and the results are shown in Table 5.4. As we can see, after the runs have been completed, there are about 30% more crystals forming in the F-200 sample during the heating scan. Since DMA experiments stop at an earlier stage, we have also examined the amount of crystals formed in these materials before 240°C, and find that relatively more crystals formed in F-200.

DMA and MDSC results can be compared directly since they are all performed under the same heating rate. The three major differences between F-300 and F-200 from MDSC suggest that F-200 and F-300 have different crystallizability. F-300 has a higher M_w, and its crystallization is slowed by the large amount of chain entanglement. Consequently, it has a slower reorganization rate. Therefore, we observe a smaller amount of crystals forming during the heating scan and a lower T_m in F-300 material. On the contrary, F-200 is a low M_w material and tends to crystallize very fast. Its also has the ability to reorganize fast. Therefore, we observe more crystals forming during the scan and a higher T_m. Generally speaking, the infinite crystal melting temperature (T_m^∞) increases as M_w increases, as it corresponds to the largest crystals possibly formed by the material. However, polymer crystallization is controlled by kinetics, rather than thermodynamics. Therefore, as the temperature increases, lower M_w PPS has better

Table 5.4 Heat of fusion of F-200 and F-300 with $t_{1/2}$ = 700s from reversing heat flow (ΔH^R), non-reversing heat flow (ΔH^{NR}) and total heat flow (ΔH^T)

	ΔH^R (J/g)	ΔH^{NR} (J/g)	ΔH^T (J/g)
F-200	42.7	-14.8	28.9
F-300	81.5	-52.2	27.3

reorganization ability to continue forming meta-stable crystal lamellae which melt at a higher temperature. We believe the difference in crystallizability and reorganization ability also account for the higher E' in F-200 and lower E' in F-300 observed at higher temperature. Because E' is not affected by the crystallization temperature, as we have found in both F-200 and F-300 samples, E' is mostly affected by the molecular weight of the materials. Since lower M_w material tends to crystallize faster and form more crystals, the amorphous polymer chains may be under constant and large constraints by the formed crystals. In contrast, the higher M_w material requires longer time to crystallize and reorganize, and therefore the constraints asserted by the crystals are less. This idea is supported by the smaller amount of RAP formed in the F-300 material. Thus, at higher temperature, we observe a lower E' for F-300 and a higher E' for F-200.

5.4 CONCLUSIONS

The effect of molecular weight on the cold crystallization behavior and mechanical properties of linear PPS Fortron^{TM} has been investigated using DSC, SAXS, WAXS, DMA and MDSC. Three different M_w PPS samples are used in this study. Since different M_w polymers have different crystallization kinetics, the crystallization temperatures are chosen so that all samples can crystallize at the same crystallization rate, i.e. at the same $t_{1/2}$. Samples crystallized with both $t_{1/2}$=200s and $t_{1/2}$=700s are studied. Isothermal crystallization of different M_w PPS has been investigated using synchrotron SAXS. We observe systematic variation in the long period, lamellar thickness and linear crystallinity with both M_w and T_c from SAXS experiments. Since the changes are small compared to the error limits for the

lamellar thickness and linear crystallinity, we only observe an unambiguous increase with M_w in the long period. The same samples crystallized at a higher temperature also have a slightly larger long period.

We have observed the existence of a large amount of RAP in the cold crystallized sample compared to our previous study [38], and the lower the T_c, the higher the χ_{rap}. The same crystallinities are found in these cold crystallized samples. For different M_w samples crystallized with the same $t_{1/2}$, more mobile amorphous phase is observed in the higher M_w material, which leaves it with less RAP.

The effects of both M_w and T_c on the mechanical properties of PPS have been investigated by combining DMA and MDSC. It is found in DMA that M_w is the determining factor that affects the E' value at the higher temperature, since the same modulus E' and loss factor tanδ are observed for the samples crystallized at different T_c. A lower E' is observed for the higher M_w material. MDSC data suggest that higher M_w PPS has a slower crystallization rate and reorganization rate. Therefore, the poor ability of higher M_w PPS to form crystals during a heating scan (which would reinforce the rubbery phase) results in a lower E'. This also explains the lower T_m observed in the higher M_w sample.

Chapter 6

Modulated DSC Study of Multiple Endotherms

6.1 MDSC Study of Lower Temperature Melting Peak in Cold Crystallized PPS

6.1.1 INTRODUCTION

Multiple melting endotherms have been observed in many polymers including PEEK [35,189-194], PET [195-196], PBT [197-198] and PPS [37,112-114]. In addition to DSC, depolarized light microscopy [199], electron microscopy [200], small angle X-ray scattering [131,132,201] and dynamic mechanical analysis [196] have all been employed to correlate polymer morphology and relaxation to this multiple melting phenomenon. Many models have also been applied to explain this observation. However, we still lack strong evidence that can explain directly the origin of the multiple melting peaks. With this issue remaining unsolved, we also face the challenge to answer what constitutes the lower temperature melting peak. Some researchers consider that it comes solely from the melting of secondary crystals [112-114,131,132,189,190,195,198-200]; others argue it is solely the effect of amorphous phase relaxation [196]; and still others consider that both enthalpic relaxation and crystal melting contribute to the peak [194]. If one believes the third argument is true, there then exists the question of how we should draw the line to separate the two effects.

The confusion about this long-time unsolved issue and attempts to resolve it using thermal analysis come from the fact that normal DSC

provides only the total heat flow given by the sample as temperature increases. All the thermal activities both from the sample's previous thermal history and the changes in the sample as temperature increases are recorded and show up in the DSC data. Recently, a novel technique, Modulated DSC (MDSC), has brought a new dimension to thermal analysis [85-88]. MDSC is able to separate the total heat flow into two parts: 1) the heat flow from the heat capacity effect that usually comes from glass transition and crystal melting, and, 2) the heat flow from the non-heat capacity effect that usually comes from enthalpic relaxation and cold crystallization. With the most advanced technique MDSC in hand, we hope to clarify some of the tough issues that have been around for years in the polymer field.

In this work, we will report studies of the origin of lower temperature melting peak in cold crystallized PPS using MDSC. We will show directly from MDSC that the origin of the lower temperature peak is due to crystal melting, and show that cold crystallization occurs immediately after the sample is heated above its previous treatment temperature. The data also indicate that annealing will result in physical aging of the amorphous phase, and the amorphous phase can be aged within the temperature window between T_g and the annealing temperature (T_a). The effect of aging on the relaxation of the amorphous phase above T_g will be discussed as well.

6.1.2 EXPERIMENTAL SECTION

PPS sample used in this study is Ryton V-1 grade from Phillips Petroleum Company. The as-received material was semicrystalline sheet with a thickness of 75μm and molecular weight of 60,000. The amorphous

samples were prepared by first melting the sample at 320°C for 2min to destroy the crystal seeds, then quickly quenching into ice water. The amorphous samples were encapsulated in DSC pans and treated inside a differential scanning calorimeter from Perkin Elmer, DSC-4, under different conditions. Type A samples were prepared by heating from 60°C to 170°C at a heating rate of 20°C/min, holding at 170°C for 30min, then cooling to 40°C at a nominal cooling rate of 200°C/min. Type B samples were prepared as Type A samples, but after the annealing step at 170°C, the samples were heated momentarily to 210°C at 20°C/min, then immediately cooled to 40°C at 200°C/min. Type C samples were first treated as Type B samples, and were re-heated to 170°C and held for 30min, then cooled to 40°C at 200°C/min.

In order to reveal the details of the effects of thermal history on the sample crystallization and melting behavior, a Modulated DSC from TA Instruments has been used in this study. Both temperature and baseline were calibrated as in conventional DSC. High density polyethylene was used to calibrate heat capacity. A scan rate of 4°C/min was used with a temperature modulation amplitude of 0.42°C and a temperature modulation period of 40sec. These modulation parameters were chosen so that the heating rate was always above zero, i.e., no cooling occurred during the scanning process. In order to maximize the signal as well as to reduce the heat transfer delay, an average sample weight of 10mg was used. Helium was used as a heat transfer gas at a flow rate of 30ml/min.

6.1.3 RESULTS

In Figure 6.1.1, we present the MDSC raw data obtained from Type A sample. The upper curve gives the modulated heat flow, while the lower curve shows the simultaneous heating rate. Almost at all times, the heating

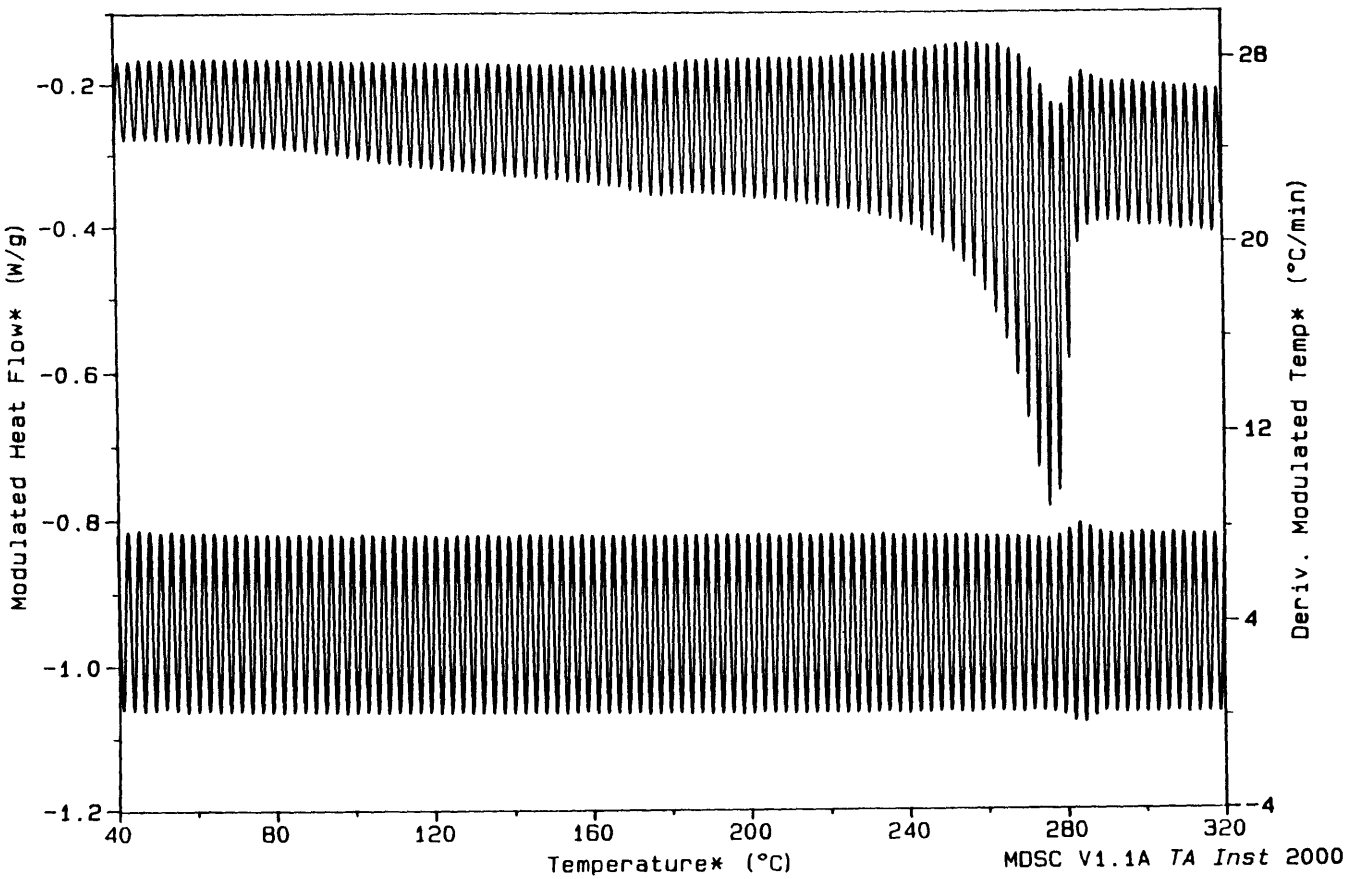

Figure 6.1.1 MDSC raw data from Type A sample. The upper curve (left axis) represents the modulated heat flow. The lower curve (right axis) represents the actual heating rate.

rate is above zero, i.e. the sample does not experience cooling. The slightly negative heating rate at the higher temperature end is the result of previous large crystal melting. As we have discussed earlier, three heat flow curves can be derived from these raw data. The results are shown in Figure 6.1.2a, b, c for Type A, B, and C samples, respectively. Each plot consists of three curves, representing reversible heat flow (R), total heat flow (T) and non-reversing heating flow (NR), respectively.

The total heat flow (T) curve shows the sum of all the thermal response of the sample, and provides the same level of information as normal DSC. In the T curve for Type A sample (Figure 6.1.2a), a glass transition is observed followed by a small melting endotherm with a peak maximum at 180°C. The curve then drives slightly up away from the baseline. Finally, a major melting peak is observed afterwards with a peak maximum at 280°C. In the T curve for Type B sample (Figure 6.1.2b), after the glass transition, no endo- or exo-thermic activities are found until 210°C, the temperature to which the sample had been briefly exposed. After 210°C, the total heat flow (T) curve again goes up away from the baseline, and is followed by the major melting endotherm with a peak maximum at 280°C. In the T curve from Type C sample (Figure 6.1.2c), a smaller endothermic peak is first observed at the exact temperature where the small endothermic peak of Type A sample appears. As temperature increases, the same kind of features are seen in Type C sample as are seen in Type B sample. It is not an exaggeration to say that it is hard to tell exactly what the thermal history effect is on either the amorphous phase or crystalline phase if judging by these total heat flow curves alone. To separate the thermal history effect, we have to go

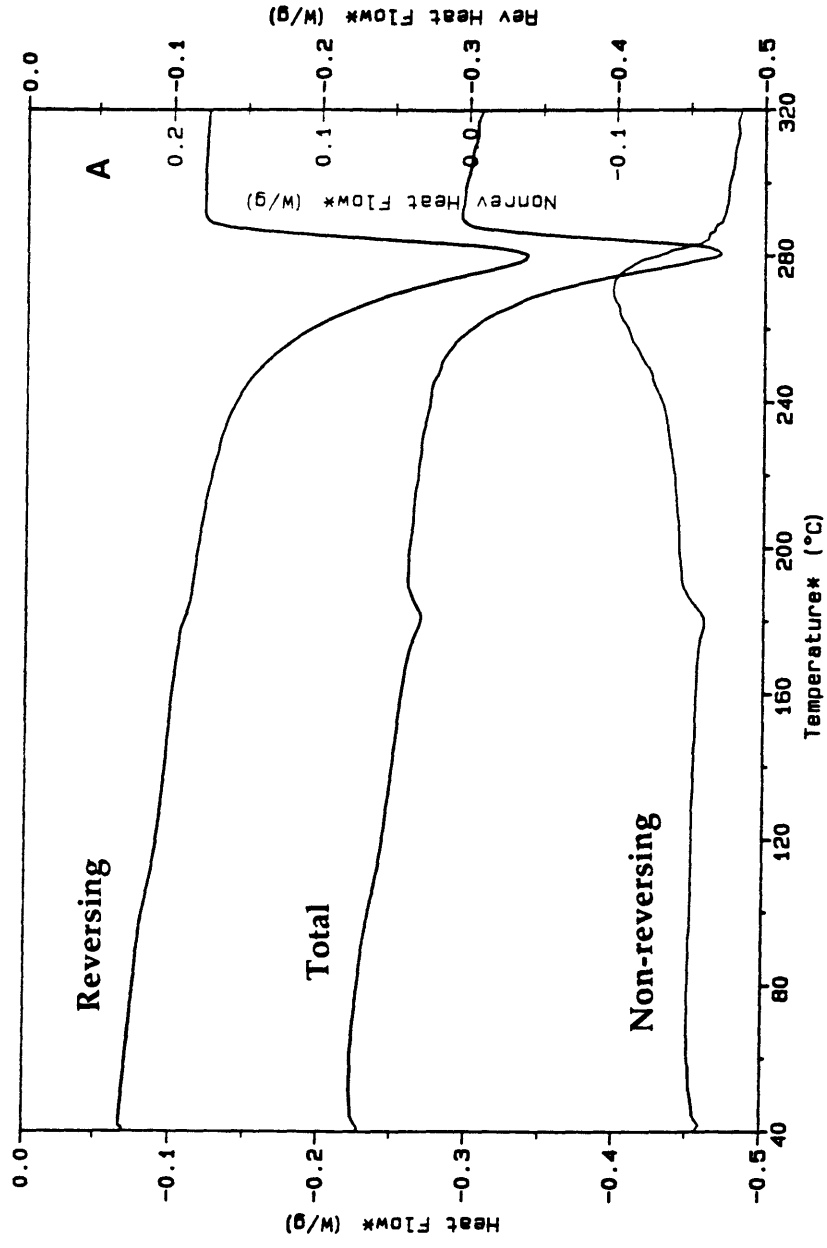

Figure 6.1.2 Total heat flow (T), reversing heat flow (R) and non-reversing heat flow (NR) obtained from MDSC for three types of samples: a) type A, b) type B, and c) type C.

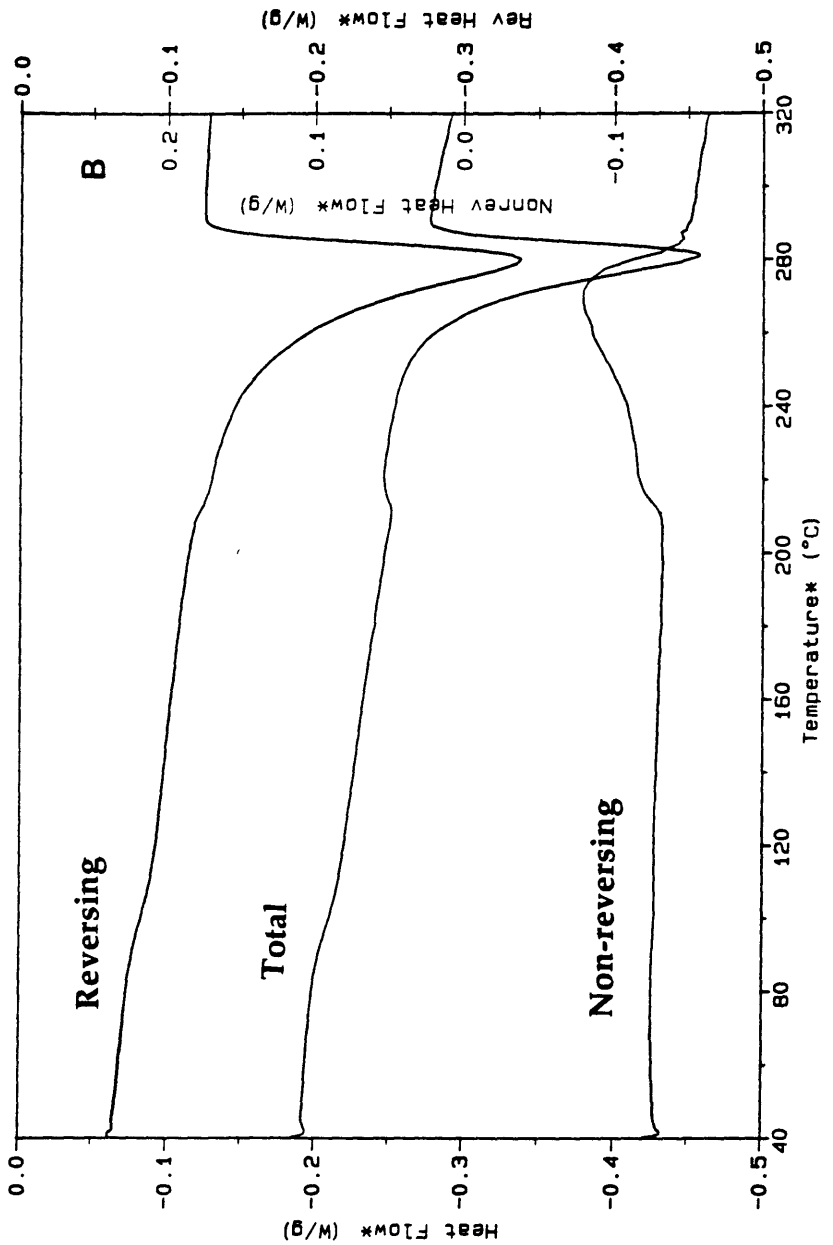

Figure 6.1.2, Continued

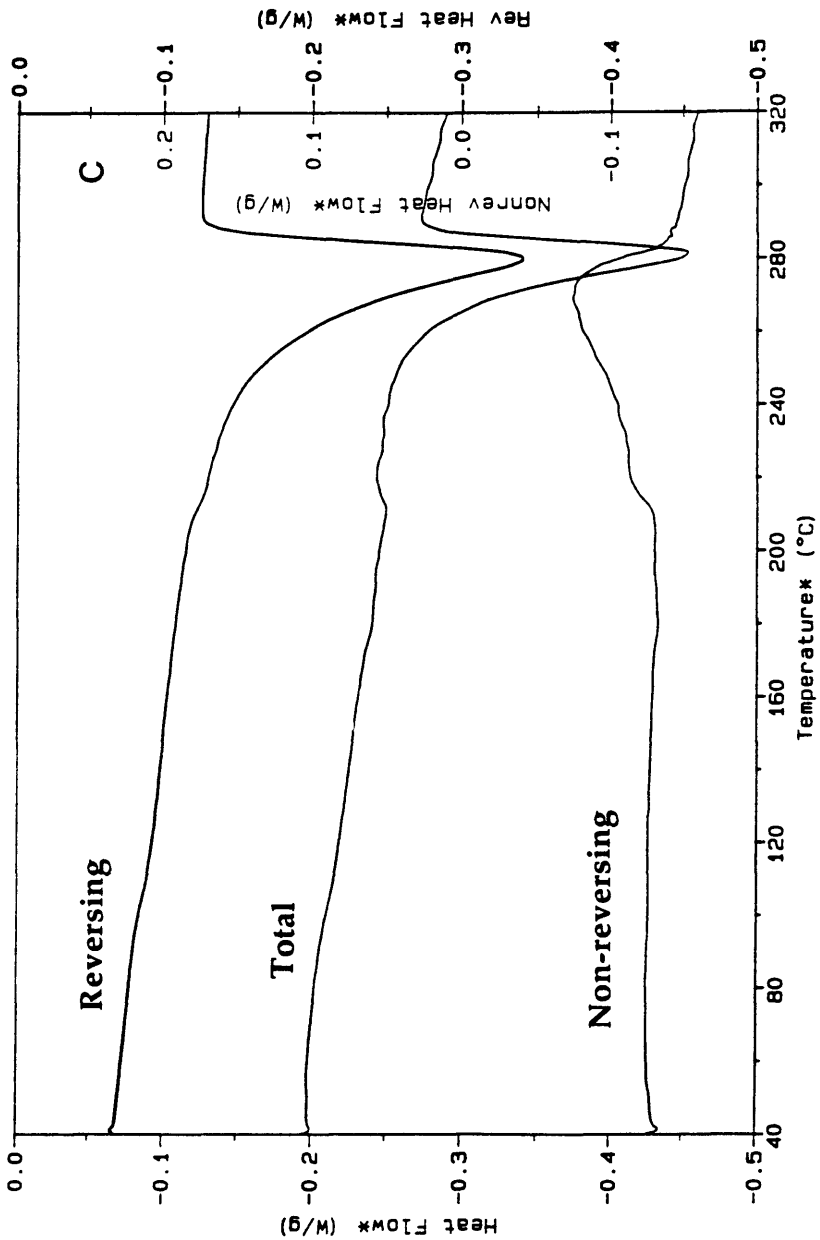

Figure 6.1.2, Continued

to two other heat flow curves, R and NR, that represent different physical processes.

For the non-reversing heat flow (R) curve, Type A sample (Figure 6.1.2a) shows a broad glass transition, an endothermic step and a melting endotherm. For Type B sample (Figure 6.1.2b), the endothermic step shifts to a higher temperature, while the major melting peak stays at the same temperature. The same features are observed in Type C sample (Figure 6.1.2c) as in Type B sample, as no appreciable change is observed in the re-annealed temperature region. In order to show these features more clearly, we have plotted the derivatives of the R and NR curves, and the results are shown in Figure 6.1.3. The curves are plotted in an expanded scale to show the lower temperature region since no differences between the curves in the higher temperature region are observed. In Figure 6.1.3a (derivative of R curves), the first shallow peak is the result of the glass transition, while the second represents the lower melting peak. The results show clearly that brief heating to the higher temperature shifts the lower temperature peak up. Re-annealing at a lower temperature leaves no mark even on the derivatives of the R curves.

We also note in Figure 6.1.3a the difference between these samples at the glass transition region. After careful analysis of the R curves, we list in Table 6.1.1 the glass transition temperature T_g and the amount of liquid-like amorphous phase, χ_a. χ_a is the ratio of the heat capacity step at T_g of semicrystalline sample to amorphous sample, and is expressed as $\chi_a(T) = C_p^{sc}(T)/C_p^{a}(T)$. Type A and C show similar T_g and χ_a, while Type B shows a much lower T_g and higher χ_a. Thus briefly heating to high temperature

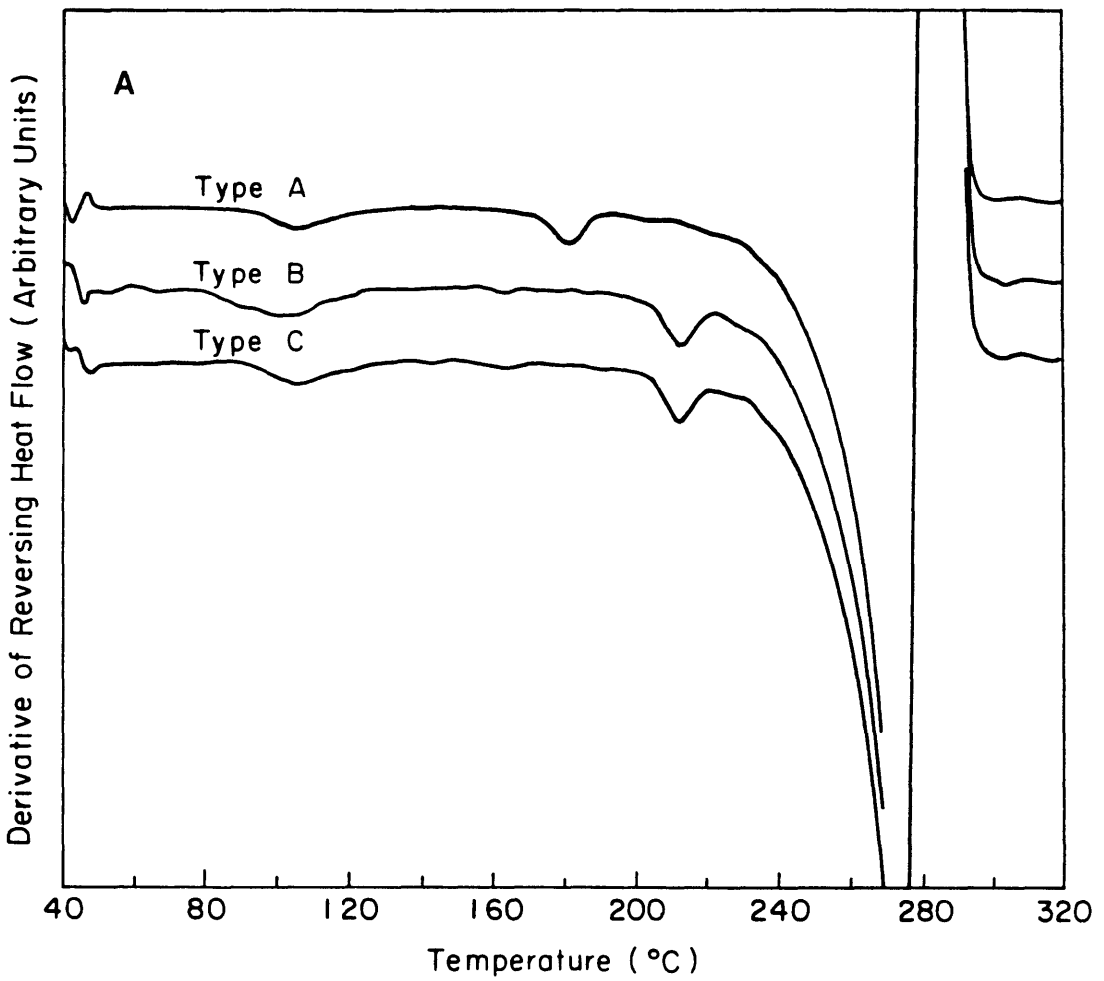

Figure 6.1.3 Derivative curves of: a) reversing heating flow, and b) non-reversing heat flow for three types of samples. Refer to the text for the different thermal treatments for Type A, Type B and Type C samples.

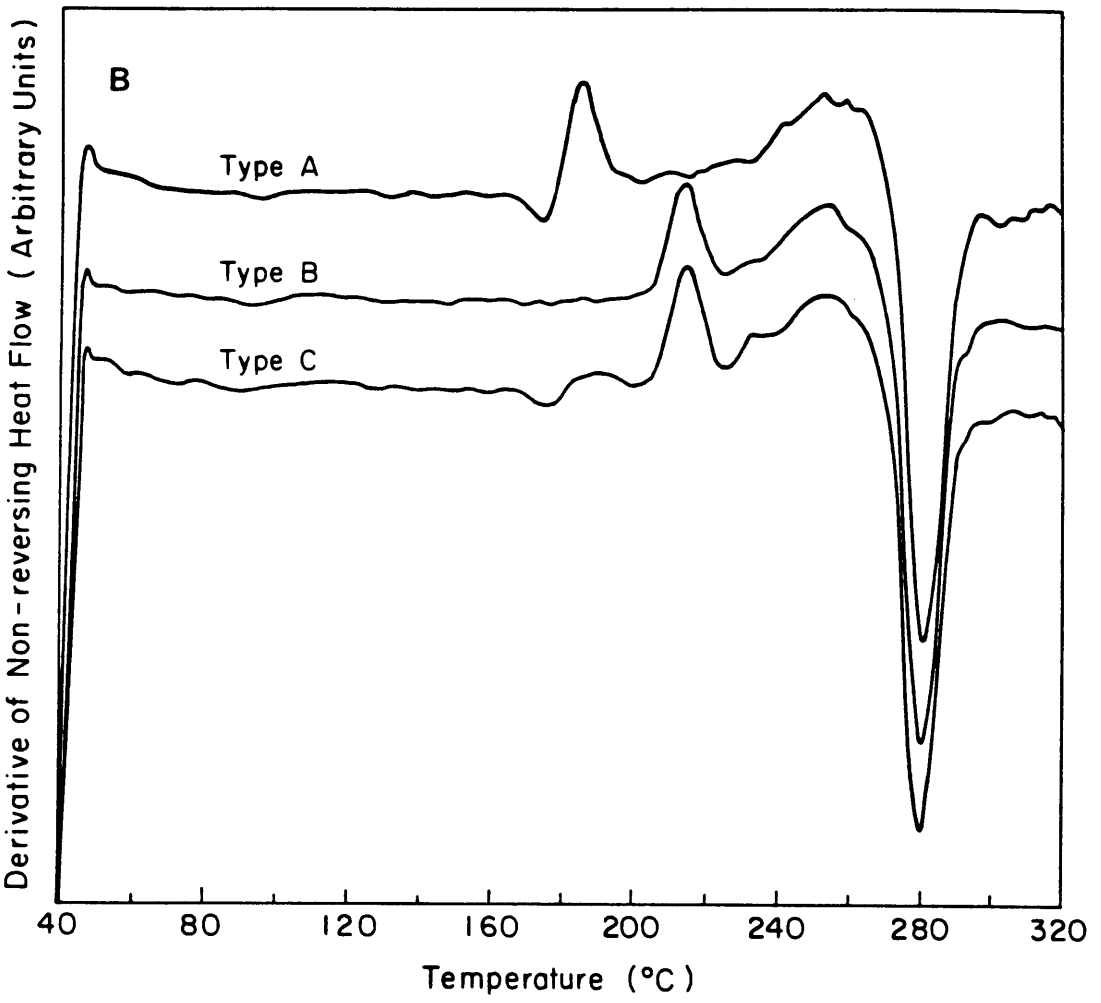

Figure 6.1.3, Continued

Table 6.1.1 Thermal properties of PPS samples: glass transition temperature, heat of fusion from total, reversing and non-reversing heat flow, and weight fraction of crystal, amorphous and rigid amorphous phases.

	T_g (°C) (±0.3°C)	ΔH_f^T (J/g)	ΔH_f^R (J/g)	ΔH_f^N (J/g)	χ_c (±0.01)	χ_a (±0.01)	χ_{rap} (±0.01)
Type A	104.5	32.9	86.5	- 53.5	0.30	0.41	0.29
Type B	98.1	34.0	80.4	- 43.8	0.31	0.64	0.05
Type C	105.6	34.1	80.4	- 43.4	0.31	0.41	0.28

increases the amount of amorphous phase that is able to relax at T_g. Also listed in Table 6.1.1 are the crystal heat of fusion, ΔH_f^i, where the superscript i represents from which curve the value has been derived. ΔH_f^T has been used to calculate the crystallinity of the sample using 111.6J/g [37] as the heat of fusion of 100% crystalline PPS. Little difference is observed among these samples. Since the reversing heat flow (R) curves indicate the melting of already-formed crystals and those which crystallized during the scan, a decrease in ΔH_f^R from A to B and C reflects the fact that few crystals formed during the scans in sample B and C.

Many features not accessible through normal DSC can be observed in the NR curves. First, cold crystallization exotherms have been observed for all the samples. The exothermic heat flow starts right after the highest temperature to which the samples have been exposed. Second, some small features can be observed in the lower temperature region which are shown more clearly in the derivative curves, shown in a composite plot in Figure 6.1.3b. For Type A sample, a downward peak is seen around 174°C, followed first by an immediate upturn peak at 185°C, then by a broader peak at 250°C and a large downward peak. In Type B curve, no downward peak shows up before the upturn peak that appears around 210°C. At higher temperature, the same features have been observed as in Type A sample. In Type C curve, a downward peak occurs at a temperature of 174°C. It is followed later by an upturn peak appearing at 214°C with a peak shape similar to that seen in Type B sample. The same features are observed once again in the higher temperature region as in the previous two curves. These observations suggest that re-annealing at lower temperature does affect the shape of the NR curve.

6.1.4 DISCUSSION

For the sample cold crystallized at 170°C (Type A), we observe changes in both R and NR curves when the temperature reaches 170°C. The step-like transition in the R curve is the result of melting of crystals formed at the treatment temperature, while the small downward peak from the NR curve is the result of the enthalpic relaxation of associated amorphous phase. The step-like melting peaks have also been observed in our MDSC study of PEEK polymer [see section 6.2]. Both the re-crystallization effect and the asymmetry of the higher temperature melting peak are considered to be the reasons [see section 6.2]. Therefore, the normal DSC lower temperature peak, which is seen in the T curve from MDSC, results from both crystal melting and enthalpic relaxation. The major contribution to the lower temperature endotherm near 174°C comes from crystal melting. Amorphous phase enthalpic relaxation contributes a very minor component in the cold crystallized samples. This component disappears in the Type B sample after brief heating to 200°C and then reappears in Type C sample after re-annealing at 170°C. Sauerbrunn et al. [202] studied the effect of aging on the relaxation of amorphous PET. They found that enthalpic relaxation obtained from the NR curve reflected the degree of physical aging of the amorphous phase. Here we observe enthalpic relaxation from the sample cold crystallized at T_a. Therefore, we suggest that amorphous phase can also be aged at a temperature higher than the glass transition temperature normally given by the expressed heat capacity increment (here occurring near 105°C). The aged amorphous phase, however, can only be relaxed once the temperature increases above its T_a. We find more support for this point as we study further the results from Type B and Type C samples.

For the sample annealed briefly by heating to a higher temperature of 200°C (Type B), we observe in the R curve a shift in the step-like melting peak to a corresponding higher temperature. Because only extremely brief annealing at this higher temperature has been applied, no downward peak is observed in the NR curve before the exothermic cold crystallization. This is shown more clearly in the derivatives of the NR curves where no downward peak is observed before the previous treatment temperature.

For the sample re-annealed at 170°C (Type C), we observe no appreciable changes compared to Type B sample in either the R curve or its derivative. This indicates that re-annealing the sample at a lower temperature after exposure to higher temperature does not change the crystal phase. More importantly, we observe in the derivatives of NR curve an enthalpic relaxation occurring at the re-annealing temperature, exactly at the same place as we observe the relaxation for Type A sample. This observation supports strongly our previous suggestion that the amorphous phase in semicrystalline polymers can be annealed above its nominal T_g. Additionally, the amorphous phase can be annealed within the temperature window between T_g and T_a.

Another interesting observation we have concerns the mass fraction of the amorphous phase of these three types of samples. It has long been found that there exists a third phase, the so called rigid amorphous phase, that does not contribute to the increase of heat capacity at the polymer T_g. Using Eqn. 1.1, one can calculate the amount of this third phase. Here χ_c is the crystallinity of the sample obtained from either the ΔH_f^T or wide angle X-ray scattering and χ_a is the mobile amorphous phase which is the sole

contributor to the heat capacity increment at T_g. We list in Table 6.1.1 the mass fractions for all three samples. A significant increase in χ_a has been found in Type B sample over Type A sample, resulting in a decrease in χ_{rap}. At the same time, T_g taken from the inflection point of the step transition also decreases indicating a less constrained amorphous phase system. However, after re-annealing, as in the Type C sample, both χ_{rap} and T_g return to values very close to those of the Type A sample. In our prior dielectric study of the properties of RAP [38], we observed an increase in the fraction of RAP as the cold crystallization temperature increased. Current data tell the kinetic aspect of RAP, i.e., the development of RAP with time. Provided with the fact that annealing ages the amorphous phase and increases T_g, we suggest that annealing may be responsible for the increase of RAP. The origin of RAP thus seems to be within the amorphous phase

It is also worth pointing out that in all cases, re-organization was observed right above T_a as indicated by the exothermic peak observed in the NR curve. Since cold crystallization usually results in small and imperfect crystals, once the samples have been melted at higher temperature, they tend to form more perfect crystals that are stable at a higher temperature. Quantitatively, we observe a decreased value in ΔH_f^{NR} for Type B and Type C samples. This is simply because the temperature window for re-organization becomes narrower as cold crystallization temperature increases. These results are the direct evidence that support the re-organization theory.

6.1.5 CONCLUSIONS

MDSC has been employed to study the relaxation and melting behavior of cold crystallized PPS. The lower endothermic peak from the normal DSC has been shown to be the result of both melting from the crystals formed at

that temperature and the enthalpic relaxation of the associated amorphous phase. We also have observed that once the sample has been exposed to a higher temperature, a lower temperature treatment does not change the thermal behavior of the crystalline phase. It can only change the relaxation of the amorphous phase and increase the enthalpic relaxation at that temperature. From NR curve direct evidence has been obtained for the re-organization process in the sample after the temperature reaches the previous treatment temperature. The nature of RAP is believed to be the amorphous phase constrained by the crystalline phase. For the first time, we have shown the kinetic aspect of RAP that exists in this semicrystalline polymer. Annealing results in an increase in the amount of RAP.

6.2 MDSC STUDY OF MULTIPLE MELTING PEAKS IN MELT CRYSTALLIZED PEEK

6.2.1 INTRODUCTION

Semicrystalline polymers crystallized from their molten state (referred to as melt crystallization) usually show double melting peaks in the differential scanning calorimeter (DSC) even when only one crystallographic unit cell type is present. In addition to DSC, optical microscopy and electron microscopy have been utilized to explore the origin of this double melting peak phenomenon. Three different models have been proposed to explain the experimental data. One model says that there exists different crystal morphologies crystallized under different constraints [203-204]. The second model proposes the existence of lamellar crystals having two different sizes, i.e. different perfection of lamellar crystals which melt at two different

temperatures [131,132,149,192]. The third model explains that the double melting peaks are the result of melting first of pre-melting crystals and then of re-crystallized crystals formed during heating [35,190,191]. Recent investigations have shown that it is also possible to obtain more than two melting peaks by step-wise cooling from the melt and annealing at different temperatures [189,201]. Once again this imposes the question of whether there exist crystal lamellae of different thickness, and how they behave as temperature increases.

The purpose of this study is to investigate the cause and constitution of the multiple endotherms. Both single stage and multiple stage melt crystallized PEEK samples have been studied using an advance technique, MDSC, that is able to separate the total heat flow into the heat capacity component and non-heat capacity component. This allows us to obtain direct information about the composition of normal DSC peaks, and gives a direct explanation of the origin of the multiple endotherms.

6.2.2 EXPERIMENTAL SECTION

Transparent amorphous PEEK films with a thickness about 0.1 mm were obtained from ICI America, Inc. The samples showed no Bragg scattering peaks in the wide angle X-ray scattering (WAXS) pattern. The film samples were first encapsulated in a DSC pan and heat treated in a Perkin Elmer DSC-4 differential scanning calorimeter. For single stage melt crystallized PEEK, the sample was first heated at 40°C/min to 380°C and held for 10 min, then cooled at a nominal rate of 200°C/min to the crystallization temperature (T_c) for a time equal to six times the half crystallization time

which had been determined according to previous study [138], and finally cooled to room temperature at 200°C/min. For multiple stage melt crystallized PEEK, the sample was cooled from the melt as single stage crystallized samples, then cooled successively to different crystallization temperatures at a rate of 200°C/min. The samples were kept at each temperature for 1 hr. The temperatures at which the samples were crystallized are listed in Table 6.2.1.

Modulated DSC has been used to study the high temperature melting behavior of PEEK. Both temperature and baseline were calibrated as in conventional DSC. High density polyethylene was used to calibrate heat capacity. A scan rate of 4°C/min was used with a temperature modulation amplitude of 0.42°C and a temperature modulation period of 40sec. These modulation parameters were chosen so that the heating rate was always above zero, i.e., there was no cooling during the scanning process. In order to maximize the signal as well as to reduce the heat transfer delay, an average sample weight of 8mg was used. He gas was used as a heat transfer agent at a flow rate of 30 ml/min. Details about MDSC techniques have been introduced in the previous section.

6.2.3 RESULTS AND DISCUSSION

6.2.3.1 Single Stage Melt Crystallization

Semicrystalline PEEK was melt crystallized at 270°C, 283°C, 290°C, 300°C, 310°C or 320°C and has been studied using MDSC. We plot the MDSC raw data in Figure 6.2.1 for PEEK melt crystallized at 300°C. The upper curve is the modulated heat flow, and the lower curve is the simultaneous heating

Table 6.2.1 Multiple Stage Melt Crystallization Temperatures (°C) of PEEK*

	T_{c1}	T_{c2}	T_{c3}	T_{c4}	T_{c5}	T_{c6}
Two-stage	316	286	---	---	---	---
Six-stage	316	301	286	270	255	239

* Crystallized in a step-wise fashion for 1 hr. at each step.

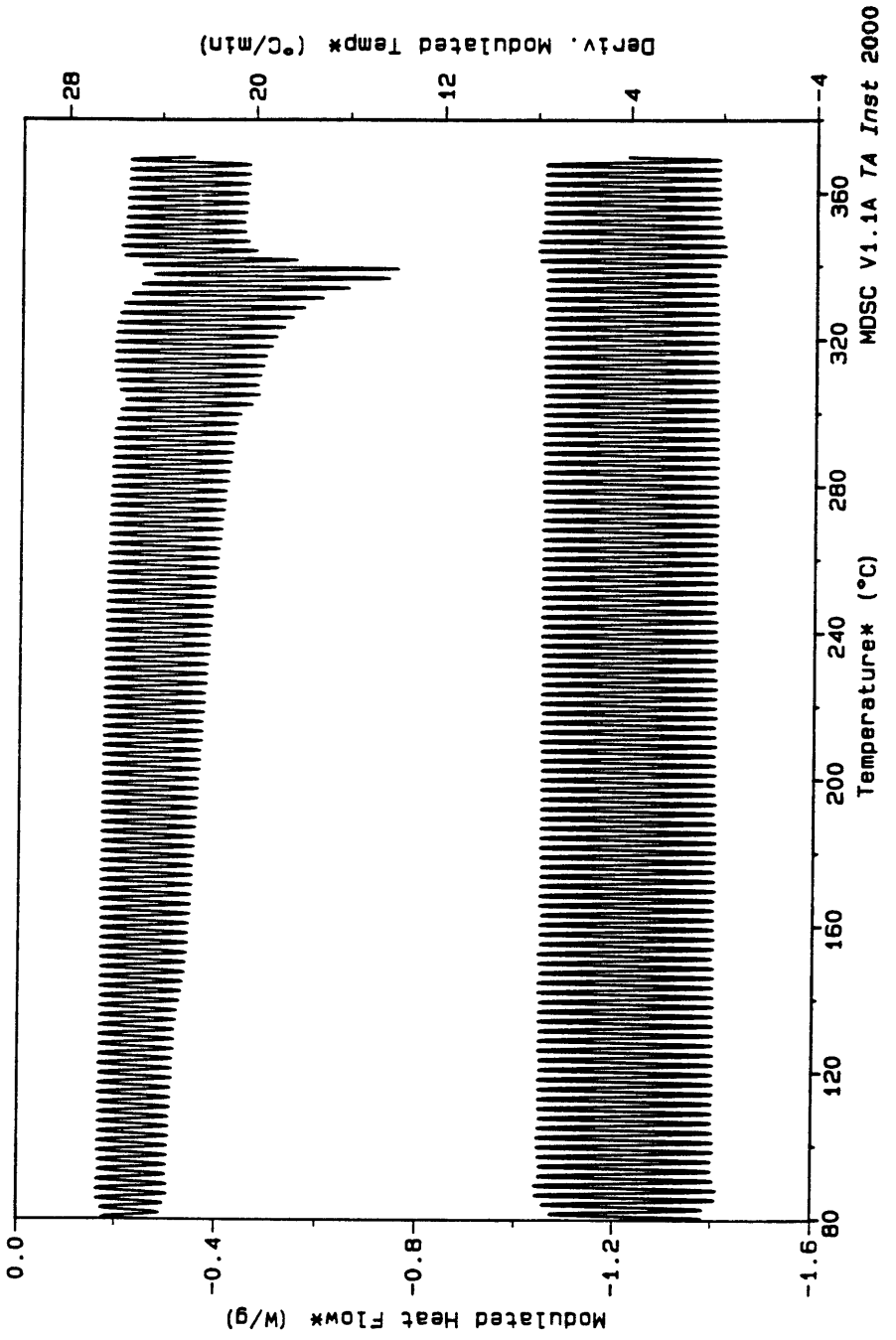

Figure 6.2.1 MDSC modulated heat flow (upper curve) and heating rate (lower curve) vs. temperature of PEEK melt crystallized at 300°C

rate. Again the experimental parameters were chosen so that the heating rate was kept above zero at all times and no cooling during the scan was allowed. In Figure 6.2.2 a-c, we present composite plots of data obtained from MDSC for the six temperatures listed above. Plots a, b, and c represent the data from total heat flow (T), reversing heat flow (R) and non-reversing heat flow (NR), respectively. In the T curve plot, Figure 6.2.2a, double melting peaks are observed after T_g: the lower temperature melting peak which increases linearly with T_c, and the higher temperature melting peak with a peak maximum that stays at almost a constant temperature. Since the T curves are the same as those found in normal DSC studies, these results agree well with many published data [35,189-194]

In Figure 6.2.2b, we observe in each reversing heat flow (R) curve a T_g followed by a step-like endothermic peak and a major melting peak. These step-like peaks occur at the same temperatures as the lower melting peaks in the total heat flow curves (Figure 6.2.2a), thus their peak positions also increase with T_c. Two reasons can be considered to account for the shape of the R curves. First, crystal reorganization happens right above T_c for $T_c <$ 300°C. This can be recognized by the obvious exothermic heat flow found in Figure 6.2.2c in the non-reversing heat flow (NR) curves. Therefore, melting of just-crystallized crystals provides enough heat flow to keep the R curves flat at a higher temperature. Not surprisingly, when T_c is higher than 300°C, where no exotherms are observed in the NR curves, more distinct lower melting peaks show up. Second, the major melting peak at the higher temperature also contributes to the plateau in the reversing heat flow curves because of the asymmetry observed in the shape of this peak.

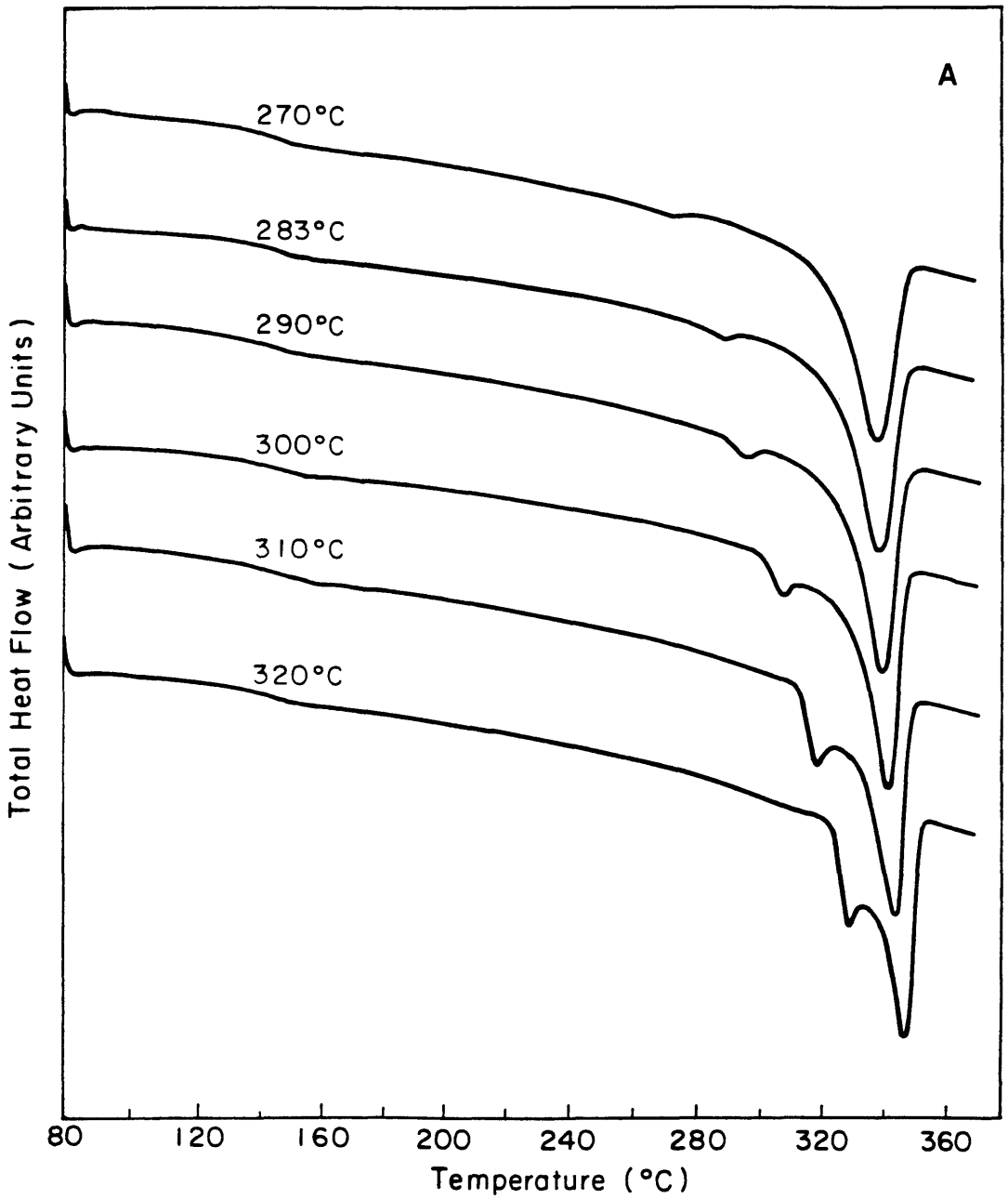

Figure 6.2.2 MDSC heat flow vs. temperature for single stage melt crystallized PEEK samples: a) total heat flow (T), b) reversing heat flow (R), c) non-reversing heat flow (NR).

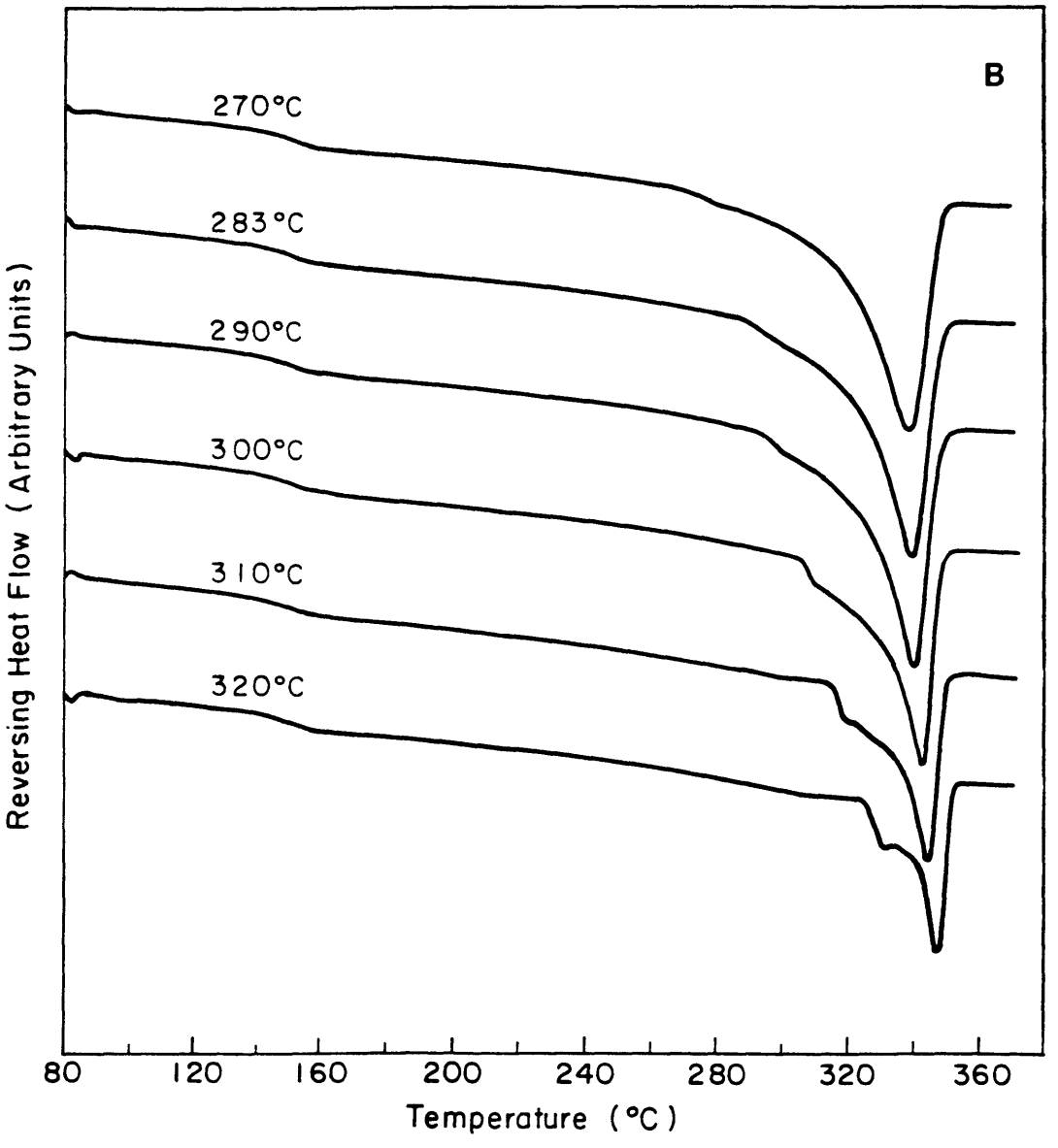

Figure 6.2.2, Continued

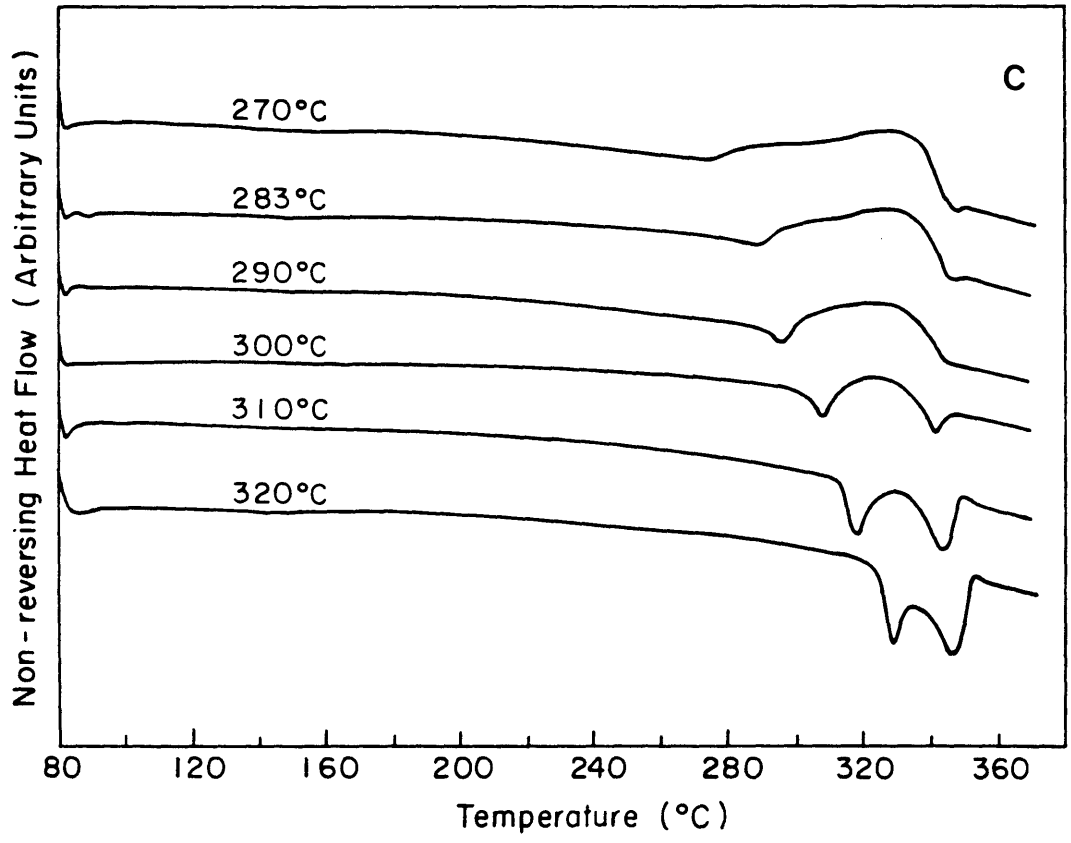

Figure 6.2.2, Continued

Figure 6.2.2c shows the composite plot of the non-reversing heat flow (NR) curves of PEEK samples. A downward deviation from the baseline is observed in every curve when the temperature gets to T_c. As we have discussed in the previous section, this is considered as the enthalpic relaxation of the amorphous phase. As temperature increases, immediate systematic changes in the NR curves with increasing T_c are observed. The exothermic halo becomes smaller and smaller, and finally disappears completely when T_c is above 300°C. At the same time, a second endothermic peak appears in the NR curves at the higher temperature end when T_c is at 300°C, and becomes more intense as T_c increases.

The plots of the lower (T_{m1}) and the upper (T_{m2}) melting peak temperatures vs. T_c from both T and R curves are presented in Figure 6.2.3a,b, respectively. T_{m1} increases linearly with T_c in both cases. In contrast, T_{m2} is independent of T_c when T_c is below 300°C and remains constant. When T_c is above 300°C, T_{m2} increases with T_c. We find that the slope of T_{m1} vs. T_c is very close to unity in both cases, which indicates that the crystals do not thicken for this material.

Heats of fusion, ΔH_f^i, are calculated for each type of heat flow and summarized in Table 6.2.2. Here superscript i represents the curve from which the value was obtained. Also listed in the Table are the samples' T_g, mobile amorphous phase fraction, χ_a, crystalline fraction, χ_c and rigid amorphous phase fraction, χ_{rap}. Here, a three phase model is assumed as expressed by Eqn. 1.1. We have plotted ΔH_f^T (solid circles), ΔH_f^R (empty squares), and ΔH_f^{NR} (empty circles) as a function of T_c as shown in Figure 6.2.4. We observe that ΔH_f^T increases linearly with T_c, while ΔH_f^R and

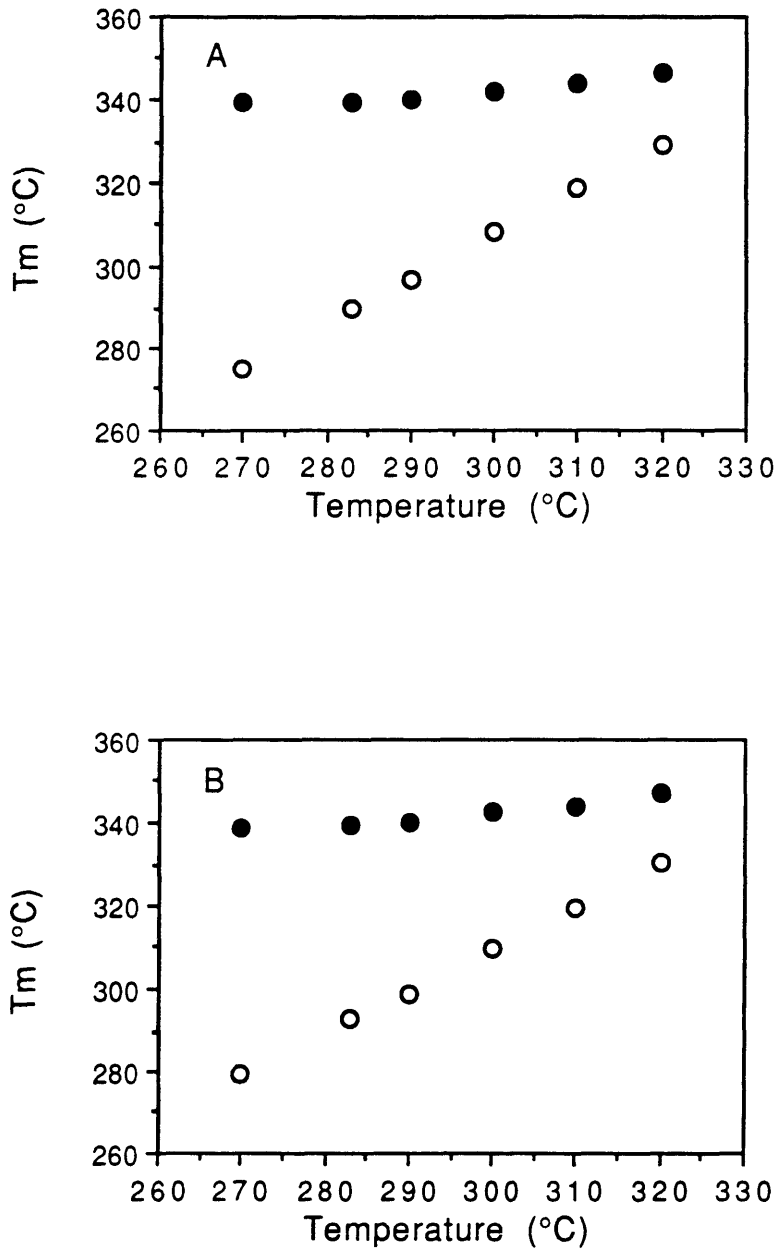

Figure 6.2.3 T_{m1} and T_{m2} as a function of crystallization temperature obtained from a) total heat flow, and b) reversing heat flow for melt crystallized PEEK.

Table 6.2.2 Thermal properties of single stage melt crystallized PEEK: heat of fusion from total, reversing and non-reversing heat flow, and weight fraction of crystal, amorphous and rigid amorphous phase.

Temp (°C)	ΔH_f (T) (J/g)	ΔH_f (R) (J/g)	ΔH_f (NR) (J/g)	Tg (°C)	χ_a (%)	χ_c (%)	χ_{RAP} (%)
270	35.0	63.8	29.0	150.0	50.2	26.9	22.9
283	36.6	57.8	21.6	149.6	50.6	28.1	21.3
290	38.6	53.5	15.5	149.3	51.0	29.7	19.3
300	38.9	41.3	3.0	149.2	51.0	29.9	19.1
310	39.9	30.6	-9.7	149.1	50.2	30.7	19.1
320	42.1	26.3	-14.9	148.5	50.2	32.4	17.4

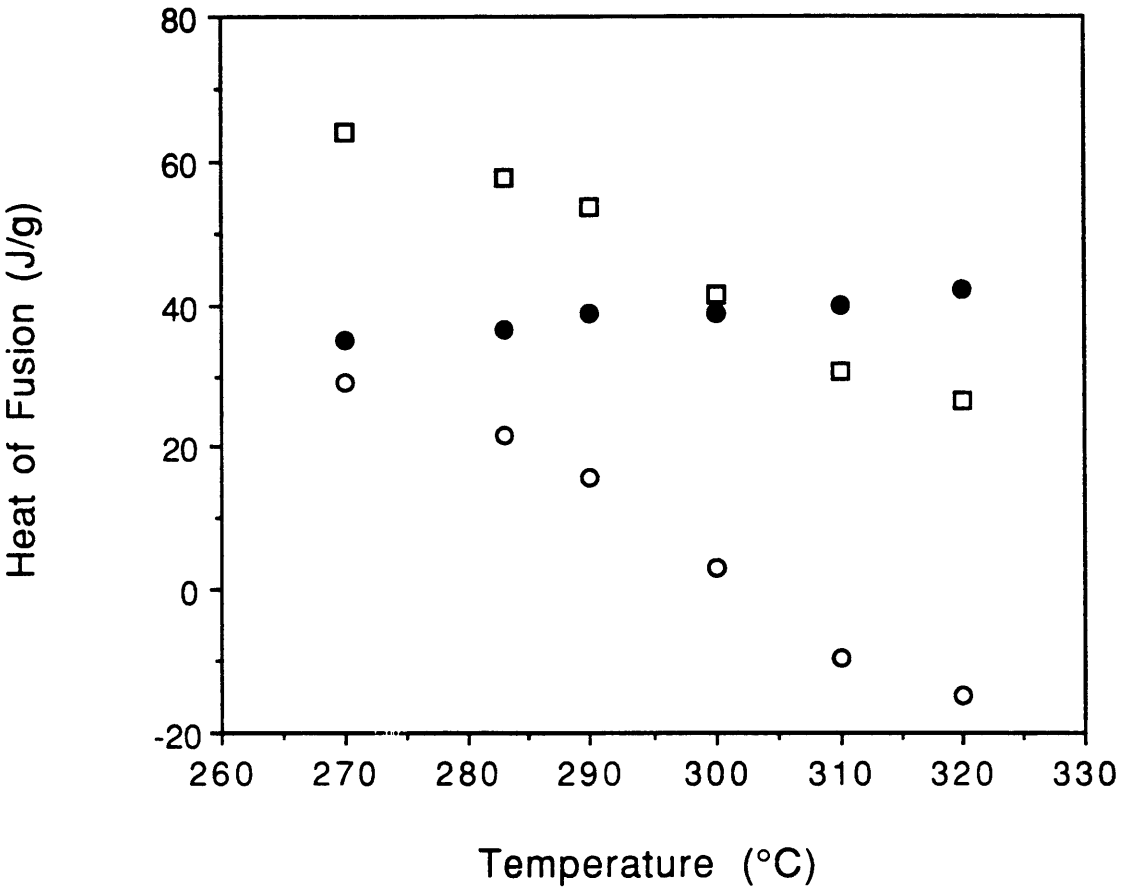

Figure 6.2.4 Heat of fusion of melt crystallized PEEK samples obtained from MDSC total heat flow (solid circles), reversing heat flow (empty squares) and non-reversing heat flow (empty circles).

ΔH_f^{NR} decrease with T_c. Careful inspection shows that the decreasing trends do not go linearly with T_c, but a maximum drop in ΔH_f^{R} and ΔH_f^{NR} occurs at 300°C. This is also the temperature where previously we observed the disappearance of the cold crystallization exotherm and the appearance of a higher temperature relaxation endotherm in the non-reversing heat flow curves of Figure 6.2.2c. The difference between ΔH_f^{R} and ΔH_f^{NR} matches ΔH_f^{T} very well.

From the analysis above, we conclude that 300°C is the transition temperature (T_{tran}) separating two melt crystallization mechanisms. When T_c is below 300°C, only one type of crystal lamellae exists. When the temperature just gets above T_c, these crystals will melt, and then re-crystallize to form better crystals that finally melt at a higher temperature T_{m2}. Since this reorganization process does not depend on when the sample starts to recrystallize, we observe a constant value for T_{m2}. When T_c is above 300°C, two types of crystal lamellae exist in the sample. The two melting peaks therefore correspond to the melting of these two types of crystals. This conclusion supports the recent morphological studies of PEEK performed by Lovinger et al. [200] using transmission electron microscopy (TEM). They observed the same kinds of spherulitic lamellae growing along the crystallographic b direction for samples crystallized at both higher and lower temperature. However, at lower temperature (T_c < 300°C), the spherulites usually contained narrow lamellae, whereas at higher temperature (T_c > 300°C), the spherulites contained "large, branched, bundle-like stacked lamellae besides the narrow species"[200].

The method of determination of T_{tran} between the two melting mechanisms was first proposed by Chung and Cebe [113] in their DSC study of melt crystallization of PPS. From the present MDSC study, we have found direct and strong support for this method. We suggest that using T_{m2} from MDSC to determine T_{tran} has general applications to other semicrystalline polymers. The knowledge of how the crystals behave with an increasing temperature has profound engineering benefit especially when considering that polymers are used as composite materials where microstructural changes are important with respect to other components.

6.2.3.2 Multiple Stage Melt Crystallization

Results of two-stage and six-stage melt crystallization of PEEK are shown in Figure 6.2.5 a,b, respectively. The temperatures of crystallization are listed in Table 6.2.1. In Figure 6.2.5a of two-stage crystallization (T_c=316°C and T_c=286°C), three peaks have been observed in all the three heat flow curves. The two lower temperature melting peaks correspond to the two T_cs, and are followed by a higher temperature melting peak. The higher temperature peak is believed to come from the melting of more perfect crystals formed at T_{c1} as we have discussed in the single stage melt crystallization. The two lower temperature peaks in the reversing heat flow (R) curve show step-like shape, and no crystallization exotherm is found in the non-reversing (NR) curve. A similar situation is found in the six-stage crystallized sample shown in Figure 6.2.5b. However, the seventh peak from T_{c6} is so small that its magnitude becomes comparable to the noise level in all the heat flow curves. The peak positions correspond well with the crystallization temperatures. Again no re-crystallization exotherms are observed in this sample from the NR curves.

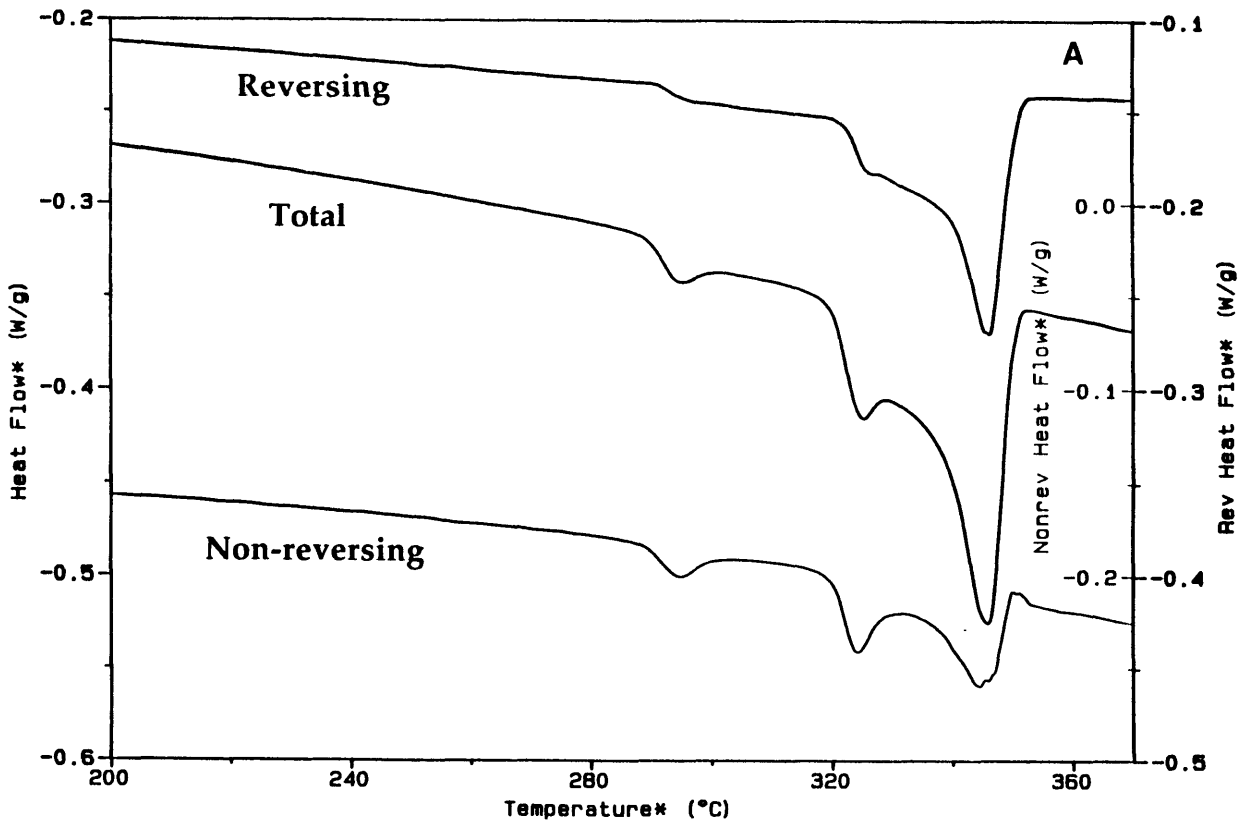

Figure 6.2.5 MDSC heat flow vs. temperature for multiple stage melt crystallized PEEK samples: a) two-stage melt crystallization, b) six-stage melt crystallization. See Table 6.2.1 for crystallization temperatures.

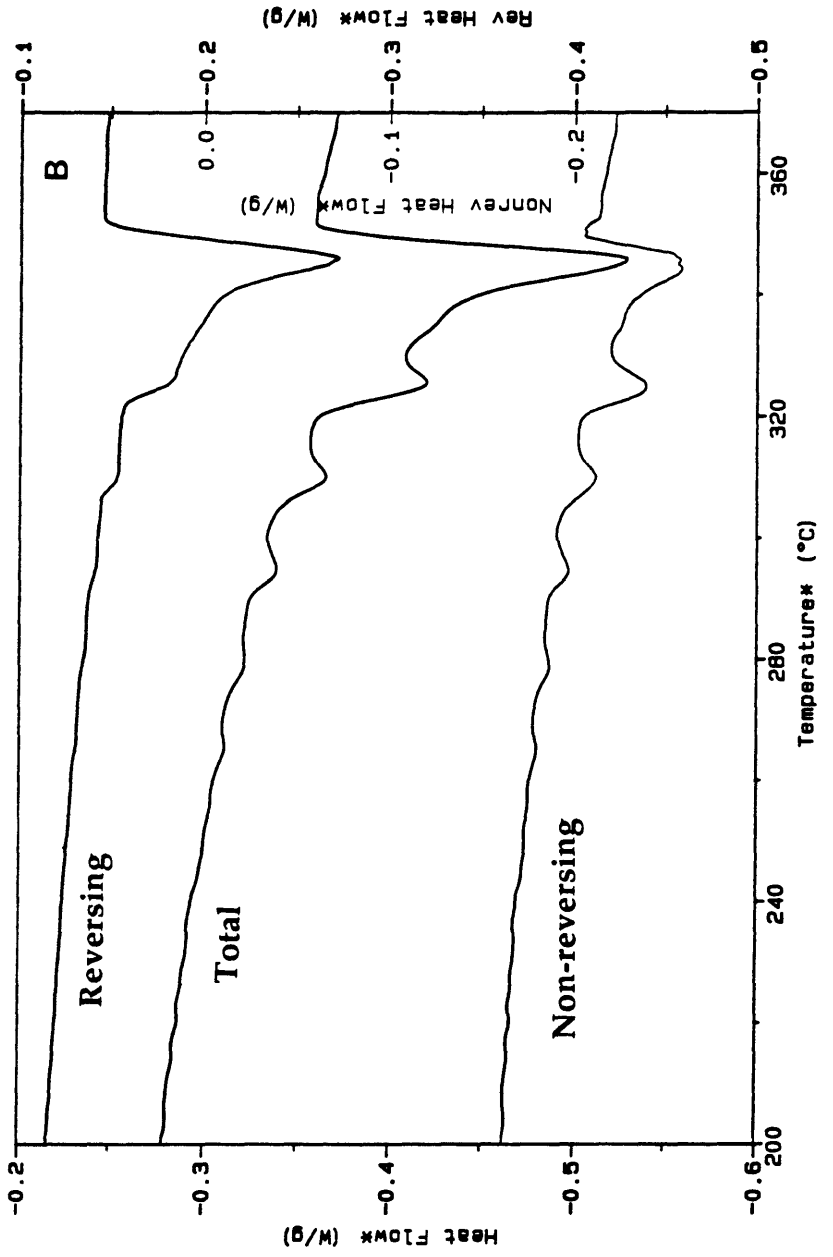

Figure 6.2.5, Continued

Multiple stage crystallization has also been observed in other semicrystalline polymers, such as PPS [114] and PEEKK [205]. The multiple endotherms are considered to come from the melting of multiple distributions of crystal lamellae having different degrees of perfection. Since the crystal lamellar thickness and crystal perfection depend strongly on the crystallization kinetics, the melting peak of the crystals will directly relate to T_c. From our MDSC results, we observe distinct melting peaks from both T and R curves, as well as the corresponding enthalpic relaxation endotherms from the NR curves. The results agree well with the single stage crystallization results, and give strong and direct support for the existence of different perfections of crystal lamellae.

Two interesting observations are obtained from the NR curves that deserve more discussion. First, no recrystallization is found after melting of the crystals formed at the lower temperatures. If the less perfect crystals were formed in an area of the sample independent of the more perfect crystals, then from the conclusions obtained from the single stage melt crystallized PEEK, we would expect recrystallization to occur after the melting of these less perfect crystals. However, after the samples were cooled from the melt and allowed to crystallize first at a higher temperature, we can assume that more perfect crystals have first formed spherulites which occupied all the space into which they can possibly grow. The crystals formed later at a lower temperature are spatially constrained by those already existing more perfect crystals. Therefore, when the samples were heated above the lower T_c, no recrystallization can be observed. A recent study by Kruger and Zackmann [201] using simultaneous SAXS and WAXS suggests that the additional melting peak is the result of melting of some thin crystals within lamellar

stacks rather than melting of complete lamellar stacks. Further TEM study may be most interesting to show this point.

Second, from both single stage and multiple stage melt crystallized PEEK, we observe multiple enthalpic relaxation peaks in the NR curves. This suggests that certain portions of the amorphous phase can be extremely rigid and relax at a temperature almost close to the crystal melting temperature. This can be explained if we consider entropic effects at the crystal surface [201]. When crystals are formed, some amorphous segments are forced to align along the crystal formation direction. Thus the entropy of the amorphous phase located at the crystal surface will be higher than that of other amorphous segments. As they are mostly constrained by the crystal phase, they can only relax when the crystals are near the melting point. Therefore, one can observe as many relaxation peaks in the NR curve as there are crystal melting peaks in the R curve.

6.2.4 CONCLUSIONS

MDSC has been used to study melt crystallization of PEEK. Single stage melt crystallized samples have shown a transition temperature between two crystallization mechanisms at 300°C. When T_c < 300°C, only one type of crystals can form, and the sample will undergo re-organization at a higher temperature. In contrast, when T_c > 300°C, two types of crystals can form, and one melts just above T_c and the other melts at a higher temperature. MDSC, as well as DSC, have been shown to be an effective way to determine T_{tran}.

Multiple stage melt crystallized samples show multiple melting peaks and relaxations. The samples contain populations of crystal lamellae with different perfection. The melting temperatures of these crystals match well with the crystallization temperatures. No recrystallization is observed in these multiple stage melt crystallized samples. The entropy effect at the crystal surface explains the existence of various amorphous relaxations in the NR curves.

Regarding the nature of the additional type of crystals that melts at the highest melting temperature observed in our single stage melt crystallized samples when T_c is above 300°C and in our multiple stage melt crystallized samples, we believe they are the dominant lamellae formed at the very early stage of crystallization. In the early stage, because the crystallization rate is slow, and no space limit or entanglement constraints are yet asserted on the polymer chains, large and perfect crystals can form. These crystals melt to form the uppermost endotherm. However, once the dominant crystals form, only thinner subsidiary crystals can form as the result of limited space and constraints from the dominant crystals. Therefore, any later forming crystals are less perfect and melt to form the lower endotherms.

Chapter 7

Summary and Suggestions for Future Work

To summarize, the relaxation behavior of both amorphous phase and RAP has been investigated using SAXS, TSDC and MDSC. It has been shown that NEW-TPI and PPS have significant differences in their structure and relaxation behavior, even though they both contain phenyl-rings in their monomer repeat units and are both used in similar applications as composite matrices and cable insulation.

NEW-TPI has been shown to be a promising thermoplastic polyimide with excellent thermal, mechanical and dielectric properties. It has the highest T_g and greatest stability against weight loss in nitrogen compared to the other high performance thermoplastics, such as PEEK, LARC-CPI and LARC-IA. It can crystallize when the temperature is above its T_g. Both isothermal and non-isothermal crystallization have been studied by SAXS.

The relaxation behavior of amorphous phase in both amorphous and semicrystalline samples show strong relaxation at T_g from TSDC experiments. No sub-T_g relaxations are observed in this material down to -80°C. The amorphous phase in semicrystalline polymer is only slightly constrained by the crystalline phase, thus it contains only a small amount of RAP. For a well crystallized semicrystalline NEW-TPI, both amorphous and crystalline phase will expand as temperature increases. Amorphous CTE is derived from the SAXS measurements for the first time. It expands four times more than the crystalline phase. The thermal expansion of amorphous phase inside the

crystal lamellae may be constrained laterally by the expansion of the crystalline phase. Amorphous phase CTE is also obtained from TMA. The values from the two measurements agree well with each other.

PPS is another very important engineering thermoplastic. Almost all the amorphous phase is found to be RAP in the film processed PPS. When this film is annealed at a temperature higher than its T_g, some of the RAP can relax and become liquid-like amorphous phase, some remains rigid, and some forms small crystals. We also obtain kinetic information concerning RAP using the advanced technique, MDSC. For the first time, we are able to link the formation of RAP to the effect of annealing. It is found that the existence of RAP increases the nominal T_g. RAP can be removed by suddenly heating the sample to a temperature T_h higher than T_c, and then quickly cooling to lower temperature. RAP can come back if the sample is re-annealed between T_g and T_h.

One interesting finding in this research is the observation of M_w effect on the crystallization behavior and mechanical properties of PPS. It is usually considered that lower M_w materials have more loose chain ends which may serve as defects resulting in poor mechanical properties. However, when amorphous sample is cold crystallized at temperatures close to T_g, we observe a higher E′ for the lower M_w sample when the sample is heated to a higher temperature. Besides, the melting temperature of the lower M_w PPS is also higher than its higher M_w counterpart. This somewhat unexpected behavior is examined using MDSC and considered to be due to the fast crystallization and reorganization rate of the lower M_w PPS.

Looking into the future research, we will continue to explore the relaxation behavior of amorphous phase and the nature of RAP in semicrystalline polymers. In addition, we want to expand the use of existing characterization techniques and develop new analytical instrumentations.

Both amorphous phase and RAP behavior must have profound effect on the ultimate properties of semicrystalline polymers and blends. Since different polymeric systems, such as polymer blends, have more complicated structures, new information may be generated providing us with more insights on these two phases. Polymer blends with one component to be a semicrystalline polymer and one to be an amorphous polymer, such as PBT/PAr, PET/PAr, and PEEK/PEI, are all interesting systems to study. Especially since we have found that MDSC can separate signals from mixed effects and complex relaxations, the relaxation behavior of these polymer blends can be better understood. It is also worth looking for other characterization techniques such as solid state NMR and neutron scattering. Besides, molecular modeling may serve as additional tool to assist our understanding in this subject.

TSDC and MDSC have been shown to be unique and effective tools to study polymer relaxation and thermal properties. Since they add new dimensions to the conventional characterization techniques, many important phenomena in the polymer field as well as many new polymeric systems can be better understood. At the same time, we must realize that both techniques are still in the developing stage. Some of the phenomena which appear during the testing are not yet well understood. Therefore, we have to be very careful in the experimental process and data interpretation. It is also

important to use conventional techniques such as DEA, DMA and DSC to study the system at the same time.

The field of high performance engineering thermoplastics is full of excitement. Lots of interesting research can be done in this area. For example, these polymers usually have high T_g and high T_m which bring the difficulty in processing. Thus blending them with liquid crystalline polymers may ease the processing. Therefore, research in the two-phase blending and three-phase blending systems would be most valuable. M_W effects on polymer structure and properties is another interesting research area as lower M_W polymer usually has lower viscosity at the same temperature compared to the higher M_W one, and therefore can be processed more easily. In addition, the M_W distribution and chain linearity will also affect polymer properties and would be another subject for future investigation.

Appendix 1

Thermally Stimulated Depolarization Current (TSDC)

A1.1 SETTING-UP THE APPARATUS

The TSDC apparatus was designed and constructed in our laboratory. Since the measured current comes from the relaxation of oriented polymer dipoles, the current value is actually not far from the theoretical limit of the measurement sensitivity. Thus design and construction of such an apparatus is critical for getting the relaxation current and not the random noise. Attempts were made to divide the whole project into six sub-systems and solve them separately before putting them together. Yet each sub-system was very closely related to the others and they had to be considered at the same time. In the following, I will describe the important considerations for each sub-system.

1) High Voltage Power Supply

In order to obtain the depolarization current, a polymer has to be poled above its T_g so that its dipoles can orient along the electric field direction. The higher the electric field, the higher the depolarization current. To achieve relatively high current signal to noise ratio, a dc power supply is required. A poling voltage of 100V is usually used in our TSDC study. An MHV connector can be connected from the output of the power supply to the TSDC cell if the sample needs to be poled.

2) Heating and Cooling System

In a typical TSDC run, the sample needs to be poled first above its T_g, and later cooled quickly at least 80°C below its T_g. Therefore, the system has to be able to be heated and cooled effectively. An Omega programmable temperature controller CN2011 is used for this purpose. It has a PID output, thus the output power is controlled by a microprocessor inside the controller proportional to the temperature difference between the actual temperature and the end temperature. The temperature profile can be input either from the front panel or from a remote computer. A Pt-RTD temperature sensor is used because it probes the average temperature of contacting surfaces. A.C. electric heating is used for fast response. Glass fiber insulated heating wire was counter-wounded around a heating cylinder to avoid any possible electromagnetic effect during the heating cycle.

3) Electrical Circuit

A high resolution electrometer is definitely required to obtain high quality data. Thus a Keithley 617 electrometer was purchased. This instrument features 4-1/2 digits display, autoranging and IEEE interface. It can measure current as small as 10^{-16}A. Low noise triaxial cable is required to connect the output of the electrometer and the body of the cell. The cable must be fixed onto some stable objects such as table or wall during the measurement.

Since the sample needs to be inside a closed environment, electric feedthroughs are required for poling and current measurement. Products from Ceramaseal are selected to carry out this task. One center connector

feedthrough is used for the current measurement and two four-conductor feedthroughs are used for the electric heating.

4) Cell Design

The main body of TSDC cell contains three layers: the outside layer is the cooling jacket, the second layer is for heating and Faraday shielding, and the center electrodes are for the current path. Only one type of material is used for the cell construction to avoid the voltage created from dissimilar metal joints. Non-magnetic 304 stainless steel is chosen for its superior hardness, corrosion resistance and poor heat conduction. Asymmetric design is avoided to the maximum extent to prevent charge creation. The diameter of disk-shaped sample holder is made slightly smaller than that of the thin layers of Au evaporated onto the polymer sample.

5) High Vacuum and Inert Gas Environment

In order to get high quality reproducible TSDC data, the sample has to stay inside a vacuum or inert gas environment to avoid moisture and possible charge movement. As we have a thermal evaporator in our lab, a brass cover is designed to fit on top of the vacuum chamber to take advantage of its high vacuum capability. A braided stainless steel hose connects the cover and the outlet of the cell. PVC and rubber hoses are not good for this purpose because they can not withstand high vacuum.

After the cell is vacuumed, inert gas is then induced into the cell through a drying tube. Helium gas is preferred than nitrogen gas for two reasons: first, since the cooling agent is liquid nitrogen, nitrogen gas if used

may condense on the cell's side wall. Second, helium conducts heat better than nitrogen because of its lower boiling temperature.

6) Data Acquisition

Taking one TSDC data run usually takes two to four hours, depending on the sample and experimental conditions. While it is not impossible to take data by hand, it would be much better if the data acquisition can be achieved by computer. An RS-232C board has been installed into the temperature controller, and the electrometer already has the IEEE interface. A computer program called 'Prague' has been written to collect the data using a 386 PC. The use of this software is described below.

Combining all the above considerations, the final design of the main body and the cover are shown in Figure A1.1a, b, respectively. A comprehensive list of materials used in the TSDC construction is shown in Table A1.1.

A1.2 OPERATION PROCEDURES

Because conducting a TSDC experiment involves poling the sample at high voltage, it is important to keep in mind the following safety precautions.

Safety precautions for TSDC

1) Wear electrically insulated gloves when you operate this machine.
2) Use lower voltage if possible. If you have to use a poling voltage higher than 36V, consult Prof. Cebe first.
3) Training is required if you want to use this instrument.
4) If you don't know, ASK!!!

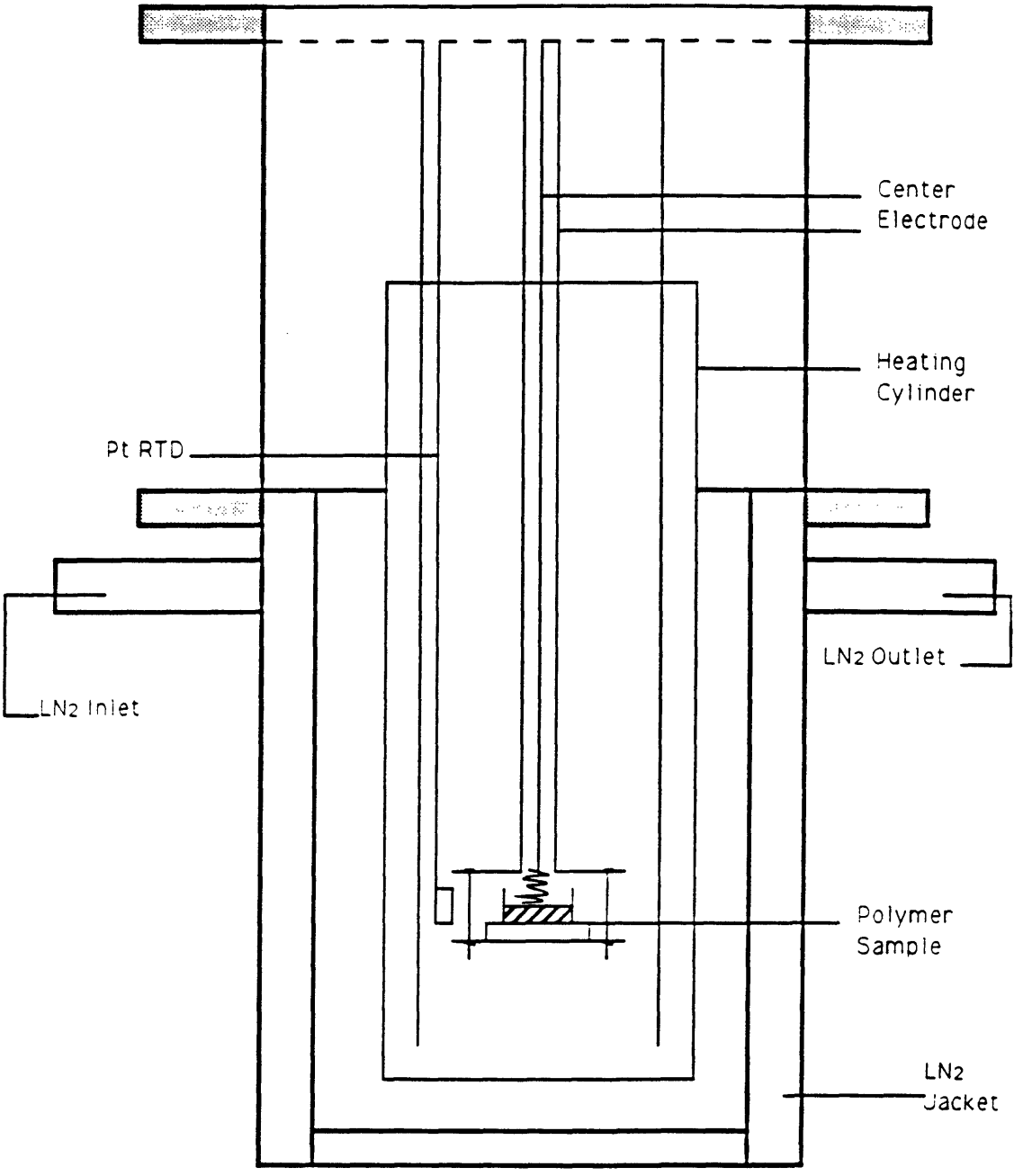

Figure A1.1 TSDC cell construction: a) main body, b) cover

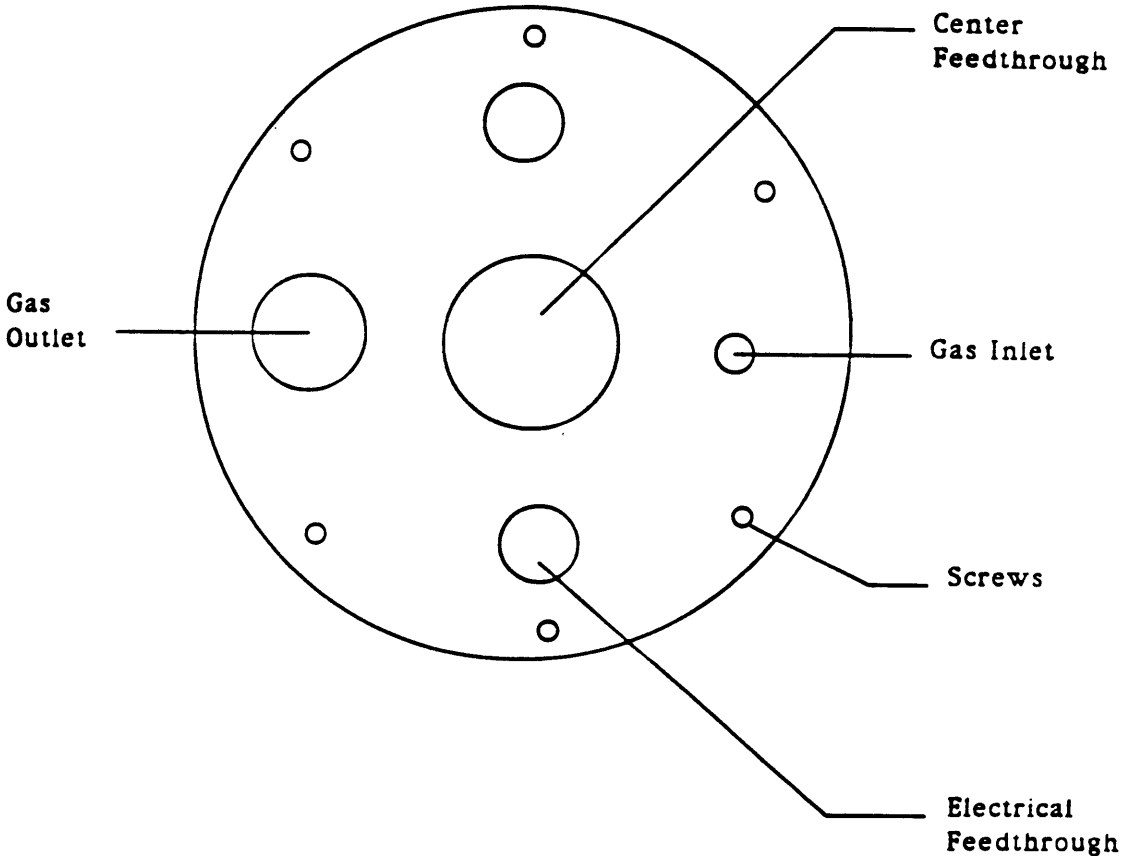

Figure A1.1, Continued

Table A1.1 List of materials used in TSDC cell construction

Materials	Company	Series/ Model No.	Features
Electrometer	Keithley	617	4-1/2 digits, current resolution 10^{-16}A
Connector	Keithley	6147	2-slot triax to BNC adaptor
Connector	Keithley	6146	2-slot triax tee adapter
Cable	Keithley	7025-10	low noise triax input
Temperature Controller	OMEGA	CN-2011	ramp & soak, programmable, Pt-RTD sensor, RS-232C communication
Temperature Sensor	OMEGA	DP116-MC1	Pt-RTD sensor, range -200°C to 850°C
Electric Feedthrough	Ceramaseal	807B 8177-02-w	stainless steel rod, adapter design, bakeable to 400°C
MHV Connector	Ceramaseal	807B 8177-02-w	floating shield, adapter, vacuum flange
Heating Wire	ACE Glass	12065	maximum temperature 596°C, glass fiber insulation
Power Supply	EG&G ORTEC	456	either polarity of output voltage, 50-3000V, build-in overload & short-circuit protection
Connector	Kings	KV-99-27	right-angle, M-BNC to M-MHV
O-rings	Parker	_ _	depends on applications, temperature range, etc.
Valves	MDC	AV-103M	ultra-high vacuum application, Viton O-ring, sealed poppets, manually operated
Flanges	MDC	K050-CA	complete hinged clamp assemblies
Fittings	MDC	K075-C	hinged clamps, aluminum
Hose	MDC	KFRL-075-181-2	braided, 304 stainless steel, flexible, K-075 kwik-flange both ends
Disconnects	MDC	410003	stainless steel quick-disconnects
S. S. Tube, Rod	MIT	_ _	hardness, corrosion resistance
Brass Plate	MIT	_ _	hardness
Helium Gas	MIT	_ _	99.999% purity

The following is a general procedure for conducting a global TSDC experiment. We want to first heat the sample to T_p, start poling the sample at T_p, hold at T_p for t_p, then cool the sample to T_o. At T_o, we want to disconnect the voltage supply, short the two electrodes, and start heating the sample and record the current and temperature data simultaneously.

TSDC operation procedures

1) Load the sample onto the sample holder. Tighten the two screws.
2) Put on the heating cylinder. Screw it using the four screws provided. Connect the heating wires to the corresponding feedthrough copper leads.
3) Put the inner cell into the outer shell. Screw the the six screws onto the top cover. Close the gas inlet valve of the cell.
4) Vacuum the cell. (See procedure on thermal evaporation).
5) Connect a ground wire between electrometer and the outer shell of the cell. Tighten the six screws a little bit more.
6) Set the heating parameters for the temperature controller.
7) Open helium tank valve. Connect the helium hose to the gas inlet of the cell.
8) After vacuum goes to 7×10^{-5} Torr, close the stainless steel valve on top of the brass cover. Open the green valve to inlet the helium gas for a couple of seconds and close it.
9) Press the 'START' on temperature controller to start the heating process. Turn on the heat gun and put some insulation around the outer cell if the end temperature is above 180°C.
10) Plug the high voltage power supply's output connector into the center feedthrough of the cell. Set the voltage to correct value.

11) When the temperature gets close to T_p, press 'EMIS' to turn off the cold cathode gauge. Close the diffusion pump valve. Open the stainless steel valve. Vacuum the chamber to low vacuum. Turn the high voltage power supply switch on. Record the time for poling. The temperature show be constant now.

12) Wait until 2 min before t_p and poling is finished, vacuum the cell to high vacuum. Pour LN_2 into the outer jacket.

13) When t_p has been reached, press 'STOP' on the temperature controller. Close the stainless steel valve. Immediately open the green helium valve to inlet the helium gas. The temperature should drop immediately.

14) Keep adding more LN_2 until the temperature drops to T_o. Use heating gun's cooling fan if necessary.

15) Reset the temperature controller for ramping process.

16) At T_o, turn off the high voltage power supply. Quickly unplug it and use some conductive metal, such as a screw driver, to short the inner and outer electrodes. Connect triaxial connector to the center feedthrough of the cell. Make sure all the connections are good. Take off the ground wire.

17) Turn on the temperature controller. Set the electrometer to current measurement and start recording the data.

18) Use PC to record the temperature and current data automatically.

Collecting TSDC data using PC

1) Connect Keithley 617 electrometer to the GPIB-PCIIA port of the PC. Connect Omega temperature controller to the LP1 (Temperature Controller /Hot Stage) port of the PC.

2) The computer program is in the sub-directory 'prague'. Type 'cd prague' under 'c:>' to get in.

3) The following is the computer program 'samp.par' for the operation of 'prague.exe' to collect both the temperature and current simultaneously. One needs to edit this program in order to tell the computer how to take the data and where to save the data. For a typical data collection process, those parameters that are often changed are typed in underlined letters in the following.

'Samp.par'

#The is a sample parameter file for prague.exe
#Any line, or part of a line, after '#' is considered comments
#Each parameter occupy one line,
and is expressed using three fields: type, name and value
#Valid types are: i (integer), f (floating point),
d (double precision floating point),
n (file name, i.e. continuous un-quoted string)
#Parameter names are limited to 16 characters of continuous un-quoted
string.
#Floating point values have to have decimal point.

#sampling period; in seconds
i SampPer 30
#1 Hz operation is unstable due to electrometer conversion delay.

#total sample points
i DPC 10

```
#start (begin) condition:
#       set both resulted in && (wait for Kb first, then temp)
#keyboard start enable
i SKbE 1

#keyboard start character
n SKbC s

#temperature start;
#       condition derived from hi lo temp bound and ramp direction
i STE  0

# AND the two start conditions?
i SAnd 0

#lower temperature bound; only useful to 1/10 degree centigrade
f TbLo  0.0

#high temperature bound;
f TbHi  250.0

#ramp direction: +1 for heating, -1 cooling
i RampDir +1

#termination condition:
#keyboard termination enable
```

i TKbE 1

#keyboard termination character

n TKbC t

#data point count termination enable

i TDPE 0

#temperature termination enable

i TTE 0

#output file name

n OpFN test.dat

3) After the 'samp.par' has been modified and saved, one can start to collect the data by running 'prague test.dat' under 'c:\prague>'.

4) After the experiment is finished, one can quite the program.

5) The data file is designed to be read by Mac. Bring the disk to our Mac that has the data file in it. Using Macrosoft Word™ to 'open' the data file. Highlight the whole file, 'copy' it, then 'past' it into the Cricket Graph™.

Bibliography

1. Flory, P.J. 'Principles of Polymer Chemistry', Cornell University Press, Ithaca, 1990.
2. Hiemenz, P.C. 'Polymer Chemistry', John Wiley & Sons, New York, 1980.
3. Young, R.J. 'Introduction to Polymers', Chapman & Hall, New York, 1980.
4. Wunderlich, B. 'Macromolecular Physics', Vol. 2, Academic Press, New York, 1976.
5. Cebe, P. and Chung, S.Y. *J. Mater. Sci.* 1990, **25**, 2367.
6. CERIUS^{TM} 'Version 3.2 Updated Software Manual', Molecular Simulations Inc., 1993.
7. POLYGRAF^{TM} 'Version 3.1 Reference Manual', Molecular Simulations Inc., 1993.
8. Brillhart, M.V. M.S. Thesis (Massachusetts Institute of Technology, Cambridge, MA, 1993).
9. Cheng, Y.Y. Ph.D. Thesis, (Massachusetts Institute of Technology, Cambridge, MA, 1994).
10. Tsukruk, V. *Polymer* 1992, **33**, 2610.
11. Nitzsche, S.A., Wang, Y.K. and Hsu, S.L. *Macromol.* 1992, **25**, 2397.
12. Cargill, G.S. III 'Solid State Physics', Vol. 30, Academic Press, New York, 1975.
13. Flory, O.J *J. Ame. Chem. Soc.* 1962, **84**, 2587.
14. Roe, R.J. *J. Chem. Phys.* 1974, **60**, 4192.
15. DiMarzio, E.A. and Guttman, C.M. *Polymer* 1980, **21**, 734.
16. Popli, R. and Mandelkern, R. *Polym. Bul.* 1983, **9**, 260.
17. Mansfield, M.L. *Macromol.* 1983, **16**, 914.
18. Flory, P.J., Yoon, D.Y. and Dill, K.A. *Macromol.* 1984, **17**, 862.
19. Yoon, D.J. and Flory, P.J. *Macromol.* 1984, **17**, 868.
20. Kumar, S.K. and Yoon, D. *Macromol.* 1989, **22**, 3458.
21. Kumar, S.K. and Yoon, D. *Macromol.* 1989, **22**, 4098.
22. Kumar, S.K. and Yoon, D. *Macromol.* 1991, **24**, 5414.

23. Gibbs, J.W. 'The Scientific Papers of J. Willard Gibbs', Dover, New York, 1961.
24. Blythe, A.R. 'Electrical Properties of Polymers', Cambridge University Press, Cambridge, 1979.
25. Mort, J. and Pfister, G. 'Electrical Properties of Polymers', John Wiley & Sons, Inc., New York, 1982.
26. Rabek, J.F. 'Experimental Methods in Polymer Chemistry', John Wiley & Sons, New York, 1980.
27. Fava, R.A. 'Methods of Experimental Physics', Academic Press, New York, 1980.
28. Wendlandt, W.W. and Gallagher, P.K. *Instrumentations*, Wunderlich, B. *The Basis of Thermal Analysis* in 'Thermal Characterization of Polymeric Materials', Turi, E.A., Ed., Academic Press, Inc., New York, 1981.
29. Suzuki, H., Grebowicz, J. and Wunderlich, B. *Macromol. Chem.* 1985, **186**, 1109.
30. Loufakis, K. and Wunderlich, B. *Macromol.* 1987, **20**, 2474.
31. Lau, S.F. and Wunderlich, B. *J. Polym. Sci., Polym. Phys. Ed.* 1984, **22**, 379.
32. Grebowicz, J., and Lau, S.F. and Wunderlich, B. *J. Polym. Sci., Polym. Symp.* 1984, **71**, 19.
33. Cheng, S.Z.D. and Wunderlich, B. *Macromol.* 1987, **20**, 1630.
34. Cheng, S.Z.D., Wu, Z.Q. and Wunderlich, B. *Macromol.* 1987, **20**, 2802.
35. Cheng, S.Z.D., Cao, M.Y. and Wunderlich, B. *Macromol.* 1986, **19**, 1868.
36. Cheng, S.Z.D., Pan, R. and Wunderlich, B. *MaKromol. Chem.* 1988, **189**, 2443.
37. Huo, P.P. and Cebe, P. *Colloid Polym. Sci.* 1992, **270**, 840.
38. Huo, P. and Cebe, P. *J. Polym. Sci., Polym. Phys. Ed.* 1992, **30**, 239.
39. Huo, P. and Cebe, P. *Macromol.* 1992, **25**, 902.
40. Bassett, D.C. 'Principles of Polymer Morphology', Cambridge University Press, Cambridge, 1981.
41. Feigin, L.A. and Svergun, D.I. 'Structure Analysis by Small-Angle X-ray and Neutron Scattering', Taylor, G.W., Ed., Plenum Press, New York, 1987.
42. Glatter, O. and Kratky, O. 'Small Angle X-ray Scattering', Academic Press Inc., New York, 1982.

43. Koberstein, J.T., Morra, B. and Stein, R.S. *J. Appl. Cryst.* 1980, **13**, 34.
44. Russell, T.P., Ito, H. and Wignall, G.D. *Macromol.* 1988, **21**, 1703.
45. Strobl, G.R. and Schneider, M.J. *J. Polym Sci., Polym. Phys. Ed.* 1980, **18**, 1343.
46. Porod, G. and Kolloid, Z.Z. *Polymer* 1951, **124**, 83.
47. Debye, P., Anderson, H.R. and Brumberger, H. *J. Appl. Phys.* 1957, **28**, 679.
48. Hedvig, P. 'Dielectric Spectroscopy of Polymers', Hilger, A. Ed., John Wiley & Sons, New York, 1977.
49. Chelkowski, A. 'Dielectric Physics', Elsevier Sci. Pub. Co., Amsterdam, 1980.
50. Huo, P. Ph.D. Thesis (Massachusetts Institute of Technology, Cambridge, MA, 1993).
51. McCrum, N.C., Read, B.E. and Williams, G. 'Anelastic and Dielectric Effects in Solids', John Wiley, New York, 1967.
52. Cebe, P. and Huo, P. *Thermochimica Acta* 1994, **238**, 229.
53. Braunlich, P. 'Thermally Stimulated Relaxation in Solids', Springer-Verlag, Berlin, 1979.
54. van Turnhout, J. 'Thermally Stimulated Discharge of Polymer Electrets', Elsevier, Amsterdam, 1975.
55. Saffell, J.R., Matthiesen, A., McIntyre, R. and Ibar, J. P. *Thermochimica Acta* 1991, **192**, 243-264.
56. Ibar, J.P., Denning, P., Thomas, T., Bernes, A., de Goys, C., Saffell, J.R., Jones, P. and Lacabanne, C. *Adv. in Chem. Series No. 227, Polym. Character.: Phys. Prop., Spectroscopic, and Chromatographic Methods* American Chemical Society, 1990, **227**, 167.
57. Bucci, C. and Fieschi, R. *Phys. Rev. Lett.* 1964, **12**, 16.
58. Jostopoulos, D., Varotsos, P. and Mourikis, S. *J. Phys., C., Solid State* 1980, **13**, 3303.
59. Cava, R.J., Fleming, R.H., Rietman, E.A., Dunn, P.G. and Scheenmeyer, L.F. *Phys. Rev. Lett.* 1984, **53**, 1677.
60. Muccilo, R. and Campos, L.L. *Phys. Stat. Sol., A.* 1980, **52**, K183.
61. von Bardeleben, H.J., Sehwab, C., Scharager, C., Muller, J.C., Siffert, P. and Feigelson, R.S. *Phys. Stat. Sol., A* 1980, **58**, 143.
62. Hong, C.M. and Day, D.E. *J. Mater. Sci.* 1979, **14**, 2493.
63. Hong, C.M. and Day, D.E. *J. Appl. Phys.* 1979, **50**, 5355.

64. Vanderschueren, J. Ph.D. Thesis (University of Liege, Belgium, 1974).
65. Lacabanne, C. Ph.D. Thesis (University of Toulouse, France, 1974).
66. Chatain, D. Ph.D. Thesis (University of Toulouse, France, 1974).
67. Chen, R. and Kirsh, Y. 'Analysis of Thermally Stimulated Processes', Pergamon Press, Oxford, 1981.
68. Ku, C.C. and Liepins, R. 'Electrical Properties of Polymers', Hanser Publishers, Munich, 1987.
69. Sauer, B.B. and Avakian, P. *Polymer* 1992, **33**, 5128.
70. del Val, J.J., Alegria, A., Colmenero, J. and Barandiaran, J.M. *Polymer* 1986, **27**, 1771.
71. Bernes, A., Chatain, D. and Lacabanne, C. *Polymer* 1992, **33**, 4682.
72. Sauer, B.B., Avakian, P., Starkweather, H.W. and Hsiao, B.S. *Macromol.* 1990, **23**, 5119.
73. Brostow, W., Kaushik, B.K., Mall, S.B. and Talwar, I.M. *Polymer* 1992, **33**, 4687.
74. Sauer, B.B. and Hsiao, B.*J. of Polym. Sci.: Polym. Phys.* 1993, **31**, 917.
75. Sauer, B.B., Avakian, P. and Cohen, G.M. *Polymer* 1992, **33**, 2666.
76. Sauer, B.B., Beckerbauer, R. and Wang, L. *J. of Polym. Sci: Polym. Phys.* 1993, **31**, 1861.
77. Tanaka, T., Hayashi, S., Hirabayashi, S. and Shibayama, K. *J. Appl. Phys.* 1978, **49**, 2493.
78. Chafai, A., Chatain, D., Dugas, J., Lacabanne, C. and Vayssie, J. *J. Macromol. Sci, Phys.* 1983, **B22**(5&6), 633.
79. Talwar, I.M., Sinha, H.C. and Srivastava, A.P. *Thin Solid Films* 1984, **113**, 251.
80. Dechesne, J.P., Vanderschueren, J. and Jaminet, F. *J. Pharm. Belg.* 1984, **39**, 341.
81. Mourgues-Martin, M., Bernes, A., Lacabanne, C., Nouvel, O. and Seytre, G. *IEEE Transactions on Electrical Insulation* 1992, **27**, 795.
82. Bernes, A., Boyer, R.F., Chatain, D., Lacabanne C. and Ibar, J.P. *Thermally Stimulated Current Studies of Transitions in Amorphous Polymers*, in 'Order in the Amorphous State of Polymers', Keinath, S.E., Ed., Plenum Press, London, 1987, p. 305.
83. Reading, M., Hahn, B.K. and Crowe, B.S. US Patent 5,346,306, 1994.
84. Marcus, S.M. and Reading, M. US Patent 5,335,993, 1994.
85. TA Instruments, Inc. 'Modulated DSC Workshop', 1994.

86. Wunderlich, B., Jin, Y. and Boller, A. *Thermochim. Acta.* 1993, **238**, 277.
87. Jin, Y., Boller, A. and Wunderlich, B. *J. Thermal Analysis* submitted, 1993.
88. Boller, A., Jin, Y. and Wunderlich, B. J. *Thermal Analysis* 1994, **42**, 307.
89. Hergenrother, P.M. 'SPE Conference on High Temperature Polymers and Their Uses', Case Western Reserve University, October 2-4, 1989.
90. Okuyama, K., Sakaitani, H. and Arikawa, H. *Macromol.* 1992, **25**, 7261.
91. Hou, T.H. and Reddy, R.M. *SAMPE Quarterly* 1991, **22**(2), 38.
92. Huo, P.P. and Cebe, P. *Polymer* 1993, **34**, 696.
93. Huo, P.P., Friler, J.B. and Cebe, P. *Polymer* 1993, **34**, 4387.
94. Friler, J.B. and Cebe, P. *Polym. Eng. Sci.* 1993, **33**, 587.
95. Aihara, Y. and Cebe, P. *Polym. Eng. Sci.* 1993, **34**, 1275.
96. Brillhart, M. and Cebe, P. *J. Polym. Sci., Polym. Phys. Ed.* accepted, 1994.
97. Lu, S.X., Cebe, P. and Capel, M. *J. Appl. Polym. Sci.* in press, 1995.
98. Hsiao, B., Sauer, B. and Biswas, A. *J. Polym Sci., Polym. Phys. Ed.* 1993, **32**, 737.
99. Mitsui Toatsu Chem., Inc. Tokyo, Japan. Technical Data Sheet A-00.
100. Yuasa, S., Truji, M. and Takahashi, T. *Polym. Prepr. Jpn.* 1991, **40**, 491.
101. Hirade, T., Hama, Y., Sasuga, T. and Seguchi, T. *Polymer* 1991, **32**, 2499.
102. Sasuga, T. *Polymer* 1991, **32**, 1539.
103. Sauer, B.B. and Hsiao, B.S. *Polymer* 1993, **34**, 3315.
104. Blizard, K.G. and Haghighat, R.R. *Polym. Eng. Sci.* 1993, **33**, 799.
105. Miyazaki, N., Hamao, T. and Munakata, T. *J Soc. Mat. Sci., Jpn.* 1994, **43**, 457.
106. Lu, S.X., Cebe, P. and Capel, M. *Polymer*, submitted.
107. Cebe, P. and Hsiao, B.S. *Polyimides, NEW-TPI: Semicrystalline Thermoplastic*, in 'The Polymeric Materials Encyclopedia: Synthesis, Properties and Applications', Salamone, J., Ed., CRC Press, Boca Raton, Fl, in press, 1995.
108. Brady, D.J. *J. App. Polym. Sci.* 1976, **20**, 2541.
109. Tabor, B.J., Magre, E.P. and Boon *Eur. Polym. J.* 1971, **7**, 1127.
110. Lopez, L.C. and Wilkes, G.L. *Polymer* 1988, **29**, 106.
111. Lopez, L.C., Wilkes, G.L. and Geibel, J.F. *Polymer* 1989, **30**, 147.
112. Chung, J.S. and Cebe, P. *J. Polym. Sci., Polym. Phys. Ed.* 1992, **30**, 163.
113. Chung, J.S. and Cebe, P. *Polymer* 1992, **33**, 2312.
114. Chung, J.S. and Cebe, P. *Polymer* 1992, **33**, 2325.

115. Lovinger, A.J., Padden, F.J. and Davis, D.D. *Polymer* 1984, **29**, 229.
116. Lovinger, A.J., Davis, D.D. and Padden, F.J. *Polymer* 1985, **26**, 1595.
117. Menczel, J.D. and Collins, G.L. *Polym. Eng. Sci.* 1992, **32**, 1264.
118. Collins, G.L. and Menczel, J.D. *Polym. Eng. Sci.* 1992, **32**, 1270.
119. Huo, P.P., Chung, J.S. and Cebe, P. *Polym. Composites* 1992, **13**, 346.
120. Cebe, P. and Chung, S. *Polym. Composites* 1990, **11**, 265.
121. Lopez, L.C. and Wilkes, G.L. *J. Macromol. Sci., Rev. Macromol. Chem. Phys.* 1989, **C29**, 83.
122. Geibel, J.F. and Campbell, R.W. *Polymers, Polyarylene sulfide* In 'Encyclopedia of Chemical Processing and Design', Marcle Dekker, New York, 1992, Vol. 40, p. 94.
123. Geibel, J.F. and Campbell, R.W. *Poly(phenylene sulfide)s* In 'Comprehensive Polymer Science', Pergamon Press, 1989, Vol. 5, p. 543.
124. Cebe, P. *Polymers and Polymer Composites* in press, 1995.
125. Muellerleile, J. and Wilkes, G. *Polymer Comm.* 1991, **32(6)**, 176.
126. Muellerleile, J., Risch, B., Rodrigues, D. and Wilkes, G. *Polymer* 1993, **34(4)**, 789.
127. Cheng, S., Wu, Z., Eashoo, M., Hsu, S. and Harris, F. *Polymer* 1991, **32(10)**, 1803.
128. Cheng, S., Park, J., Lee, C. and Harris, F. *American Chemical Society, Polym. Preprints* 1993, **34**, 774.
129. Cheng, S., Mittleman, M., Janimak, J., Shen, D., Chalmers, T, Lien, H., Tso, C., Gabori, P. and Harris, F. *American Chemical Society, Polym. Preprints* 1992, **33**, 449.
130. Matlab Reference Guide, The Math Works Inc., Natick, MA, 1992.
131. Hsiao, B.S., Gardner, K.H., Wu, D.Q. and Chu, B. *Polymer* 1993, **34**, 3986.
132. Hsiao, B.S., Gardner, K.H., Wu, D.Q. and Chu, B. *Polymer* 1993, **34**, 3996.
133. Santa Cruz, C., Stribeck, N. and Zachmann, H.G. *Macromol.* 1991, **24**, 5980.
134. Song, H.H., Stein, R.S., Wu, D.Q., Ree, M., Phillips, J.C., LeGrand, A. and Chu, B. *Macromol.* 1988, **21**, 1180.
135. Song, H.H., Wu, D.Q., Chu, B., Satkowski, M., Ree, M., Stein, R.S. and Phillips, J.C. *Macromol.* 1990, **23**, 2380.
136. Tashiro, K., Satkowski, M.M., Stein, R.S., Li, Y., Chu, B. and Hsu, S.L. *Macromol.* 1992, **25**, 1809.

137. Hoffman, J.D., Davis, G.T. and Lauritzen, I. In 'Treatise on Solid State Chemistry', Hanney, N.B., Ed., Plenum Press, New York, 1976.
138. Blundell, D.J. and Osborn, B.N. *Polymer* 1993, **24**, 953.
139. Keller, A. IUPAC Int. Symp., *Macromol. Proc.* Florence, 1980, p. 135.
140. Lu, S.X., Russell, W.C. and Cebe, P. 'Proc. of Mat. Res. Soc., Symp. on Crystallization and Related Phenomena in Amorphous Materials: Ceramic, Metal, Polymers, and Semiconductors', M. Libera, T.E. Haynes, P. Cebe and J.E. Dickinson, Eds., 1994, **321**, 197.
141. Lu, S.X. and Cebe, P. *American Chemical Society, Proc. of the Div. of Polym. Mats. Sci.& Eng.* 1994, **70**, 443.
142. J. van Turnhout, *Polym. J.* 1971, **2**, 173.
143. Kumar, N. and Chand, S. *Physics Letters A* 1986, **119**, 185.
144. Attwood, T.E., Dawson, P.C., Freeman, J.L., Hoy, R,J., Rose, J.B. and Staniland, P.A. *Polymer* 1981, **22**, 1096.
145. Dawson, P.C. and Blundell, D.J. *Polymer Reports* 1980, **21(5)**, 577.
146. Rueda, D.R., Ania, F., Richardson, A., Ward, I.M., and Balta-Calleja, F.J. *Polymer Comm.* 1983, **24(9)**, 258.
147. Hay, J.N., Kemmish, D.J., Langford, J.I. and Rae, A.I.M. *Polymer Comm.* 1984, **25(6)**, 175.
148. Lovinger, A.J. and Davis, D.D. *J. Appl. Phys.* 1985, **58**, 2843.
149. Cebe, P. and Hong, S.-D. *Polymer* 1986, **27(8)**, 1183.
150. Lovinger, A.J. and Davis, D.D. *Macromol.* 1986, **19**, 1861.
151. Zoller, P., Kehl, T.A., Starkweather, H.W. and Jones, G.A. *J. Polym Sci., Polym. Phys. Ed.* 1989, **27**, 993.
152. Hay, J.N., Langford, J.I. and Lloyd, J.R. *Polymer* 1989, **30**, 489.
153. Choy, C.L. and Leung, W.P. *J. Polym Sci., Polym. Phys. Ed.* 1990, **28**, 1965.
154. Abraham, R.J. and Haworth, I.S. *Polymer* 1991, **32**, 121.
155. Blundell, D.J. and D'Mello, J. *Polymer* 1991, **32**, 304.
156. Nishino, T., Tada, K. and Nakamae, K. *Polymer* 1992, **33(4)**, 736.
157. Kruger, K.N. and Zachmann, H.G. *Macromol.* 1993, **26**, 5202.
158. Hay, J.N., Rae, A., Langford, J.I. and Kemmish, D.J. *Polym. Communications* 1985, **26**, 283.
159. Hsiao, B.S., Cheng, I.Y. *American Chemical Society Polymer Preprints* 1991, **32**, 264.
160. Roger, J.H. *American Chemical Society Polymer Preprints* 1991, **32**, 262.

161. Gardner, K.C., Hsiao, B., Matheson, R.R. and Wood, B.A. *Polymer* 1992, **33**, 2483.
162. Hergenrother, P.M., Wakelyn, N.T. and Havens, S.J. *J Polym. Sci., Polym. Chem. Ed.* 1987, **25**, 1093.
163. Hergenrother, P.M., Wakelyn, N.T. and Havens, S.J. *J Polym. Sci., Polym. Chem. Ed.* 1989, **27**, 1161.
164. Hergenrother, P.M., Beltz, M.W. and Havens, S.J. 'International SAMPE Symposium and Exhibition Book 1', SAMPE, Covina, 1989, p 963.
165. Hergenrother, P.M. and Havens, S.J. *SAMPE J.* 1988, **24**, 13.
166. Hergenrother, P.M. and Havens, S.J. *High Performance Polym.* 1993, **5**, 177.
167. Progar, D.J. and St. Clair, T.L. *J Adhesion Sci. Technol.* 1990, **4**, 527.
168. Progar, D.J. and St. Clair, T.L. *NASA Tech. Memo.* 1990, NASA-T102586, 39.
169. Teverovsky, J.B., Rich, D., Aihara, Y. and Cebe, P. *J Appl. Polym. Sci.* 1994, **54**, 497.
170. Rich, D.C., Huo, P.P., Liu, C. and Cebe, P. *American Chemical Society Polym. Mater. Sci. Eng.* 1993, **68**, 124.
171. Cebe, P. unpublished data.
172. Friler, J.B. M.S. Thesis (Massachusetts Institute of Technology, Cambridge, MA, 1991).
173. McHerron, D.C. and Wilkes, G.L. *J. Appl. Polym. Sci.* 1992, **46**, 1313.
174. Numata, S., Fujisaki, K. and Kinjo, N. *Polymer* 1987, **28**, 2282.
175. Numata, S., Oohara, S., Fujisaki, K., Imaizumi, J. and Kinjo, N. *J. Appl. Polym Sci.* 1986, **31**, 101.
176. Numata, S., Oohara, S., Imaizumi, J. and Kinjo, N. *Polym. J.* 1985, **17**, 981.
177. Numata, S. and Miwa, T. *Polymer* 1989, **30**, 1170.
178. Huo, P.P., Cebe, P. and Capel, M. *J. Polym. Sci., Polym. Phys. Ed.* 1992, **30**, 1459.
179. Russell, T. Private communication.
180. Scott, C. Private communication.
181. Hsiao, B.B, Chang, I.Y. and Sauer, B.B. *Proc. 49th SPE ANTEC*, **XXXVII**, 1991, 2084.
182. Devoy, C. and Mandelkern, L. *J. Polym. Sci. (A-2)* 1969, **7**, 1883.

183. Hoffman, J.D. and Weeks, J.J. *J. Chem. Phys.* 1962, **37**, 1723.
184. Lovering, E.G. *J. Polym. Sci. (C)* 1970, **30**, 329.
185. Hoffman, J.D. *Polymer* 1982, **23**, 656.
186. Magill, J.H. and Li, H.M. *Polymer* 1978, **19**, 416.
187. Cheng, S.Z.D. and Wunderlich, B. *J. Polym. Sci., Polym. Phys. Ed.* 1986, **24**, 595.
188. Ward, I.M. *Mechanical Properties of Polymers* John Wiley & Sons, New York, 1974.
189. Chang, S.S. *Polymer Communications* 1988, **29**, 138.
190. Lee, Y. and Porter, R.S. *Macromol.* 1987, **20**, 1336.
191. Blundell, D.J. *Polymer* 1987, **28**, 2248.
192. Bassett, D.C., Olley, R.H. and Raheil, I.A.M. *Polymer* 1988, **29**, 1745.
193. Jonas, A. and Legras, R. *Macromol.* 1993, **26**, 813.
194. Velikov, V., Verma, R., Prabhu, V., Dillard, D. and Marand, H. *American Chemical Society, Proc. of the Div. of Polym. Chem.* 1995, **36**, 344.
195. Zhou, C. and Clough, S.B. *Polym. Eng. Sci.* 1988, **28**, 65.
196. Vigier, G., Tatibouer, J., Benatmane, A. and Vassoille, R. *Colloid Polym. Sci.* 1992, **270**, 1182.
197. Nichols, M.E. and Robertson, R.E. *J. Polym. Sci., Polym. Phys. Ed.* 1992, **30**, 755.
198. Yeh, J.T. and Runt, J. *J. Polym. Sci., Polym. Phys. Ed.* 1989, **27**, 1543.
199. Marand, H. and Prasad, A. *Macromol.* 1992, **25**, 1731.
200. Lovinger, A.J., Hudson, S.D. and Davis, D.D. *Macromol.* 1992, **25**, 1752.
201. Kruger, K.N. and Zackmann, H.G. *Macromol.* 1993, **26**, 5202.
202. Sauerbrunn, S.R., Blaine, R.L. and Foreman, J.A. *Proc. of the Twenty-second Conf. of the North American Therm. Analysis Soc.*, Sept. 1993, 514.
203. Bell, J.P. and Murayama, T.J. *J. Polym. Sci.* 1969, **7**, 1059.
204. Roberts, R.C. *Polymer* 1969, **10**, 117.
205. Konnecke, K. *Angew. Makromol. Chem.* 1992, **198**, 15.